eman ta zabal zazu

Universidad del País Vasco
Euskal Herriko Unibertsitatea

Universidad del país vasco,
Facultad de ciencia y tecnología,
Departamento de Fisica Aplicada II

CIC Energigune
Power storage, batteries and supercaps

Understanding the kinetic limitations of $NaFePO_4$ as cathode active material for Na-ion batteries

by

Henri ANNE

Thesis Supervisor:

Damien SAUREL

Thesis tutor:

Tomasz BRECZEWSKI FILBEREK

2019

Acknowlegements

This thesis, as the result of several years of work, would not have been possible without collaborations from various people and institutions, whom contribution I intend here to highlight.

My first wish is to express my gratitude to the CIC Energigune for awarding me the PhD grant and hosting me along these years, in particular Teofilio Rojo for welcoming me in the Na-based batteries research line, and the members of the administrative staff of CIC Energigune: Jesús-Maria Goiri, Jose M. Castellanos, Nuria Gisbert, Begoña Ortiz de Latierro, Sara Ortiz, Iñaki Goyeneche, Asier Urzelai, Elena Vozmediano and Cristina Luengo, without which this work would not have been possible.

Then, my most sincere thanks go to my thesis director Damien Saurel, for his dedication, incredible patience, and all the fruitful discussions that guided me all along this work.

As a large part of this work consisted in laboratory work, I would like to highlight the contributions of Carlos manuel berlanga, Nuria Gomez, Begona Acebedo, Francisco Bonilla, María Jáuregui, Uxue Oteo and Begoña Silvan, who considerably helped me for material synthesis, design of experiments and material characterization. Also, I wish to thank Montse Galceran, Montse Casas-Cabanas, Miguel Angel Muñoz, Elena Gonzalo, Javier Carasco, Emilie Bekaert, Roshan Shanmukaraj Devaraj, Marine Reynaud and Amaia Saracibar, for the fruitful scientific discussions and help in the laboratory that greatly contributed to the achievement of this work.

Hereafter, I wish to express my gratitude to Francesco Nobili for accepting me at Camerino University for three months, and for the fruitful discussions we had about electrochemical characterization techniques. Also, I wish to thank Fabio Maroni and Marta Pasqualini for their help in the laboratory at this occasion.

From the University of Basque Country, I wish to express my gratitude to Tomasz Breczewski Filberek, Inigo Etxebarria and Javier Zuniga for their guidance and, of course, Itziar Ezkubi for her help in administrative matters.

Subsequently, I wish to acknowledge Dr. Neeraj Sharma, Dr. Valérie Pralong and Dr. Joel Gaubicher for reviewing this manuscript.

In less scientific matters, I would like to thank my fellow PhD students mates: Adrianna Navarro-Suarez, Morgane Giner, Antonio Fernandez, Marya Baloch and Maria-Jose Piernas for their heartwarming welcome which greatly facilitated my integration; and Michal Piszcz and Frederic Aguesse for the climbing sessions which were greatly valuable for disconnecting from work.

At last, I would like to address my warmest thanks to my wife, Angela, who always succeeded in pushing me toward the end of this work.

Table of contents

Abstract

The use of lithium-ion batteries (LIBs) for electrical energy storage has become unavoidable in the last twenty years, driven by environmental concerns and new consumer behavior, and thanks to their excellent performances compared to other electrical storage technologies. However these batteries remain relatively expensive and may face some limitations with regard to large scale production due to potential shortage of lithium. In this context a growing interest has risen in Na-ion batteries (SIBs) as potential low cost replacement to Li-ion batteries.

Since Li and Na are very similar, most of the knowledge accumulated on LIBs can be applied on SIBs and similar materials can be used, although the optimum material compositions for Na usually differ from those of Li. However, compared to their lithium counterparts, most intercalation materials used as electrodes in SIBS show poorer performances which are mainly ascribed to the fundamental differences in the interactions between the two alkali elements and the host structure, leading to kinetic limitations to the Na (de)intercalation mechanism. A deeper understanding of these differences is needed to overcome these limitations.

The main scope of this thesis is to understand the origin of the kinetic limitations to Na (de)intercalation in similar insertion compounds, by taking the Li/$NaFePO_4$ cathode material as system of study. The choice of this material is driven by is good stability, low cost and its ability to reversibly (de)intercalate both Li and Na ions with relatively good electrochemical performances, which makes it being already used in commercial LIBs, and a good candidate for commercial SIBs.

After presentation of the advantages of this material with regard to energy storage and the actual knowledge concerning Li and Na (de)intercalation within it, the theoretical background for electrochemical characterization of the (de)intercalation kinetics and the experimental techniques used within the present study, the experimental part of this work is divided into four axes:

- The comparison of the electrochemical performances of $LiFePO_4$/C and $NaFePO_4$/C electrodes to ascertain that kinetic limitations are at the origin of the poorer performances of the material upon Na (de)intercalation.
- The comparison of the diffusivity of Li and Na within the material at electrode scale. In this part, a thorough methodology is developed to determine accurately the diffusion coefficients of Li and Na from electrochemical techniques.
- The comparison of the activation energies for diffusion of Li and Na.
- The morphological study of cycled electrodes as possible extrinsic cause for the kinetic limitations upon Na (de)intercalation.

Resumen

El desarrollo del uso de baterías litio-ion (LIBs) para el almacenamiento de energía eléctrica ha sido inevitable en los últimos veinte años, impulsado por preocupaciones ambientales y nuevos comportamientos de los consumidores, y gracias a sus excelentes prestaciones en comparación con otras tecnologías de almacenamiento eléctrico. Sin embargo, estas baterías siguen siendo relativamente caras y pueden enfrentarse a algunas limitaciones con respecto a la producción a gran escala debido a la posible escasez de litio. En este contexto, ha aumentado el interés en las baterías Na-ion (SIBs) como un posible reemplazo de bajo coste para las baterías Li-ion.

Dado que Li y Na son muy similares, la mayor parte del conocimiento acumulado en LIBs se puede aplicar en SIBs y se pueden usar materiales similares, aunque, con mayor frecuencia las composiciones óptimas son diferentes. Sin embargo, en comparación con sus contrapartes de litio, la mayoría de los materiales de intercalación utilizados como electrodos en SIBs muestran rendimientos más pobres comparados con los de litio, que se atribuyen más a menudo a las diferencias fundamentales en las interacciones entre los dos elementos alcalinos y la estructura del material hospedante, lo que conduce a limitaciones cinéticas al mecanismo de (de)intercalación de Na. Se necesita una comprensión más profunda de estas diferencias para superar estas limitaciones.

El objetivo principal de esta tesis es la investigación del origen de las limitaciones cinéticas a la (de)intercalación de Na en compuestos de inserción similares, tomando el material de cátodo $(Li,Na)_xFePO_4$ como sistema de estudio.

La elección de este material se basa en varios factores. La contraparte de litio, $LiFePO_4$, ya se utiliza como material de cátodo comercial para LiBs, gracias a su buena estabilidad, bajo coste y su constante voltaje operativo en funcionamiento debido a su mecanismo reversible de transformación bifásica tras la inserción-extracción de Li. Además, es uno de los pocos materiales de inserción para electrodos que tiene la capacidad de (de)intercalar reversiblemente los iones Li y Na con rendimientos electroquímicos relativamente buenos, y sin necesidad de más cambios en la composición del material, lo que lo convierte en un buen sistema de estudio para comprender el origen de las limitaciones cinéticas a la (de)intercalación de Na en los electrodos de inserción en comparación con la (de)intercalación de Li. Por fin, cabe destacar que gracias a sus prestaciones teóricas relativamente buenas la contraparte de sodio, $NaFePO_4$ será un candidato prometedor como material de cátodo para NiBs comerciales, una vez superadas las limitaciones cinéticas a la (de)intercalación de Na.

Tras la (de)intercalación de Na, se observan dos mesetas de potenciales en carga (extracción) atribuidas a mecanismos de transformación solución sólida y bifásica, respectivamente, y separados por una fase estable intermedia $Na_{2/3}FePO_4$. Además, previamente a esta tesis, se había reportado una sola meseta en descarga, donde se había observado la coexistencia de las tres fases estables $FePO_4$, $Na_{2/3}FePO_4$ y $NaFePO_4$.

Después de presentar, en un capítulo introducción, las ventajas de este material con respecto al almacenamiento de energía en más en detalle, el conocimiento actual sobre la (de)intercalación de Li

y Na en este material, la base teórica para la caracterización electroquímica de la cinética de (de)intercalación y las técnicas experimentales utilizadas en el presente estudio, la parte experimental de este trabajo se divide en cuatro ejes:

- Comparación de los rendimientos electroquímicos de los electrodos $LiFePO_4$/C y $NaFePO_4$/C, para validar el proceso de preparación de los electrodos, evaluar el rendimiento de los electrodos $NaFePO_4$/C y certificar que las limitaciones cinéticas son el origen de las pobres prestaciones del material ante la (de)intercalación de Na.
- Búsqueda de la fuente de estas limitaciones cinéticas a través de técnicas electroquímicas avanzadas:
    - Difusividad efectiva de Li y Na y cinética de transferencia de carga a partir de la combinación de experimentos de PITT y PEIS.
    - Variación de la energía de activación para la difusión de Li y Na a partir de PEIS a varias temperaturas.
- El estudio morfológico de electrodos ciclados como posible causa extrínseca a las limitaciones cinéticas ante la (de)intercalación de Na, y la confirmación de la influencia de estos cambios morfológicos en los rendimientos electroquímicos de Na_xFePO_4.

Para ese propósito, se prepararon electrodos de $LiFePO_4$/C a partir de polvo comercial de $LiFePO_4$/C. Los electrodos de Na_xFePO_4/C se prepararon a partir de la delitiación electroquímica de los electrodos $LiFePO_4$/C para que, para cada técnica electroquímica utilizada en el presente estudio los resultados de las mediciones no fueran afectados por parámetros extrínsecos como la morfología del material o la arquitectura del electrodo. Estos electrodos se montaron en media celdas, con Li o Na como contra-electrodos y $LiPF_6$ o $NaPF_6$ disueltos en EC / DMC a 1M como electrolito.

Comparación de los rendimientos electroquímicos de los electrodos $LiFePO_4$/C y $NaFePO_4$/C

Las excelentes prestaciones de los electrodos $LiFePO_4$/C (100% de la capacidad teórica del material alcanzado a C/10, 90% a 1C y 55% a 20C) validaron el proceso de fabricación de los electrodos. Comparado con su contraparte de Li, $NaFePO_4$ alcanzó el 60% de su capacidad teórica a C/10, 40% a 1C y casi 0% a 20C. 1C corresponde una velocidad de carga o descarga de 1 hora para alcanzar la capacidad tórica, C/10 a 10 horas y 20C a 1/20 horas. La dependencia de la capacidad de $NaFePO_4$ a velocidad de carga y descarga bajas sugirió que se podría alcanzar una capacidad reversible más alta a velocidades más bajas, sugiriendo limitaciones relacionadas con una cinética lenta. La dependencia del potencial de reacción con la velocidad de carga y descarga permitió el cálculo de las resistencias de reacción que resultaron ser entre 5 y 10 veces más altas en el caso de la (de)intercalación de Na, confirmando que una cinética lenta es el origen de la capacidad limitada de Na_xFePO_4. Por fin, se observó una sobre-polarización de 150 mV durante la primera inserción de Na en $FePO_4$, lo que sugirió cambios morfológicos o microestructurales, ocurriendo durante este primer ciclo de inserción/extracción de Na. No sería sorprendente considerando la expansión de volumen de 17,5% del material entre sus fases sodiadas y desodiadas, en comparación a la de 6.8% entre las fases litiadas y delitiadas. Estos cambios morfológicos o microestructurales podrían ser responsables de la capacidad reversible limitada de $NaFePO_4$.

Las Técnicas de valoración intermitente potenciostática y galvanostática (Galvanostratic/Potentiostatic Intermittent Titration Technique, GITT/PITT) mostraron que solo el 80% de la capacidad teórica de $NaFePO_4$ podía lograrse de forma reversible a tasas de carga y descarga muy bajas. Mas precisamente, con estas dos técnicas, se alcanzó fácilmente el estado completamente sodiado de Na_xFePO_4 (x = 1) mientras que no fue posible alcanzar el estado completamente desodiado (x = 0), sugiriendo que la limitación era principalmente a final de carga.

Antes del principio de esta tesis, se había reportado que el proceso de inserción de Na era continuo, con la coexistencia de las tres fases estables $FePO_4$, $Na_{2/3}FePO_4$ y $NaFePO_4$. Las técnicas de valoración (GITT y PITT) permitieron establecer que consiste en dos mecanismos distintos con potenciales de reacción muy cerca uno del otro, lo que sugiere que estos dos mecanismos pueden superponerse dependiendo de la velocidad de descarga. El estudio de la dependencia del perfil de potencial de descarga a la velocidad de descarga permitió demostrar que estos dos mecanismos se separan a velocidad más alta, debido al hecho de que sus resistencias de reacción son distintas. Medidas de DRX o*perando* realizadas por otros miembros del CIC Energigune permitieron su identificación como dos mecanismos de transformación bifásica que implican $FePO_4/Na_{2/3}FePO_4$ y $Na_{2/3}FePO_4/NaFePO_4$, respectivamente. El rango de composición por el cual se observa la coexistencia de tres fases siendo simplemente el fruto del solapamiento de estos dos mecanismos bifásicos debido a sus potenciales de reacción muy cercanos.

Comparación de la difusividad efectiva de Li y Na:

Un estudio exhaustivo de estudios previamente publicados sobre este tema permitió establecer una metodología que permitiera determinar los coeficientes de difusión Li y Na en Li_xFePO_4 y Na_xFePO_4 con precisión. Este método se estableció en colaboración con la universidad de Camerino y consistió en realizar PITT en carga y descarga con baja amplitud de los pasos de valoración (25 mV), junto con medidas de espectroscopia de impedancia al final de cada paso de valoración. El coeficiente de difusión de Li y Na se determinó a partir de la evolución del corriente de la celda durante los pasos de valoración PITT, y a partir de los datos de espectroscopia de impedancia.

El coeficiente de difusión de Li se determinó en las dos fases rica en Li ($x \approx 1$) y pobre en Li ($x \approx 0$), en cuyos casos se encontraron valores relativamente cercanos. El coeficiente de difusión de Na solo pudo determinarse en la fase rica en Na ($x \approx 1$) y la fase estable intermedia ($x \approx 2/3$), debido al hecho de que la composición x = 0 no pudo ser alcanzada. A la misma composición ($x \approx 1$), el coeficiente de difusión de Na se encontró entre 10 y 20 veces menor que el de Li, indicando una menor difusividad de Na en el material del electrodo de inserción, sugiriendo que efectivamente la difusividad de Na es una posible origen de las limitaciones cinéticas en Na_xFePO_4.

Comparación de las energías de activación para la difusión de Li y Na

Con el fin de confirmar la difusividad más pobre de Na en comparación con la de Li en Li/Na_xFePO_4 ($x \approx 1$), se determinó la energía de activación para la difusión. Este parámetro representa la energía necesaria para el salto de un ion de Li o Na entre dos sitios de inserción vecinos del material huésped. Se determina a partir de la dependencia del coeficiente de difusión con la temperatura según la ley de Arrhenius, y su determinación es entonces independiente de la influencia de parámetros extrínsecos como la morfología del material o la arquitectura del electrodo.

Este parámetro se determinó tanto para Li como para Na, en todo el rango de composición de Li/Na_xFePO_4. En cada composición, se realizaron una serie de mediciones de espectroscopia de impedancia electroquímica mientras se escaneaba la temperatura de la celda. El uso del equipo de medidas físicas PPMS disponible en CIC Energigune permitió aprovechar de su control de temperatura muy preciso para realizar mediciones cada 2^oC en un rango de temperatura muy estrecho de 20^oC, lo que nunca se había reportado con anterioridad y asegura que se minimiza la deterioración del electrolito.

Se supone que la difusión de Li y Na en la estructura ideal sin defecto ocurre a lo largo de canales de difusión unidimensionales. En el caso de $LiFePO_4$, se ha demostrado que defectos antisitios Li-Fe puntuales suelen bloquear estos canales de difusión pero permiten el salto de Li entre ellos y, por lo tanto, permiten una difusividad de Li a 2 o 3 dimensiones. La concentración de estos defectos depende de la ruta de síntesis del material, pero su presencia es casi sistemática. La influencia de este tipo de defectos en la difusividad de Na no era conocida al comienzo de esta tesis.

La energía de activación de Li para su difusión en Li_xFePO_4 a $x = 0$ y $x = 1$ se encontró relativamente cerca de las predicciones teóricas para la difusión de Li^+ a lo largo de los canales de difusión unidimensionales en la estructura ideal sin defectos. A estas composiciones el material es conocido por responder como una solución sólida, en cuyo caso, como consecuencia de las leyes de Fick, la difusión se limita en la capa externa de las partículas mediante las medidas de PEIS. El hecho de que la difusión a estas composiciones no parece ser sensible a los defectos sugiere que la profundidad de esta capa externa no alcanza la distancia media entre defectos. Para las composiciones intermedias, se encontraron valores de energía de activación más grandes, relativamente cerca de las predicciones teóricas para la difusión de Li^+ asistida por defectos antisitios. A estas composiciones el material es bifásico, lo que necesariamente cambia la topología de los gradientes de composición, y entonces de la difusión. El hecho de que a estas composiciones la difusión aparece asistida por defectos sugiere que ocurre a mayor profundidad mediante las medidas de PEIS, seguramente como consecuencia de la reacción bifásica.

La energía de activación para la difusión de Na como función de la concentración de Na presentó un perfil muy similar al de Li, lo que permitió concluir que el mecanismo de difusión de Na es muy similar al de Li, íntimamente relacionado con la presencia de defectos antisitios, y permitió la determinación de las energías de activación para la difusión de Na libre de defectos a $x= 1$ y controlada por defectos antisitios a las composiciones intermediarias.

Sorprendentemente, las energías de activación para la difusión de Li y Na en Li/Na_xFePO_4 en x ≈ 1, tanto como su máximo a composiciones intermediarias (≈ 700 meV) se encontraron muy próximas, correspondiente a una relación de coeficientes de difusión un orden de magnitud menor que la de los coeficientes de difusión efectivos determinados a partir de las PITT y PEIS.

Estudio morfológico de electrodos ciclados como posible causa extrínseca de las limitaciones cinéticas durante la (de)intercalación de Na:

Cabe destacar que la determinación de los coeficientes de difusión efectivos se deduce de las medidas de PITT y PEIS teniendo en cuenta parámetros morfológicos. Estos últimos se supusieron idénticos para Li y Na siendo los electrodos y el material idénticos. Sin embargo, la discrepancia entre la energía de activación y el coeficiente de difusión efectivo podría explicarse por la ocurrencia de cambios morfológicos durante la primera inserción de Na, en acuerdo con la sobre polarización de 150 mV observada a la primera descarga a baja velocidad vs Na.

Basándose en trabajos anteriores reportados para $LiFePO_4$ y $NaFePO_4$, dos posibles manifestaciones de cambios morfológicos del material podrían ocurrir como consecuencia de la gran expansión de volumen de Na_xFePO_4 durante la (de)intercalación de Na:

- Degradación del recubrimiento de carbono en la superficie de los electrodos
- Grietas en las partículas, reportadas paralelas a la dirección (*b*) en el caso de Li y perpendiculares en el caso del Na, como consecuencia de la expansión de volumen anisotrópica distinta para Li y Na.

Estos dos cambios pueden ser correlacionados, y en el caso de Na ambos afectarían tanto la superficie electroactiva efectiva como la capacidad alcanzable porque cortan los canales de difusión en la dirección b. La observación vía TEM de partículas de Na_xFePO_4 cicladas confirmó la presencia de grietas en estas partículas, en algunas ocasiones cortando completamente las partículas por la mitad y aislando completamente algunos fragmentos de material activo del resto del volumen de las partículas.

Para confirmar que estas grietas eran realmente responsables de la difusividad más pobre de Na al nivel del electrodo en comparación con la de Li, se realizaron varios ciclos de inserción/extracción de Li en un electrodo ciclado previamente con Na, junto con mediciones de EIS realizadas al final de cada carga y descarga. A partir de este experimento, se esperaba observar en $LiFePO_4$ los mismos efectos que las grietas perpendiculares a los canales de difusión unidimensionales tenían supuestamente sobre $NaFePO_4$: mayor resistencia de transfer de carga y capacidad reversible limitada a 60% de la teórica.

La presencia de Na restante en el material, incluso después de un procedimiento de desodiacion electroquímico intenso, se demostró mediante la derivada del perfil electroquímico de los ciclos siguientes vs Li, y se confirmó por la evolución de la resistencia de transfer de carga. Este Na restante desapareció progresivamente durante los 8 siguientes ciclos vs Li, después de los cuales la capacidad vs Li se estabilizo a 90% de la capacidad inicial. Esta recuperación de 30 % de la capacidad teórica

sugiere que existe otra fuente no identificada de limitaciones cinéticas para la inserción/extracción de Na. Podría no ser relacionada con cambios morfológicos, sino intrínseca a las interacciones entre Na y el material huésped como por ejemplo una caída de la conductividad electrónica del material con bajo contenido de Na, o con la formación dinámica de defectos antisitios. Igualmente, podría estar relacionado con la geometría de separación de las distintas fases, que ocurre en el plano (*bc*) para $LiFePO_4$ y en el plano (*ac*) para $NaFePO_4$, lo que podría cambiar la consecuencia de las grietas sobre la difusión en masa efectiva. Estudios adicionales aparecen necesarios para comprobar estas hipótesis, en particular basados en métodos numéricos sobre la base de las conclusiones del presente trabajo de tesis.

Publicaciones y presentaciones en conferencias:

Se publicaron dos artículos en relación con el presente trabajo. El primero, en colaboración con el grupo de simulación computacional de CIC Energigune, estudió los potenciales de reacción de Na_xFePO_4 durante la extracción de Na. El segundo en colaboración con el grupo de materiales electroactivos avanzados del CIC Energigune, identificó el mecanismo de transformación del material mediante la inserción de Na. Un tercero manuscrito, en colaboración con la universidad de Deakin, está en el proceso de revisión.

- *Investigation of sodium insertion-extraction in olivine Na_xFePO_4 (0≤x≤1) using first principle calculations;* A. Saracibar, J. Carrasco, D. Saurel, M. Galceran, B. Acebedo, H. Anne, M. Lepoitevin, T. Rojo, M. Casas-Cabanas; Physical Chemistry Chemical Physics 18, 13045 (2016). DOI:10.1039/C6CP00762G
- *Rate dependence of the phase transformation in olivine $NaFePO_4$*; D. Saurel, M. Galceran, M. Reynaud, H. Anne, M. Casas-Cabanas; International Journal of Energy Research (2018). DOI : 10.1002/er.4078
- *Stable cycling of $NaFePO_4$ cathodes in high salt concentration ionic liquid electrolytes*; P. C. Howlett, D. Saurel, H. Anne, M. Casas-Cabanas, M. Armand, T. Rojo, D. R. MacFarlane, M. Forsyth; Submitted to J. Power Sources, under review.

La metodología de determinación de la energía de activación y los resultados obtenidos en el presente estudio se presentaron en varias conferencias internacionales:

- H. Anne, D. Saurel, *New insights into the kinetics of Na insertion/extraction into the $FePO_4$/$NaFePO_4$ system*, Lithium battery discussions, Arcachon, june 2015 (poster)
- D. Saurel, H. Anne, M. Galceran Mestres, B. Acebedo, M. Lepoitevin, T. Rojo, M. Casas-Cabanas, *New insights into the kinetics of Na insertion and extraction into the $FePO_4$/$NaFePO_4$ system*, 228th ECS meeting, Phoenix, 2015 (poster)
- D. Saurel, H. Anne, M. Galceran Mestres, B. Acebedo, M. Lepoitevin, T. Rojo, M. Casas-Cabanas, *New insights into the kinetics of Na insertion and extraction into the $FePO_4$/$NaFePO_4$ system*, International Battery Association, Nantes, 2016 (poster)
- H. Anne, D. Saurel, F. Nobili, *A comparative study of the ionic diffusion kinetics in $Li_xFePO_4$and Na_xFePO_4 for Li and Na ion batteries*, E-MRS-Fall 2016, Varsovia (oral presentation)

Varios artículos están todavía en preparación, con respecto a la anisotropía de la difusividad de Na en Na_xFePO_4 como consecuencia de la presencia de defectos antisite en la estructura cristalina; los valores de energía de activación determinados experimentalmente en el presente estudio (difusividad de Li y Na en los canales de difusión unidimensionales y a través de los defectos antisite); y el origen de las limitaciones cinéticas para la (de)intercalación de Na en Na_xFePO_4: cambios morfológicos a nivel de electrodo inducidos por la alta expansión de volumen del material.

1. Introduction

The worldwide growing energy consumption and the transformation of the energy sector due to environmental concerns and new consumer behavior are responsible for an increasing need for energy storage capacity, which led to the rise of Li-ion batteries (LIBs) over the last 25 years. Na-ion batteries (NIBs) which have the same working principles and use the same families of materials are promising low-cost alternatives to LIBs, but, to date, show poorer performances due to the differences between the two alkali ions. This study aims at understanding the fundamental differences between the (de)intercalation of lithium and sodium in similar host materials, using $LiFePO_4$/$NaFePO_4$ as a case study. The choice of this material is driven by its ability to reversibly (de)intercalate Li and Na ions with interesting electrochemical performances, and its good stability and low cost compared to other insertion materials which make it a promising cathode material for NIBs. The knowledge acquired on this system is a good base to understand the differences between lithium and sodium (de)intercalation mechanisms in other compounds.

This introduction chapter will first expose the problematic and challenges concerning energy storage and the potential technological solutions which could fulfill the growing storage capacity need. The advantages of Li-ions batteries compared to the other electrochemical energy storage systems will be presented as well as their drawbacks. The advantages and limitations of Na-ion batteries as promising low-cost alternative to Li-ion batteries will be then exposed, as well as the advantages of

$NaFePO_4$ as cathode material. At last, the actual knowledge concerning Li/Na (de)intercalation within Li/$NaFePO_4$, that was available at the beginning of this PhD thesis work, will be presented.

1.1. Energy production and storage overview

1.1.1. Market estimations

The world energy consumption was estimated to about 375 quadrillion British thermal units (Btu)[i] in 1990. Twenty-five years later, after an almost constant increase of 5 % every five years, it had reached 575 quadrillion Btu and is expected to increase by about 10% every five years in the next twenty five years to reach 736 quadrillion Btu in 2040. As seen in Figure 1-1 (a) this increase shall be mainly driven by non OECD countries such as China or India.[1]

As can be observed from Figure 1-1 (b), the main sources of energy are fossil fuels (coal, peat, oil and natural gas), nuclear and renewable (hydro, solar, wind and biomass), with natural gas and renewable sources expected to have an increasing weight in the forthcoming years.

The growth of renewable energy production led by environmental concerns is expected to be one of the fastest in the next twenty-five years to gradually replace fossil fuels, mainly coal, blamed for their high CO_2 emissions, although it would still remain about 15 % of the total energy produced.[1] The principal emerging renewable power sources are solar and wind, transformed into electric energy by solar plants or wind farms.[1]

The three main sectors for energy consumption are buildings, transport and industry. The industrial sector consumes more than half of the worldwide energy while transport and buildings consume almost half of the rest each.[1] More than 99 % of the total energy consumed in the transport sector is provided by fossil fuels and natural gases.[1]

[i] 1 quadrillion BTU = 2.93 e^{14}Wh

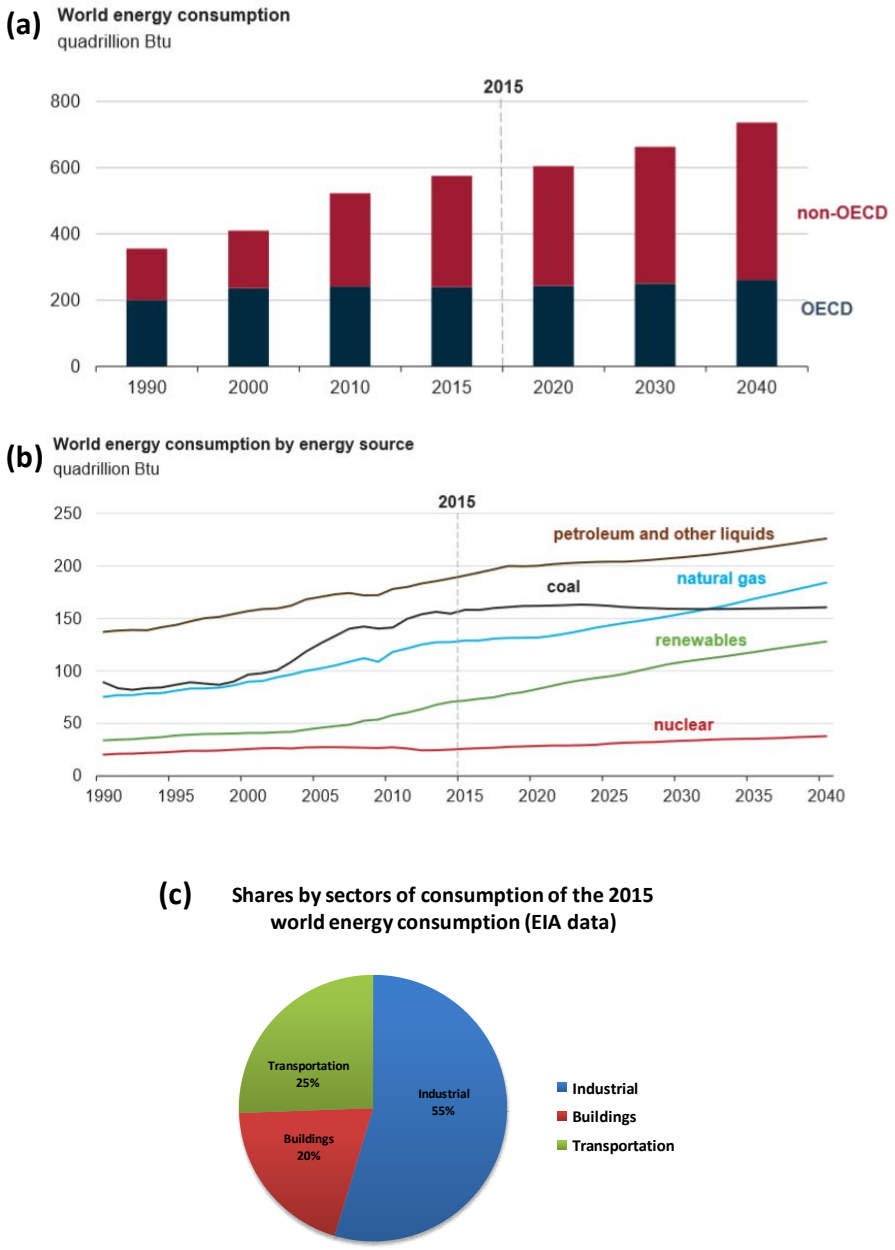

Figure 1-1 : (a) World energy consumption between 1990 and 2015, and estimation toward 2040. (b) World energy consumption by energy source, (c) shares of energy consumption by sector. Source: International energy Outlook 2017

1.1.2. The importance of energy storage

In the case of electricity, energy is transported from the power plants to the consumption sites through a vast connecting network. Electricity is usually produced at the same time it is consumed and this network must be able to sustain a continuous power supply which can be subject to failures and intermittence in the production. A short voltage drop can have tremendous impact at consumer level which imposes to dispose of energy reserves at grid or consumer level to sustain the energy

flow during interruptions. These energy storage systems are required to operate from milliseconds to hours.[1]

The daily profile of energy consumption is maximal during daytime and is minimal at night.[2] The minimum energy supply is provided by coal or nuclear power plants. The fluctuations during daylight are ensured by more flexible sources like oil and gas power plants which are more expensive and results in a difference in the daytime and nighttime cost of electricity. Rationalization of the energy production is obtained through peaks shaving which consists in storing electrical energy in low cost production periods (nighttime) to release it during high cost production periods (daytime). This allows smoothing of the daily energy production and reducing the production cost. Large grid energy storage systems capable of operating for hours or days are used, from domestic to industrial scale, on both consumer and producer levels.[1,3]

In the case of renewable energy sources, the solar and wind power generation are by nature incontrollable as they strongly depend on the weather conditions and thus do not correspond accurately to the electricity demand.[4] Load balancing consists in storing energy in high production periods to release it in high consumption periods. Large energy storage systems thus are required at producer level, capable of storing the energy corresponding to hours or days of consumption.[4,3]

The electrical grid is expected to evolve toward the *smart grid contempt*, in which a large amount of small, dispersed power plants and electricity storage facilities all interconnected would improve its flexibility, efficiency and reliability.[5] Domestic batteries, which market recently emerged, are a good illustration of this evolution.[6]

The electric mobility market, driven by the rising of fuel costs for combustion engines and objectives of reduction of CO_2 emission lead by environmental concerns is well illustrated by the projections concerning global electric car sales which was of 2 million cars in 2014 and is expected to reach 16 million in 2025, to pass from 0.5% to 2.5% of the global vehicle sales.[7] This market has created the demand for high performance energy storage systems, featuring high energy and power density and to be used in all sorts of vehicles like electric bikes, plug-in or hybrid vehicles or trains.[8] Similarly, the portable devices market (smartphones, laptops) which has boomed since the 90's is also very demanding in top of the line products with high energy density.[1]

Many ways of storing energy are actually used, each with their advantages and constraints and adapted to particular applications depending on their cost, energy and power density and electrical performances. The main energy storage systems are presented in the next part of this chapter, and an overview of their global power and capacities is displayed in Figure 1-2.

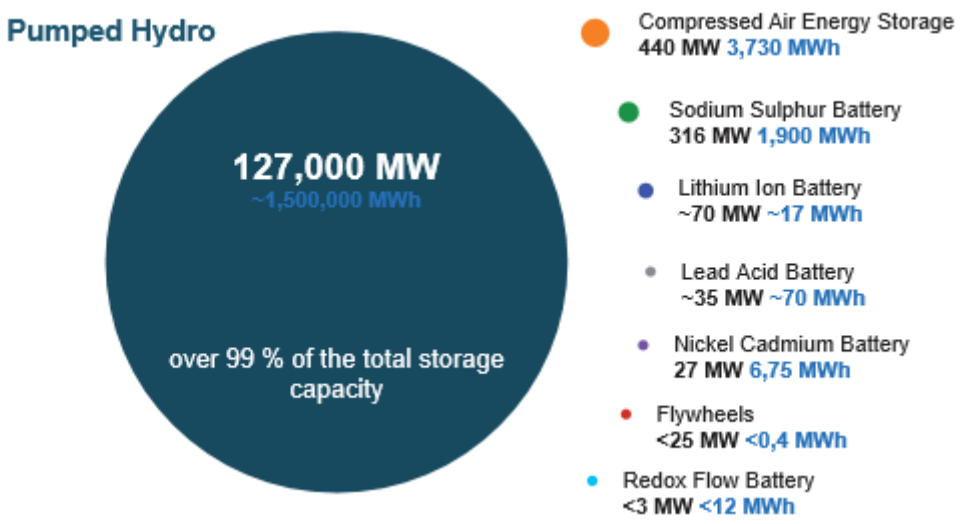

Figure 1-2 : Overview of the global power and capacity of the principal energy storage systems in 2007.[9]

1.1.3. Energy storage systems

1.1.3.1. Mechanical energy storage

The pumped hydro storage power stations represent almost 99% of the worldwide energy storage capacity, holding over 1500 GW. These power stations consist in two water reservoirs with distinct elevations. Production excess, which would be lost otherwise, is used to pump water from the lower reservoir to the higher one. Electricity is released when water flows from the higher reservoir to the lower one through a turbine. The seawater can be used as lower reservoir. The advantages of these plants are their huge energy capacity and durability. These systems are found worldwide but need space and good site topography. Their efficiency is comprised between 70 and 85% and they are generally used for peak shaving by accumulating energy during nighttime to release it during daytime.[1]

Electricity can also be used to compress air and store it in air tanks. This stored compressed air is released through a turbine to produce electricity within the grid. The compression process generates heat, as well as the release of the gas which has to be heated, leading to low efficiencies below 40 % when the heat is not stored and instead dissipated into the atmosphere. Caverns or abandoned mines can be used for air storage. These systems are also used for peak shaving.[1]

Electricity can also be converted into rotating speed in flywheel energy storage systems. These systems consist in heavy cylinders rotating at up to 50 000 rpm. They have a good durability but suffer from energy losses due to air resistance. They are mainly used for power balance of the grid.[1]

1.1.3.2. Thermal energy storage

Thermal energy storage systems are used to store heat obtained from a source of thermal energy. Thermally insulated reservoirs are used, featuring many distinct technologies including high specific heat capacity materials in the case of sensible heat storage or phase change materials in the case of latent heat storage. The advantage of phase change materials is their higher gravimetric capacity. The application fields of these systems go from industrial to residential as on-grid or off-grid power systems. They can be used to improve the efficiency of compressed air energy storage or electrolysis of water (see below) and at residential scale for home heating or hot water. These systems unfortunately suffer from heat losses, which decrease their efficiency for long term energy storage.[10]

1.1.3.3. Electrochemical flow processes

1.1.3.3.1. Electrolysis of water and H_2 storage

The current produced by a power station can be used in a process of electrolysis of water to generate hydrogen and oxygen.[11] The hydrogen can later be converted into synthetic natural gas after reaction with carbon dioxide in a methanation reactor. Oxygen is usually not stored and released into the atmosphere while the hydrogen or the methane are stored under pressure in gas tanks. To produce again electricity the gases are then mixed again in the reactor. The efficiency of the reverse electrolysis process is 40 % because it is exothermic.[11] This efficiency can be improved in heat/electricity combined power stations.[1] Very large amounts of electricity can be stored this way, and the energy reserve (H_2 or natural gas tank) is mobile and can be distributed to other power plants or fed to the gas grid for heating or transport (natural gas combustion engine or fuel cell electric vehicle). The density of synthetic natural gas is heavier than that of hydrogen which makes it more suitable for transport through pipelines. Water electrolysis power stations are built worldwide since the 90's and have a global capacity of about 160 MW.[1]

1.1.3.3.2. Flow batteries

In this type of batteries, reactants and products of redox reactions are dissolved in electrolytes stored in tanks which are pumped toward electrodes to control the redox reaction rate of the cell.[1] In hybrid flow batteries at least one of the reactants is not dissolved within the electrolyte and remains in a solid form at one of the electrodes.[3] Since the electrolytes are stored in closed containers separately to the electrochemical cells, the capacity of these systems (amount of electrolyte stored) is independent from its available power (electrolyte flow) which allows good energy/power/design flexibility and limits the losses for long term storage. The pumping of the electrolytes however decreases their energy efficiency (65-80%). As examples, the vanadium redox battery and the polysulfide bromide battery are used for large on-grid stationary applications, in the range of 1kWh to 10 MWh, for peak shaving and load balancing.[3,12]

1.1.3.4. Supercapacitors

Supercapacitors have similar working principles to those of classical capacitors used in electronics. They consist in two conductive electrodes separated by an ionic conductive and electronic insulator material called electrolyte.[13] Under polarization the electrostatic forces at the electrode/electrolyte interfaces create a Helmoltz double layer where charges accumulate in a few angstrom layers. Electrochemical pseudocapacitors combine the double layer capacitor with adsorption of an electroactive specie contained within the electrolyte at the surface of the electrodes.[13]

These systems have very high capacitance up to several hundred farads and are very fast at (dis)charging because of their low internal resistance.[13] Compared to traditional electrochemical storage systems (batteries) they have a high-power density, a high efficiency and an almost unlimited cycle life. However, their drawbacks feature electrolytes degradation after a few years regardless of the use of the system and a high self-discharge rate compared to other systems, as well as a lack of energy density limiting its use to niche markets. Indeed, due to their electrical performances, these systems are more suitable for power applications featuring short and fast cycles and are actually used in either mobile or stationary applications. Supercapacitors are used in power electronics and in the grid to prevent short voltage failures. As an example, electric buses made in China by Sunwin use supercapacitors as energy reservoirs, taking advantage of the frequent stops of the vehicle to rapidly recharge them.[14]

1.1.3.5. Secondary batteries

Secondary (or rechargeable) batteries represent the majority of electric energy storage systems for mobile and portable applications although their characteristics in term of energy and power density make them also suitable for stationary on-grid and off-grid applications.[3] These systems are constituted of two electrodes with distinct reaction potentials, each connected to a terminal of the battery and separated by an electronic insulator and ionic conductor electrolyte. These reactions, an oxidation and a reduction, generating and consuming electrons, respectively, take place on each electrode. These electrons travel from one electrode to the other between the terminals of the battery. A positive ion simultaneously travels between the electrodes within the battery through the electrolyte and serves as both the reactant and product of the redox reactions occurring on the electrodes.[3]

A single electrochemical reactor is called a cell. In the nomenclature related to batteries the electrodes are identified through their potential: the high potential electrode is the cathode and the low potential electrode is the anode.[3] High cathode and low anode operating potentials, and large specific capacity of the electrode materials are very important features for batteries as they determine their voltage and capacity and therefore their energy density. The power of the battery also depends on the rate of the redox reaction and the ability of the charge carriers to move within the battery materials. In battery packs, up to several hundred cells are assembled in parallel and series in order to obtain specific performances.[3]

Several technologies exist, with distinct performances in terms of cost, safety, voltage, energy density, lifetime, efficiency and characteristic operating time. The principal characteristics in terms of performance of the most common of these technlogies are compiled in Table 1-1 and their specific powers and energies are compared in the Ragone plot of Figure 1-3 (a) along with those of supercapacitors. Their advantages, drawbacks and application fields will be presented in the next sections.

Technology	Average operating voltage (V)	specific density (Wh/kg)	Operating temperature	Self discharge (% per month) at room T°	Energy efficiency (%)	Cost ($/KWh)	Ref
Lead-acid	2.1	30 - 40	-40 – 60 °C	5-50	50-75	100-200	[17],[3],[18],[35],[15]
Nickel cadmium	1.35	40 - 60	-50 – 70 °C	5-20	55-70	300-600	[22],[35],[15]
Nickel metal-hydride	1.2	60 - 120	-30 – 75 °C	5	65	300-600	[23] ,[15]
Sodium sulphur	2.1	150-240	300 – 350 °C	Negligible	75-90	300	[19],[35] ,[15]
ZEBRA	2.6	95-120	300 – 350 °C	Negligible	75-90	300	[20],[35] ,[15]
Lithium ion (LCO Vs C)	3-4	155	-25 – 40 °C	2	94-99	300-1000	[24],[35] ,[15]
Lithium ion (LFP Vs LTO)	1.7	50-70	-25 – 40 °C	2	94-99	300-1000	[24],[35] ,[15]

Table 1-1 : Principal characteristics of the main electrochemical storage systems.

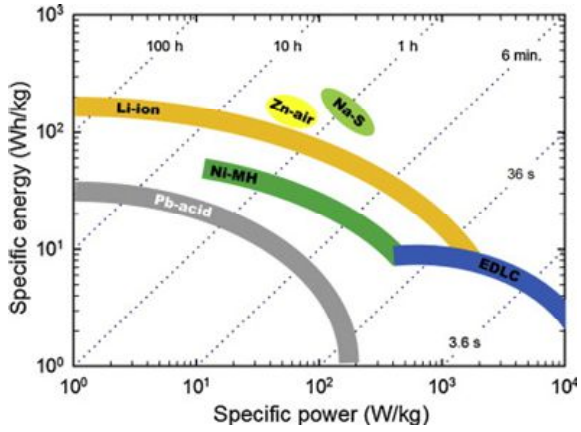

Figure 1-3 : (a) Ragone plot of electrical and electrochemical energy storage technologies.[16]

1.1.3.5.1. Lead acid

These batteries are constituted of two electrodes made of lead and load oxide, respectively, and a solution of sulphuric acid as electrolyte.[17] Due to these constituting materials, these batteries are cheap and easy to recycle. They are also robust, neither air nor moisture sensitive and can thus be easily opened to change internal components. Some constraints exist however because of the toxicity of lead as a heavy metal, and the potential release of H_2 on the cathode side.[17] Furthermore, because of the weight of the electrode materials, they have a low energy density and power density (40 Wh/kg and 200 W/kg respectively). The average operating voltage is 2.1 V per cell.[17,3]

They have been commercialized since 1890 and are one of the most used battery types worldwide. Their most popular utilization is as starter battery in vehicles although they are also used in large scale systems as emergency power stations or for load balancing as their low cost compensates their low energy density. Concerning mobile applications, these batteries are also used in rail transport.[18]

1.1.3.5.2. Molten salt batteries

These batteries use molten metals and salts as electrode or electrolyte. These elements are made of cheap and abundant materials (Na, S, Al, Ni, Cl) which make them cost-competitive compared to other battery technologies.[3] For the metals or salts to remain liquid the batteries are heated to a temperature close to 300 ^{o}C. Their own electricity is used to maintain this high temperature which decreases their efficiency. These batteries can be stored at room temperature for years as the solidified salts prevent any self-discharge. The power density is good as result of the high conductivity of the molten salt.[19,20]

Several types of molten salt batteries exist. Sodium-sulphur batteries are currently used for space and defense applications and for on-grid applications for load balancing of the renewable energy production.[19] They operate at 2.1 V and have a good energy density of approximately 200 Wh/kg.[19] Sodium nickel chloride batteries (ZEBRA) were used in the Modec commercial vehicle,[21] and are

currently employed for grid storage. They feature a 2.6 V operating voltage and approximately 100 Wh/kg of energy density.[3,20]

1.1.3.5.3. Nickel Cadmium and metal hydride

The nickel cadmium battery (Ni-Cd) electrodes are made of Nickel hydroxide $Ni(OH)_2$ and cadmium respectively.[3] The electrolyte is a solution of potassium hydroxide (KOH). The main advantages of these batteries are their robustness, their long lifetime and their capacity to operate in a large temperature window. They however contain cadmium which is a heavy metal and creates constraints regarding its recycling (in Europe in particular their cadmium content prevents their domestic use) and they are also subject to memory effect, which decreases their capacity if not used for a long time. They have an average operating voltage of 1.35V and their energy density is comprised between 40 and 60 Wh/kg.[3] They are used for security (emergency lamps for example) and power applications.[22]

Nickel metal hydride batteries (Ni-MH) were first developed to replace Ni-Cd batteries because of their heavy metal content.[3] Their electrodes are constituted of Nickel oxide hydroxide NiO(OH) and metal hydride MH (M = metal) respectively. The electrolyte used is also a solution of potassium hydroxide (KOH). Compared to Ni-Cd batteries, they have a lower operating voltage (1.2V) but a higher energy density (≈ 60-120 Wh/kg) and are still subject to memory effect. Also, their energy density is much higher than that of lead-acid batteries and they operate at room temperature, which make them very valuable for portable applications. They were used massively for portable devices and electric mobility before Li-ion batteries started to be competitive.[8,23]

1.1.3.5.4. Lithium ion

Amongst all elements, lithium is the one that possesses the lowest redox potential (-3.04 V *Vs* SHE), and one of the lightest, which makes it very valuable for high performances batteries featuring better power and energy density than the others battery technologies.[24]

These batteries have several advantages compared to the other electrical energy storage systems, featuring high energy density, comparable to that of the Ni-MH batteries, and operation at normal temperature.[3] In addition to that, their voltage is up to 3.7 V, three times higher than that of Ni-MH, which means that similar levels of power are obtained with much lighter battery packs, they present very little memory effect and little self-discharge (≈ 2 % a month compared to the 20 – 50 % of Ni and Pb-based batteries) and have a good efficiency (95-100 %).[3] These performances make them unavoidable for portable or mobile applications where they gradually replace the nickel-type batteries since their commercialization in the 90's. As of today they approximately represent 60 % of the total energy storage for portable applications and are also largely used as energy storage systems in electric vehicles. Their performances make them also suitable for on-grid stationary applications for peak-shaving or load balancing; as well as for household applications as illustrated by the newly expanding home battery market.[1] However, although their price has dropped by down to 80% during

the last few years, it still constitutes one of their main drawbacks compared to other battery technologies, especially for stationary applications.[25,26]

If Li-ion batteries were relatively minor in 2007 with a global storage capacity of 17 MWh, they are expected to experience a spectacular growth to reach a total of 417 GWh in 2025, at which time 70% of their global storage capacity should be dedicated to electric vehicles, 18% to electric bikes and 12% to stationary energy storage, mainly for peak shaving.[7] This growth is well illustrated by the projections concerning electric mobility as the global electric vehicle sales is expected to be multiplied by 8 between 2014 and 2025.[7] In Europe and USA, large industrial plants like the future Northvolt plant of Skelleftea (Sweden) or the Tesla Gigafactory (USA) are expected to fulfill this growing need.

These batteries are built with two solid state electrodes, usually insertion compounds storing Li in their crystalline structure through an intercalation mechanism or alloying compounds, each separated by an electrolyte. The lithium ions act as charge carrier as they move from one electrode to the other and are consumed and released by the redox reactions at their surface.[24]

1.1.3.5.4.1. Cathode materials

The crystalline structures of the commercial cathode active materials are divided in three categories: layered, spinel and olivine.[27] Each of these structures shows a distinct geometry of Li mass diffusion, as illustrated in Figure 1-4 (a), which affects its electrochemical performance. In layered materials the lithium ions are intercalated between the crystalline plans and the diffusion is bi-dimensional. In spinel materials the diffusion is tri-dimensional. In olivine the diffusion occurs in one-dimensional diffusion channels. The layered cathodes are used mostly in high energy systems while the spinel and olivine cathodes are preferentially used high power systems.[24]

$LiCoO_2$ (LCO) was the first commercialized cathode material for Li-ion batteries and remains one of the most popular.[24] This layered material has a high theoretical capacity of 274mAh/g; a high discharge voltage of 3.8 V vs Li^+/Li and shows good cycling performances upon Li insertion/extraction.[28] It however features several drawbacks: its voltage-composition profile is sloppy which causes a variation of the voltage of the battery upon operation; and irreversible structural changes of the material occur if too much Li is extracted which limits its practical capacity to about 150mAh/g and imposes accurate control of its composition while operating. This material also shows poor thermal stability as its exothermic decomposition starting above 200°C goes on in a thermal runaway.[29] It is also expensive and its extreme sensibility to moisture and air creates constraints with regard to its post-synthesis process.[24]

Layered $LiNiO_2$ (LNO) was considered as a promising cathode material for being cheaper than LCO but with similar operating voltage and specific capacity. It shows however poorer cyclability and thermal stability, which were later improved by partial substitution of Ni with Co, Mg and Al which resulted in the layered $LiNi_{0.8}Co_{0.15}Al_{0.05}O_2$ (NCA) and $LiNi_{1/3}Mn_{1/3}Co_{1/3}O_2$ (NMC) commercial materials.[24] These two materials have both an operating voltage of 3.7 V vs Li^+/Li and a theoretical specific capacity of

280 mAh/g. Their reversible capacity is however still limited by irreversible structural changes occurring when too much Li is extracted.[30,31]

Compared to the layered materials, spinel $LiMn_2O_4$ (LMO) is cheap and uses abundant and environmentally friendly materials.[32] It has a similar operating voltage compared to the layered materials (4.1 V vs Li^+/Li) but a lower reversible capacity (150mAh/g). The main drawbacks of this material are its poor cycle life.

Compared to the other commercial cathode materials, olivine $LiFePO_4$ is cheap, nontoxic and made of more abundant and environmentally friendly elements.[33] Its operating voltage and specific capacity are relatively low (160 mAh/g and 3.4 V respectively) but it shows a better cyclability than $LiMn_2O_4$ and better stability than the layered materials as it can sustain complete Li (de)intercalation without decomposition or structural changes. Another main advantage of this material is its flat potential plateau, as illustrated in Figure 1-4 (b) which is very valuable for energy storage applications as it allows maintaining a constant power upon discharge of the battery.[33] This material needs small particle size with carbon coating onto their surface to deliver good power capability, which affect its processing cost and lower its tap density, although carbon coated $LiFePO_4$ remains a relatively cheap materials compared to layered oxides.[33] Moreover, $LiFePO_4$ is stable in air,[34] further reducing its processing cost.

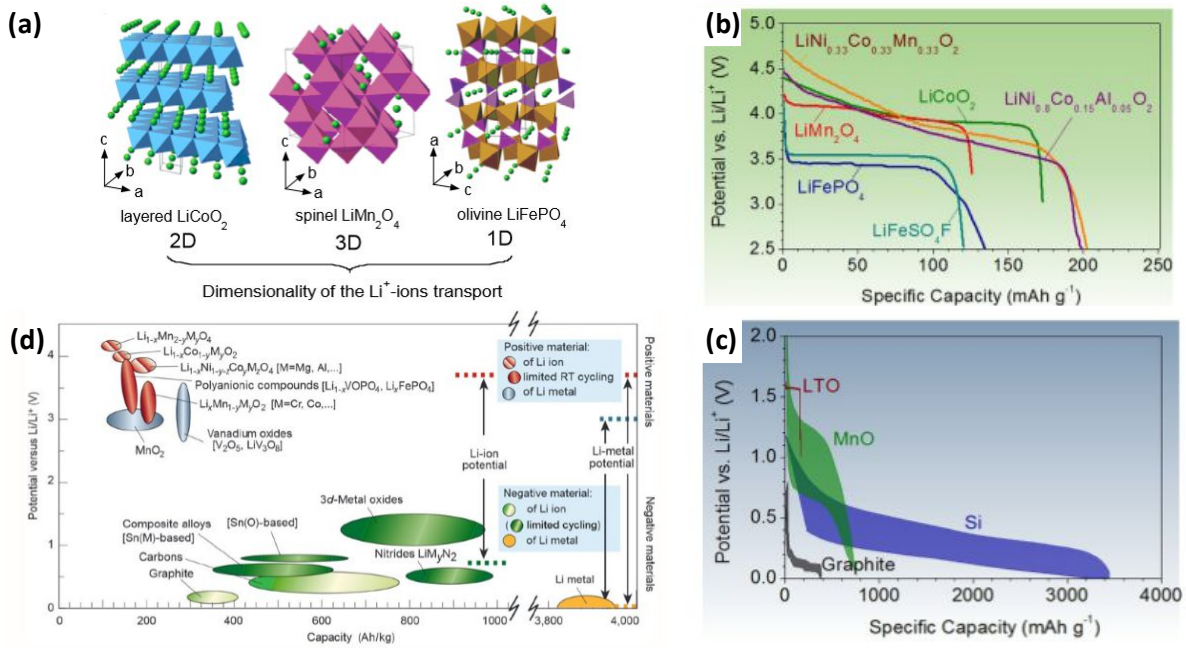

Figure 1-4: (a) Crystalline structures of the three types of insertion electrode materials[27] (b) Discharge profile of intercalation cathodes[45] (c) Charge and discharge profiles of intercalation anodes[45] (d) Potential vs capacity of currently used or under study cathode and anode materials[35]

1.1.3.5.4.2. Anode materials

Amongst anode insertion materials, graphite has the advantage of being cheap, abundant, and environmentally friendly and to show a low delithiation potential, comprised between 0.1 and 0.23 V Vs Li^+/Li.[36] The reversible capacity of this layered material is also good (372 mAh/g) but its volumetric capacity is small compared to other insertion electrode materials (330-430 mAh/cm^3). Also, the low operating potential can bring safety issues with dendrite formation and electrolyte decomposition.[24,36]

Compared to graphite, spinel $Li_4Ti_5O_{12}$ is more expensive, has a significantly lower specific capacity (175 mAh/g) and a higher operating voltage (1.55 V Vs Li^+/Li).[37,38] This material however compensates these drawbacks with better power capability and thermal stability and a higher volumetric capacity (600 mAh/cm^3). It is also safer than graphite as its relatively high potential prevents the formation of dendrites and decomposition of the electrolyte. At last, it shows a flat potential plateau upon Li (de)intercalation which as explained above is very valuable for battery applications, and the zero volume change this material experiences upon Li (de)intercalation ensures great cycle life.[37,38]

Si and Sn (de)alloy reversibly with lithium at room temperature, reaching outstanding theoretical capacities of 4000 and 1158 mAh/g at average operating voltages of 0.3 and 0.5 V vs Li^+/Li, respectively, but show poor cyclability due to their very large volume expansion (up to 300%) upon reaction, which induce mechanical stress and destroys the electrodes.[39] This type of material is commercialized in composite anodes with mixed elements, like Si-C or Sn-Co-C with reversible capacities of 1200mAh/g and 400mAh/g corresponding to 30% and 43% of their theoretical capacities, respectively, and operating at an average potential of 0.45 V vs Li^+/Li.[40]

The voltage-composition profiles of some of the above-mentioned cathode and anode materials upon discharge and charge are displayed in Figure 1-4 (b) and (c) respectively. The shape of these profiles depends on the nature of the transformation mechanism upon Li (de)intercalation. Sloping or multiple potential plateaus is a direct consequence of the formation of single or multiple phases depending on their lithium content. The theoretical and experimental specific capacities, operating potentials and energy densities of the above mentioned commercial materials, as well as their relative cost and lifetime are reported in Table1-2, and their operating potentials and experimental capacity in Figure 1-4 (d).

Material	Specific capacity (experimental / theoretical) (mAh/g)	Average operating potential Vs Li^+/Li (V)	Specific energy (experimental / theoretical) (Wh/kg)*	Cost	Lifetime	Ref
		Cathodes				
$LiCoO_2$	148/272	3.8	391/581	Medium	Medium	24,25,28
$LiNi_{1/3}Mn_{1/3}Co_{1/3}O_2$	160/280	3.7	402/575	High	High	24,25,30
$LiNi_{0.8}Co_{0.15}Al_{0.05}O_2$	199/280	3.7	466/575	High	Medium	24,25,31
$LiMn_2O_4$	120/148	4.1	362/423	Low	Low	24,25,32
$LiFePO_4$	170	3.4	385	Medium	High	24,25,33
		Anodes				
Graphite	372/372	0.1	391/581	Medium	Medium	24,25,36
$Li_4Ti_5O_{12}$	175/175	1.55	180/239	High	High	24,25,37,38
Sn-Co-C	400/917	0.45	361/702	medium	low	24,39
Si-C	1200/4000	0.3	499/891	low	low	24,39,40

* Vs graphite for cathodes and Vs LCO for anodes

Table1-2 : Comparison of the theoretical and experimental specific capacities, volumetric capacities, average operating potentials *vs* Li^+/Li and cost and lifetime of commercial insertion electrode materials.

1.1.3.5.4.3. Beyond Li-ion batteries:

Surpassing actual LIBs electrochemical performances should pass through dramatic increase of their energy density and operating potential. Intense research work was made in the last years to improve these parameters. Lithium metal is considered as potential anode material because of its low redox potential and high theoretical capacity (3860 mAh/g) but much work still has to be done to overcome safety issues caused by uncontrollable dendrite formation.[41] Lithium sulphur (Li-S) cathodes with a theoretical capacity of 1675 mAh/g and operating around 2 V vs Li^+/Li are also very promising but show low cyclability.[42,43]

Lithium oxygen batteries, which use oxygen from the air as cathode, and operating at 3.4 V vs Li^+/Li are very promising in terms of energy density, but some intense research work is still needed to overcome the poor reversibility of these systems.[44]

The electrolytes used in Li-ion batteries usually consist in a lithium salt (e.g. $LiPF_6$, $LiClO_4$, $LiBF_4$…) in an organic ester based solvent such as ethylene carbonate, propylene carbonate, dimethyl carbonate or diethyl carbonate (referred as EC, PC, DMC, DEC).[45] These electrolytes are relatively cheap and light but their limited stability voltage window and ease of combustion (particularly in the case of the exothermic decomposition of layered oxides) is a drawback concerning the safety of Li-ion batteries; especially that they do not impede the formation of dendrites which can lead to electrical shortcuts.[46] An intense research work is currently made on solid electrolytes to circumvent these safety issues although it would induce lower energy and power density and do not impede systematically dendrite formation.[46]

The market increase of Li-ion batteries is well illustrated by the evolution of the overall lithium consumption in the last eight years which has passed from 101 to 235kT LCE[ii] between 2009 and 2017, and a yearly 8 % expansion of the overall lithium consumption in the next ten years is expected

[ii] Kiloton of lithium carbonate equivalent

to fulfill the increasing LIB demand as 60% of its production would be dedicated to energy storage.[7] Lithium shortage is expected to occur within between 15 and 100 years following various estimations; this scenario of lithium shortage and its non-uniform worldwide distribution (mainly Bolivia, Argentina, Chili and China) having the Andean sates to be called "the new middle east".[47]

Thus, in the context of a future exhaustion of the lithium reserves and low cost mass production, interest ultimately raised in others alkali elements in the periodic table, sodium and magnesium, cheaper and more earth abundant, as potential replacement of lithium as charge carrier in electrical energy storage systems.[52] Magnesium has the advantage to carry two electrons, which is beneficial for high capacity batteries but research on these systems is still at its basic stage.[48,52] On the other hand, the physical and chemical properties of sodium are very similar to those of lithium and these two elements are able to intercalate is similar compounds. Most of the knowledge accumulated on LIBs can be applied to this element, making Na-ion batteries (NIBs) a potential drop-in technology for fast commercialization.[49,50] The application foreseen for these batteries are similar to those already covered by Li-ion batteries although they are more likely to be used for stationary storage.[49,50]

1.2. Na-ion batteries

1.2.1. Sodium as battery charge carrier

The rising interest in NIBs is well illustrated by the number of scientific publications concerning this topic published in the past three decades in Figure 1-5 (a), which led them to a high degree of readiness.[51] Historically they were already studied when attention came to Li-ion batteries but suffered from a loss of interest after the commercial success of LIBs.[51]

The intercalation electrode materials to be used in sodium-ion batteries are similar in nature to those already used in lithium ion batteries although the larger size of sodium compared to that of lithium (1.02 Å vs 0.76 Å respectively) affects the phase stability, the transport properties and the phase formation within same materials and distinct compositions have to be used.[51,52]

With similar insertion materials, replacement of sodium by lithium induces a loss of specific energy at material level due to its heavier mass (23 g/mol vs 6 g/mol) and its 330 mV higher redox potential.[53,54] At battery level, however, the mass of the charge carrier is small compared to the total weight of a battery, and this loss of specific energy shall be partially compensated by the replacement of the copper current collector by lighter aluminum. Indeed, aluminum is improper to use in LIBs since it alloys with lithium but does not react with sodium.[53,54]

Several studies highlighted the cheap cost of sodium precursors for synthesis of insertion compounds compared to the lithium ones, although a greater cost reduction at battery scale shall be obtained from the replacement of copper current collectors currently used in Li-ion batteries into cheaper and lighter aluminum as seen from the comparison of the manufacturing costs of LIBs and NIBs in Figure 1-5 (b).[53,54] These lower costs make NIBs a potential low-cost alternative to Li-ion batteries for high performance applications if similar or better performances are reached.

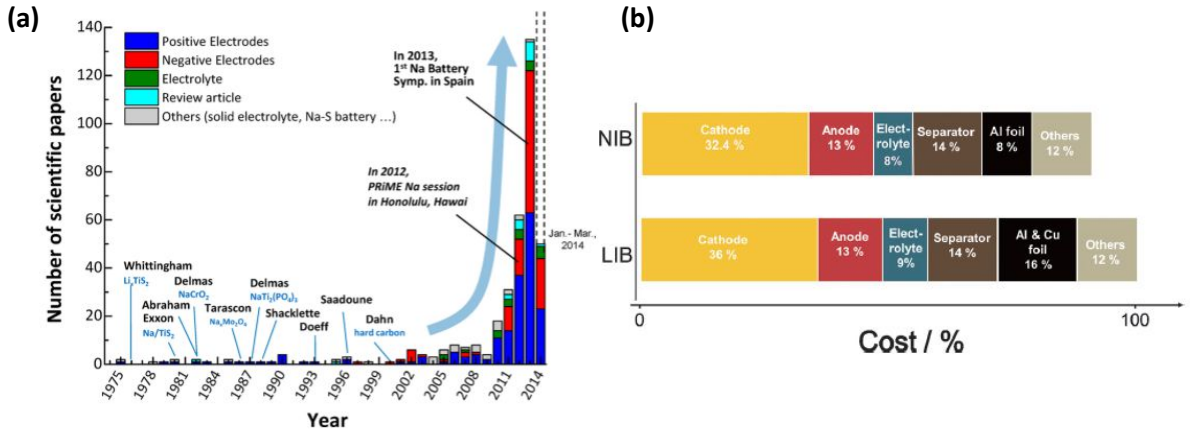

Figure 1-5 : (a) Number of publications related to sodium-ion batteries from 1975 to 2015 (database of Web of Science, Thomson Reuters)[51] (b) Comparison of the manufacturing costs of Li-ion and Na-ion batteries.[53]

Research on sodium-ion batteries is currently focused on the identification of suitable electrode materials for commercial applications. The main categories of cathode materials under study for sodium-ion batteries are layered transition metal oxides, polyanionic compounds and organic compounds. Amongst anodes, carbonaceous materials, titanium oxides, alloys and organic compounds are also under study. The electrochemical properties of some of the most relevant insertion electrode materials are reported in Table1-3; most of them belonging to the same family of compounds as of Li-ion batteries. The operating voltages and experimental capacities of the materials under study as cathode and anode for sodium-ion batteries are reported in Figure 1-6 (a) and (b) respectively.

Type	material	structure	Specific capacity (experimental / theoretical) (mAh/g)	Average operating voltage Vs Na^+/Na (V)	Specific energy (experimental / theoretical) (Wh/kg)*	ref
			Anodes			
Carbons	Hard carbon	Layered disordered	300	0.4	260/345	62
Metal oxides	TiO_2	anatase	150/250	1	150/244	64
	$Ti_{0.94}Nb_{0.06}O_2$	rutile	160/250	1	154/244	65
	$Li_4Ti_5O_{12}$	spinel	145/175	1	147/202	67,68
	$Na_4Ti_5O_{12}$	monoclinic	56/137	1	81/174	69,70
	$Na_2Ti_3O_7$	layered	115/177	0.6	156/244	71
Alloys	Sn-based		600/847	0.5	300/466	55
	Sb-based		629/660	0.5	363/526	56
	Red-P		1890/2596	0.4	361/569	73
			Cathodes			
Layered oxide	$NaCoO_2$	layered	150/239	3	260/345	74
	$NaFe_{0.5}Mn_{0.5}O_2$	layered	190/264	3	300/365	57
	$NaNi_{0.25}Fe_{0.5}Mn_{0.25}O_2$	Layered	150/250	3.2	280/381	78
Prussian blue	$KFe_2(CN)_6$	perovskite	100/170	3	195/282	81
Polyanionic compounds	$NaFePO_4$	Maricite	142/154	2.3	183/193	82
	$NaFePO_4$	olivine	123/154	2.8	209/244	83
	$NaMnPO_4$	olivine	80/154	3	164/264	85
	$Na(FeMn)_{0.5}PO_4$	olivine	92/154	2.5	147/213	84
	$Na_2Fe_2(SO_4)_3$	alluaudite	120/141	3.8	291/326	86
	Na_2FePO_4F	Layered	110/122	2.9	201/216	88
	$Na_2FeP_2O_7$	triclinic	80/97	2.7	145/168	89
	$Na_3V_2(PO_4)_3$	Nasicon	93/117	2.5	205/244	91

* Vs hard carbon for cathodes and vs $NaCoO_2$ for anodes

Table1-3 : Electrochemical characteristics of a selection of insertion electrode materials for NIBs.

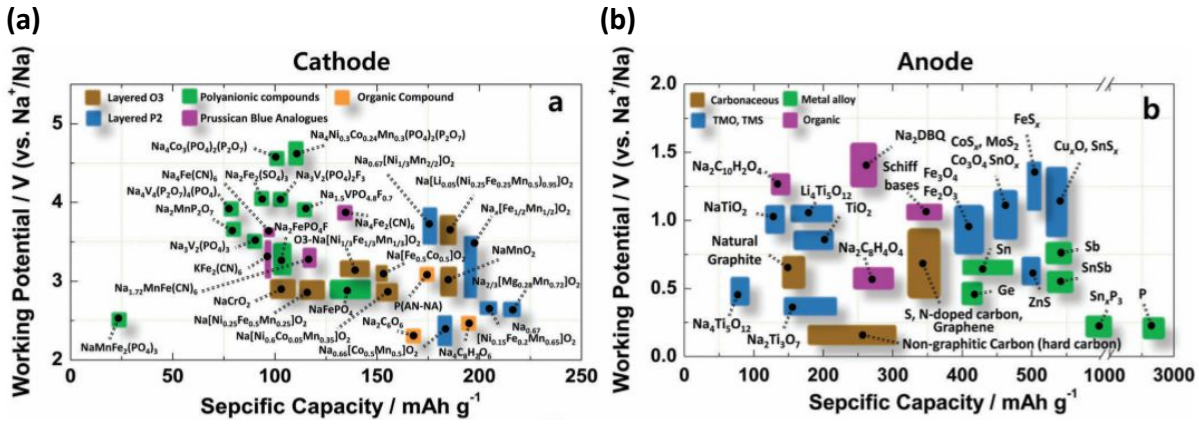

Figure 1-6 : Reversible capacity and average operating voltages of currently studied cathodes and anodes.[58]

1.2.2. Na-ion anode materials

In addition to the risk of dendrite formation similarly to lithium metal anode of LIBs, the lower melting point of sodium (97.7 ^{o}C) and its constant corrosion when in contact with organic electrolyte prohibits its use as anode for safety reasons.[59] The anode materials considered for Na-ion batteries consist in carbonaceous and titanium based oxides. The advantages of these materials are similar to their lithium counterparts and feature low cost, environmental friendliness, availability of elements, ease of synthesis and non toxicity.[60]

1.2.2.1. Carbonaceous materials

While graphite, made of ordered parallel graphene planes is the most widely used anode material within Li-ion batteries, the reversible capacity this material provides upon Na (de)intercalation is limited to about 30 mAh/g, preventing its use as anode material for NIBs.[61] The highly disordered counterpart of graphite, hard carbon, exhibits a reversible capacity of about 300 mAh/g upon Na (de)intercalation at an average voltage near 0.3-0.5V. The Na storage mechanism of hard carbon appears intricate and is still under discussion,[62,49,61] although it appears to be essentially a mixture of intercalation, pseudo-adsorption and Na clustering occurring into its nanopore structure. Because of its good electrochemical performance hard carbon is considered by several groups to be the best anode material for the first generation of sodium-ion batteries.

1.2.2.2. Titanium oxides

Titanium compounds have lower specific capacity and higher operation potential than hard carbon. This higher operation potential, although decreasing the energy density at cell level, has the expected benefice to prevent sodium plating and dendrite formation at their surface. The main compounds studied so far are titanium dioxide (TiO_2), and lithium and sodium titanates ($Li_4Ti_5O_{12}$, $Na_4Ti_5O_{12}$, $Na_2Ti_3O_7$).[60,63]

Amongst all the forms of TiO_2, anatase is the most studied.[51,60] This material has a theoretical specific capacity of 250mAh/g and was initially considered inactive with regard to Na (de)intercalation until more than 150 mAh/g of reversible capacity were obtained with nanosized and C-coated particles (< 30 nm) at an average potential of 1 V.[64] Other forms of titanium dioxide are also under study, such as rutile TiO_2 with 160 mAh/g of reversible capacity and excellent cycling performances after 6% of Nb doping.[65] The experimental capacity of TiO_2 in all its forms is limited by the sluggish Na (de)intercalation kinetics caused by the large size of Na ions. Improvement strategies consist in reducing the particle size and using them in composite electrodes with conductive carbon.[66] Despite its promising rate performances, the potential profile of this material is sloppy and does not present any plateau.

As discussed above, spinel lithium titanate $Li_4Ti_5O_{12}$ is widely used amongst commercial Li-ion batteries. Na intercalation within $Li_4Ti_5O_{12}$ leads to a reversible capacity of 145 mAh/g at 1 V vs Na^+/Na with a constant voltage upon operation.[67] The electrochemical performances of this material were improved through reduction of the particle size in combination with carbon coating and a reversible capacity of nearly 175 mAh/g, corresponding to the insertion of three Na ions per formula unit, was obtained with 44nm particles.[63,68] The sodium counterpart of this compound, $Na_4Ti_5O_{12}$, showed reversible capacities of 50 and 56mAh/g in its trigonal and monoclinic forms while operating at an average of 1 V vs Na^+/Na.[69,70]

Finally, sodium titanate $Na_2Ti_3O_7$ is also particularly interesting as it operates at 0.6 V vs Na^+/Na, and up to two Na ions can be intercalated within the structure leading to a theoretical capacity of 177 mAh/g.[71] Upon cycling, however, this material delivers a reversible capacity of 115 mAh/g with low coulombic efficiency and continuous capacity fading due to decomposition of the particle surface, which can be prevented with a protective coating.[60, 63]

1.2.2.3. Alloys

While silicon shows very poor performance when cycled vs Na,[72] Sn-based and Sb-based alloys in the form M-Sn/Sb (M = metal) or Sn/C or Sb/C composites are extensively studied because of their high theoretical capacities and low operating voltages.[60] However, similarly to their lithium counterparts, the high volume change upon Na (de)intercalation induces poor stability of the electrode and large capacity fading, which are improved using composite anodes with mixed elements of the type Sn/Sb-M-C with M as an active or inactive metallic element (Co, Fe, Cu, Ni).[60] Other compounds like amorphous red phosphorus which delivered 1890 mAh/g of reversible capacity and good rate performances combined with carbon in a composite electrode are also very promising.[73]

1.2.3. Na-ion cathode materials

1.2.3.1. Layered transition metal oxides

Layered transition metal oxides in the form Na_xMO_2 (M = Fe, Mn, Co, Ni, Ti, Cr, Vo, Ru) are promising cathode materials for Na-ion batteries for their ability to reversibly (de)intercalate Na-ions at moderately high potential (2-4 V vs Na^+/Na) with a high theoretical capacity, comprised between 235 and 280 mAh/g and earth abundant elements composition.[74,75] These materials can be categorized in two main groups: P2 and O3 (P for prismatic, O for octahedral) depending on the Na-ion occupancy sites between layers and its packing number.[74] Same composition P2 and O3 compounds have distinct stability depending on their sodium content: O3 type is stable for high Na content while intermediate compositions ($0.3 < x < 0.7$) are favored for P2 type compounds, although P2 ones are more stable and show better Na diffusivity. In both cases, similarly to their Li counterparts, complete Na (de)intercalation usually leads to irreversible structural changes which limit their practical specific capacities.[74,76] They still present, however, some of the largest reported capacities for cathode

materials in SIBs, as seen in Figure **1-7**. These materials also typically suffer from capacity fading which closely depends on the voltage at which they are charged, which induces important first cycle capacity loss in full cells;[75] and many compositions have not been yet reported fully sodiated at pristine state. Finally, several compositions present multiple voltage plateaus caused by complex transformation mechanisms which limit their practical use,[74,75,76] e. g., the voltage-capacity profile of $NaCoO_2$ in Figure 1-7. Several strategies exist to improve the electrochemical performances and structural stability of this class of materials, like binary and ternary combinations in the form $Na_xM_yM'_{1-y}O_2$ or $Na_xM_yM'_zM''_{1-y-z}O2$; or cationic substitution with inactive metals (Mg, Ti and Ca).[77] Also, similarly to their lithium counterparts, they show poor thermal stability as their exothermic degradation leads to a thermal runaway above 200 °C and are highly sensible to air and moisture which creates constraints with regard to their synthesis.[75]

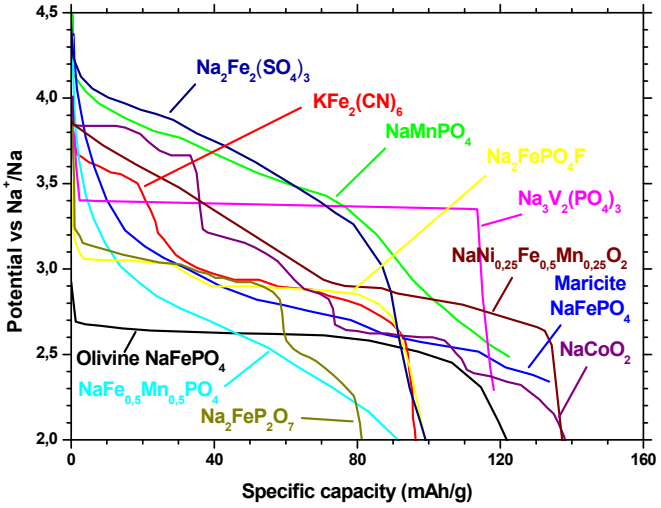

Figure 1-7 : Discharge profiles of a selection of cathode materials for Na-ion batteries: $NaCoO_2$[51], $NaNi_{0.25}Fe_{0.5}Mn_{0.25}O_2$ upon discharge at C/10[78], $KFe_2(CN)_6$ upon discharge at C/20[81], olivine Na_xFePO_4 discharge at C/20[79], maricite Na_xFePO_4 upon discharge at C/20[82], $NaMnPO_4$ upon discharge at C/20[85], $Na/Na(FeMn)_{0.5}PO_4$ upon discharge at C/40[84], $Na_2Fe_2(SO_4)_3$ upon discharge at C/20[86], Na_2FePO_4F[88], $Na_2FeP_2O_7$[80], $Na_3V_2(PO_4)_3$ upon discharge at C/20[91].

1.2.3.2. Prussian blue analogues

Prussian blue analogues in the form $KMFe(CN)_6$ with M as transition metal (Fe, Mn, Ni, Cu, Co, Zn) are also investigated as promising cathode materials for sodium-ion batteries. These materials are low cost, nontoxic themselves; operate between 3.5 and 2.5 V upon Na intercalation and show up to 100 mAh/g of reversible capacity, as seen from Figure 1-7.[81] However they may face issues concerning their synthesis as the processing of their precursors may involve environmental issues.[50]

1.2.3.3. Polyanionic compounds

Similarly to their lithium counterparts, polyanionic compounds show better thermal stability than the transition metal oxides thanks to their strong covalent bonds and a relatively high operating

voltage.[49] These advantages make these materials very appealing candidates for NIBs as well, despite their tendency to display lower available capacity than the transition metal oxides.[49,51]

The direct synthesis of the sodium counterpart of $LiFePO_4$ leads to the thermodynamically stable maricite $NaFePO_4$ which is inactive with regard to Na (de)intercalation in its bulk form. However, recent works proved that a reversible capacity of 142 mAh/g, corresponding to 92% of the theoretical capacity of the material could be obtained from nanostructured material at the cost of a poorer coulombic efficiency.[82] In the olivine phase, this material exhibits 123 mAh/g of reversible capacity at low rates with good cyclability, which corresponds to 80% of its theoretical capacity. To date the olivine phase can only be synthesized through ionic exchange from $LiFePO_4$.[83] Similarly to its lithium counterpart this material is particularly interesting for its flat plateau potential upon Na intercalation at 2.8 V vs Na^+/Na which is very valuable for battery applications.

Partial substitution of Fe with Mn is interesting as it allows increasing the operating voltage of the material due to the higher Mn^{2+}/Mn^{3+} redox potential.[84] Similarly to $NaFePO_4$, direct synthesis of $NaMnPO_4$ is only possible in its maricite form which is electrochemically inactive.[84] However, after ionic exchange from $LiMnPO_4$, this material is able to sustain 80 mAh/g of reversible capacity at an average voltage of 3V.[85] Synthesis of $NaFe_yMn_{1-y}PO_4$ ($y < 0,5$) olivine nanorods has been demonstrated by low temperature topotactic synthesis and this material is able to sustain 92mAh/g of reversible capacity which corresponds to 60% of its theoretical capacity at an average of 2.5 V.[84]

Using sulfate SO_4^{2-} with greater ionicity than phosphate PO_4^{3-} leads e.g. to alluaudite $Na_2Fe_2(SO_4)_3$ able to deintercalate Na ions at an average potential of 3.8 V vs Na^+/Na, which is the highest potential reported for the Fe^{2+}/Fe^{3+} reaction vs Na^+/Na.[86] 120 mAh/g of reversible capacity are reached, corresponding to 85% of the theoretical capacity of the material. Likewise, layered fluorinated iron phosphate Na_2FePO_4F is able to deliver 100mAh/h of reversible capacity at a discharge potential of 2.9 V vs Na^+/Na, corresponding to 80% of its theoretical capacity.[87,88] This later material however shows poor electric conductivity which limits its electrochemical performances.

Pyrophosphates in the form $Na_2MP_2O_7$ (M = Co, Cu, Fe) operate at 3 V vs Na^+/Na but their low theoretical capacity close to 100 mAh/g and sloping operating voltage make them poorly competitive for sodium ion batteries.[89] Nasicon $Na_3V_2(PO_4)_3$ shows two potential plateaus upon Na intercalation at 3.4 and 1.6 V with respective theoretical capacities of 117 and 50 mAh/g.[90,91]

As seen from Table1-3, the experimental capacity of these materials remain far from their theoretical values, and from Figure 1-7, they mostly present multiple potential plateaus upon Na (de)intercalation which is usually ascribed to increased interactions between the Na ion and the host structure, and could be also responsible for their limited rate capabilities compared to their lithium counterparts.[52] Their energy densities reported in Table1-3 are found lower than that of the commercial LIBs materials (see Table1-2) although, as explained above, this is expected to be partially compensated at battery pack level by the use of lighter Al as current collector. To date, the experimental performances of these materials in terms of rate capability are similar or lower than those of the materials already used in commercial Li-ion batteries. The research effort is currently moving toward improvement of the previously identified battery materials although deeper understanding of their Na (de)intercalation mechanism is needed to overcome these limitations.[51]

Compared to the other cathode materials, $NaFePO_4$ shows a relatively high voltage and theoretical capacity. Furthermore, it is made of nontoxic and abundant elements, and its potential upon Na insertion (discharge) is almost constant which, as explained above, is particularly valuable for energy storage applications as it allows maintaining a constant power upon discharge of the battery. This and the fact that $NaFePO_4$ is stable under air and against moisture makes this material a fairly good candidate as cathode material for NIBs, should the issue of difficult direct synthesis be effectively circumvented at low cost. Finally, to the ability of this material to reversibly (de)intercalate Li and Na ions, with the Li counterpart used in commercial Li-ion batteries, makes it a very good system of study to better understand the differences between Li and Na (de)intercalation.

1.3. $LiFePO_4$ and $NaFePO_4$

1.3.1. $LiFePO_4$

$LiFePO_4$ as cathode material for lithium ion batteries owns its commercial success to its good electrochemical performance, stability, ease and low cost of synthesis and safety upon operation.[24] Indeed, as seen from Table1-2, the reversible specific capacity that this material is able to sustain is similar to that of the layered transition metal oxides. Furthermore, its operating potential, although being the lowest of all commercial cathode materials, is the sole being constant upon Li insertion which, compared with the other cathode materials that operate in a broader potential window due to solid solution transformation reactions and/or successive transformation reactions, is particularly advantageous as it allows to maintain a constant voltage upon battery operation, and generated an intense research activity around this material.[24] It also shows higher cycle lifetime and safety since decomposition starts at much higher temperature than the metal oxide electrodes and does not occurs upon Li (de)intercalation at room temperature. Finally, although being relatively cheaper, it is less sensible to moisture than the metal oxides and is therefore easier to synthesize.[24]

Olivine $LiFePO_4$ has an orthorhombic lattice structure in the space group P_{nma}. Its structure consists in corner-shared FeO_6 octaedra and edge-shared LiO_6 running parallel to the *b*-axis, which are linked together by the PO_4 tetrahedra.[33] This material was first identified as a promising insertion material by Padhi et al. in 1997,[33] who obtained a reversible capacity of 100 mAh/g at a constant reaction

voltage of about 3.4V. This constant reaction potential, leading to a flat plateau in the voltage-composition curve (see Figure 1-8 (a)) was ascribed to a biphasic transformation mechanism involving a delithiated phase $FePO_4$ and a lithiated phase $LiFePO_4$. Remarkably the structural framework is not modified after Li de-intercalation, only the cell parameters are changing, as seen in Table 1-6.[33] Later on, very limited solid-solution ranges of the two separated phases were identified, thus near x = 0 and x = 1 in Li_xFePO_4.[92,93,94] The solubility of Li and vacancies in the Li-poor and Li-rich phases, respectively, depends on the particle size and temperature due to interface energy effects and is believed to be less than 5% at room temperature for particles larger than 100 nm and to vary with the overall Li concentration within the particles.[95,96]

The capacity reported by Padhi et al. was significantly lower than the theoretical value of near 170 mAh/g. This rather poor electrochemical performance was attributed to its poor intrinsic electronic conductivity.[97,98] This electrochemical performance was greatly improved by reducing the particle size to decrease the diffusion path for Li ions,[99] and using carbon coating at the surface of the active material particles to ease the electron path,[100] which allowed to reach 100% of the theoretical capacity of the material. Cationic doping was also reported,[97] although its actual effect on bulk conductivity is subject to controversy.[101,102] Upon charge and discharge the operating voltage of the material is found respectively at 3.45 V and 3.4 V vs Li^+/Li.[98] The 0.05 V voltage hysteresis between charge and discharge was attributed to strain between the two phases coexisting within the particles caused by their 6.81% volume mismatch, leading to interfacial energy cost.[33,103,110] Numerous studies were published for further understanding of the transformation mechanism of the material upon Li (de)intercalation and several transformation mechanisms were proposed based on observation at particle as well as electrode levels.[104] The “spinodal-decomposition” model is based on the observation of several lithiated and delithiated domains within a same particle and considers that the movement of the phase boundaries is the limiting factor for transformation of the active material particles, leading to the coexistence of multiple domains in partially delithiated particles.[105] The “domino-cascade” model is based on the observation of coexisting lithiated and delithiated particles within a same electrode, and considers that the movement of the boundaries is extremely fast leading to complete transformations of the particles as soon as the new phase appears. At electrode level, following this model, all the particles would transform sequentially and there is no phase coexistence within the particles at equilibrium.[106] These two apparently opposite mechanisms are actually in direct competition and their balance depends directly on the speed of the boundaries between the lithiated and delithiated domains, which depend themselves on the interfacial strain energy and therefore on the particle size distribution.[104]

Malik et al. determined the free energy of formation of Li_xFePO_4 in the whole x composition range, as presented in Figure 1-8 (b), and didn’t found any stable composition range except for the end members, which explains the biphasic equilibrium state of the material at intermediate compositions.[107] These authors attributed the fast (de)lithiation kinetics of the material reported by some authors[97,108,109] to its ability to overcome the kinetic barriers induced by the biphasic transformation mechanism by following a faster transformation path distinct from its equilibrium path. Following their model the particles would transform in a monophasic transformation mechanism and formation of the new phase would occur only after relaxation.

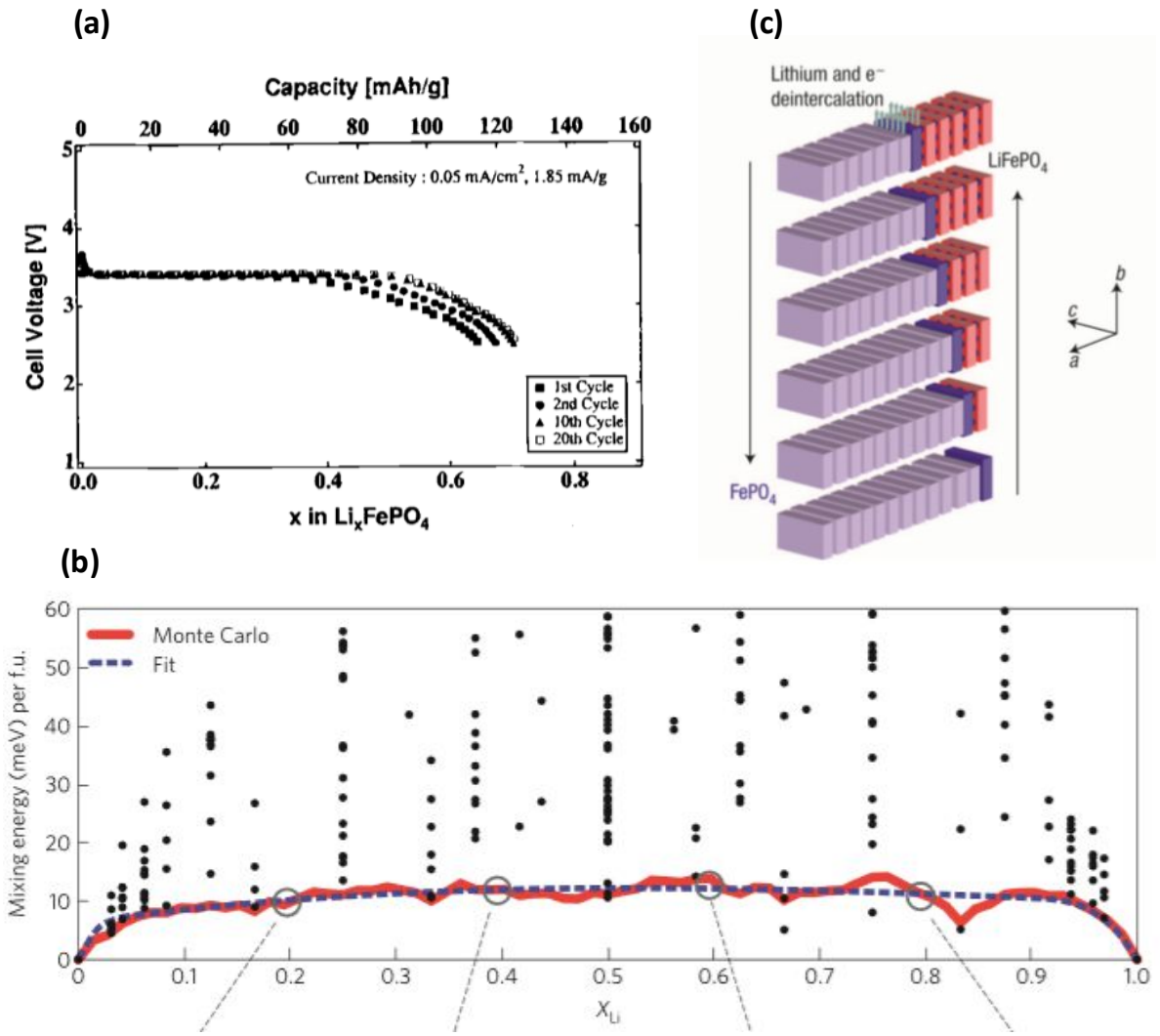

Figure 1-8 : (a) Potential-composition profile of Li_xFePO_4 as determined form Padhi et al.[33] (b) Free energy of Li_xFePO_4 as function of its composition.[107] (c) Schematic view of Li (de)intercalation in a single particle.[106]

The diffusivity of Li within the material is a critical parameter for fast (de)lithiation kinetics and was extensively studied.[104] Maxisch et al. found strong Li^+-polaron binding energies suggesting that lithium ions and electrons may diffuse together through the crystal, with thus intimately interdependent ionic and electronic conductivities.[110] Islam et al. determined from theoretical calculations that the inserted Li ion migration is anisotropic, being one-dimensional along the [010] axis (*b* axis).[111] Chen et al. showed that the interface between the Li-rich and Li-poor phases is comprised in the (*bc*) plane, allowing minimization of the strain between the phases by keeping the larger mismatch out of the direction of the interface.[112] The resulting Li diffusion and interface motion mechanism is schematized in Figure 1-8 (c). Later, Amin et al. found similar activation energy values for lithium diffusion within $LiFePO_4$ along the (*b*) and (*c*) directions from impedance spectroscopy measurements performed on single crystals and concluded that lithium diffusion was two-dimensional.[113] This two-dimensionality of the Li diffusion was ascribed to the presence of Li-Fe antisite defects which, although blocking the one-dimensional diffusion channels, open paths from one channel to another.[114] The concentration of these defects is believed to be typically less than 3%[114,115,116,] and depends on the synthesis route of the material.[114,117,118]

Many authors who studied the diffusivity of Li within Li_xFePO_4 determined its diffusion coefficient from a large variety of computational and experimental techniques. A large dispersion of diffusion coefficient values was found depending on the determination method. These values and the corresponding method are reported in Table 1-4. A possible explanation for this dispersion of values will be discussed in chapter 5 of this thesis.

Authors	Diffusion coefficient (cm^2/s) x	Li_xFePO4	Na_xFePO4
Computationalstudies			
Morgan et al.[119]	0	$1e^{-6}$	
	1	$1e^{-7}$	
Impedance spectroscopy on single crystals			
Amin et al.[117]	1	$4e^{-9}$ (150-200°C)	
Electrochemical studies			
Prosini et al.[120] (GITT)	$0.1 \le x \le 1$	$1e^{-17}$-$2e^{-17}$	
Prosini et al.[121] (EIS, GITT)	$0.1 \le x \le 0.9$	$7.6e^{-17}$-$1.3e^{-14}$	
Franger et al.[122] (EIS)	$0 \le x \le 1$	$1e^{-12}$-$1e^{-13}$	
Liu et al.[123] (EIS)	1	$1e^{-15}$ w/o C coating $1e^{-13}$-$5e^{-12}$ w/ C coating	
Molenda et al.[124] (EIS)	$0 \le x \le 0.4$	$3e^{-13}$-$3e^{-16}$	
Gao et al.[125] (EIS)	$0.1 \le x \le 1$	$8.8e^{-18}$-$1.2e^{-16}$	
Xie et al.[126] (PITT,EIS,CV)	≈ 0 (3.6V) ≈ 1 (3.4V)	$1.2e^{-13}$ $3e^{-14}$-$2e^{-13}$	
Tang et al.[127] (PITT)	≈ 0 (3.65V) ≈ 1 (3.3V)	$5e^{-14}$-$2e^{-13}$ $1e^{-13}$	
Churikov et al.[128] (GITT,PITT)	≈ 0 (3.7 V) ≈ 1 (3.1 V)	$7e^{-15}$-$2e^{-14}$ $6e^{-15}$-$7e^{-11}$	
Zhu et al.[103] (GITT,PITT)	$0 \le x \le 1$	$2e^{-13}$-$3e^{-12}$	
Meethong et al.[129] (PITT)	≈ 0 (3.55V) ≈ 1 (3.35V)	$1e^{-14}$ $1e^{-14}$	
Park et al.[130] (CV,EIS)	$0.2 \le x \le 0.9$	$1e^{-15}$-$2e^{-14}$	
Zhu et al.[144] (EIS,GITT)	0.9 (Li 2.9V, Na 2.4V)	$6.7e^{-16}$-$1.8e^{-15}$	$8.7e^{-17}$

Table 1-4 : Diffusion coefficient values of Li and Na within Li/Na_xFePO_4 determined from computational and experimental studies as of 2014.

Similarly, several authors determined activation energies for diffusion within Li_xFePO_4, taking into account electronic, ionic or polaronic mobility. These activation energies correspond to the energy necessary for a single jump of the mobile particle along the (*b*) axis within the crystalline structure,

were found relatively dispersed as seen from the values reported in Table 1-5, ranging from 175 to 650 meV depending on the methodology used and the composition of the material.

In comparison, the activation energy values for diffusion in the directions of the [101] and [001] Miller indices within a defect-free material, determined from a computational technique, were found much higher, as 3360 and 2890 meV respectively.[132]

Furthermore, the activation energy for Li jumping from one tunnel to a neighboring one through antisite defects was found as 490 meV within $LiFePO_4$ by Malik et al.[114] and as 710 and 350 meV within $LiFePO_4$ and $FePO_4$ respectively by Dathar et al.[135] These activation energies can be compared to those determined experimentally by Amin et al. for ionic diffusion along the (*a*) and (*c*) axis, which were found as 740 and 620 meV.

authors	Activation energies (meV) Type of diffusion	Li_xFePO_4 x = 0	Li_xFePO_4 x = 1	Na_xFePO_4 x = 0	Na_xFePO_4 x = 1
Computational studies					
Morgan et al. (2004)[119]	Ionic	200	270		
Ouyang et al. (2004)[131]	ionic		600		
Fisher et al. (2008)[132]	ionic		550		
Liu et al. (2010)[133]	Ionic	270	500		
Ong et al. (2011)[134]	polaron	164	280	277	370
Dathar et al. (2011) [135]	Ionic polaronic	290 510	190 130		
Hoang et al. (2011)[136]	Polaronic ionic		480 320		
Tripathi et al. (2013)[137]	ionic				320
Xu et al. (2014)[138]	ionic		320		
pellets					
Chung et al. (2002)[97]	Electronic		502		
Delacourt et al. (2005)[98]	electronic		540-630		
Zaghib et al. (2007)[139]	electronic		650		
Amin et al. (2008)[113]	Ionic electronic		620 590		

Table 1-5 : Activation energy for diffusion values of Li and Na along the (*b*) axis within Li/Na_xFePO_4 as of 2014.

1.3.2. $NaFePO_4$

Olivine $NaFePO_4$ shares the same structure with its lithium counterpart but, as can be appreciated from Table 1-6, its lattice parameters are larger due to the larger size of the Na ions.[83]

Moreau et al. were the first to extensively study this material and reported its electrochemical profile with two potential plateaus upon Na extraction and a single one upon Na insertion. They identified the charge potential discontinuity to be caused by the formation of an intermediate phase at a composition of x = 0.7.[83] The transformation mechanism of the material upon Na (de)intercalation was extensively studied by Casas-Cabanas et al., who showed that its asymmetrical voltage profile results from distinct Na insertion and extraction paths,[140] and later on by Galceran et al.[141] and Gaubicher et al.[142] which presented a complete description of the mechanism. Na is extracted from $NaFePO_4$ following a monophasic path until formation of the $Na_{2/3}FePO_4$ phase. Further Na extraction occurs following a biphasic mechanism involving the $Na_{2/3}FePO_4$ phase and a $FePO_4$ phase. These three phases are simultaneously present upon Na insertion. Distinctly to the lithium counterpart, phase separation between the $Na_{2/3}FePO_4$ and $FePO_4$ phases was found to occur in the (*ac*) plane, perpendicularly to the diffusion channels in the (*b*) axis as it allows minimizing the strain caused by the 13.48% volume mismatch between the phases by keeping the direction of largest mismatch perpendicular to the interface, as seen in Table 1-6.[141] From theoretical calculations, Tripathi et al.[137] determined that the diffusion of the inserted Na within the ideal material structure is anisotropic, being unidimensionnal along the (*b*) axis, similarly to that of Li.

	Lattice parameters (Å)			
	$LiFePO_4$ [33]	$FePO_4$ [33]	$Na_{2/3}FePO_4$ [140]	$NaFePO_4$ [83]
(a)	10.334	9.821	10.2894	10.4063
(b)	6.008	5.792	6.0843	6.2187
(c)	4.693	4.788	4.9396	4.9469
Volume ($Å^3$)	291.392	272.35	309.23	320.14

Table 1-6 : Comparison of the lattice parameters of the stable Li/Na_xFePO_4 phases.

Several issues however hamper the development of olivine $NaFePO_4$ as SIB cathode. First of all, its synthesis is only possible so far by ionic exchange from $LiFePO_4$ although some efforts are in progress for low cost ion exchange, driven by the regularly decreasing cost of $LiFePO_4$ thanks to its commercial use and the possibility of recycling of the extracted lithium;[143] Furthermore, the electrochemical performances of this material appears to show margin for improvement vs Na. Indeed, as an illustrative example, Oh et al. reported the electrochemical performances of carbon-coated $NaFePO_4$ particles, reaching 80% and 55% of the theoretical capacity of the material at C/20 and C/2 respectively, while 100% of the theoretical capacity of the material was obtained upon Li (de)intercalation at 0.1C.[79] Still, the stable capacity upon Na (de)intercalation these authors reported over 50 cycles is encouraging.

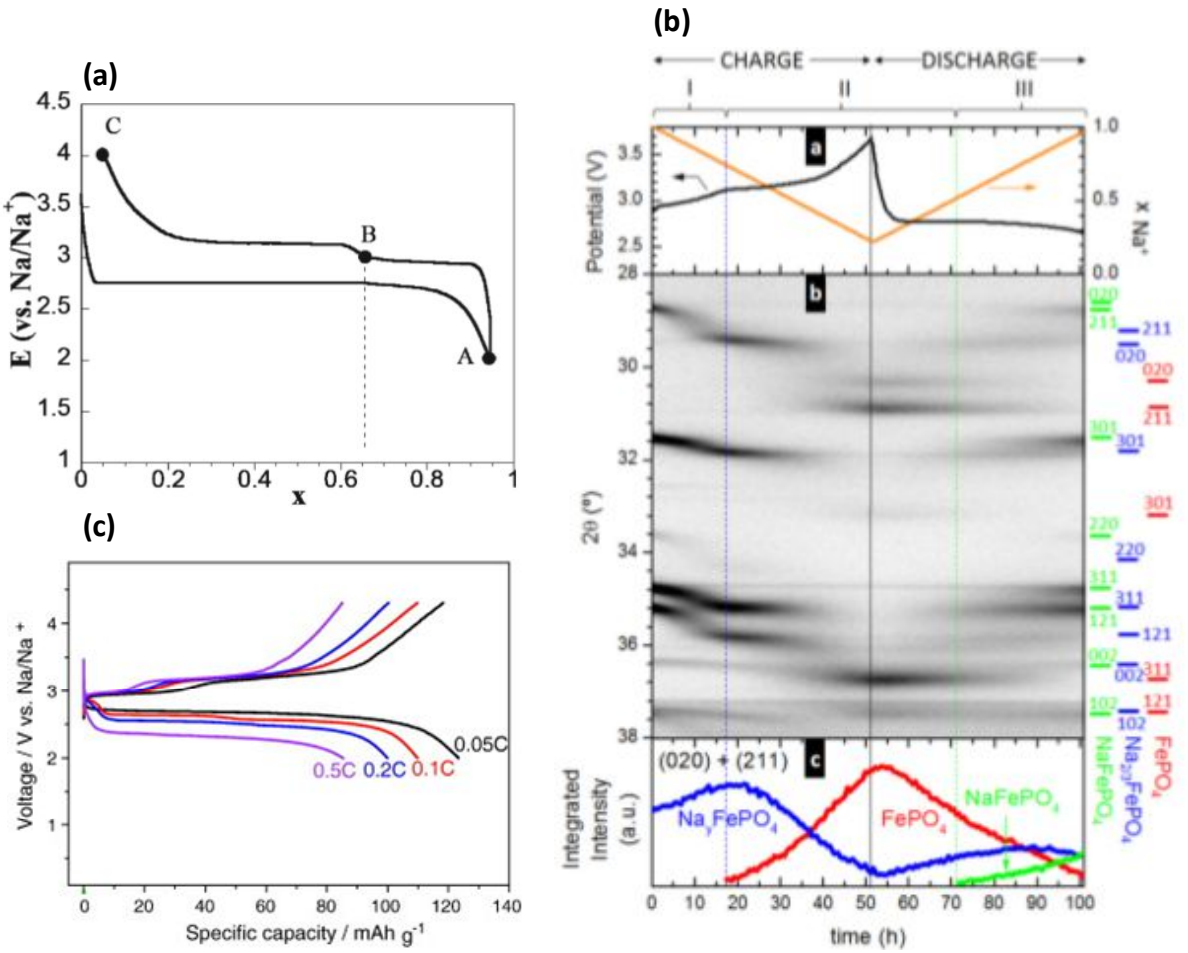

Figure 1-9 : (a) Potential/composition profile of Na_xFePO_4 as determined from PITT by Moreau et al.[83] (b-a) Voltage vs time of a $NaFePO_4$ vs Na cell upon charge and discharge at low rate, (b-b) 2θ vs time plot of the XRD patterns of the Na_xFePO_4 material measured in-situ upon cycling, (b-c) Sum of the integrated intensity of the (020) and (211) reflections for each of the phases involved versus time.[141] (c) Voltage/composition profile of a $NaFePO_4$ vs Na cell upon charge and discharge at increasing rates.[79]

At the beginning of this thesis few authors had studied the diffusivity of Na within Na_xFePO_4. Ong et al.[134] determined and compared the activation energies for diffusion of Li and Na within Li/$NaFePO_4$ along the (*b*) direction from computational technique and found a higher value for Na from which they concluded that the poorer diffusivity of Na was responsible for the poorer electrochemical performances of $NaFePO_4$ compared to $LiFePO_4$. Zhu et al.[144] compared the diffusion coefficient of Li and Na at a composition of x = 0.9 (thus probably corresponding to a biphasic state of the material, although these authors did not comment on that aspect) from electrochemical characterization on functional electrodes. They found a diffusion coefficient of Li between 8 and 20 times higher than that of Na, which led them to the same conclusion. Surprisingly, Tripathi et al.[137] determined an activation energy for diffusion of Na lower than that of Li at a composition of x = 1, in contradiction with the above-mentioned studies. These diffusion coefficient and activation energy values are reported in Table 1-4 and Table 1-5 next to these of lithium.

Interestingly, the formation energy of Na-Fe antisite defects was found lower in $NaFePO_4$ (0.86 eV)[137] than in $LiFePO_4$ (1.33 eV).[111] This low Na-Fe antisite formation energy is consistent with the better stability of the maricite $NaFePO_4$ phase, where the Na and Fe sites are switched in the structure.[145]

This suggests that antisite defects are at least as probable to be present in $NaFePO_4$ as in the case of $LiFePO_4$, and thus have a significant influence on the Na diffusion properties of $NaFePO_4$, although their influence on Na diffusivity is unknown yet.

1.4. Aim of this work

This study aims at understanding the fundamental differences between the (de)intercalation of lithium and sodium in $(Li,Na)FePO_4$ in order to identify the origin of the limitation of the performances of $NaFePO_4$. This is the first step toward the optimization of this material, which presents good stability, low cost and, should its kinetic limitations be overcome, present promising electrochemical performances compared to other candidate cathode materials for sodium-ion batteries. Moreover, the knowledge acquired on this system is a good base to understand the differences between lithium and sodium insertion mechanisms in others insertion compounds, which will open way to improvement of the performances of SIBs in order to be competitive in front of LIBs.

[1] International energy outlook 2017, EIA, https://www.eia.gov/outlooks/ieo/pdf/0484(2017).pdf
[2] K. H. Chua, Y. S. Lim, S. Morris, International Journal of Energy Sector Management, 10(1), 3 (2016)
[3] Z. Yang, J. Zhang, M. C. W. Kintner-Meyer, X. Lu, D. Choi, J. P. Lemmon, J. Liu, Che. Rev., 111, 3577 (2011)
[4] P. Denholm, E. Ela, B. Kirby, M. Millign, The Role of Energy Storage with Renewable electricity Generation, Technical Report NREL/TP-6A2-47187, National Renewable Energy Laboratory (2010)
[5] J. Eyer, G. Corey, Energy Storage for the Electricity Grid: Benefits and Market Potential Assessment Guide, A study for the DOE Energy Storage Systems Program, Sandia Reports SAND2010-0815, Sandia National Laboratories (2010)
[6] J. Arteaga, H. Zareipour, V. Thangadurai, Curr. Sustainable/Renewable Energy Rep., 4(4), 197 (2017)
[7] Lithium 101, Markets Research Deutshe Bank, may 2016
[8] K. Yong, C. Wang, L. Y. Wang, K. Strunz, Chapter 2: Electric Vehicle Battery Technologies, in R. Garcia-Valle, J. A. Pecas Lopes, *Electric Vehicle Integration into Modern Power Networks*, Power Electronics and Power Systems, Springer Science+Business Media New York (2013)
[9] C. Dötsch, Electrical energy storage from 100 kW – State of the art technologies, fields of use. 2nd , 2nd Int. Renewable Energy Storage Conference, Bonn/Germany, 22 Nov 2007
[10] A. Sharma, V. V. Tygi, C.R. hen, D. Buddhi, Renewable and Sustanaible Energy Reviews, 13(2), 319 (2009)
[11] M. Götz, J. Lefebvre, F. Mörs, A. McDaniel Koch, F. Graf, S. Bajohr, R. Reimert, T. Kolb, RenewableEnergy, 85, 1371 (2016)
[12] P. Alotto, M. Guarnieri, F. Moro, Renewable and Sustainable Energy reviews, 29, 325 (2014)
[13] A. Gonzalez, E. Goikolea, J. A. Barrera, R. Mysyk, Renewable and Sustanaible Energy Reviews, 58, 1189 (2016)
[14] A. Burke, Z. Liu, H. Zhao, Present and future applications of supercapacitors in electric and hybrid vehicles, Electric Vehicle Conference (IEVC), Florence, Italy, IEEE International (2014)
[15] Battery university, BU-1006 cost of mobile and renewable power, 2017-05-19, http://batteryuniversity.com/learn/article/bu_1006_cost_of_mobile_power
[16] H. D. Yoo, E. Markevich, G. Salitra, D. Sharon, D. Aurbach, Materials Today, 17(3), 110 (2014)
[17] P. Ruetschi, J. Power Sources, 2 (1), 3 (1977)
[18] D.G. Enos, Chapter 3 – Lead-acid batteries for medium and large-scale energy storage, in Advances in Batteries for Medium and Large-Scale Energy storage, pp 57-71, Woodhead Publishing Series in Energy (2015)
[19] C.-H. Dustmann, J. Power Sources, 127 (1-2), 85 (2004)
[20] D. Kumar, S. K. Rajouria, S. B. Kuhar, D. K. Kanchan, Solid State Ionics, 312, 8 (2017)
[21] A. Babu, S. Ashok, Trends in Electrical Engineering, 2 (2), 1 (2012)
[22] F. Putois, J.Power Sources, 57 (1-2) , 67 (1995)
[23] P. Ruetshi, F. Meli, J. Desilvsetro, J. Power Sources, 57 (1-2), 85 (1995)

[24] N. Nitta, F. Wu, J. T. Lee, G. Yushin, Materials today, 18, 5, 252 (2015)
[25] G. Berckmans, M. Messagie, J. Smekens, N. Omar, L. Vanhaverbeke, J. Van Mierlo, Energies, 10, 1314 (2017)
[26] F. Lambert, Electric vehicle battery cost dropped 80% in 6 years down to %227/kWh, Electrek.co, 30 Jan. 2017
[27] C. M. Julien, A. Mauger, K. Zaghib, H. Groult, Inorganics, 2, 132 (2014)
[28] K. Mizushima, P. C. Jones, P. J. Wiseman, J. B. Goodenough, Mater. Res. Bull., 15 (6), 783 (1980)
[29] E. Antolini, M. Ferretti, J. Solid State Chem., 117 (1), 1 (1995)
[30] S. Albrecht, J. Kümpers, M. Kruft, S. Malcus, C. Vogler, M. Wahl, M. Wohlfahrt-Mehrens, J. Power Sources, 119, 179 (2003)
[31] N. Yaabuchi, T. Ohzuku, J. Power Sources, 119, 171 (2003)
[32] A. R. Armstrong, P. G. Bruce, Nature, 381, 499 (1996)
[33] A. K. Padhi, K. S. Nanjundaswamy, J. B. Goodenough, J. Electrochem. Soc., 144(4), 1188 (1997)
[34] P. Prosini, Iron Phosphates Materials as Cathdes for Lithium Batteries, Springer-Verlag London, p71 (2011)
[35] J.-M. Tarascon, M. Armand, Nature, 414(6861), 359 (2001)
[36] N. A. Kaskhedikar, J. Maier, Adv. Mater., 21 (25-26), 2664 (2009)
[37] G.-N.Zhu, Y.-G. Wang, Y.-Y. Xia, Energy Environ. Sci., 5, 6652 (2012)
[38] Z. Chen, I. Belharouak, Y.-K. Sun, K. Amine, 23 (8), 959 (2013)
[39] M. N. Obrovac, V. L. Chevrier, Chem. Rev., 114, 11444 (2014)
[40] Q. Fan, P. J. Chupas, M. S. Whittingham, Electrochem. Solid State Lett., 10, A274 (2007)
[41] W. Xu, J. Wang, X. Chen, E. Nasybulin, Y. Zhang, J.-G. Zhang, Energy Environ. Sci., 7, 513 (2014)
[42] X. He, R. Jianguo, W. Li, P. Weihua, J. Changyin, W. Chunrong, J. Power Sources, 190 (1), 154 (2009)
[43] A. Manthiram, Y. Fu, S. H. Chung, C. Zu, Y.-S. Su, Chem. Rev., 114, 11751 (2014)
[44] A. C. Luntz, B. D. McCloskey, Chem. Rev., 114, 11721 (2014)
[45] Q. Li, J. Chen, L. Fan, X. Kong, Y. Lu, Green Energy &Environment, 1 (1), 18 (2016)
[46] K. Kerman, A. Luntz, V. Viswanathan, Y.-M. Chiang, Z. Chen, J. Electrochem. Soc., 164 (7), A1731 (2017)
[47] J.-M. Tarascon, Nat. Chem., 2, 510 (2010)
[48] D. Aurbach, G. S. Suresh, E. Levi, A. Mitelman, O. Mizrahi, O. Chusid, M. Brunelli, Adv. Mater. 19, 4260 (2007)
[49] V. Palomares, P. Serras, I. Villaluenga, K. B. Hueso, J. Carretero-Gonzalez, T. Rojo, Energy Environ. Sci, 5, 5884 (2012)
[50] H. Pan, Y.-S. Hu, L. Chen, Energy Environ. Sci., 6, 2338 (2013)
[51] N. Yaabuchi, K. Kubota, M. Dahbi, S. Komaba, Chem. Rev., 114(23), 11636 (2014)
[52] J. W. Choi, D. Aurbach, Nat. Rev., 1, 1 (2016)
[53] M. D. Slater, D. Kim, E. Lee, C. S. Johnson, Adv. Funct. Mater., 23, 947 (2013)
[54] Y. Kim, K.-H. Ha, S. M. Oh, K. T. Lee, Chem. Eur. J., 2, 11980 (2014)
[55] L. Baggetto,P. Ganesh, R. P. Meisner, R. R. Unocic,J.-C. Jumas, C. A. Bridges, G. M. Veith, J. Power Sources, 234, 48 (2013)
[56] J. Quian, Y. Chen, L. Wu, Y. Cao, X. Ai, H. Yang, Chem. Commun., 48, 7070 (2012)
[57] N. Yaabuchi, M. Kajiyama, J. Iwatate, H. Nishikawa, S. Hitomi, R. Okuyama, R. Usui, Y. Yamada, S. Komaba, Nat. Mater., 11, 512 (2012)
[58] J.-Y. Hwang, S.-T. Myumg, Y.-K. Sun, Chem. Soc. Rev., 46, 3529 (2017)
[59] D. I. Iermakova, R. Dugas, M. R. Palacin, A. Ponrouch, J. Electrochem. Soc., 162(13), A7060 (2015)
[60] M. A. Muñoz-Marquez, M. Zarrabeitia, E. Castillo-Martinez, A. Eguia-Barrio, T. Rojo, M. Casas-Cabanas, ACS Appl. Mater. Interfaces,,7, 7801 (2015)
[61] D. A. Stevens, J. R. Dahn, J. Electrochem. Soc., 147(4), 1271 (2000)
[62] C. Bommier, T. W. Surta, M. Dolgos, X. Ji, Nano Lett., 15, 5888–5892 (2015)
[63] Y. Mei, Y. Huang, X. Hu, J. Mater. Chem. A, 4, 12001–12013 (2016)
[64] F. Legrain, O.Malyiand, S.Manzhos,J.PowerSources, 278, 197 (2015)
[65] H. Usui, S. Yoshioka, K. Wasada, M. Shimizu, H. Sakaguchi, ACS Appl. Mater. Interfaces, 7, 6567 (2015)
[66] K. T. Kim, G. Ali, K. Y. Chung, C. S. Yoon, H. Yashiro, Y.-K. Sun, J. Lu, K. Amine,S. T. Myung, Nano Lett., 14, 416 (2014)
[67] Y. Sun, L. Zhao, H. Pan, X. Lu, L. Gu, Y. S. Hu, H. Li, M. Armand, Y. Ikuhara, L. Chen, X. Huang, Nat. Commun., 4, 1870 (2013)
[68] X. Yu, H. Pan, W. Wan, C. Ma, J. Bai, Q. Meng, S. N. Ehrlich, Y. S. Hu, X. Q. Yang, Nano Lett., 13, 4721 (2013)
[69] S. H. Woo, Y. Park, W. Y. Choi, N.-S. Choi, S. Nam, B. Park, K. T. Lee, J. Electrochem. Soc., 159, A2016 (2012)
[70] P. J. P. Naeyaert, M. Adveev, N. Shara, H. B. Yahia, C. D. Ling, Chem. Mater., 26, 7067 (2014)
[71] P. Senguttuvan, G. Rousse, V. Seznec, J.-M. Tarascon, M. R. Palacin, Chem. Mater., 23, 4109 (2011)

[72] L. D. Ellis, B. N. Wilkes, T. D. Hatchard, M. N. Obrovac, J. Electrochem. Soc., 161, A416 (2014)
[73] Y. Kim, Y. Park, A. Choi, N.-S. Choi, J. Kim, J. Lee, J. H. Ryu, S. M. Oh, K. T. Lee, Adv. Mater., 25, 3045 (2013)
[74] C. Delmas, C. Fouassier, P. Hagenmuller, Physica B & C, 99, 81 (1980)
[75] M. H. Han, E. Gonzalo, G. Singh, T. Rojo, Energy Environ. Sci., 8, 81 (2015)
[76] H. Su, S. Jaffer, H. Yu, Energy storage materials, 5, 116 (2016)
[77] X. Xiang, K. Zhang, J. Chen, Adv. Mater., 27, 5343 (2015)
[78] S.-M. Oh, S.-T. Myung, C. S. Yoon, J. Lu, J. Hassoun, B. Scrosati, K. Amine, Y.-K. Sun, Nano Letters, 14, 1620, (2014)
[79] S.-M. Oh, S.-T. Myung, J. Hassoun, B. Scrosati, Y.K. Sun, Electrochem. Commun., 22, 149 (2012)
[80] P. Barpanda, T. Ye, S.-I. Nishimura, S.-C. Chung, Y. Yamada, M. Okubo, H. Zhou, A. Yamada, Electrochem. Commun., 24, 116 (2012)
[81] Y. Lu, L. Wang, J. Cheng, J. B. Goodenough, Chem. Commun., 48, 6544 (2012)
[82] J. Kim, D.-H. Seo, H. Kim, I. Park, J.-K. Yoo, S.-K. Jung, Y.-U. Park, W. A. Goddard, K. Kang, Energy Environ. Sci., 8, 540 (2015)
[83] P. Moreau, D. Guyomard, J. Gaubicher, F. Boucher, Chem. Mater., 22, 4126 (2010)
[84] K.T. Lee, T. N. Ramesh, F. Nan, G. Botton, L. Nazar, Chem. Mater., 23, 3593 (2011)
[85] T. Boyadzhieva, V. Koleva, E. Zhecheva, D. Nihtianova, L. Mihaylov, R. Stoyanova, RSC Adv., 5, 87694 (2015)
[86] P. Barpanda, G. Oyama, S. Nishimura, S.-C. Chung, A. Yamada, Nat. Commun., 5, 4358 (2014)
[87] B. L. Ellis, W. R. M. Makahnouk, Y. Makimura, K. Toghill, L. F. Nazar, Nat. Mater., 6, 749 (2007)
[88] Y. Kawabe, N. Yabuuchi, M. Kajiyama, N. Fukuhara, T. Inamasu, R. Okuyama, I. Nakai, S. Komaba, Electrochemistry, 80, 80 (2012)
[89] P. Barpanda, S.-I. Nishimura, A. Yamada, Adv. Energy Mater., 2(7), 841 (2012)
[90] Z. Jian, L. Zhao, H. Pan, Y.-S. Hu, H. Li, W. Chen, L. Chen, Electrochem. Commun. 14, 86 (2012)
[91] K. Saravanan, C. W. Mason, A. Rudola, K. H. Wong, P. Balaya, Adv. Energy Mater., 3, 444–450 (2013)
[92] V. Srinivasan, J. Newmann, J. Electrochem. Soc., 151, A1517 (2004)
[93] A. Yamada, H. Koizumi, N. Sonoyama, R. Kanno, Electrochem. Solid State Lett. 8, A409–A413 (2005)
[94] A. Yamada, H. Koizumi, S.I. Nishimura, N. Sonoyama, R. J. Kanno, M. Yonemura, T. Nakamura, Y. Kobayashi, Nat. Mater., 5, 357 (2006)
[95] N. Meethong, H. S. Huang, S. A. Speakman, W. C. Carter, Y. M. Chiang, Electrochem. Solid State Lett., 10(5), A134 (2007)
[96] M. Wagemaker, F. M. Mulder, A. Van der Ven, Adv. Mater., 21, 2703 (2009)
[97] S. Y. Chung, J. T. Bloking, Y. M. Chiang, Nat. Mater., 1, 123 (2002)
[98] C. Delacourt, L. Laffont, R. Bouchet, C. Wurm, J. B. Leriche, M. Morcrette, J. M. Tarascon, C. Masquelier, J. Electrochem. Soc., 152, A913 (2005)
[99] W. J. Zhang, J. Electrochem. Soc., 157, A1040 (2010)
[100] M. Armand, M. Gauthier, J.-F. Magnan, N. Ravet, Method for synthesis of carbon-coated redox materials with controlled size, Google patents US (2004)
[101] N. Ravet, A. Abouimrane, M. Armand, Nat. Mater. 2, 702 (2003)
[102] P. S. Herle, B. Ellis, N. Coombs, L. F. Nazar, Nat. Mater., 3, 147 (2004)
[103] Y. Zhu, C. Wang, J. Phys. Chem. C., 114, 2830 (2010)
[104] R. Malik, A. Abdellahi, G. Ceder, J. Electrochem, Soc., 160(5), A3179 (2013)
[105] C.V. Ramana, A. Mauger, F. Gendron, C. M. Julien, K. Zaghib, J. Power Sources, 187, 555 (2009)
[106] C. Delmas, M. Maccario, L. Croguennec, F. le Cras, F. Weill, Nat. Mater., 7, 665 (2008)
[107] R. Malik, F. Zhou, G. Ceder, Nat. Mater., 10, 587 (2011)
[108] B. Kang, G. Ceder, Nature, 458, 190 (2009)
[109] D. H. Kim, J. Kim, Electrochem. Solid State Lett., 9, A439 (2006)
[110] T. Maxisch, F. Zhou, G.Ceder, Phys. Rev. B, 7310, 104301 (2006)
[111] M. S. Islam, D. J. Driscoll, C. A. J. Fisher, P. R. Slater, Chem. Mater., 17(20), 5085 (2005)
[112] G. Y. Chen, X. Y. Song, T. J. Richardson, Electrochem. SolidState Lett. 9, A295 (2006).
[113] R. Amin, J. Maier, P. Blaya, D. P. Chen, C. T. Lin, Solid State ionics, 179, 1683 (2008)
[114] R. Malik, D. Burch, M. Bazant, G. Ceder, Nano Letters, 10, 4123 (2010)
[115] J. Chen, M. J. Vacchio, S. Wang, N. Chernova, P. Y. Zavalij, M. S. Wittingham, Solid State Ionics, 178, 1676 (2008)
[116] S. Y. Chung, S. Y. Choi, T. Yamamoto, Y. Ikuhara, Phys. Rev. Lett., 100, 125502 (2008)
[117] R. Amin, P. Balaya, J. Maier, J. electrochem. Solid-State Lett., 10(1), A13 (2007)
[118] S. F. Yang, Y. N. Song, P. Y. Zavalij, M. S. Wittingham, Electrochem Commun., 4(3), 239 (2002)

[119] D. Morgan, A. Van der Ven, G. Ceder, Electrochem. Solid State Lett., 7 (2), A30-A32 (2004)
[120] P. P. Prosini, M. Lisi, S. Scaccia, M. Carewska, F. Cardellini, and M. Pasquali, J. Electrochem. Soc., 149, A297 (2002)
[121] P.P. Prosini, M. Lisi, D. Zane, M. Pasqualini, Solid State Ionics 148 45–51 (2002)
[122] S. Franger, F. L. Cras, C. Bourbon, H. Rouault, Elec. Solid State Lett., 5, A231 (2002)
[123] H. Liu, C. Li, H.P. Zhang, L.J. Fu, Y.P. Wu, J. Power Sources, 159, 717 (2006)
[124] J. Molenda, W. Ojczyk, K. Swierczek, W. Zajac, F. Krok, J. Dygas, R.-S. Liu, Solid State Ionics, 177, 2617 (2006)
[125] F. Gao, Z. Tang, Electrochim. Acta, 53, 5071 (2008)
[126] J. Xie, N. Imanishi, T. Zhang, A. Hrano, Y. Takeda, O. Yamamoto, Electrochimica Acta, 54 4631 (2009)
[127] X.-C. Tang, L.-X. Li, Q.-L. Lai, X.-W. Song, L.-H. Jiang, Electrochimica Acta, 54, 2329 (2009)
[128] A. V. Churikov, A. V. Ivanishchev, I. A. Ivanishcheva, V. O. Sycheva, N. R. Khasanova, E. V. Antipov, Electrochim. Acta, 55, 2939 (2010)
[129] N. Meethong, Y.-H. Kao, W. C. Carter, Y.-M. Chiang, Chem. Mater., 22, 1088 (2010)
[130] C. K. Park, S. B. Park, H. C. Shin, W. I. Cho, H. Jang, Bull. Korean Chem. Soc., 32 (1), 191 (2011)
[131] C. Ouyang, S. Shi, Z. Wang, X. Huang, L. Chen, Physical Review B 69, 104303 (2004)
[132] C. A. J. Fisher, V. M. H. Prieto, M. S. Islam, Chem. Mater., 20 (18) (2008)
[133] Z. Liu, X. Huang, Solid State Ionics, 181, 907 (2010)
[134] S. P. Ong, V. L. Chevrier, G. Hautier, A. Jain, C. More, S. Kim, X. Ma, G. Ceder, Energy Environ. Sci., 4, 3680 (2011)
[135] G. K. P. Dathar, D. Sheppard, K. J. Stevenson, G. Henkelman, Chem. Mater., 23, 4032 (2011)
[136] K. Hoang, M. Johannes, Chem. Mater., 23(11), 3003 (2011)
[137] R. Tripathi, S. M. Wood, M. S. Islam, L. F. Nazar, Energy Environ. Sci., 6, 2257 (2013)
[138] G. Xu, K. Zhong, J.-M. Zhang, Z. Huang, Journal of Applied Physics, 116, 063703 (2014)
[139] K. Zaghib, A. Mauger, J. B. Goodenough, F. Gendron, C. M. Julien, Chem. Mater., 19, 3740 (2007)
[140] M. Casas-Cabanas, V. V. Roddatis, D. Saurel, P. Kubiak, J. Carretero-Gonzalez, V. Palomares, P. Serras, T. Rojo, J. Mater. Chem., 22, 17421 (2012)
[141] M. Galceran, V. Roddatis, F. J. Zuñiga, J. M. Perez-Mato, B. Acebedo, R. Arenal,I. Peral, T. Rojo, M. Casas-Cabanas, Chem. Mater., 26(10), 3289 (2014)
[142] J. Gaubicher, F. Boucher, P. Moreau, M. Cuisinier, P. Soudan, E. Elkaim, D. Guyomard, Electrochem. Commun., 38, 104 (2014)
[143] W. Tang, X. Song, Y. Du, C. Peng, M. Lin, S. Xi, B. Tian, J. Zheng, Y. Wu, F. Pan, K. P. Loh, J. Mater. Chem. A, 4, 4882 (2016)
[144] Y. Zhu, Y. Liu, C. Lou, C. Wang, Nanoscale, 5, 780 (2013)
[145] Y. Lepage, G. Donnay, Can. Mineral, 15, 518 (1977)

2. Electrochemical characterization background

2.1. Introduction

This chapter aims at clarifying the physical and chemical phenomena leading to the creation of a current between the two terminals of a battery. It also intends to explain how these physical and chemical phenomena are related to the electrochemical performance of a battery and how the analysis of the electrical signal it provides allows characterizing and quantifying these phenomena.

2.2. Transformation of chemical energy into electrical energy

All the information about the relation between a material's potential and its thermodynamic properties can be found in ref. [1].

2.2.1. Basic battery working principles

The simplest description of a secondary battery consists in two pieces of materials called electrodes, each connected to a different terminal of the battery. These two materials can sustain reversible oxidation and reduction reactions with uneven standard redox potentials. The oxidation and reduction reactions occur at the same time on each electrode and the products of the oxidation reaction are the reactants of the reduction reaction. These chemical reactions are driven by the standard redox potential difference between the electrodes which depends on the thermodynamic properties of the species involved in it. Considering the electrochemical reactions upon spontaneous discharge of the battery, $A^{n+} + ne^- \leftrightarrows A$ on the low potential electrode and $AB \leftrightarrows A^{n+} + ne^- + B$ on the high potential electrode, the net cell reaction is $AB \leftrightarrows A + B$.

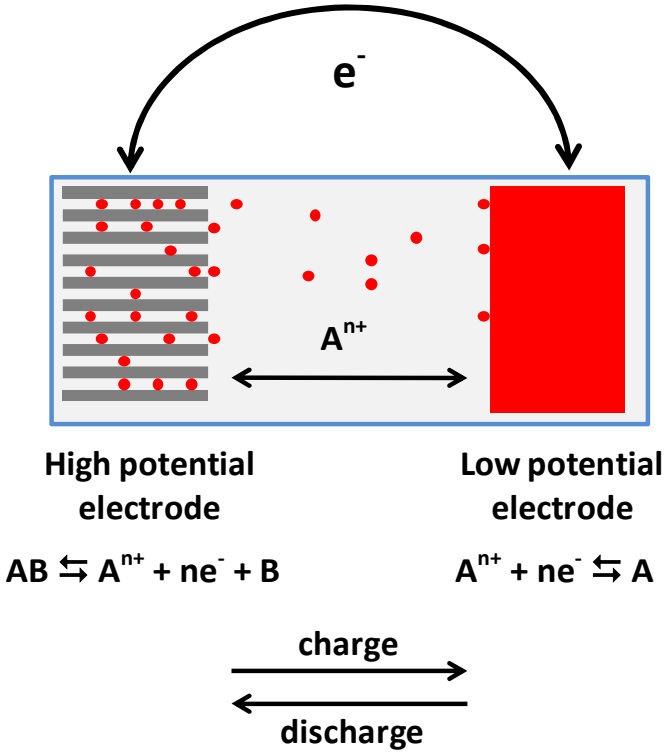

Figure 2-1: Basic battery working principle

The products and reactants of the redox reactions, usually an ion and an electron, are mobile within the battery materials and are consumed by the reduction reaction at the same rate they are produced by the oxidation reaction. To sustain this parallel ion/electron production/consumption, these two charge carriers travel from one electrode to the other, within the battery for the ions and outside the battery for the electrons. This separation of ion and electron paths is ensured by the medium, the electrolyte, which separates the two electrodes within the battery and which should be ionic conducting and electronic insulating. The mobile ions move from the electrode where the

oxidation reaction takes place to the electrode where the reduction reaction takes place within the electrolyte, driven by their concentration gradient induced by their simultaneous production and consumption.

The mobile electrons also travel from the electrode where the oxidation reaction takes place to the electrode where the reduction reaction takes place through the external electrical circuit connected to the battery terminals. This flux of electrons between the two electrode materials is driven by the electromotive force induced by the difference of redox reaction potential between the two electrodes.

2.2.2. Driving force and voltage

The maximum work that can be obtained from the redox reaction is defined by its Gibbs free energy ΔG_{cell}. It is defined as the difference between the free energies of the products and the reactants of the reactions:

$$W = \Delta G_{cell} = \sum z_{product} \Delta G_{products} - \sum z_{reactant} \Delta G_{reactants} \quad (2\text{-}1)$$

With z_i as the stoichiometric quantity of the i specie consumed or produced upon the reaction.

When ΔG_{cell} is positive, energy is required for the reaction to occur. On the contrary, when ΔG_{cell} is negative, the electrochemical reaction occurs spontaneously by converting chemical energy into electrical energy.

The chemical potential μ_i of a chemical specie i is defined as the partial molar free energy of that specie:

$$\mu_i = \frac{\partial G_i}{\partial n_i} \quad (2\text{-}2)$$

n_i being the number of moles of i. This quantity represents the rate of change of free energy of a system with respect to an infinitesimal quantity variation of the specie i while the other species quantity remains constant.

This chemical potential is also defined as:

$$\mu_i = \mu_i^0 + RT ln\, a_i \quad (2\text{-}3)$$

Where μ_i^0 is the standard chemical potential of the pure i specie, calculated under a defined set of standard conditions. R is the gas constant, T is the temperature of the system, and a_i is the thermodynamic activity of the specie i. This activity a_i depicts the variations of the chemical potential of the specie from its standard chemical potential because of non-standard conditions (pressure, temperature) or interactions with its environment.

In terms of chemical potentials, considering the battery operates at fixed temperature and pressure, the Gibbs free energy ΔG_{cell} corresponding to a single reaction step of the net cell reaction is written:

$$\Delta G_{cell} = W_s = \sum z_i \mu_i \tag{2-4}$$

When a net cell reaction step occurs, electrons move from one electrode to another within the electrical circuit connected to the battery terminals. The electrical work that can be obtained from the mobile electrons flow within this electrical circuit is defined by the product of the voltage between the electrodes and the amount of charges that pass through.

$$W = -\int i(t) E_{cell}(t) dt \tag{2-5}$$

The voltage of the cell E_{cell} being defined as the difference between the electrical potentials of the electrodes:

$$E_{cell} = E_{high\ potential\ electrode} - E_{low\ potential\ electrode} \tag{2-6}$$

The electrical potential of a chemical specie is a measure of the amount of energy needed by the specie to acquire an electron situated at an infinite distance in vacuum. In the case of a single reaction step, with n as the number of electrons produced and consumed upon the net cell redox reaction and F as the Faraday constant, this work can be written as:

$$W_s = -nFE_{cell} \tag{2-7}$$

Leading to the relation between the voltage of the cell and the chemical potentials of the species involved in the redox reaction from equations (2-4) and (2-7):

$$\sum z_i \mu_i = -nFE_{cell} \tag{2-8}$$

Considering the electrochemical reactions upon spontaneous dischargeof the battery $A^{n+} + ne^- \leftrightarrows A$ on the low potential electrode, $AB \leftrightarrows A^{n+} + ne^- + B$ on the high potential electrode, and the net cell reaction $AB \leftrightarrows A + B$; the relation between the voltage of the cell and the chemical potentials of the species involved in the redox reaction can be written:

$$E_{cell} = -\frac{(\mu_A - \mu_{A^{n+}} - n\mu_{e^-}) + (\mu_{A^{n+}} + n\mu_{e^-} + \mu_B - \mu_{AB})}{nF} \tag{2-9}$$

and, by combining with (2-3):

$$E_{cell} = \frac{\left(\mu^0_{AB} - \mu^0_{A^{n+}} - n\mu^0_{e^-} - \mu^0_B\right) - \left(\mu^0_A - \mu^0_{A^{n+}} - n\mu^0_{e^-}\right) -}{nF} + \frac{RT}{nF} ln \frac{a_{AB}}{a_A a_B} \tag{2-10}$$

This equation is known as the Nernst equation. It describes the evolution of the voltage of the cell as function of the thermodynamic properties of the species involved within the redox reactions.

The quantities $\frac{\left(\mu^0_{AB} - \mu^0_{A^{n+}} - n\mu^0_{e^-} - \mu^0_B\right)}{nF}$ and $\frac{\left(\mu^0_A - \mu^0_{A^{n+}} - n\mu^0_{e^-}\right)}{nF}$ represent the potentials of the reduction reactions, i.e. the electrical potentials at which the two respective reduction reactions occur

individually on their respective electrodes in standard conditions. These terms are named standard electrode potential, and respectively abbreviated $E^0_{A^{n+}/A}$ and $E^0_{B/AB}$.

The Nernst equation in terms of electrical potentials is similar to equation (2-6) and for this case can be summarized as:

$$E_{cell} = E^0_{B/AB} - E^0_{A^{n+}/A} + \frac{RT}{nF} ln \frac{a_{AB}}{a_A a_B} \quad (2\text{-}11)$$

The voltage of the cell depends therefore on the thermodynamic activities of the species involved in the redox reaction. A specie in solid state will be found in its standard thermodynamic state and have a thermodynamic activity a_i of 1. This case applies for example to metallic electrodes. Highly diluted solutions are usually considered as ideal systems where the interactions between the specie themselves and with their environment are negligible. In this case the standard thermodynamic state is taken as the solution at a concentration of 1M and the thermodynamic activity of the specie is equivalent to its actual concentration. In the case of an insertion material the thermodynamic activity of the host material or the inserted specie depends strongly on the interactions between the inserted species themselves and their environment. The strength of these interactions and therefore the thermodynamic activity of the host or the inserted specie will vary depending on the amount of inserted specie (i.e. its concentration within the insertion material). The voltage of a battery made of a metallic electrode and an insertion electrode is therefore set by the Nernst equation and depends on both the nature of the electrodes and the concentration in species involved in the redox reaction within the insertion material.

Within particular composition ranges, however, some insertion materials tend to present a separation between phases, each presenting different concentrations of inserted species. In this case, a discontinuity is observed in the concentration profile of the inserted specie at the interfaces between the phases. Being in direct contact and able to exchange inserted species the two phases have the same chemical potential at equilibrium. The composition of each phase and the voltage of the cell are determined by the equilibrium condition:

$$\mu^0_{phase\ 1} + RTln\ a_{phase\ 1} = \mu^0_{phase\ 2} + RTln\ a_{phase} \quad (2\text{-}12)$$

The voltage of the battery cannot be predicted by the Nernst equation as two phases are present, limiting the degree of liberty of the intensive physical variables within the material. This degree of liberty is defined by the Gibbs phase rule[2]:

$$F = C - P + 2 \quad (2\text{-}13)$$

Where F is the number of independent intensive physical parameters of the studied specie (pressure, temperature, concentration, potential etc), C is the number of components of the species in presence and P the number of phases presents in the active material.

In the case of a pure metallic electrode like lithium or sodium, only Li atoms are present within the material, so the C parameter is 1. The metallic material is single phase so the P parameter is 1. The degree of liberty of the intensive parameters of the electrode material is therefore equal to two.

However, the pressure and temperature are fixed within the cell, leaving no degree of liberty for the potential of the metallic electrode material which only depends on temperature and pressure.

In the case of a Li_xFePO_4 electrode, the number of components is equal to 4 (Li, Fe, P and O). The number of phases is equal to 1 or 2 whether the electrode material is single-phase or biphasic. The degree of liberty of the intensive physical parameters of the electrode material is equal to 5 in the case the material is single-phase and equal to 4 in the case the material is biphasic. However in these two cases, the temperature, pressure and Fe:P and Fe:O ratios are fixed. This lets one degree of liberty in the case of the single-phase material which allows the potential of the material to change with x following the Nernst equation. In the case of the biphasic Li_xFePO_4 material, the degree of liberty is 0. The potential of this material is therefore fixed as long as two phases are present and will not depend on the respective amounts of phases in presence. In this case, the potential of the material is defined by the potentials of the two phases in presence, the equilibrium conditions between them (strain between the phases in presence for example) and the temperature and pressure.

2.3.Movement of mobile species within the battery materials

A battery's electrical performance is not only linked to its voltage but also to the current it is able to sustain while in operation. The current sustained by the battery corresponds to the flow of electrons produced and consumed by the redox reactions at the surface of the electrodes. This electronic flow is directly proportional to the ionic flow between the electrodes inside the battery. The electrical signal provided by the battery gives thus indications about the different ionic and electronic transport phenomena within its materials. This part aims at explaining and quantifying the typical transport phenomena within Li-ion type batteries. The information presented below on electrochemical impedance spectroscopy, if not otherwise referred to other work, is issued from ref. [3], while more details on the charge transfer kinetics can be found in ref. [4].

2.3.1. Electrochemical impedance spectroscopy

A battery's electrochemical performance can be characterized through two main parameters: its voltage and the current between its terminals. If the cell is at open circuit state, the electronic flow between the electrodes is cut and, as a consequence, the ionic flow as well. At equilibrium, the concentration of mobile species within the battery materials is uniform, and the voltage of the cell at this state is named equilibrium voltage. When a potential or a current perturbation is set to the battery, the current or potential response to this excitation is determined by a large panel of physiochemical mechanisms related to redox reactions and charge carrier transport.

At a given state of charge the overpotential of the battery is defined as the difference between its measured voltage and its equilibrium voltage:

$$\Delta E = E_{measured} - E_{equilibrium} \quad (2\text{-}14)$$

The impedance of a cell is defined as the ratio of this overpotential over its current.

$$Z = \frac{\Delta E}{I} \quad (2\text{-}15)$$

Each of the physiochemical phenomena occurring within the battery upon operation have a particular signature in terms of impedance and usually a behavior that is equivalent to a combination of common electrical components. Electrochemical Impedance spectroscopy (EIS) is a characterization technique that allows separating the contributions of these physiochemical phenomena to the response of the cell to a current or potential excitation.

In an EIS experiment, a sinusoidal current excitation in the form of $i(t) = i_0 \sin(\omega t)$ or a potential excitation in the form $E(t) = E_{eq} + E_0 \sin(\omega t)$ is applied to the cell at the thermodynamic equilibrium state. A potential sinusoidal response is observed in the case of a current excitation. A current sinusoidal response is observed in the case of a potential excitation. The phase of the response signal, as well as its amplitude, depends on the frequency of the excitation, the nature of the mechanism inducing the cell impedance and the amplitude of the excitation signal.

Each of the physiochemical phenomena mentioned below have a different characteristic time response. The longer in time the excitation, the more phenomena are triggered. At high frequency, only the fastest ones are triggered while all of them are at very low frequency.

The impedance of a cell is defined in the complex plan either by its phase and amplitude, or by its real and imaginary parts.

$$Z(\omega) = \frac{\Delta E(\omega)}{I(\omega)} = |Z|e^{j\theta} = Re(Z) \mp jIm(Z) \quad (2\text{-}16)$$

A very common representation of impedance data, convenient for the qualitative identification of the various phenomena involved, is the Nyquist plot $-Im(Z)$ vs $Re(Z)$. In this case, the inverse of the imaginary part is represented as it typically presents negative values for electrochemical cells.

2.1.1. Ionic transport within the electrolyte

Usually in the case of Li-ion batteries the fastest transport phenomena are the transport of the electrons between the redox reaction sites and that of the mobile ions within the electrolyte.[5] These charge carriers are generated upon the oxidation reaction at the surface of one of the electrodes, and consumed at the same rate they are created, at the surface of the electrode where the reduction reaction takes place.

In terms of impedance, the electronic transport is limited by the electrical resistance induced by the current collector and the electrical circuit between the electrodes.

Within the electrolyte, the simultaneous ion generation on one electrode and consumption on the other electrode creates a solvated ion concentration gradient which drives their transport from one

electrode to the other following the principle of the Fick's first law, while the net overall concentration of the electrolyte remains constant. In terms of impedance, the response of the transport of the solvated ions from one electrode to the other in the electrolyte is equivalent to a resistance R_{el}. The value of this resistance depends on the nature of the electrolyte, its concentration, and the diffusion path length induced by the geometry of the battery. Since the corresponding impedance is purely real with no frequency dependence, it is characterized by a single point in the ordinate axis on the Nyquist plot.

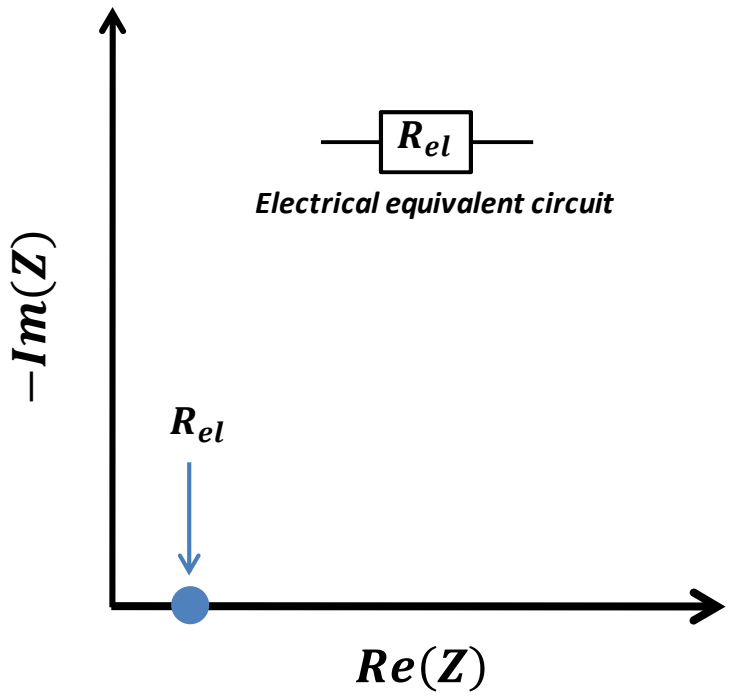

Figure 2-2: Nyquist plot of the electrolyte resistance

2.3.3. Charge transfer

The redox reaction takes place at the interface between the electrode and the electrolyte. The rate of this reaction is limited by the energy necessary for the charge transfer, i.e. the (de)solvation of the mobile specie on the electrolyte side of the interface and the transfer of the electron from/to the ionic charge carrier. The temperature dependence of this reaction rate follows the Arrhenius law:

$$k = Ae^{\frac{E_a}{k_B T}} \tag{2-17}$$

with k as the reaction rate, A as a pre-exponential factor, E_a as the activation energy for charge transfer, k_B as the Boltzmann constant and T as the temperature of the system. The quantity E_a represents the amount of energy that must be available in the system for the reaction to occur. The limiting kinetic rate of this charge transfer reaction is equivalent in terms of impedance of the cell to an electrical resistance R_{ct}. The value of this charge transfer resistance is inversely proportional to the rate of the redox reaction and to the total surface of the electrode/electrolyte interface.[6]

2.3.4. Electrical double layer capacitance

When a cell is under polarization i.e. when its voltage differs from its equilibrium voltage, the limiting rate of the redox reaction causes accumulation of mobile species on both sides of the electrode/electrolyte interface in a few angstrom layers. As these species are electrically charged (ion, electron) this results in a fast and reversible accumulation of charge within two thin layers on both sides of the interface. The total charge accumulated is proportional to the overpotential between the electrodes. This behavior of the electrode/electrolyte interface is that of an electrical capacitor. The impedance of this capacitor is in the form $\frac{1}{jC_{dl}\omega}$. The value of the double layer capacitance C_{dl} depends on the total surface of the electrode/electrolyte interface and the nature of the mobile species and cell materials.

This charge accumulation occurs in parallel to the charge transfer at the surface of the electrodes. The electrical equivalent circuit corresponding to these two phenomena result in a parallel resistance/capacitor circuit. The total impedance of these phenomena is written in the form:

$$Z_{R//C} = \frac{R_{ct}}{1 + jR_{ct}C_{dl}\omega} \tag{2-18}$$

On the Nyquist plot of the impedance, these surface phenomena create a semi-circle. The width of this semi-circle corresponds to the charge transfer resistance R_{CT}. The higher value of the semi-circle is reached for a frequency of $\omega_m = \frac{1}{R_{ct}C_{dl}}$.

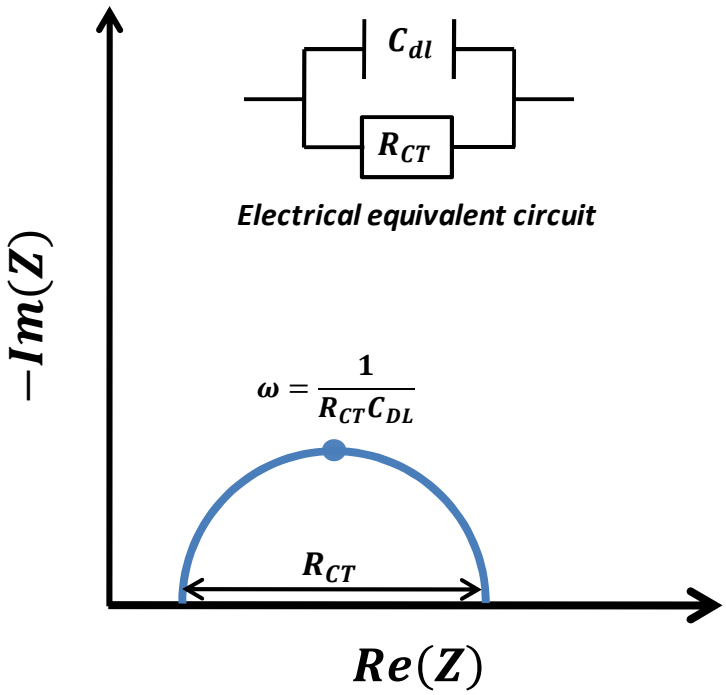

Figure 2-3: Nyquist plot of the interfacial transport phenomena

2.3.5. Passivation layer

A passivation layer, consequence of electrolyte decomposition at the surface of anodes (solid electrolyte interphase - SEI) or cathodes (solid permeable interface - SPI), covering the electrodes induce typically a semi-circle on the Nyquist plot of the impedance, similar to the charge transfer. Indeed, ionic diffusion within this layer is driven by the Fick's first law and in terms of impedance is equivalent to a resistance, similar to the resistance related to the electrolyte transport. Furthermore, the ionic concentration gradient within this layer induces accumulation of charges at its surfaces, inducing a capacitive behavior which results in a R // C equivalent electrical circuit similar to that described above for charge transfer. The size of this semi-circle is usually small compared to that of charge transfer, as result of the thinness of the layer.

2.3.6. Mass diffusion

At equilibrium the chemical potential of a single-phase insertion material is uniform in space, with no gradient of inserted specie's concentration.

Immediately after the application of a potential perturbation to an insertion electrode previously at equilibrium, its chemical potential and concentration of inserted specie are modified at its surface. At this stage, the inserted specie concentration is different between the surface and in the core of the

insertion material. This creates an inserted specie's concentration gradient which induces a flux of mobile species in the opposite direction, i.e. diffusion from the higher concentration region to the lower concentration one. This flux progressively extends in space and decreases the concentration gradient from the surface of the insertion material toward its core, until the inserted specie's concentration is uniform as illustrated in Figure 2-4 (a).[7]

When an insertion material previously at equilibrium sustains a constant ionic flow (constant current regime), a constant concentration gradient appears at its surface, which value is proportional to the current's intensity. At the surface of the insertion material, the flux of mobile specie induced by this constant concentration gradient will carry on until complete insertion or extraction. If the current is stopped before complete insertion/extraction, the flux of inserted specie of the insertion material is stopped at the surface as well, but continues within its core until the concentration profile becomes uniform in space.[7]

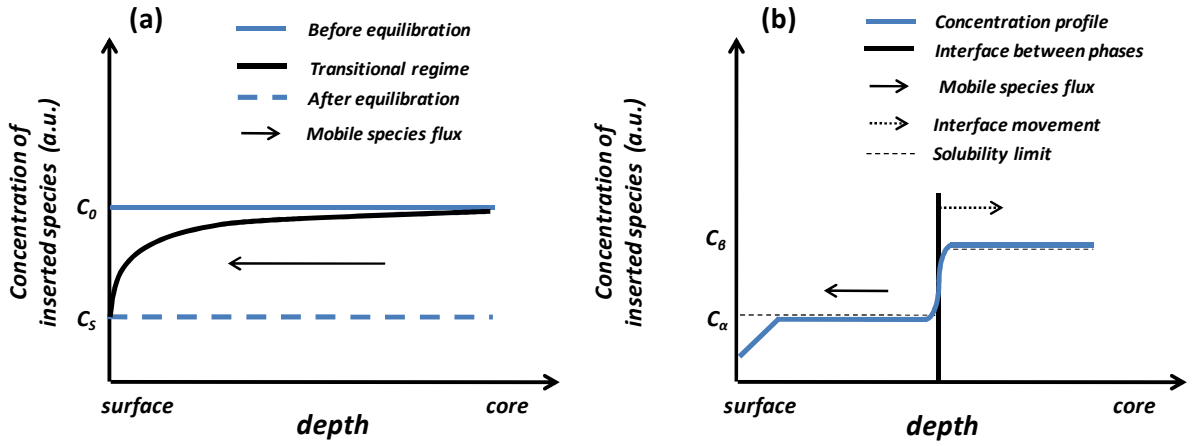

Figure 2-4 (a) Concentration profile of a mobile specie in an insertion material under constant potential excitation and in linear diffusion conditions. (b) in non-linear diffusion conditions.

The transition between single phase and biphasic state of the insertion material occurs when the inserted specie concentration reaches locally its solubility limit. In this case the initial phase splits into two phases with distinct compositions, typically upon nucleation, and a discontinuity appears in the concentration profile of the inserted specie at the interface between these two phases. Upon insertion and extraction of the inserted mobile specie, the concentration profile within the two phases remains continuous while the interface moves toward the higher or lower concentration phase as illustrated in Figure 2-4 (b).[7]

In the case the insertion material is single phase, the mobile specie's transport is limited by its diffusivity within the insertion material following the Fick's first law. If the diffusion coefficient of the mobile specie does not depend on its concentration, the diffusion is said to be linear as it occurs under similar conditions within the whole insertion material. In the case several phases are present in the insertion material the interface mobility also participates in the mobile specie transport limitations, and the diffusion occurs under non-linear conditions.[7]

Linear diffusion occurs under distinct regimes depending on the duration of the perturbation. As long as the concentration perturbation is limited to a small region near its surface, the induced mobile specie's diffusion can be considered as occurring under semi-infinite linear conditions (SILD). This condition is fulfilled when the travel during the perturbation is short compared to diameter of the particles; it requires thus short time excitation, low diffusivity of the insertion material or short diffusion depth compared to the overall depth of the insertion material. If the mobile specie's concentration perturbation affects the whole diffusion depth of the insertion material, the diffusion occurs under finite-space diffusion conditions. This condition is fulfilled in the case of large time excitations, fast diffusion, or large diffusion depth compared to the overall depth of the insertion material. Usually, when a short perturbation is applied to the cell the diffusion of the mobile specie occurs under semi-infinite linear diffusion conditions, and shifts to finite-space diffusion conditions for larger perturbation times.[7]

Under semi-infinite linear diffusion conditions the impedance of the cell can be modeled by a Warburg element W, which impedance can be written in the form[8]:

$$Z_W = \frac{A_W}{\sqrt{2\omega}} - j\frac{A_W}{\sqrt{2\omega}} \tag{2-19}$$

with A_W as the Warburg coefficient which depends on the diffusion coefficient D of the mobile specie. An expression of the Warburg coefficient is given by Ho et al.[9] as:

$$A_W = \frac{V_M}{zFS\sqrt{D}}\left(\frac{dE}{dx}\right) \tag{2-20}$$

with V_M as the molar volume of the insertion material, z as the number of charges transported by a single mobile element, Fas the Faraday constant, S the total surface of the insertion material, ω as the excitation frequency, D as the diffusion coefficient and $\left(\frac{dE}{dx}\right)$ as the slope of the equilibrium potential-composition profile of the insertion material. The origin of this formula will be discussed in part 2.4.1.2 of this chapter. The real and imaginary parts of the Warburg impedance Z_W are identical and both vary as the square root of the frequency of the excitation. It results on the Nyquist plot of the impedance spectra in a 45^o slope in the frequency range where SILD conditions are fulfilled, as can be seen in the schematic Nyquist plot of Figure 2-5. The variations of the impedance with the frequency of the excitation depend on the diffusion coefficient of the mobile specie within the insertion material.

For lower frequencies in finite space linear diffusion conditions the insertion material behaves like a capacitor because its response is mainly the consequence of its voltage-composition profile E(x). The finite space diffusion results in a vertical slope on the Nyquist plot of the impedance spectra of the cell at low frequency, as can be seen in Figure 2-5. At this stage the impedance of the cell can be written in the form[9]:

$$Z_\omega = j\frac{1}{\omega C_L} \tag{2-21}$$

with C_L as the limiting low frequency capacitance, as:

$$C_L = \frac{zFLS}{V_M}\frac{dE}{dx} \tag{2-22}$$

with L as the diffusion depth within the electrode material.

More details on the derivation of Fick's law leading to expressions (2-21) and (2-22) will be given in the following sections.

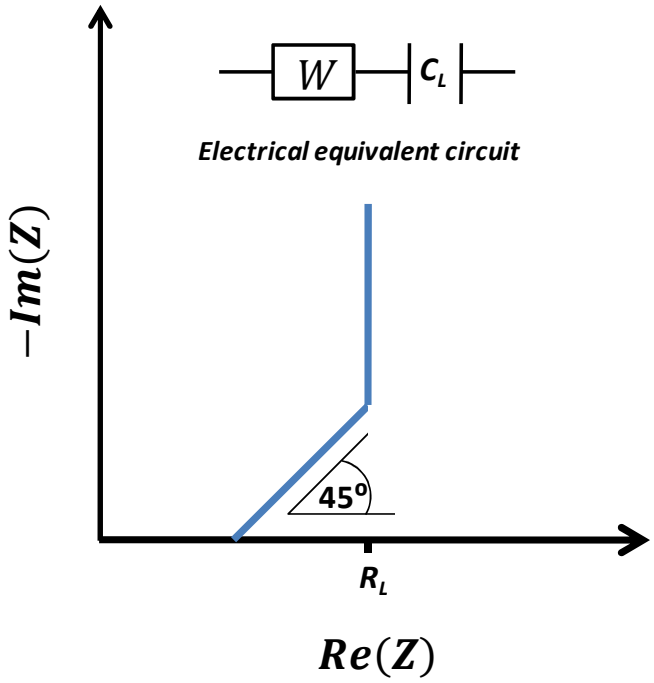

Figure 2-5: Nyquist plot of the Warburg element and low frequency capacitor

2.3.7. Randles circuit

The ionic transport within the electrolyte and the possible surface layers, the charge transfer and the ionic diffusion within the bulk insertion material all occur simultaneously upon steady charge or discharge of a battery. However, along its path from one electrode to the other one, a single ion will go through all these transport phenomena consecutively upon time. The total equivalent electrical circuit of a battery is therefore an assembly in series of the characteristic equivalent circuits described above, as represented in Figure 2-6. This particular circuit, shown in Figure 2-6, was first described by Randles et al.[10]

In practice the experimental result of an EIS experiment may depart from an ideal Randles circuit, due to several factors. First, heterogeneities in the morphology of the electrode (roughness of the electrode surface, particle size distribution) induce a dispersion of the values of the elements of the Randles circuit (resistance, capacitance or Warburg coefficient), which will affects the shape of the Nyquist plot of its impedance. This can lead e.g. to a flattening of the semi circle, a change of the

slope of the Warburg element, or merging of the response of the various processes (black discontinuous line in Figure 2-6).[11]

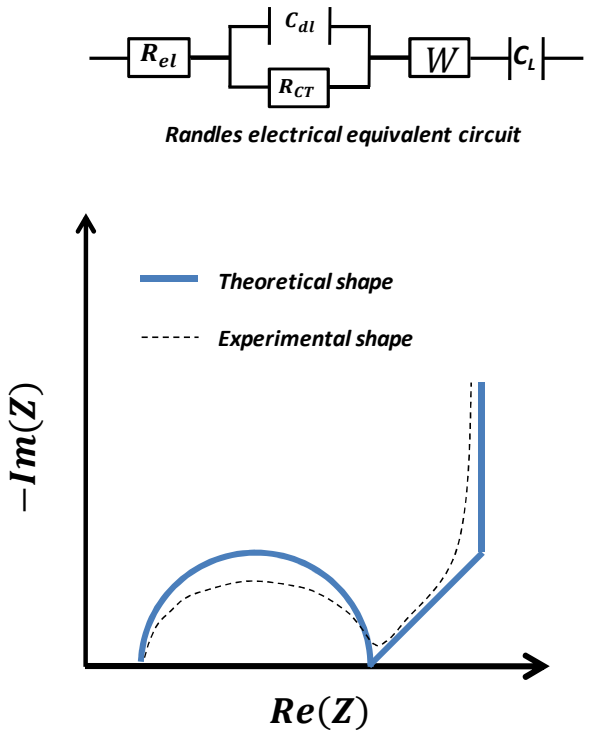

Figure 2-6 : Randles Nyquist plot and equivalent electrical circuit.

2.4. Diffusivity characterization

This part presents how electrochemical characterization techniques allow quantifying the diffusivity of a mobile specie within an insertion material.

2.4.1. Diffusion coefficient

In an unidimensional and linear diffusion process, defining r as the depth within the insertion electrode ($r = 0$ at the surface of the electrode, $r = L$ at the core of the electrode), the diffusion coefficient D of the inserted specie A is defined by the first Fick's law, which relates the relation between the mobile specie concentration gradient and its flux:[12]

$$J = -D\frac{\partial C_A}{\partial r} \tag{2-23}$$

The Fick's second law can be derived from the first one and the principle of mass conservation.[12]

$$\frac{\partial C_A}{\partial t} = D\frac{\partial^2 C_A}{\partial r^2} \tag{2-24}$$

In the case the material remains single phase upon insertion/extraction, the concentration profile of the mobile specie is continuous within the whole insertion material and the differential equation presented by Fick's second law can be solved under a set of initial, final and boundary conditions which depend on the nature of the perturbation applied to the cell material.

2.4.1.1. Constant potential excitation

A sudden potential step applied to the electrode material at equilibrium at a time $t = 0$ will modify the chemical potential at its surface, inducing a surface concentration of mobile specie, C_S, that differs from the concentration in the core of the material, C_0, which was the concentration at equilibrium prior to the perturbation. This change of concentration at the surface of the material creates a concentration gradient which induces a flux of mobile specie in the opposite direction, while the flux of mobile specie at the core of the insertion material (i.e. for $r = L$) is zero.

This set of initial, final and boundary conditions for the diffusion of the mobile specie as a response to a potential step are resumed below:

$$C_A = C_0 \qquad 0 \leq r \leq L \qquad t < 0 \tag{2-25}$$

$$C_A = C_S \qquad r = 0 \qquad t \geq 0 \tag{2-26}$$

$$\frac{\partial C_A}{\partial r} = 0 \qquad r = L \qquad t \geq 0 \tag{2-27}$$

Two solutions of the resolution of the second Fick's law differential equation (2-24) under this set of initial, final and boundary conditions are given by Wen et al.[13] The first consists in a series of error functions (2-28), the second one is a series of trigonometric functions (2-29):

$$\frac{C_A(r,t) - C_0}{C_S - C_0} = \sum_{n=0}^{\infty}\left[(-1)^n\left(erfc\frac{(n+1)L - r}{\sqrt{Dt}} + erfc\frac{nL + r}{\sqrt{Dt}}\right)\right] \tag{2-28}$$

or

$$\frac{C_A(r,t) - C_0}{C_S - C_0} = -\frac{4}{\pi}\sum_{n=0}^{\infty}\left[\frac{1}{2n+1}sin\frac{(2n+1)\pi r}{2L}exp\left(-\frac{(2n+1)^2\pi^2 Dt}{4L^2}\right)\right] \tag{2-29}$$

In the conditions of a potential step, the response current of the cell is proportional to the flux of mobile species through the electrolyte/electrode interface. As defined by Fick's first law, this current is proportional to the concentration gradient of mobile specie at the surface of the insertion material.

$$I(t) = -ZFSD\left(\frac{\partial C_A}{\partial r}\right)_{r=0} \quad (2\text{-}30)$$

with Z as the number of electrons exchanged per mobile specie upon the redox reaction at the surface of the insertion material, F as the Faraday constant and S as the total surface of the insertion material. The concentration gradient of mobile specie at the surface of the material is determined from derivation of the equations (2-28) and (2-29). Neglecting the high order terms within the two series of equations constituting the solutions of the diffusion differential equation, the current of the cell can be expressed as:

$$I(t) = ZFS(C_S - C_0)\sqrt{\frac{D}{\pi t}} \quad \text{If } t \ll L^2/D \quad (2\text{-}31)$$

or as

$$I(t) = \frac{2ZFS(C_S - C_0)D}{L} exp\left(-\frac{\pi^2 Dt}{4L^2}\right) \quad \text{If } t \gg L^2/D \quad (2\text{-}32)$$

In the short times approximation, the diffusion occurs within a thin layer near the electrolyte/electrode interface. The diffusion can be considered semi-infinite as the mobile specie concentration perturbation has not yet been affected by the limited volume of the electrode. In the case the electrode material is made of round shaped particles, the diffusion of the mobile species occurs perpendicularly to the surface of the particles in the direction of its center which process can be approximated to planar diffusion if the diffusion path remains short compared to the radius of the particles. Within this short time approximation in which semi-infinite linear diffusion condition are expected to apply, the current decays as the inverse of the square root of the time. This expression of the current as function of the time in a potential-controlled experiment, for a diffusion-controlled redox reaction, with planar and semi-infinite diffusion conditions was given by Cottrell at al.[14] In this Cottrellian behavior, the product $i\sqrt{t}$ is invariant with time and proportional to the diffusion coefficient of the mobile specie within the insertion material. In the large time approximation, diffusion occurs in finite space diffusion conditions, where the value of the current depends on the overall depth of the electrode.[13]

If a new thermodynamic equilibrium state is reached at the end of the potential step, the mobile specie concentration is again uniform within the insertion material and equal to C_S. The change of overall composition Δx of the insertion material between the beginning and the end of the potential step is directly related to the concentration change at beginning of the step between the surface and the core of the particles $(C_S - C_0)$ and the molar volume of the electrode insertion material V_M:

$$\Delta x = V_M(C_S - C_0) \quad (2\text{-}33)$$

By substituting equation (2-33) in equations (2-31) and (2-32) we may rewrite the time dependence of the current as:

$$I(t) = \frac{ZFS\Delta x\sqrt{D}}{V_M\sqrt{\pi t}} \quad t \ll L^2/D \quad (2\text{-}34)$$

$$I(t) = \frac{2ZFS\Delta xD}{V_M} exp\left(-\frac{\pi^2 Dt}{4L^2}\right) \qquad t \gg L^2/D \qquad (2\text{-}35)$$

Following eq. (2-34), in the semi-infinite linear diffusion conditions, the diffusion coefficient of the mobile specie within the insertion material can be written as:

$$D = \left(\frac{V_M}{ZFSSA}\right)^2 \left(\frac{\Delta E}{\Delta x}\right)^2 \left(\frac{I\sqrt{t}}{m\Delta E}\right)^2 \qquad t \ll L^2/D \qquad (2\text{-}36)$$

with SSA as the specific surface area of the electrode material, m its mass and ΔE as the value of the potential step.

According to expression (2-36), three factors contribute to the value of the diffusion coefficient. The $\left(\frac{V_M}{ZFSSA}\right)^2$ factor consists in an intensive parameter taking into account the morphology of the insertion electrode material (molar volume V_M and specific surface SSA). The $\left(\frac{\Delta E}{\Delta x}\right)^2$ factor takes into account the thermodynamic properties of the material and represents the derivative of the voltage-composition profile of the material at equilibrium. The $\left(\frac{I\sqrt{t}}{m\Delta E}\right)^2$ factor accounts for the dynamic response of the insertion material to the constant potential excitation.

2.4.1.2. Warburg coefficient

The resolution of the differential equation of the Fick's second law in the case of a sinusoidal excitation of the cell was described by Ho et al.[9] In the case of potential controlled electrochemical impedance spectroscopy (PEIS), a small sinusoidal potential excitation is applied to the insertion electrode in the form:

$$E = E_{eq} + \delta E = E_{eq} + v_0 sin\ \omega t \qquad (2\text{-}37)$$

with E_{eq} as the equilibrium potential of the cell, v_0 the amplitude of the potential excitation and ω as the frequency of the excitation. This potential excitation affects the mobile specie concentration at the surface of the insertion material x_A which is modified into $x_A + \delta x_A$. Considering very small potential oscillations, the composition change of the insertion material can be approximated by its first order partial derivative:

$$\delta x_A(t) = \left(\frac{dx_A}{dE}\right)_{x_A} \delta E = v_0 \left(\frac{dx_A}{dE}\right)_{x_A} sin\ \omega t \qquad (2\text{-}38)$$

with $\left(\frac{dx}{dE}\right)_{x_A}$ as the slope of the equilibrium potential-composition of the insertion material at the composition x_A. In term of mobile specie concentration c_A the equation (2-38) can be written:

$$\delta c_A(t) = \frac{v_0}{V_M}\left(\frac{dx_A}{dE}\right)_{x_A} sin\ \omega t \qquad (2\text{-}39)$$

with N and V_M as respectively the Avogadro number and the molar volume of the insertion material.

The concentration of mobile specie is uniform within the whole insertion material before the sinusoidal potential excitation is applied to the cell, and no flux of mobile specie occurs at the core of the insertion material where the depth is L. This set of limit and boundary conditions, along with the evolution of the mobile specie concentration at the surface of the insertion material (2-39) allows solving the Fick's second law differential equation.

$$\delta c_A(r,0) = 0 \tag{2-40}$$

$$\frac{\partial \delta c_A(L,t)}{\partial r} = 0 \tag{2-41}$$

The solution is given by Carslaw et al.[15] in the form:

$$\delta c_A(r,t) = \frac{\nu_0}{V_M}\left(\frac{dx_A}{dE}\right)_{x_A} B sin(\omega t + \varphi) \tag{2-42}$$

with
$$B = \left|\frac{\cosh(1+j)kx}{\cosh(1+j)kl}\right| \tag{2-43}$$

$$\varphi = \arg\left(\frac{\cosh(1+j)kx}{\cosh(1+j)kl}\right) \tag{2-44}$$

and
$$k = \sqrt{\frac{\omega}{2D}} \tag{2-45}$$

In the conditions of a potential excitation, the response current of the cell is proportional to the flux of mobile species through the electrolyte/electrode interface. As defined by Fick's first law, this flux is proportional to the concentration gradient of mobile specie at the surface of the insertion material.

$$I(t) = -ZFSD\left(\frac{\partial \delta c_A}{\partial r}\right)_{r=0} \tag{2-46}$$

This current is, like the potential excitation, a sinusoidal signal in the form:

$$I(t) = i_0 sin(\omega t + \beta) \tag{2-47}$$

with
$$i_0 = -\frac{ZF\nu_0\sqrt{\omega D}}{2V_M}\left(\frac{dx}{dE}\right)\sqrt{\frac{h^2+s^2}{d^2}} \tag{2-48}$$

and
$$\beta = -\arctan\left(\frac{h+s}{h-s}\right) \tag{2-49}$$

with $$h = \sinh(2kl) \tag{2-50}$$

$$s = sin(2kl) \tag{2-51}$$

$$d = cosh^2(kl)cos^2(kl) + sinh^2(kl)sin^2(kl) \tag{2-52}$$

In order to go further into the comprehension of the behavior of the current response of the cell under a sinusoidal potential excitation, its amplitude and phase have to be simplified into two asymptotical tendencies. Introducing k as $k = \sqrt{\frac{\omega}{2D}}$, the kL parameter can be considered high ($kL \gg 1$) in the case of high frequencies, large depth of the insertion material, or small diffusion coefficient, i.e. in the case of semi-infinite diffusion conditions. In this case, the amplitude and phase of the current oscillations can be simplified as:

$$i_0 = -\frac{zFv_0\sqrt{\omega D}}{V_M}\left(\frac{dx}{dE}\right) \tag{2-53}$$

and $$\beta = \arctan 1 = \frac{\pi}{4} \tag{2-54}$$

The impedance of the cell, corresponding to the ratio of the overpotential over the current can be then written as:

$$Z_\omega = |Z|cos\left(\frac{\pi}{4}\right) - j|Z|sin\left(\frac{\pi}{4}\right) \tag{2-55}$$

or $$Z_\omega = \frac{|A_w|}{\sqrt{2}}\left(\omega^{-\frac{1}{2}}\right) - j\frac{|A_w|}{\sqrt{2}}\left(\omega^{-\frac{1}{2}}\right) \tag{2-56}$$

with $$|Z| = \frac{A_w}{\sqrt{2}}\left(\omega^{-\frac{1}{2}}\right) \tag{2-57}$$

and $$A_w = \left|\frac{v_0}{i_0 S}\right| = \frac{V_M}{zFS\sqrt{D}}\left(\frac{dE}{dx}\right) \tag{2-58}$$

A_w being the Warburg coefficient. The phase of the current is independent of the frequency. The real and imaginary parts of the impedance are identical resulting in a 45° slope on the Nyquist plot.

In the opposite case, when the kl parameter is low ($kL \ll 1$) corresponding either to fast diffusion, small depth of the insertion material or low frequency i.e. finite space diffusion conditions, the amplitude of the sinusoidal current and its phase can be written:

$$i_0 = -\frac{zFv_0L\omega}{V_M}\left(\frac{dx}{dE}\right) \tag{2-59}$$

and $$\beta = \arctan \infty = \frac{\pi}{2} \tag{2-60}$$

The phase of the current is here also independent of the frequency and equals 90°.

The impedance of the cell in this case can be written:

$$Z_\omega = j\frac{1}{\omega C_L} \tag{2-61}$$

with

$$C_L = \frac{zFLS}{V_M}\frac{dE}{dx} \tag{2-62}$$

At this stage, the insertion material behaves like a single capacitor. The low frequency capacitance C_L accounts for the maximum amount of mobile specie that the insertion material can reversibly insert/extract in the potential range of the excitations and is proportional to the slope of the voltage-composition profile of the insertion material, as explained above.

In the case of semi-infinite linear diffusion conditions, the diffusion coefficient of the mobile specie can be derived from equation (2-57) in the form:

$$D = \left(\frac{V_m}{zFSSA}\right)^2 \left(\frac{dE}{dx}\right)^2 \left(\frac{1}{m\sqrt{2}A_w}\right)^2 \tag{2-63}$$

As for expression (2-36), three factors contribute to the value of this diffusion coefficient, with the two first ones, morphological factor and thermodynamic factor, identical to those of expression (2-36). The dynamic factor is now expressed $\left(\frac{1}{m\sqrt{2}A_w}\right)^2$, and accounts for the dynamic response of the insertion material to the sinusoidal potential excitation and is determined from the impedance evolution of the cell with the excitation frequency.

2.4.1.3. Constant current regime

A constant current applied to a cell causes the passage of a constant flux of mobile species at the surface of the electrode material. The concentration gradient near the surface of the insertion material depends on the rate of charge transfer which is fixed by the current value. This concentration gradient will gradually extend toward the core of the electrode material generating a flux of inserted specie. The electrical voltage of the cell depends on the concentration of mobile specie at the surface of the insertion material. This concentration also depends on the ability of the mobile specie to move toward or away from the surface. At the end of the current step, the voltage of the cell will gradually drift toward its thermodynamic equilibrium value due to uniformization of the concentration profile of the mobile specie within the insertion material.

Wen et al.[16] described a method for the determination of the diffusion coefficient of a mobile specie within an insertion electrode material from the observation of the potential of the electrode under a constant current excitation in particular conditions.

At thermodynamic equilibrium the concentration profile of the mobile specie $C_A(r)$ is uniform within the insertion material, with a value of C_0 prior to the current perturbation, leading to expression (2-64). At t = 0 a constant current is applied, inducing a fixed concentration gradient at the surface of the particle following the Fick's first law and leading to expression (2-65). No flux of mobile specie occurs at the core of the insertion material where the depth is L (expression 2-66). These initial and boundary conditions are summarized below:

$$C_A = C_0 \qquad 0 \leq r \leq L \qquad t = 0 \qquad (2\text{-}64)$$

$$-D\frac{\partial C_A}{\partial r} = \frac{I}{ZFS} \qquad r = 0 \qquad t > 0 \qquad (2\text{-}65)$$

$$\frac{\partial C_A}{\partial r} = 0 \qquad r = L \qquad t \geq 0 \qquad (2\text{-}66)$$

As for a constant potential excitation, the solution of the differential equation (2-24) following these conditions has the form of an infinite series of error functions which can be approximated by its first term in the short time approximation ($t \ll L^2/D$). In these conditions, the diffusion coefficient of the inserted mobile specie is written as:

$$D_{iff} = \left(\frac{V_m}{ZFSSA}\right)^2 \left(\frac{dE}{dx}\right)^2 \left(\frac{2I}{m\sqrt{\pi}}\frac{d\sqrt{t}}{dE}\right)^2 \qquad (2\text{-}67)$$

As in the case of a single potential step between two equilibrium positions, three factors contribute to the value of this diffusion coefficient: morphologic, thermodynamic and dynamic, the two first ones being identical to the case of constant potential (expression 2-36) and sinusoidal potential excitation (2-63). The dynamic factor $\left(\frac{2I}{m\sqrt{\pi}}\frac{d\sqrt{t}}{dE}\right)^2$ accounts for the dynamic response of the insertion material to the constant current excitation, i.e. the time dependence of its potential.

2.4.2. Activation energy for diffusion

At macroscopic level the flow of inserted species within the insertion material is driven by its concentration gradient, as described by Fick's first law (2-23). At microscopic level this flow consists in discrete jumps of mobile species between two neighboring interstitial sites. This jump is only possible when this neighboring site contains a vacancy. Through this jump the mobile specie has to repel elastically the neighboring atoms constituting the crystal matrix of the insertion material to clear its passage which constitutes an energy barrier ΔG. This barrier can be passed thanks to the thermal agitation with a probability that depends on the temperature of the system and that can be written in the form:

$$p_i = e^{-\frac{\Delta G}{k_B T}} \qquad (2\text{-}68)$$

with ΔG as the energy barrier of the transition between the two interstitial sites, k_B as the Boltzmann constant and T as the temperature of the system. The jump frequency depends on both the vibrational frequency ν of the atom along the reaction path and its probability to pass the energy barrier:

$$\Gamma_i = \nu e^{-\frac{\Delta G}{k_B T}} \tag{2-69}$$

Defining a as the distance between two interstitials sites, the diffusion coefficient of the mobile atom is expressed as:

$$D = \nu a^2 e^{-\frac{\Delta G}{k_B T}} \tag{2-70}$$

The energy barrier ΔG actually corresponds to the difference between the values of the maximum Gibbs free energy of the mobile atom along the diffusion path between two interstitial sites and its Gibbs free energy on the interstitial site. The development of the diffusion coefficient from atomistic diffusion was first performed by Zener et al.[17]

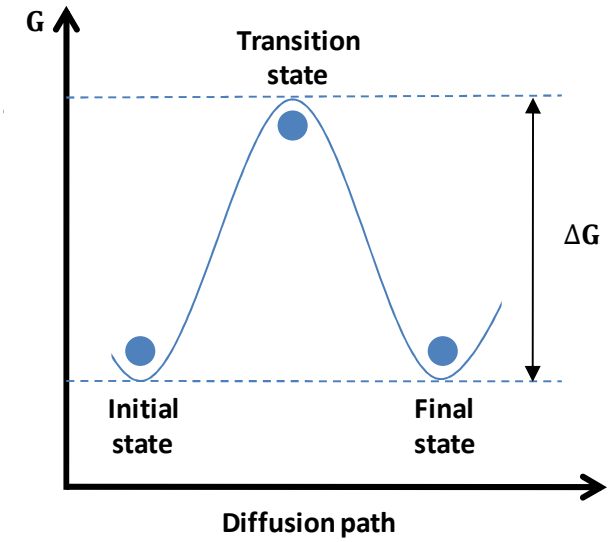

Figure 2-7 : Energy of a mobile atom upon an interstitial single diffusion step

The Eyring equation[18] extends the energy of the atom to a Gibbs free energy which can be separated into an enthalpy term and an entropy term:

$$\Delta G = \Delta H - T\Delta S \tag{2-71}$$

Following this expression, the diffusion coefficient of the mobile specie can be expressed as:

$$D = D_0 e^{-\frac{E_a}{k_B T}} \quad (2\text{-}72)$$

with

$$D_0 = \nu a^2 e^{\frac{\Delta S}{k_B}} \quad (2\text{-}73)$$

and

$$E_a = \Delta H \quad (2\text{-}74)$$

The diffusion coefficient shows thus an Arrhenius dependence with the temperature with an activation energy that corresponds to the enthalpy barrier that the mobile specie has to jump. This activation energy of diffusion can be intuitively assimilated to the energy necessary for the jump of the mobile specie to occur. The pre-exponential factor D_0 takes into account the crystalline structure of the host material and its morphology.

This activation energy is an interesting parameter for evaluation of the diffusivity of a mobile specie within a host insertion material as it is related to the transport mechanism at microscopic level and rules out all the macroscopic parameters that might influence the diffusion coefficient value (morphology of the electrode in particular) that were present in the expressions (2-36), (2-67) and (2-63) of the diffusion coefficient.

[1] O. Petrii, G. Tsirlina, *Electrode potentials*, in A. J. Bard, M. Stratmann, E. Gileadi, M. Urbakh, Encyclopedia of Electrochemistry, Vol. 1, Thermodynamics and electrified interfaces,Wiley-VCH, pp 1–25 (2002)
[2] J. Gibbs, J. Willard, *On the equilibrium of heterogeneous substances*, Transactions of the Connecticut Academy of Arts and Science, 3 (1878)
[3] S. Krause, *impedance methods*, in A. J. Bard, M. Stratmann, P. Unwin, Encyclopedia of Electrochemistry, Vol. 3, Instrumentation and electroanalytical chemistry,Wiley-VCH, pp 196–229 (2003)
[4] A. J. Bard, L. R. Faulkner, Electrochemical methods Fundamentals and applications, chapter 3: kinetics of electrode reactions, pp87-136, Second edition, John Wiley & sons, inc (2001)
[5] A.V. Churikov, A.V. Ivanishchev, I. A. Ivanishcheva, V.O. Sycheva, N.R. Khasanova, E. V. Antipov, Electrochim. Acta, 55, 2939 (2010)
[6] Z. Ogumi, Electrochemistry, 78(5), 319 (2010)
[7] A. J. Bard, L. R. Faulkner, Electrochemical methods Fundamentals and applications, chapter 1: Introduction and overview of electrode processes, pp1-44, Second edition, John Wiley & sons, inc (2001)
[8] E. Warburg, Ann. Physik, 67, 493 (1899); 6, 125 (1901)
[9] C. Ho, I. D. Raistrick, R. A. Huggins, J. Electrochem. Soc., 127, 343-350 (1980)
[10] J. E. B. Randles, Discuss. Faraday Soc., 1, 11 (1947).
[11] A. Lasia, J. Electroanal. Chem., 397,(1-2), 27 (1999)
[12] A. Fick, *"on liquid diffusion"*, PoggendorffsAnnalen., 94, 59 (1855) – reprinted in *"On liquid diffusion*", Journal of Membrane Science,100, 33 (1995)
[13] C. J. Wen, B. A. Boukamp, R. A. Huggins, W. Weppner, J. Electrochem. Soc., 126, 12, 2258 (1979)
[14] F.G. Cottrell, Z. Phys. Chem., 42 , 385 (1903)
[15] H. S. Carslaw, J. C. Jaeger, "Conduction of Heat in Solids," 2nd Ed., p. 105, Oxford Univ. Press, Oxford (1959)
[16] W. Weppner, R. A. Huggins, J. Electrochem. Soc., 124, 10, 1569 (1977)
[17] C. Zener, J. Appl. Phys., 22, 4, 372 (1951)
[18] M. G. Evans, M. Polanyi, Trans. Faraday Soc., 31, 875 (1935)

3. Experimental techniques

3.1. Chemical preparation of $NaFePO_4$/C

Chemical preparation of $NaFePO_4$/C has been performed from commercial carbon coated $LiFePO_4$/C which has been successfully oxidized (Li removal or "delithiation") and reduced (Na insertion or "sodiation"). Delithiation of $LiFePO_4$/C was performed following the route reported by Jones et al.[1] and Zhu el al.[2], by stirring a mixture of commercial $LiFePO_4$/C powder and NO_2BF_4 in acetonitrile (Sigma-Aldrich) at room temperature. The reaction was carried out in a glove box under argon atmosphere (O2 and H2O ppm ≤ 5). After the reaction was completed the mixture was vacuum filtered and the delithiated collected powder washed with acetonitrile twice and dried under vacuum at 80 °C overnight. Chemical sodiation of the obtained product was performed by stirring it with NaI (Sigma-Aldrich) in acetonitrile under argon atmosphere as reported by Casas-Cabanas et al.[3] and Ali et al.[4] The mixture was then filtered and washed with acetone, and further dried at 80°C overnight. The purity of the synthesized phases has been checked systematically by X-ray diffraction with a Bruker D8 Advance diffractometer.

3.2.Electrode preparation

$NaFePO_4$/C or $LiFePO_4$/C electrodes were prepared by the slurry casting method on an aluminum current collector. For that purpose, a powder containing 80% of commercial $LiFePO_4$/C powder (ALEEES), 10% of polyvinylidene fluoride (Solef PVDF, Solvay) as binder and 10% of Super C65 (Ymerys) was first mixed by hand in an agate mortar. The slurry was then prepared by wetting this powder with N-methyl-2-pyrrolidone (NMP, Sigma-Aldrich) followed by magnetic agitation for one hour. 1.6 ml of NMP was typically used for 0.4 g of mixed powder. The obtained slurry was then poured on a 100µm thick aluminum foil and spread thanks to a Dr. Blade with a blade height set to 150µm. The coated Al foil was then dried overnight under vacuum at 120°C. 12mm or 11mm electrodes were punched from the laminate and pressed at 2 T/cm^2. The electrodes were then again dried overnight at 80°C before introduction into an Ar filled Glove box for cell assembling.

3.3.Cell assembly

In the case of half cells, sodium or lithium metal is used as counter electrode while the working electrode contains the material under study. These cells were assembled using Swagelok-type tube connection with linear connector (Figure 3-1 (a) and (b)) as the cell body, except when electrochemical measurement was performed with varying temperature in the PPMS where CR2032 button-type cells (Hohsen) were used (Figure 3-1 (c)).

In 2 electrodes Swagelok cells, as seen in Figure 3-1 (a) and (b), two stainless steel plungers at both ends of the cell compress the battery components and assure good electrical contact. The two nylon ferrules around each plunger act as gaskets, assuring a perfect sealing of the cell thanks to the pressure applied by the nuts. Between both plungers are found a stainless-steel spring to apply pressure on the cell components and a stainless disk assuring an equal repartition of the pressure within the cell as well as a perfect electrical contact by acting as a current collector. A disk of Li or Na metal is pasted on the stainless steel disk, which in placed in front of the working electrode, separated by a porous membrane or “separator” (Whatmann GF/D glass fiber) saturated with electrolyte. Identical springs were systematically used for all the Swagelok cell in order to ensure a reproducible internal pressure.

In the coin cells as shown in Figure 3-1 (c), the stack of cell components is similar to that in a Swagelok body, at the difference that the upper and lower half of the casing act as the plungers, and a flat spring is placed between the body of the cell and the stainless steel disk, ensuring even pressure. The sealing of the two half body parts of the coin cell is ensured by a nylon ring. A silver-epoxy electrically conductive adhesive was used to stick Copper strips the cell, that has been cured at 80°C prior to cell assembly. These copper strips were used to connect electrically the cell to the measuring device, while ensuring perfect thermal coupling with the heater stage.

In the case of Li cells, a commercial electrolyte was used to wet the separator: $LiPF_6$ 1M in EC/DMC 1:1 (LP30, Solvionics). In the case of Na cells, a laboratory-made electrolyte with similar composition, $NaPF_6$ 1M in EC/DMC 1:1 (all components from Aldrich) was used.

In a two-electrode cell the current flows between the counter electrode and the working electrode and the voltage of the cell is measured as the difference between the potentials of these two electrodes while operating. If the potential of the counter electrode varies with the state of charge of the cell it is impossible to distinguish the respective evolutions of the electrodes potentials. Also, in the case of a half-cell where the Li or Na counter electrode potential is supposed to be constant with the state of charge of the cell, the current of the cell may generate a non negligible overpotential and bring imprecision regarding the determination of the potential of the working electrode. This overpotential increases with the rate, or intensity of the current, which is traduced for time or frequency dependent techniques (such as PITT, GITT, EIS) by a contribution of the counter electrode to the overall cell response which may become non negligible at high frequency or short time response. In this case, a third electrode can be added to the cell to be used as reference to measure the potentials of both the counter and working electrodes separately and with a better precision. Since this reference electrode is only used to measure the potential, no current flow through it, so that its potential does not depend neither on the current flowing between the working and the counter electrode nor on the state of charge of the cell.

For three-electrode cells, a third plunger body was used in order to place a disk of metallic Li or Na used as a reference electrode in contact with the electrolyte, and T-shaped connectors were used as cell bodies (see Figure 3-1 (e) and (f)).

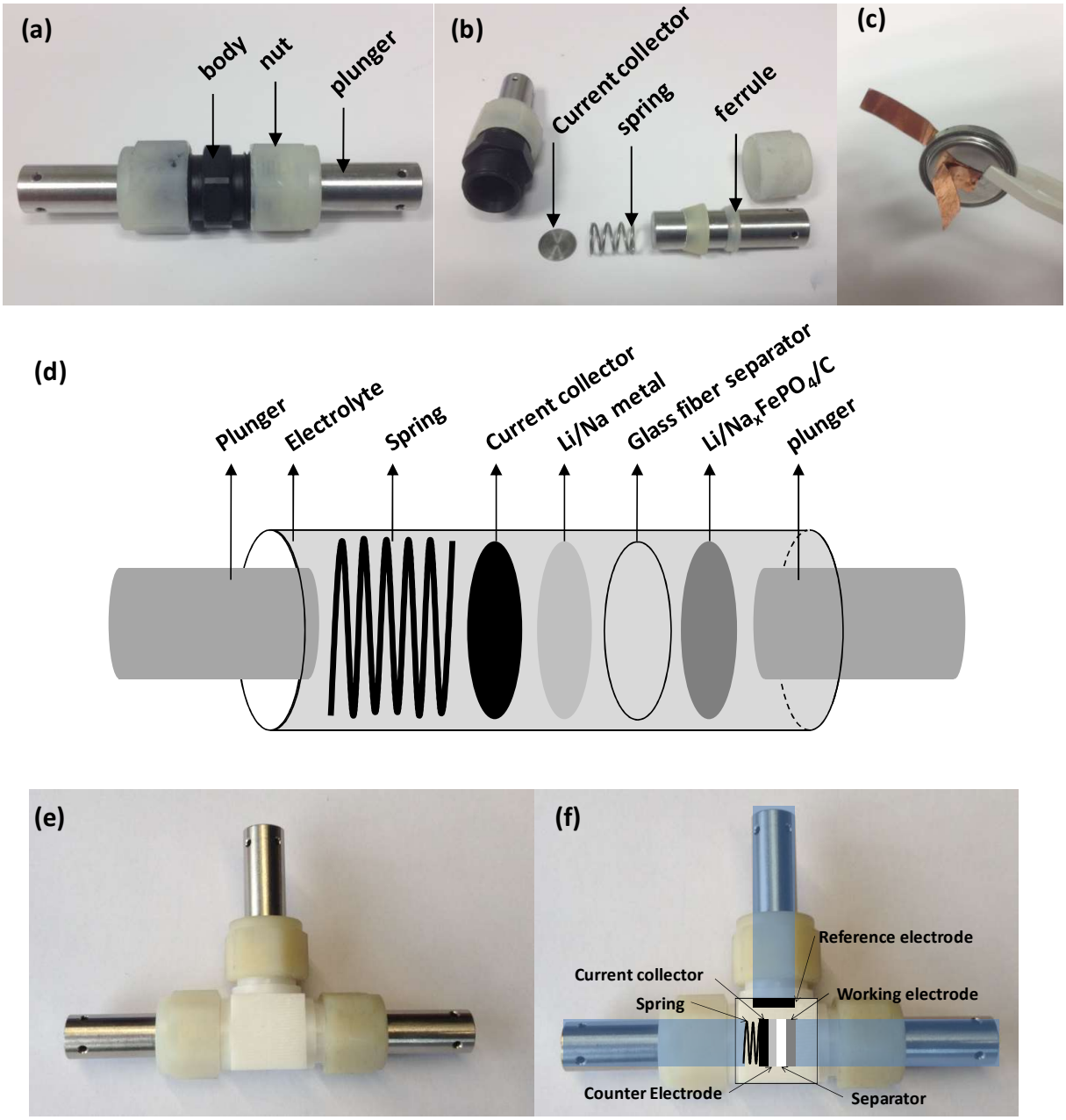

Figure 3-1 (a) Assembled Swagelok cell, (b) Disassembled Swagelok cell, (c) Assembled coin cell with Cu strips fixed with silver-epoxy adhesive, (d) Stack within a cell, (e) Assembled 3-electrode Swagelok cell, (f) Three electrode Swagelok cell configuration.

3.4.Electrochemical delithiation

This procedure was used in order to obtain lithium free $FePO_4$/C electrodes. For that purpose, half Swagelok cells were used with Li as counter electrode and a $LiFePO_4$/C electrode as working electrode. It was systematically performed for every $LiFePO_4$/C electrodes to verify that the electrode presented the theoretical capacity, except for those on which was performed galvanostatic cycling.

It consisted in a constant current charge-discharge cycle at C/10 between 2 and 4.5 V, immediately followed by a constant current constant-voltage (CCCV) charge to 4.5V, at a constant current rate of C/10 and a hold of the final voltage until the current of the cell reached C/1000. The nomenclature is set as 1C to be rate for which a complete charge or discharge of the cell would occur in one hour, so that C/10 corresponds to a theoretical charge or discharge in 10 hours. At the end of this procedure all the lithium would be theoretically removed from the electrode.

When the obtained $FePO_4$/C electrodes were dedicated to be further cycled vs Na, the electrode were extracted by disassembling the cell, were then washed with dimethyl-carbonate (DMC) (sigma-Aldrich), and finally placed in a new cell with Na as counter electrode and $NaPF_6$at 1M in EC/DMC as electrolyte.

3.5.Electrochemical characterization techniques

3.5.1. Galvanostatic cycling and rate capability

Galvanostatic cycling of a cell consists in applying consecutive constant current charge-discharge cycles to the cell, here performed at a rate of C/10. The charge and discharge are stopped when the voltage of the cell has reached an upper or a lower limit, respectively. These voltage limits are set to avoid parasitic reactions, such as electrolyte decomposition. The voltage window was set as 2-4.5V vs Li^+/Li for the lithium half-cells and 1.5-4V vs Na^+/Na for the sodium half-cells. Rate capability consisted in consecutive series of 5 galvanostatic cycles performed at each of the following rates: C/10, C/5, C/2, C, 2C, 5C, 10C, 20C and C/10 again. For these measurements a MACCOR 4000 series battery tester or a Biologic VMP3 potentiostat-galvanostat were used depending on availability. No difference of performance was observed depending on the instrument used.

3.5.2. Galvanostatic intermittent titration technique (GITT)

The GITT consists in sequential scanning of the equilibrium voltage of a cell as function of its state of charge through titration steps, which consist in a short constant current excitation followed by a large relaxation time until reaching equilibrium voltage. GITT was performed on sodium half cells with $NaFePO_4$/C electrodes prepared from chemically delithiated and sodiated $LiFePO_4$/C powder.

The cells sustained 10 cycles of galvanostatic cycling before they were brought to the charged state through constant current charge to 4 V followed by a constant voltage hold at 4V (CCCV) until the current of the cell would reach C/500. A single GITT step consists in applying a C/50 current to the cell during one hour, followed by a relaxation period until the voltage of the cell has reached the equilibrium condition of 2mV/h. This operation was repeated 50 times while discharging the cell then 50 times while charging the cell.

A Biologic VMP3 potentiostat-galvanostat was used.

3.5.3. Potentiostatic Intermittent Titration Technique (PITT)

The PITT consists in a sequential scanning of the equilibrium voltage of a cell with its state of charge through constant potential steps. The evolution of the current of the cell during the potential step gives information about its (dis)charge kinetics.

Several galvanostatic cycles were applied to the half cells previously to the PITT. They were five cycles in the case of the lithium cell and three cycles in addition to the delithiation procedure in the case of the sodium cell. The half cells were then brought to the discharged state after a constant current discharge followed by a potential hold at 2 V for the lithium half-cells and 1.5 V for the sodium half-cells until the current would reach C/500.

A single PITT step consists in applying a 25 mV overpotential to the cell until the current reaches C/500. This operation was repeated 100 times on the lithium cell until it had reached 4.5 V and reiterated 100 times again with a -25mV overpotential until its voltage had gone back to 2 V. The same methodology was applied to the sodium half-cell with 80 steps of +/- 25mV between 1.5 V and 3.5 V.

A Biologic VMP3 potentiostat-galvanostat was used.

3.5.4. PITT coupled with EIS

Potential controlled electrochemical impedance spectroscopy (PEIS) was performed at the end of each PITT step with frequency ranging from 100.1 KHz to 11 mHz, maintaining constant the DC potential as controlled during the PITT, and a 10 mV AC voltage amplitude. A Biologic VMP3 potentiostat-galvanostat was used.

3.5.5. EIS in 3 electrode cells

PEIS measurements were also performed on three electrodes lithium and sodium Swagelok-type half-cells, with Li or Na metal as both the counter and the reference electrodes and the same electrolyte and separator as previously used. The potential controlled EIS measurements (PEIS) were performed with frequency ranging from 100.1 KHz to 11 mHz and with a 10mV amplitude using a biologic VMP3 potentiostat-galvanostat.

3.5.6. In-situ PEIS vs temperature

The activation energy for diffusion within the insertion electrode material can be determined from the temperature dependence of the Warburg coefficient of the mobile specie within the insertion electrode. This parameter was determined from PEIS measurements at several states of charge of Li and Na half cells with coin cell type body as shown in figure 3-1 (d).

After five galvanostatic cycles at C/10 the half-cells were brought to the discharged state through galvanostatic discharge at C/10. The voltage was then maintained at 2 V until the current had reached C/500. The state of charge was controlled at 300K (27°C) from galvanostatic charge/discharge steps at C/10, followed by a relaxation in open circuit of at least 6 hours. The charged state of the cells was reached after a constant potential charge at respectively 4V for the lithium cell and 3.5 V for the sodium cell until the current had reached C/500. The impedance spectroscopy measurements were performed from 1 MHz to 50 mHz with a 10 mV amplitude. A SP-150 mobile Bio-Logic potentiostat was used.

The electrolytes used within this study decompose above 60 ^{o}C and lose their properties below -20 ^{o}C, which limits the temperature range that can be used.[5,6] On the other side, the precision of the activation energies depends on the number of measurements performed in this temperature window. Narrow temperature steps improve this precision maintaining a reasonably narrow temperature range, but this requires a very good temperature control of the cell material, better than what is possible with conventional climate chambers used for battery and cell testing. A Physical Properties Measurements System (PPMS) from Quantum Design has thus been used in order to provide the required temperature control, see Figure **3**-**2**. A specially designed sample holder probe was used in which a temperature sensor is located just below and in thermal contact with the coin cell, and electrical connection is ensured by 4 shielded coaxial cables for separating current and voltage carriers. PEIS measurements were performed at various states of charge and discharge on relaxed cells (i.e. with stable OCV) at temperatures ranging from 312 K to 294 K with 2 K steps.

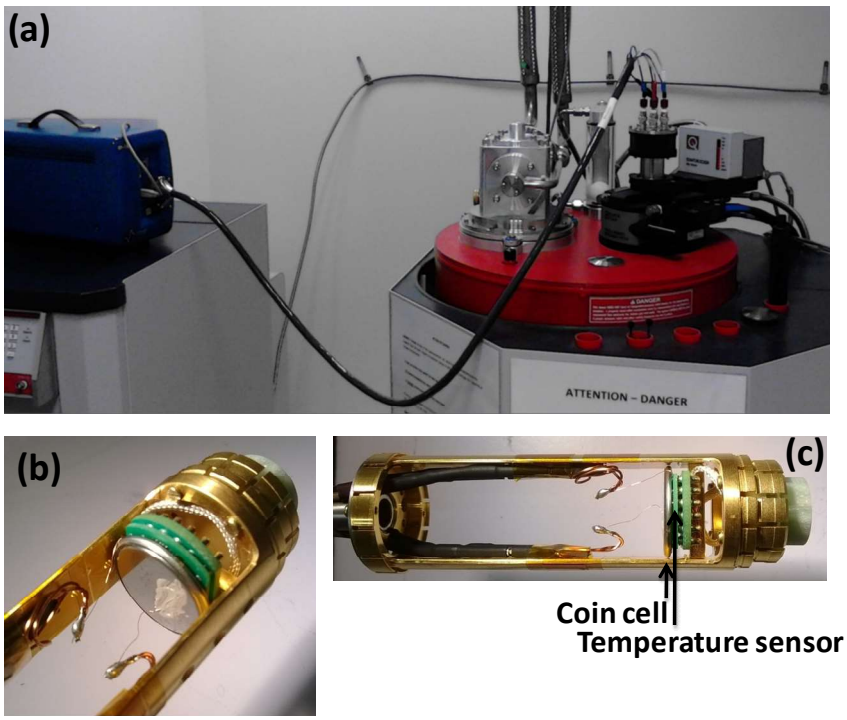

Figure 3-2 : (a) Physical Properties Measurement System (PPMS) connected to the SP-150 mobile Bio-Logic potentiostat, (b) and (c) Sample holder and coin cell

3.6.Material characterization techniques

3.6.1. X-Ray Diffraction (XRD)

X-ray diffraction is an analytical technique used to ascertain the purity of a crystalline sample and to identify its constitutive phases as well as their crystalline structures. A planar monochromatic X-ray electromagnetic photonbeam with a wavelength of a few angstroms is focused to the sample. This beam is elastically scattered by the electrons cloud of the atoms constituting the sample, creating secondary spherical electromagnetic waves with the same wavelength. When the atoms are regularly distributed in space, as it is the case in a crystal, a regular array of spherical waves is produced. Destructive interference of these spherical waves occurs in most directions where the distribution of spherical waves cancels each other but they add constructively in specific directions depending on the electrons distribution and as a consequence, in relation with atomic positions within the sample.

Considering a X-ray source illuminating a crystalline sample with an incident angle θ, constructive interferences will occur in the direction – θ depending on the distance between the crystalline planes following the Bragg's law (see Figure **3**-**3** (a)):

$$n\lambda = 2d \sin\theta$$

with θ as the scattering angle, d the interplanar distance and n, a natural number, as the diffraction order.

The diffracted beam shows distinct intensities following its scattering angle. The plot of the intensity of this diffracted beam as function of the incident angle is known as the XRD pattern of the sample material. Each material shows a unique XRD pattern depending on the distances between its crystalline plans.[7]

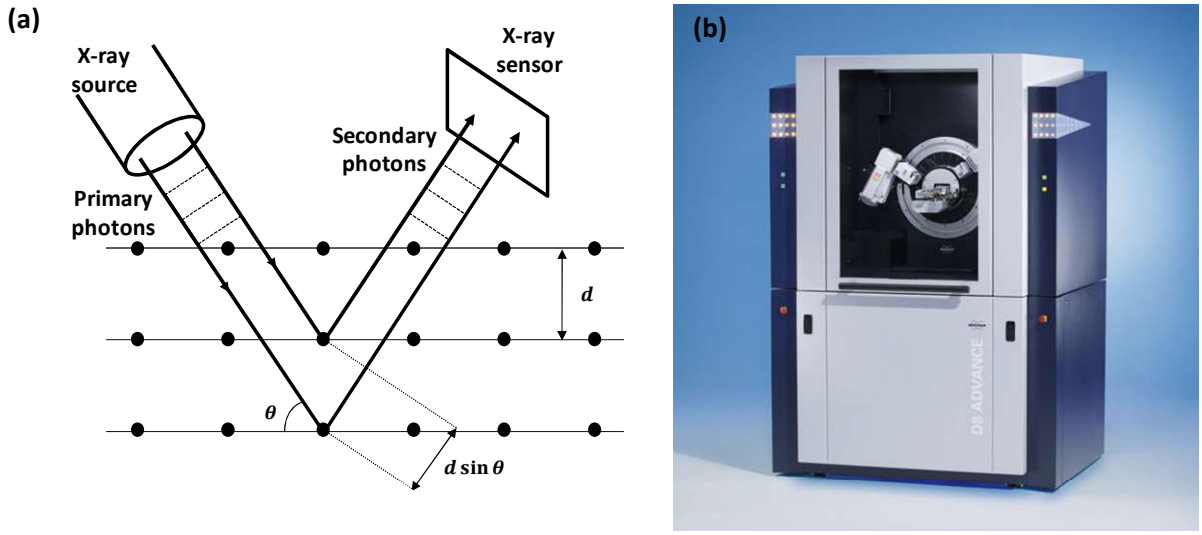

Figure 3-3 : (a) Working principle of scanning electron microscopy, (b) Brüker D8 Advance X-ray diffractometer.

In this study, XRD was performed on $LiFePO_4$/C to corroborate the purity of the material. It was performed with a Brüker D8 Advance X-ray diffractometer equipped with a LYNXEYE detector (see Figure **3-3** (b). Cu kα radiation ($\lambda_{CuK\alpha}$ = 1.54056 Å) was used with an angle range of 30-80°.

3.6.2. Small Angles X-ray Scattering (SAXS)

In the SAXS experiment, see Figure **3-4**, the transmission geometry is used instead of reflection as more appropriate for the small angle region. The sample is illuminated with a collimated X-ray beam of section of less than 1 mm^2. A 2D X-ray sensor is placed behind the sample perpendicular to the incident beam and centered at the beam axis. The entire path is evacuated to a vacuum of about 10^{-2} mbar to avoid background scattering by the air.

As for larger angle diffraction, the incident photon beam is elastically scattered by the electron clouds of the atoms constituting the sample, creating secondary spherical electromagnetic waves with the same wavelength. The shape of the zero-angle diffraction peak is studied here, which contains morphological information in the angstrom – micron range depending on the instrument instead of structural information as for the XRD technique described above.

In SAXS data analysis, it is common to use the scattering vector q instead of the 2θ angle. Considering k_i as the wave vector of the incident beam and k_s as the wave vector of the scattered beam, the scattering vector q is defined as $k_s - k_i$ and is related to the scattering angle θ as :

$$q = \frac{4\pi sin\theta}{\lambda}$$

with λ as the wavelength of the X-ray beam.

We used SAXS to estimate the surface area of the sample powder. Since the grain size is larger than 100 nm, in our experiment we can only observe the final slope scattering as defined by Porod,[8,9] which is proportional to the surface area of the powder. Considering a sample constituted of two homogeneous phases with sharp interfaces, the Porod's law describes the relation between the intensity of the scattered beam and the module of the scattering vector at small angles as:

$$I(q) = \frac{2\pi}{q^4}\Delta\rho^2 S$$

where $\Delta\rho$ is the contrast of scattering length density of the two phases, here $LiFePO_4$/C and vacuum, which depends on their electronic densities and S is the specific surface area .

The average diameter R of the particles could then be deduced from S assuming a spherical geometry:

$$R = d\frac{3}{S}$$

In order to estimate the specific surface area and diameter of the commercial $LiFePO_4$/C powder, a Bruker Nanostar U was used, equipped with a Cu K-alpha tube source, evacuated beam path, Vantec 2000 2D detector, and using a sample–detector distance of 108 cm (see Figure **3-4** (b)). The intensities were corrected for black noise, parasitic signal (empty cell), detector efficiency, spatial distortion, and spherical distortion. The incident beam had been carefully calibrated in order to obtain absolute intensities in cm^{-1}.

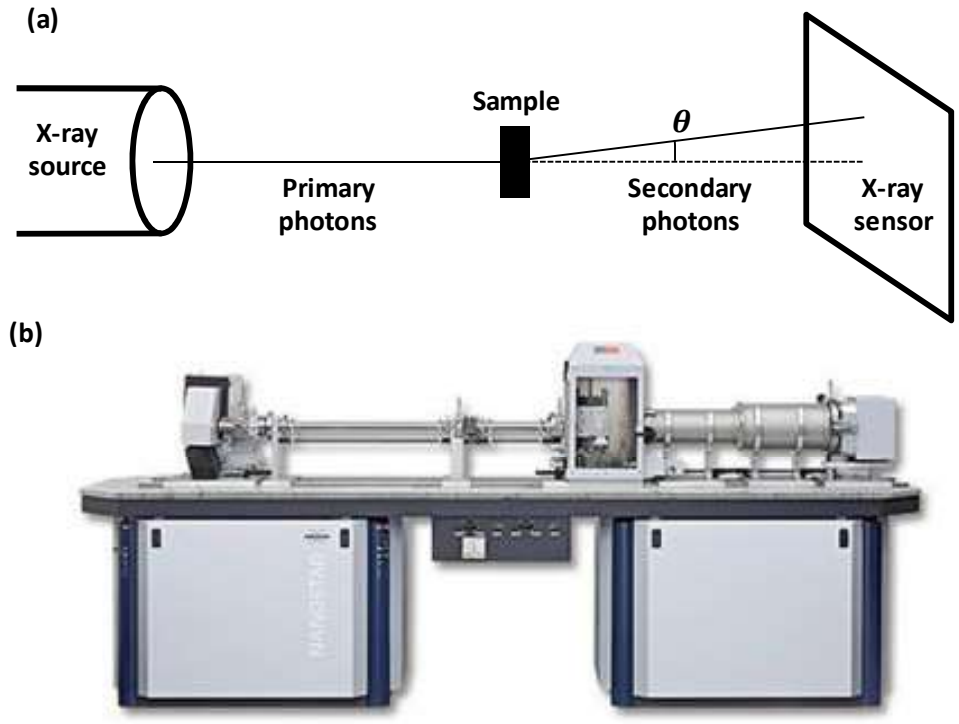

Figure 3-4 : (a) Working principle of SAXS, (b) Bruker Nanostar U instrument that has been used: the Cu K-alpha tube source is on the left, the chamber with the sample in the middle, and the 2D detector on the right.

3.6.3. Electron microscopy

The maximal resolution that can be obtained with a microscope is limited by the wavelength of the photon used, typically a few 100 nm for far field optical microscopes. With regard to photons, electrons have a much smaller wavelength which allows much higher resolution. High energy electrons are provided by an electron gun. With this device, electrons are propelled from a conductive filament to vacuum thanks to a high voltage up to several thousand volts. These electrons are directed toward the sample thanks to electromagnetic coils, similarly to the lenses used in optical microscopes. Some electrons from the incoming beam can be scattered by the sample or transmitted through it. Others can directly hit others electrons within the sample generating secondary electrons and X-ray. All these distinct electrons can be used to produce an image of the sample with an electron-sensitive detector. There are distinct types of electron microscopy, each with a particular purpose, depending on which type of electrons is used to produce the image.[10]

3.6.3.1. Scanning Electron Microscopy (SEM)

The SEM technique, presented in Figure 3-5, uses the secondary electrons that are produced near the surface of the sample to produce high resolution images of this later.[10] This imaging technique has been applied here to determine the particle size and size distribution of commercial $LiFePO_4$/C, using a Quanta 200 FEG (FEI) scanning electron microscope. In this case the powder was strewed on an adhesive carbon sample holder inserted inside the microscope.

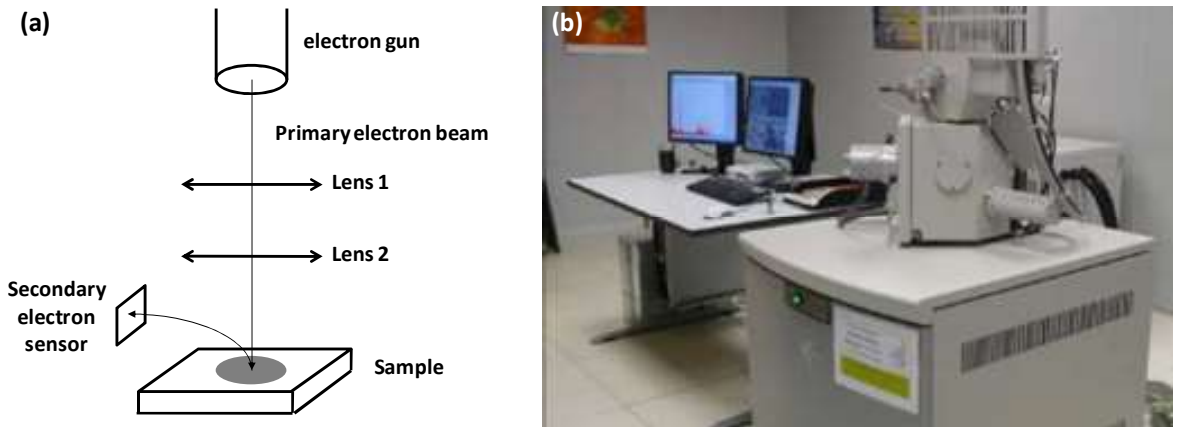

Figure 3-5 (a) SEM measurement principle, (b) Quanta 200 FEG (FEI) scanning electron microscope from CIC Energigune.

3.6.3.2. Transmission Electron Microscopy (TEM)

In the case of the TEM technique, (see Figure 3-6), the projection of the fraction of the electron beam transmitted through the sample is used to give an image of this sample up to atomic resolution. A

diffraction pattern of the sample can be also obtained by exchanging the focal plane and imaging plane of a lens. This diffraction pattern gives indications about the crystalline structure of the sample.[11] It is similar to the XRD diffraction technique described above, the major difference being that it is a single crystal diffraction technique, which means that information of the local orientation of the crystal can be accessed.

TEM images were taken from pristine and cycled material powders to examine their particle size distribution and morphology, using a FEI Tecnai G2 with 200kV field emission gun.

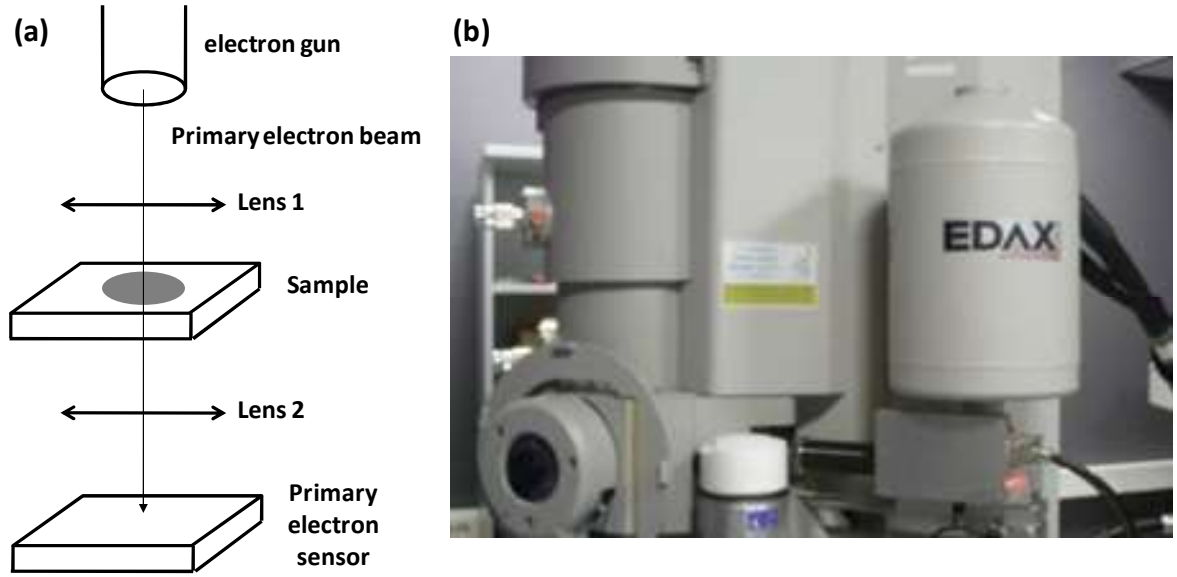

Figure 3-6 : TEM measurement principle, (b) FEI Tecnai G2 from CIC Energigune

[1] J. L. Jones, J.-T. Hung, Y. S. Meng, J. Power sources, 189, 702-705 (2009)
[2] Y. Zhu, Y. Xu, Y. Liu, C. Luo, C. Wang, Nanoscale, 5, 780 (2013)
[3] M. Casas-Cabanas, V. V. Roddatis, D. Saurel, P. Kubiak, J. Carretero, V. Palomares, P. Serras, T. Rojo, J. Mater. Chem., 22, 17421 (2012)
[4] G. Ali, J.-H. Lee, D. Susanto, S.-W. Choi, B. W. Cho, K.-W. Nam, K. Y. Chung, ACS Appl. Mater. Interfaces, 8, 24, 15422-15429 (2016)
[5] C.L. Campion, W. Li, B. L. Lucht, J. Electrochem. Soc., 152 (12), A2327-A2334 (2005)
[6] Y. Ji, Y. Zhang, C.-Y. Wang, J. Electrochem. Soc., 160 (4), A636-A649 (2013)
[7] The Basics of Crystallography and Diffraction, 2nd edition. C. Hammond. International Union of Crystallography – Oxford SciencePublications, 2011.
[8] G. Porod, in: O. Glatter, O. Kratky (Eds.), Small Angle X-ray Scattering, Academic Press, London, 1982
[9] F. Nallet, Collection SFN, 11, 17-42 (2010)
[10] Scanning Electron Microscopy and Microanalysis. J. I. Goldstein, D. E. Newbury, P. Echlin, D. C. Joy, C. E. Lyman, E. Lifshin, L.Sawyer, J. R. Michael. Springer, 3rd edition, 2003. Chapter 2 (pages 21-60)
[11] A.R, West, Solid state chemistry and its applications, John Wiley & Sons Ltd.1990

4. Characterization of commercial and synthesized materials and electrodes

4.1. Introduction

This chapter focuses on the structural, morphological and basic electrochemical characterization of the commercial $LiFePO_4/C$ powder as well as the $LiFePO_4/C$ and $FePO_4/C$ electrodes.

The structural and morphological properties of the powder have been studied through X-Ray diffraction and electron microscopy imagery (TEM and SEM). The electrochemical performances of the electrodes have been studied through cycling, rate capability, GITT and PITT. The efficiency of the electrochemical delithiation process leading to the formation of the $FePO_4/C$ electrodes has also been verified.

4.2. Structure and morphology of the commercial $LiFePO_4/C$

As seen in Figure 4-1, the XRD pattern of the commercial $LiFePO_4/C$ powder shows sharps and well separated peaks indicating the presence of a crystalline phase. The purity of the material is ascertained as all the peaks observed in the pattern of the $FePO_4/C$ powder match the ones reported by Andersson al al.[1] and taken from the ICSD database of Karlsruhe[2].

SEM images of the commercial $LiFePO_4/C$ powder are presented in Figure 4-2 (a). Agglomerates of round-shaped active material particles are observed, with a size varying from 100 to 1000 nm. This particle morphology is confirmed by the TEM images of a selection of small particles displayed in Figure 4-2 (b), (c) and (d). In these images, an agglomerate of particles is shown with different enlargements. A geometrical pattern created by the planes of the crystalline structure of $LiFePO_4$ is observed at the centre of the particles in Figure 4-2 (c) and (d), confirming the high degree of

crystallinity of the pristine material and indicating that the smaller particles at least are single crystalline. In these images, at the edge of the particles, an external layer can be observed in which no geometrical pattern is observed, corresponding to the disordered carbon coating at the surface of the active material. This carbon coating is seen homogeneous with a thickness of 5 to 10 nm, which foreshadows good electrons transport all around the active material particles once they are incorporated inside an electrode.

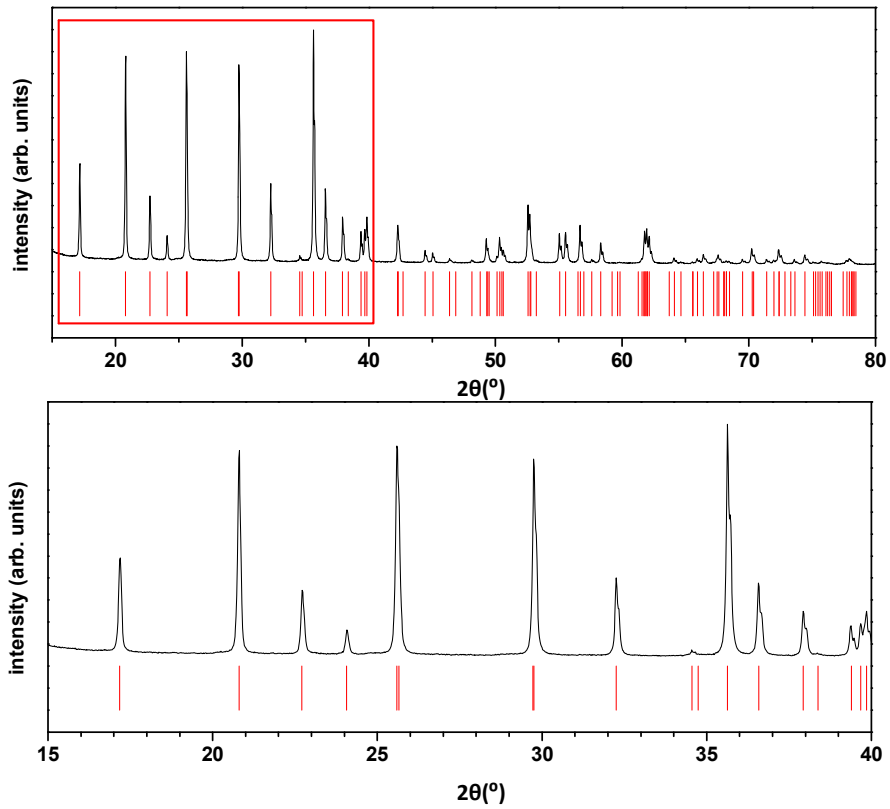

Figure 4-1: XRD pattern of the commercial $LiFePO_4$/C powder. In red, pattern from data published by Andersson at al.[1]

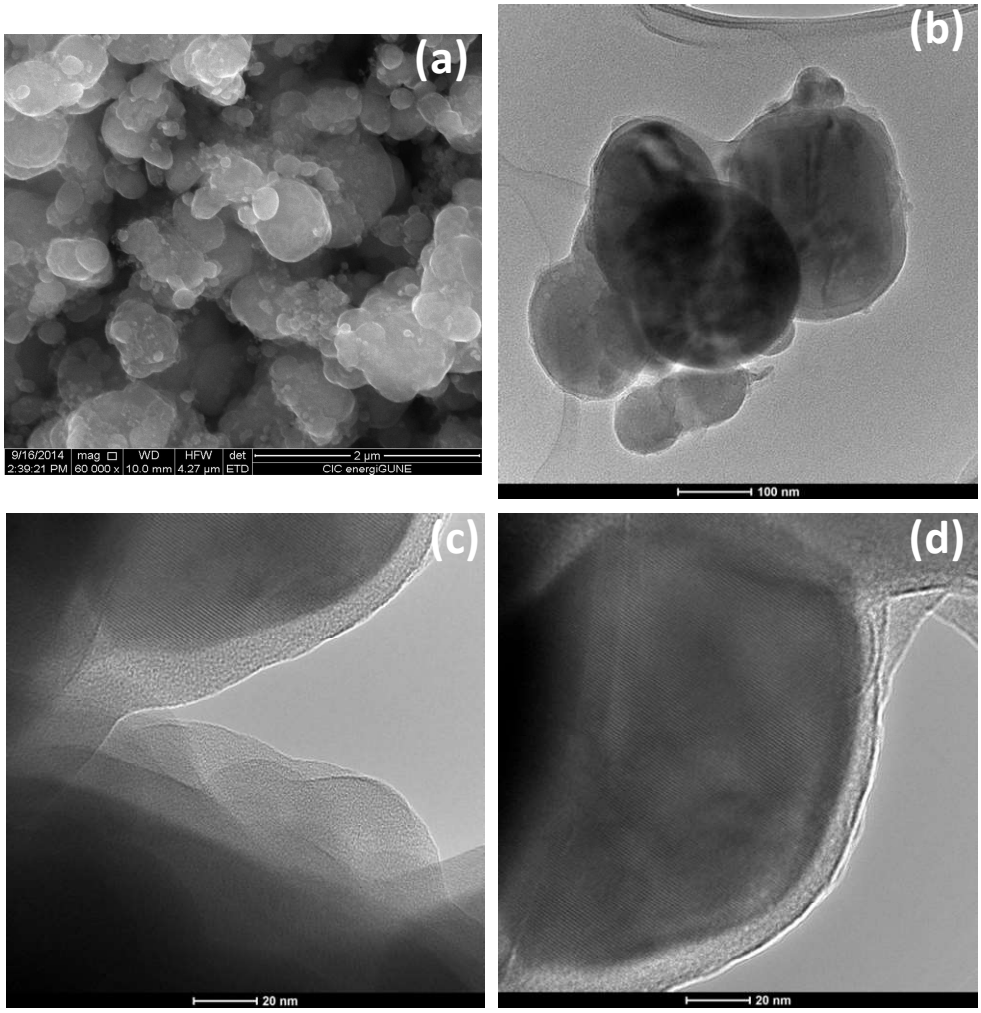

Figure 4-2: (a) SEM and (b), (c), (d) TEM images of the commercial $LiFePO_4$/C powder.

As seen in chapter 2, the electrochemically active surface area of the active material has to be determined in order to estimate the diffusion coefficient of alkali metals from electrochemical measurements. The datasheet provided by the manufacturer of the $LiFePO_4$-C powder indicates a specific surface area (SSA_{BET}) of 21.8 m^2/g determined from the Brunauer–Emmett–Teller (BET) analysis method of N_2 gas adsorption isotherms, and an average particle size of 700 nm as determined from a laser scattering particle size analyzer. Considering spherical particles ($S = 4\pi R^2$), a molar volume of 44.1 cm^3/mol and a molar mass of 157 g/mol, their average diameter deduced from SSA_{BET} should be 77 nm which is underestimated compared to the laser scattering results and the SEM/TEM observations. This discrepancy is probably due to the carbon coating, as gas adsorption actually measures the surface of the carbon coating instead of the surface of $LiFePO_4$, and disordered carbon is known for presenting a rougher surface area, leading to a larger SSA_{BET}.

As the surface area of $LiFePO_4$ is the relevant surface for charge transfer, rather than that of the carbon coating, SAXS measurements were used to determine its value. At small angles the intensity of the scattered X-ray beam typically depends on q^{-4} and is proportional to the product of the

specific surface area of the material and the square of the contrast of density of scattering length $\Delta\rho^2$, as predicted by the Porod's law (eq. (4-1):

$$I(q) = \frac{2\pi}{q^4}\Delta\rho^2 S \qquad (4\text{-}1)$$

This behavior is clearly confirmed by the shape of the intensity vs q plot in Figure 4-3. The densities of scattering length of $LiFePO_4$ and of the carbon coating were estimated as $28.85e^{10}cm^{-2}$ and $17.009e^{10}$ cm^{-2} respectively, using NIST online tool,[3] and based on densities of 3.559 g/cm^3 and 2 g/cm^3, respectively. This leads to values of $\Delta\rho^2$ of $8.32e^{22}$ cm^{-4} for LFP/vacuum and $1.4e^{22}$ cm^{-4} for C/vacuum. Since the C/vacuum contrast of scattering length density is much lower than that of LFP/vacuum, the carbon coating can be considered transparent for the SAXS, which intensity is mainly due to the LFP surface area rather than that of the carbon coating. This leads to a specific surface area of the $LiFePO_4$ particles estimated at 3.24 m^2/g.

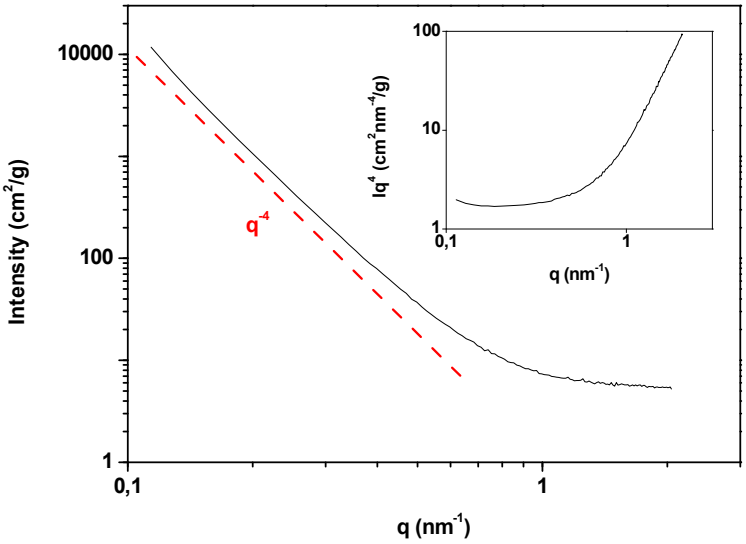

Figure 4-3 : SAXS measurement, intensity vs q. As inset, Iq^4 vs q.

Considering spherical particles ($S = 4\pi R^2$), a molar volume of 44.1 cm^3/mol and a molar mass of 157 g/mol, their average diameter was estimated from the SAXS at 520nm, which, as seen in table 1, is in good agreement with the values deduced from the particle size determined by electron microscopy and laser scattering.

Technique	Average particle diameter (nm)	Specific surface area (m^2/g)
BET	77*	21.8
Laser scattering	700	
SEM/TEM	100-1000	
SAXS	520*	3.24

Table 4-1 : Estimation of the size of the particles from various characterization techniques. (*) deduced from the measurement assuming a spherical geometry.

The 3.24 m^2/g value of the SSA determined from SAXS will thus be considered the relevant effective specific surface area for charge transfer.

4.3. Electrochemical performance of $LiFePO_4/C$ and $NaFePO_4/C$

The voltage-composition profile of $LiFePO_4/C$ upon cycling in half-cell vs Li^+/Li is shown in Figure 4-4 (a). As seen from this figure, it shows the characteristic behavior known for this material: a constant reaction potential near 3.45V related to a reversible biphasic transformation mechanism.[4,5]

The capacity of $LiFePO_4/C$ upon charge and discharge while cycling at C/10 during the first 33 cycles is plotted in Figure 4-4 (b). A capacity of about 172 mAh/g is maintained upon these Li insertion/extraction cycles. This capacity corresponds to about 101% of the theoretical capacity of the electrode confirming the complete insertion/extraction of Li ions. All the electrodes tested in this study had an experimental capacity ranging from 95 to 105% of their theoretical capacity. This variation can be explained by the experimental weighting error, possible inhomogeneities of the laminate and parts of the material possibly not as well connected electrically to the rest of the electrode. All in all, a 5% deviation from the theoretical capacity can be considered as a very good result for hand-made electrodes. This, along with the stable capacity upon cycling, validates the quality of the electrode preparation process and confirms the very good performance of the $LiFePO_4/C$ commercial material.

The first charge potential plateau, corresponding to the first Li extraction from the pristine $LiFePO_4$, is 10 mV higher than that of the following charges. This behavior was also observed by Zhu et al. and Mukhopadhyay et al.[6,7] These authors attributed this higher potential to deformations, dislocation generations and cracking induced by the 6.9% volume change between $LiFePO_4$ and $FePO_4$. These microstructural and morphological changes are expected to ease the phase transformation and the accommodation to volume change from the second cycle onwards.

The coulombic efficiency of the first Li extraction/insertion cycle is of about 93%, and gets very close to 100% from the second cycle on. Irreversible capacity during the first cycles of alkali ions batteries have been frequently reported and is generally attributed to decomposition of the organic electrolyte at the surface of the negative electrode during the first charge of the cell, forming a passivation layer which impedes further decomposition.[8,9] This is typically the case when anode materials operate out of the voltage stability window of the electrolyte, such as in the case of carbon anodes.[10] However, in half cells, the counter electrode, the anode here, is oversized so that the overall capacity of the cell is limited to that of the working electrode, the cathode here. Thus, the excess capacity observed upon the first charge of the cell cannot be ascribed to the formation of this passivation film on the counter electrode but to an irreversible reaction occurring on the working electrode.

The rate capability of $LiFePO_4/C$ in half cell has been performed to acknowledge its electrochemical performance. As previously reported for this material after carbon coating,[11] the rate capability of $LiFePO_4/C$ is very good with still 95 mAh/g available at 20C as shown in Figure 4-4 (c) which corresponds to 55% of the theoretical capacity. The voltage-composition profiles of $LiFePO_4$ among

the last cycles performed at each rate are show in Figure 4-4 (d). The voltage difference between charge and discharge increases by approximately 0.5V from C/10 to 20C. These very good rate capability results confirm the quality of both the starting commercial material and the electrode preparation.

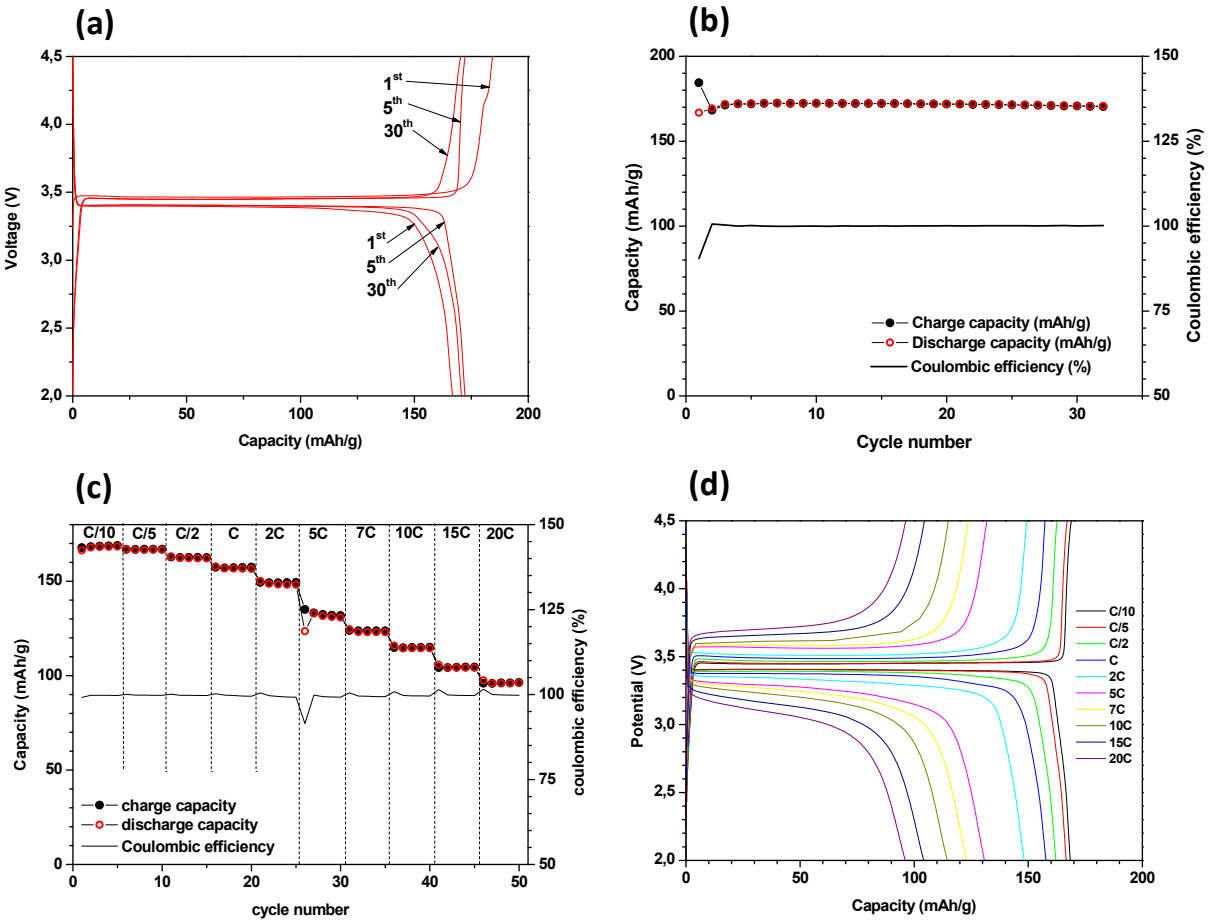

Figure 4-4 : $LiFePO_4$/C half-cell electrochemical performances: (a) Voltage-capacity profiles of the 1st, 5th and 30th cycles at C/10. (b) Charge and discharge capacities and coulombic efficiency upon cycling at C/10 for the first 30 cycles. (c) Charge and discharge capacity and coulombic efficiency evolution during the rate capability measurement. (d) Voltage-capacity profiles of the last cycle performed at each rate during the rate capability experiment.

The voltage-composition profiles of $LiFePO_4$-C in half cell during the electrochemical delithiation procedure using a Li counter electrode, and during the first Na insertions and extractions at C/10 using a Na counter electrode are shown in Figure 4-5 (a). In this figure the scales of potential for Li_xFePO_4/C and Na_xFePO_4/C have been shifted by 330 mV which corresponds to the difference between the Li^+/Li and Na^+/Na standard potentials.[12] Once removed all the lithium from the electrode by the electrochemical delithiation method the first Na insertion reaches about 80% of its theoretical capacity when discharged to 1.5V and the subsequent charge to 4V allows only 60% Na extraction. An irreversible capacity upon the first Na insertion cycle was similarly reported by Zaghib et al. for an electrochemically delithiated $FePO_4$/C electrode,[13] and, by analogy with $LiFePO_4$, could be ascribed to an irreversible reaction occurring on the working electrode. This reaction could be

possibly linked to deformations, dislocation and cracking generated during the first Na insertion as a consequence of the large volume mismatch between the sodiated and de-sodiated phases (17.58%), which is much higher than between the $LiFePO_4$ and $FePO_4$ phases (6.87%),[15] this is in accordance with the 150 mV lower discharge potential observed at the first cycle compared to the next cycles.

At C/10, the voltage-composition profile of Na_xFePO_4/C shows an asymmetrical behavior with two plateaus in charge at 2.95 and 3.1V and a single plateau in discharge at 2.8V vs Na^+/Na, in accordance with previous experimental studies.[14,15] The presence of two voltage plateaus upon Na extraction reveals the existence of an intermediate stable phase $Na_{2/3}FePO_4$. For $1 < x < 2/3$ the transformation occurs through a solid solution mechanism, to which succeeds a $Na_{2/3}FePO_4/FePO_4$ biphasic transformation for $x < 2/3$.[15,16] The single discharge plateau upon Na insertion is related with the coexistence of the three phases $FePO_4$, $Na_{0.7}FePO_4$ and $NaFePO_4$.[15,17]

The charge and discharge capacities and coulombic efficiency of Na_xFePO_4 upon the first 60 cycles at C/10 are plotted in Figure 4-5 (b). The cyclability of Na_xFePO_4/C is as good as that of $LiFePO_4$/C, with 100% of the second cycle capacity maintained after 60 cycles. Although the capacity of Na_xFePO_4 is lower than that of $LiFePO_4$ at about 65% of its theoretical value, it remains within the range of previous reports, typically comprised between 60 and 80%,[18,19,20,21] which suggests it is intrinsic to the Na insertion rather than depending on the initial $LiFePO_4$-C material.

From the second cycle on, the coulombic efficiency is slightly inferior to 100%, the charge capacity being slightly higher than that of discharge, particularly for the first cycles. This behavior was observed on every tested sodium cell and could be due to parasitic reactions at the surface of the working electrode occurring upon charge of the half cell. Indeed, the voltage stability window of various carbonate-based $NaPF_6/NaClO_4$ type electrolytes was studied by Ponrouch et al. who observed decomposition (although relatively slow) of EC/DMC based electrolytes, the decomposition rate increasing with the voltage.[22] Although this was particularly visible above 5V vs Na^+/Na, this electrolyte decomposition might not be negligible at lower potential and in this case might be responsible for an excess capacity at the end of charge.

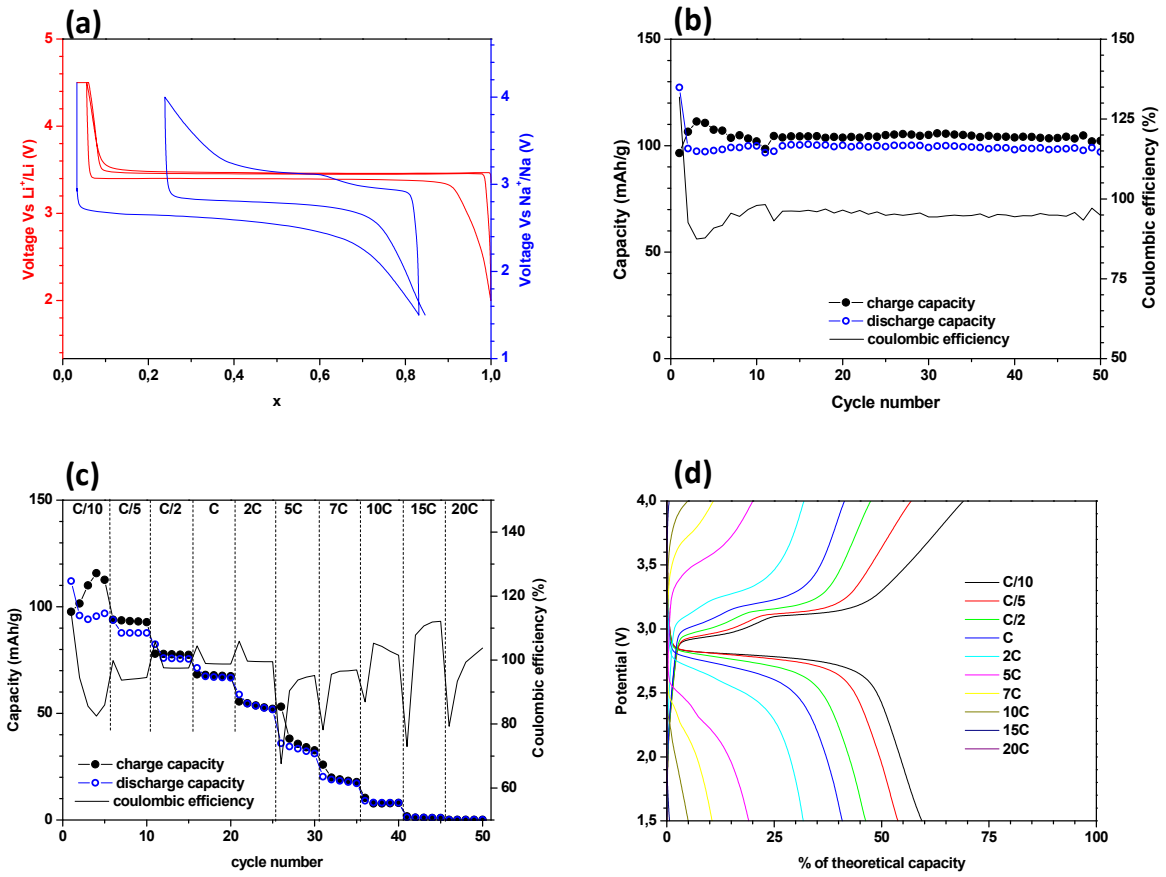

Figure 4-5 : Electrochemical performances of $FePO_4$/C electrodes vs Na: (a) Potential vs alkali concentration profiles of a $LiFePO_4$/C half cell during the electrochemical delithiation procedure (red) and of the same electrode vs Na^+/Na upon the first cycles of Na insertion extraction (blue). (b) Charge and discharge capacity and coulombic efficiency upon cycling at C/10 for the first 30 cycles. (c) Charge and discharge capacities and coulombic efficiency evolution during the rate capability measurement. (d) Voltage-capacity profiles of the last cycle performed at each rate during the rate capability experiment.

The charge and discharge capacities obtained during the rate capability test of Na_xFePO_4/C are displayed in Figure 4-5 (c). This capacity is close to 100 mAh/g at C/10, decreases to about 50 mAh/g at 2C, and becomes almost negligible beyond 10C. It can be seen from the voltage-composition profile upon the last cycle performed on each rate, represented in Figure 4-5 (c), that the reaction potentials tremendously increase with the rate in charge (decrease in discharge) and that the two charge plateaus seem to merge above 2C before disappearing above 7C. Interestingly, a second discharge plateau tends to appear upon discharge at rates of 2C and higher.

Figure 4-6 (a) compares the rate capabilities of Na_xFePO_4 and Li_xFePO_4. In addition to its lower capacity at low rates, the capacity of Na_xFePO_4 decreases significantly faster while increasing the rate compared to Li_xFePO_4. Moreover, while the capacity of $LiFePO_4$ is almost constant at low rates, that of Na_xFePO_4 varies significantly, which suggests that the capacity of Na_xFePO_4 is kinetically limited even at the lowest tested rate and thus that more capacity could be achieved by decreasing further the rate. The rate capability measurements were performed on similar electrodes with similar morphology, using similar cell architecture and in the same conditions except for the electrolyte's salt and metal counter electrode, which suggest that the kinetic limitation of the capacity of Na_xFePO_4/C is intrinsic to the active material.

The differential capacities dq/dE of the lithium and sodium cells upon rate capability, determined from the derivation of the voltage-composition profiles of Figure 4-4 (d) and Figure 4-5 (d) are plotted in Figure 4-6 (b). Here also for the sake of comparison the scales of these two figures have been shifted by the 330 mV standard potential difference between Li^+/Li and Na^+/Na. The splitting of the discharge plateau of the Na cell for rates above 2C is clearly observed on the derivative curves in Figure 4-6 (b), with the apparition of two peaks upon discharge at these rates. These curves are particularly useful to determine with precision the average reaction potentials as a plateau in the voltage-composition profile is materialized by a peak in the derivative curve.

These reaction potentials are reported in Figure 4-6 (c). For the lithium cell the reaction potentials at each rate were determined from Figure 4-4 (d) for rates ranging from C/10 to 5C and from its differential capacity (see Figure 4-6 (b)) for rates above 5C. For the sodium cell they were determined from its differential capacity (see Figure 4-6 (b)) at all rates. As seen from Figure 4-6 (c), for both $LiFePO_4$ and $NaFePO_4$ the reaction potentials increase linearly with the current indicating that, in both cases the overpotential-current relationship is controlled by the Ohm law at the tested rates, allowing calculating an equivalent reaction resistance from its slope. It has to be noted that for both materials, an offset remains at low current between the reaction potentials of the corresponding reduction/oxidation reactions, indicating the presence of a hysteresis of the equilibrium reaction voltages between charge and discharge. This hysteresis has been previously reported for $LiFePO_4$ and was attributed to mechanical stress caused by the volume mismatch between the phases in presence.[23] The hysteresis is higher in the case of $NaFePO_4$, which is consistent with the larger volume mismatch between the separated phases compared to $LiFePO_4$.

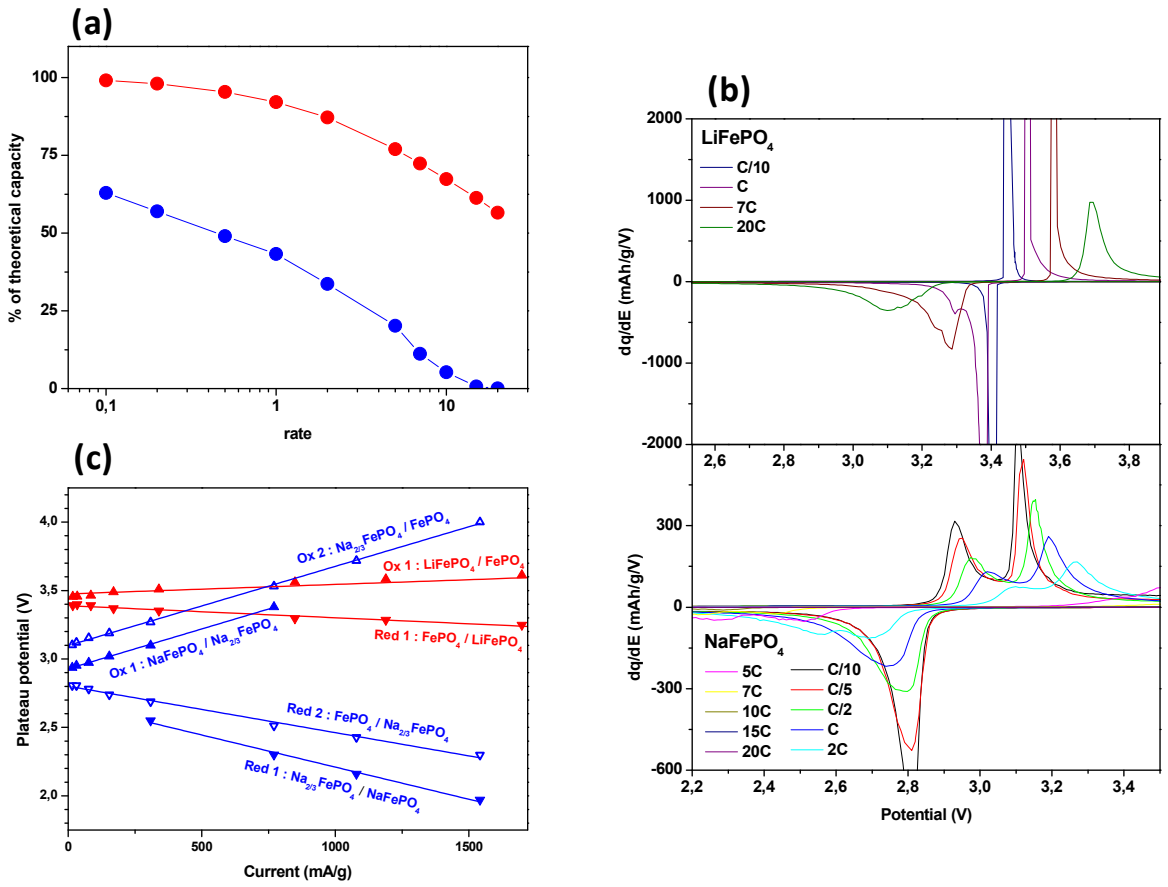

Figure 4-6: (a) Discharge capacity of the $LiFePO_4$/C (red) and $FePO_4$/C vs Na (blue) half cells during the last cycles performed upon rate capability. (b) dq/dE plots of the $LiFePO_4$/C and $FePO_4$/C vs Na half cells during the last cycle performed upon rate capability. (c) Evolution of the reaction potentials with the rate for $LiFePO_4$/C (red) and $FePO_4$/C vs Na (blue).

The reaction resistances corresponding to each reaction of Na_xFePO_4 and Li_xFePO_4 are reported in Table 4-2. The reaction resistances of Na_xFePO_4 are found almost 10 times higher than that of Li_xFePO_4 upon charge and 5 times higher upon discharge. These higher resistances confirm the poorer kinetics at electrode level of both insertion and extraction of Na compared to Li and can be directly related with the poorer rate capability.

	Reaction resistance (mΩ.g)	
	Li_xFePO_4/C	Na_xFePO_4/C
Ox1	70	580
Ox2		580
Red1	90	470
Red2		330

Table 4-2 : Reaction resistances calculated from the evolution of each potential plateau of the $LiFePO_4$/C and theNa_xFePO_4/C electrodes upon rate capability.

It is interesting to note that the two discharge reactions in the sodium cell have distinct reaction resistances, but their potentials both tend toward a very similar value at low current, which corresponds thus to the equilibrium potentials of the two reactions $FePO_4/Na_{2/3}FePO_4$ and $Na_{2/3}FePO_4/NaFePO_4$.[24] The closeness of the equilibrium potential value of these two systems is thus

responsible for the merging of the two reactions and the simultaneous presence of the three phases $FePO_4$, $Na_{2/3}FePO_4$ and $NaFePO_4$. The distinct reaction resistance, however, drives away their reaction potentials at high rates, leading to better separation of the two.[24] This is in agreement with the rate dependence of the mechanism as observed from *operando* XRD measurements by other members of our group, which observed that the three phase region is shrinking as the rate increases.[24] The value of the first discharge reaction resistance being found lower than that of the second reaction resistance, it suggests higher kinetic limitations for the $Na_{2/3}FePO_4/NaFePO_4$ biphasic Na insertion mechanism compared to that of the $FePO_4/Na_{2/3}FePO_4$ biphasic insertion mechanism.

4.4. Intermittent titration techniques

As mentioned above, in the zero current limit the potential of an electrode material asymptotically approaches its value at thermodynamic equilibrium. This potential is particularly interesting as it gives information about the nature and number of phases present within the material at each composition and therefore about the insertion material's transformation mechanism upon Na/Li (de)intercalation. The thermodynamic equilibrium potential can be determined accurately from Intermittent Titration Technique, either potentiostatic (PITT) or galvanostatic (GITT). GITT consists in scanning the composition of the cathode through short constant current steps, letting it relaxing between each step for a time large enough to consider it has reached this equilibrium. PITT consists in scanning the composition of the cathode through short constant potential steps upon which the cell is left relaxing for a time large enough to consider it has reached equilibrium.

4.4.1. GITT

4.4.1.1. Equilibrium potential

Prior to GITT the material was preconditioned by several galvanostatic cycles at C/10, followed by a last charge in constant current constant voltage (CCCV) mode. CCCV consists in charging in constant current mode, here at C/10, until reaching the cutoff voltage (here 4V). Once this later is reached, it is further hold during a few hours (10h here) in order to get as close as possible to total charge. The voltage-composition profile of Na_xFePO_4 during the last CCCV charge and during the GITT is reported in Figure 4-7(c). On this graph the expected double plateau shape of the voltage-composition profile upon charge of the material is observed. The equilibrium potential of Na_xFePO_4 determined at the end of each GITT step is plotted in Figure 4-7 (d) as function of the overall composition of the material. The equilibrium potential of the cell at the end of GITT discharge is found clearly below the charge and discharge reaction potentials indicating the completion of the Na insertion process at this stage. Hence, the composition of the electrode in Figure 4-7 (c) and (d) is adjusted to correspond to x = 1 at the beginning of the charge in GITT mode. For the sake of comparison, the evolutions of the potential and equilibrium potential of $LiFePO_4$/C, determined from a GITT experiment by a previous student of our group, are represented in Figure 4-7 (a) and (b).[25]

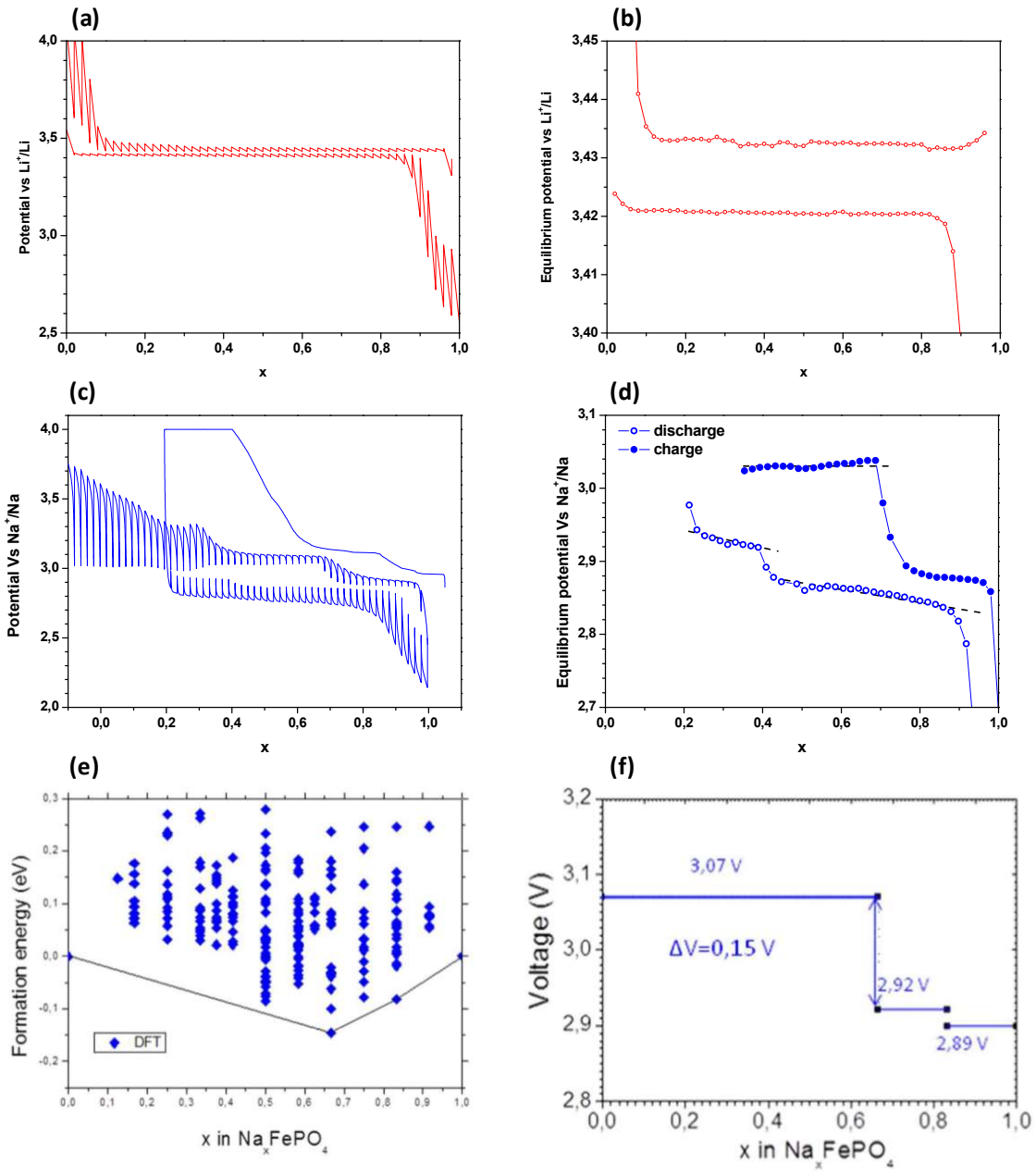

Figure 4-7 : (a) Voltage composition profile of a $LiFePO_4$/C electrode upon GITT. (b) Equilibrium voltage-composition profile of the same $LiFePO_4$/C electrode. (c) Voltage-composition profile of a sodium cell upon GITT. The GITT was performed upon discharge then charge and preceded by a constant-current charge at C/10 followed by a constant-voltage charge at 4V. (d) Equilibrium voltage-composition profile of the cell. The composition of the cell is adjusted to reach x = 1 at the beginning of the charge in GITT mode. (e) Formation energies of Na_xFePO_4 per formula unit of various compositions with different Na/vacancy arrangements.[26] (f) Computed voltage/composition profile of Na_xFePO_4 at 0K.[26]

The two charge plateaus are observed at 2.88 and 3.03 V, respectively. A. Saracibar,[26] in collaboration with CICe's computational analysis group, calculated the formation energies of Na_xFePO_4 as function of the sodium content from theoretical calculations, which is reported in Figure 4-7 (e). Contrary to Li_xFePO_4 for which Malik et al. found a convex hull with positive formation energies within the whole composition range of the material, with two unique stable phases at compositions of x = 0 and 1 (c.f. fig. 1-8 (b)),[27] a concave hull was found for Na_xFePO_4 with two stable phases with lower formation energies at the compositions x = 2/3 and 5/6, respectively, indicating that some intermediate stable phases shall appear upon Na (de)intercalation. The thermodynamic

potentials associated with the transformation mechanisms upon Na (de)intercalation were determined from these formation energies as of 2.89 V in the composition range $1 < x < 0.83$; 2.92 V for $0.83 < x < 0.66$ and 3.07 V for $x < 0.66$ as reported in Figure 4-7 (e). These theoretical values are in good accordance with the equilibrium voltages values of the material found during the GITT upon charge, although a single potential plateau is observed in the [1 – 0.66] composition range, probably caused by a merging of the two former plateaus. This can be related to the findings of Galceran et al. which observed, from *operando* XRD performed at C/50, a single phase evolution upon Na extraction for $1 < x < 2/3$.[15] However, the evolution of the cell parameters upon Na extraction reported by Galceran et al. showed a discontinuity of the (*b*) parameter at a composition close to $x = 5/6$ upon charge, suggesting a phase transition occurs at this composition, which indicates that the transformation mechanism is more complex than a simple solid solution and possibly involves an intermediate phase $Na_{5/6}FePO_4$.

The good accordance between the theoretical and experimental potentials indicates that the transformation of the material follows the thermodynamic equilibrium path upon Na extraction.[26] The distinct voltage-composition profile observed upon galvanostatic discharge indicates that when Na is inserted the reaction mechanism does not follow the equilibrium path, as proposed by Casas-Cabanas et al.[17] Indeed, these authors analyzed the ex-situ relaxation of a Na_xFePO_4 electrode partially discharged to $x \approx 0.25$, in which a tri-phasic state is initially observed, which after a few days of relaxing at 50°C showed a conversion of most of the $NaFePO_4$ phase into $Na_{2/3}FePO_4$.

Upon GITT discharge, interestingly, two very close plateaus of equilibrium potential are revealed in the GITT measurement of Figure 4-7 (a) and (b), at 2.93 and 2.86 V respectively instead of a single reaction potential, which had never been reported yet. This confirms the observation made in the previous section, based on the rate capability results that suggested that the discharge was done through two reactions of very close potential at low rate, which overlap in galvanostatic conditions, even for low specific current. If one considers that thermodynamic equilibrium has been reached at the end of each GITT step upon discharge, then a large equilibrium potential hysteresis is revealed by the GITT measurement between charge and discharge. In the case of $LiFePO_4$ an hysteresis is also present, as seen in Figure 4-7 (a) and (b), and has been ascribed by Zhu et al. to the interface formation energy related to the strain induced by the volume mismatch.[28] Taking into account that the volume mismatch is much larger in the case of $NaFePO_4$, it is not surprising that the hysteresis is much larger. What is surprising, though, is the fact that charge potential matches the results of the simulations made by Saracibar et al., which does not take into account any interface energy. This suggests that it is the discharge potential that is affected by interface energy rather than the charge, which does not make much sense as it has been demonstrated by Galceran et al. that the mechanism is symmetrical between end of charge and beginning of discharge, involving thus in both cases interfaces between FePO4 and Na2/3FePO4. One cannot discard the possibility that the reaction potentials determined by Saracibar et al. are slightly overestimated, as it is known that the method used can lead to imprecision as high as 0.2V.[29]

4.4.1.2. Polarization and relaxation time

During a GITT experiment, the polarization of the cell can be determined accurately during every titration step from the difference between its voltage at the beginning and the end of the relaxation periods and a polarization resistance can be calculated by dividing the polarization by the value of the current applied during the GITT galvanostatic steps. This resistance gives information about the alkali (de)intercalation kinetics as function of its concentration within the insertion material. The polarization resistance, determined from a GITT experiment performed on $LiFePO_4$/C before the beginning of the present study is displayed in Figure 4-8 (c) and (d) as function of the Li concentration within the material upon charge and discharge, along with the relaxation time necessary to reach an equilibrium condition of 2 mV/h.

Almost 100% of the theoretical capacity of Li_xFePO_4 was reached upon charge and discharge during the GITT experiment of Figure 4-7 (a). As seen in Figure 4-8, the potential drop at the end of discharge and the potential jump at the end of charge, which both mark the completion of the biphasic Li insertion and extraction reactions, are clearly associated with simultaneous fast increase of the polarization resistance. A similar observation was made by Tang et al.[30] and Zhu et al.[19], and were ascribed to the exhaustion of available alkali metal for extraction upon charge, or vacancies upon discharge.[19] These polarization resistance increases are also clearly associated with an important increase of the relaxation time, (c.f. Figure 4-8 (e) and (f)), suggesting that the material needs much more time to relax to reach equilibrium when close to completion of the transformation reactions.

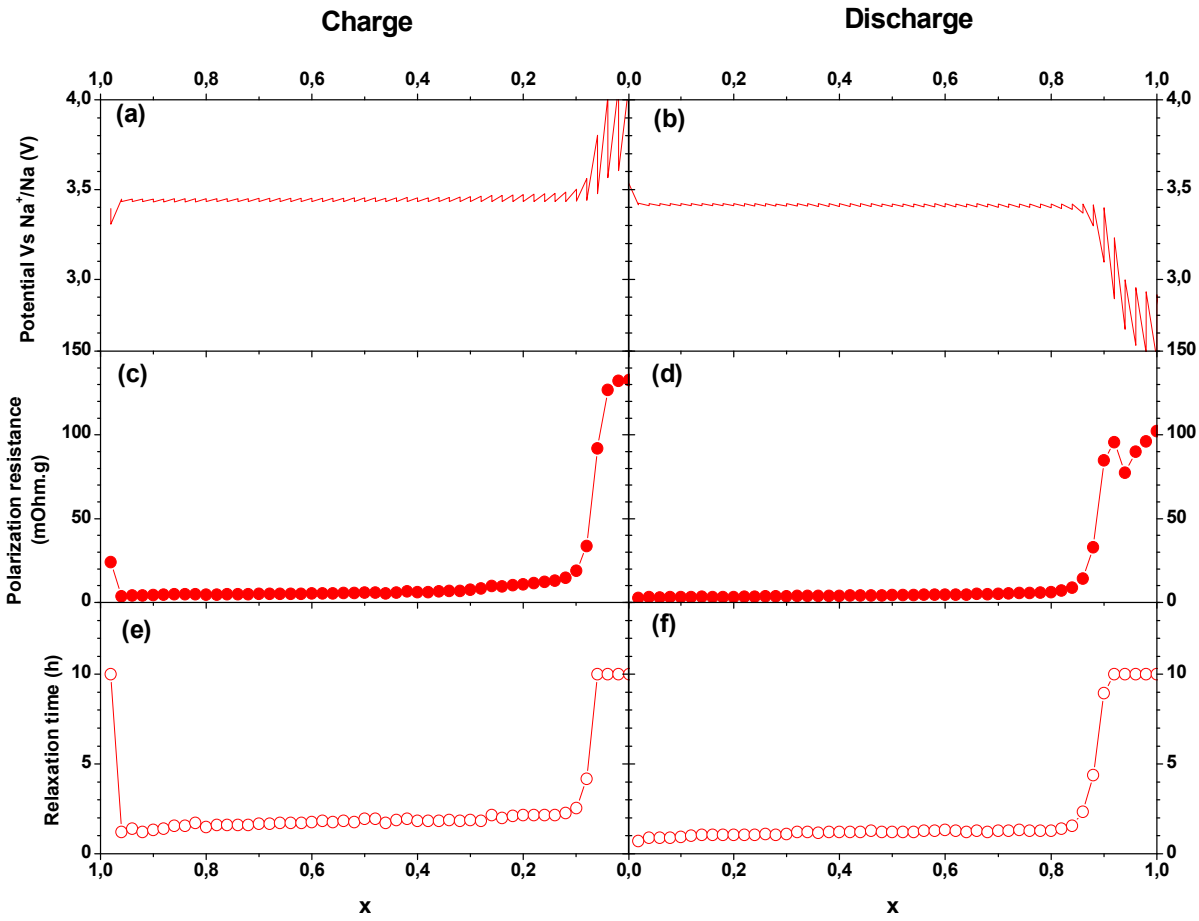

Figure 4-8 : GITT results from Ref. 25: (a) and (b) Voltage composition profile of $LiFePO_4/C$ during a GITT experiment upon discharge and charge. (c) and (d) Polarization resistance determined from GITT as function of the Li concentration within Li_xFePO_4/C. (e) and (f) Relaxation time necessary to reach the equilibrium condition of 2 mV/h.

The polarization resistance of Na_xFePO_4 deduced from the GITT potential-composition profile of Figure 4-7 (a) is plotted in Figure 4-9 (c) and (d) in charge and discharge respectively. The relaxation time necessary to reach the equilibrium condition of 2 mV/h is also plotted in Figure 4-9 (e) and (f).

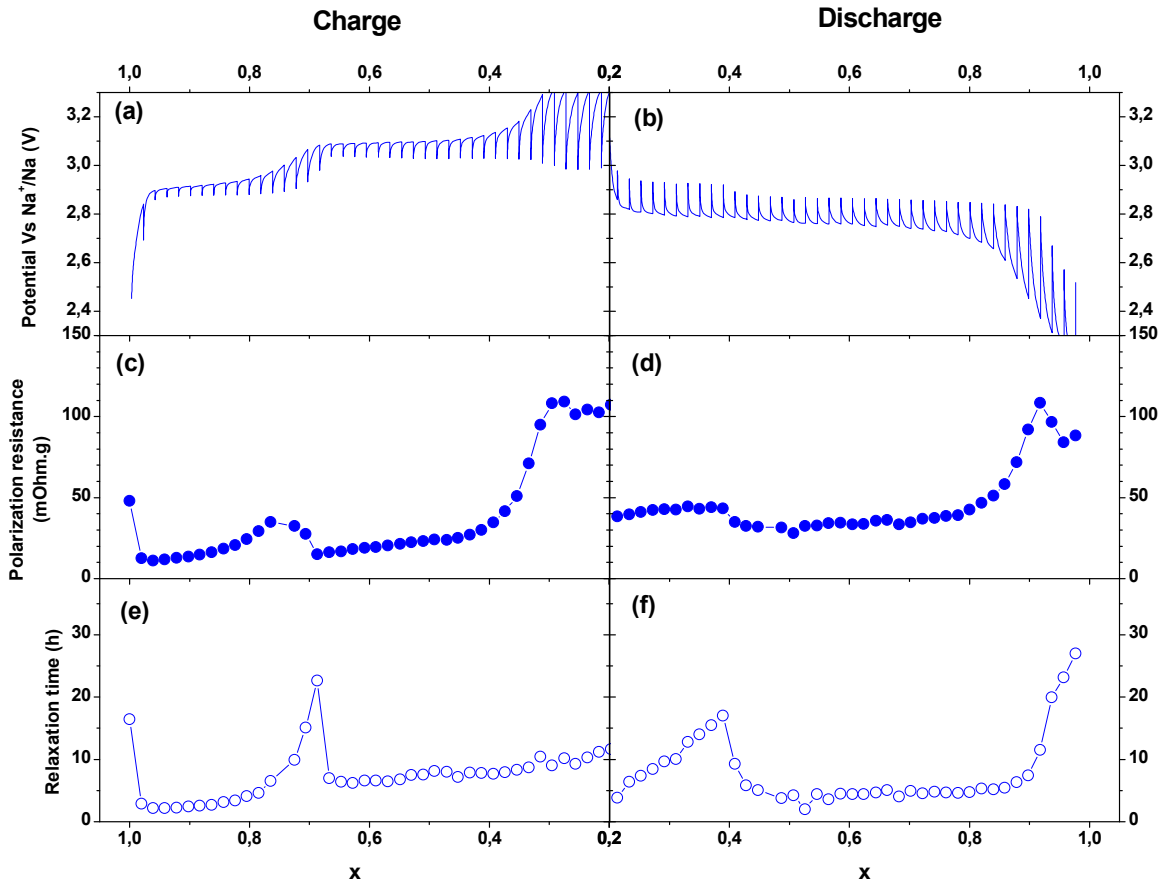

Figure 4-9 : (a) and (b) Voltage composition profile of $NaFePO_4$/C during the GITT experiment upon charge and discharge. (c) and (d) Polarization resistance determined from GITT as function of the Na concentration within Na_xFePO_4/C. (e) and (f) Relaxation time necessary to reach the equilibrium condition of 2 mV/h.

Upon charge, the polarization resistance of Na_xFePO_4 is increasing from x = 1 to x = 0.8 where it shows a maximum, after which it drops at the appearance of the 3.1 V voltage plateau (x = 2/3) and remains relatively steady until x ≈ 0.4 above which is increases. A similar polarization resistance profile for Na_xFePO_4 upon charge was reported by Zhu et al.[19] and Heubner et al.[21] The relaxation time also increases exponentially at the beginning of charge to reach a maximum at x = 2/3. Immediately after this maximum, it drops suddenly and its value remains relatively steady until the end of charge.

In the case of Na_xFePO_4, two reactions follow one another: single phase from x = 1 up to the apparition of the intermediate phase $Na_{2/3}FePO_4$, and biphasic $Na_{2/3}FePO_4$-$NaFePO_4$ for x < 2/3. The polarization resistance peak observed around x = 0.8 ends as soon as the biphasic transformation regime is established and thus may be ascribed to the nucleation of the $Na_{2/3}FePO_4$ phase. It is interesting to note that the relaxation time drop also occurs as soon as the biphasic regime is established, confirming the completion of the Na_xFePO_4 solid solution transformation reaction.

At the end of charge, when the polarization of the cell increases, no increase of the equilibrium voltage is observed. The increase of the polarization at the end of charge observed by Zhu et al.[19] and Heubner et al.[21] were coupled with an increase of the equilibrium voltage which they attributed to complete desodiation of the cathode material. If the increase of polarization observed in the present work at the end of charge of the cell might indeed be attributed to hindered extraction kinetics, the

steady behavior of the equilibrium voltage of the cell suggests that the material is still biphasic at this stage and therefore that the Na extraction is not complete, as confirmed by the steady profile of the relaxation time at this stage. The incomplete Na extraction process is probably related to the hindered extraction kinetics.

Surprisingly the GITT charge capacity exceeds that of the CCCV charge previous to the GITT where 85% of the theoretical capacity of the cell was reached, and goes beyond 1 Na per formula unit. This suggests that this excess capacity does not correspond to Na extraction from the structure but is probably due to a parasitic reaction. Indeed, as explained in section 4.3 of this chapter, the 95% coulombic efficiency of the sodium cells upon cycling at C/10 was attributed to degradation of electrolyte at the end of charge. Since the rate of the electrolyte decomposition increases with the voltage,[22] it would be enhanced by the high polarization at the end of charge and thus might be responsible for the excess capacity observed at the end of the charge in GITT mode.

Upon discharge, the polarization resistance is slightly higher on the first potential plateau ($0.2 < x < 0.4$) than on the second one ($x > 0.4$); and the relaxation time increases steadily on the first potential plateau at the end of which it reaches a maximum, before dropping suddenly when the second plateau appears. Alike the charge, the polarization resistance drop and relaxation time maximum at $x = 0.4$ seem to mark the end of the biphasic $FePO_4$-$Na_{2/3}FePO_4$ transformation and the apparition of the $NaFePO_4$ phase along with the two above mentioned ones, confirming the discontinuity in the Na intercalation mechanism upon discharge. At the end of discharge, when reaching $x = 0.8$, the polarization resistance jumps when the equilibrium potential drops, marking the end of the insertion process as confirmed by the relaxation time jump at this stage, and strongly suggesting that $NaFePO_4$ is obtained at this stage.

The reaction resistance determined from rate capability (330 – 580 mΩ.g) is about one order of magnitude higher than the polarization resistance obtained from GITT in the middle of the reaction plateau (30 – 50 mΩ.g). Although some difference can be rooted to the fact that the electrodes for the two experiments were punched from different laminates, with maybe distinct packing densities or electrode thickness, it cannot account for such large difference, especially taking into account that the values given here are specific, i.e. normalized to the active material's mass. This suggests that the relation between polarization and current is not linear at low rates, as the rate capability was determined with rates superior to C/10, while the GITT measurement has been performed at C/50 followed by long relaxations, as seen from Figure 4-10.

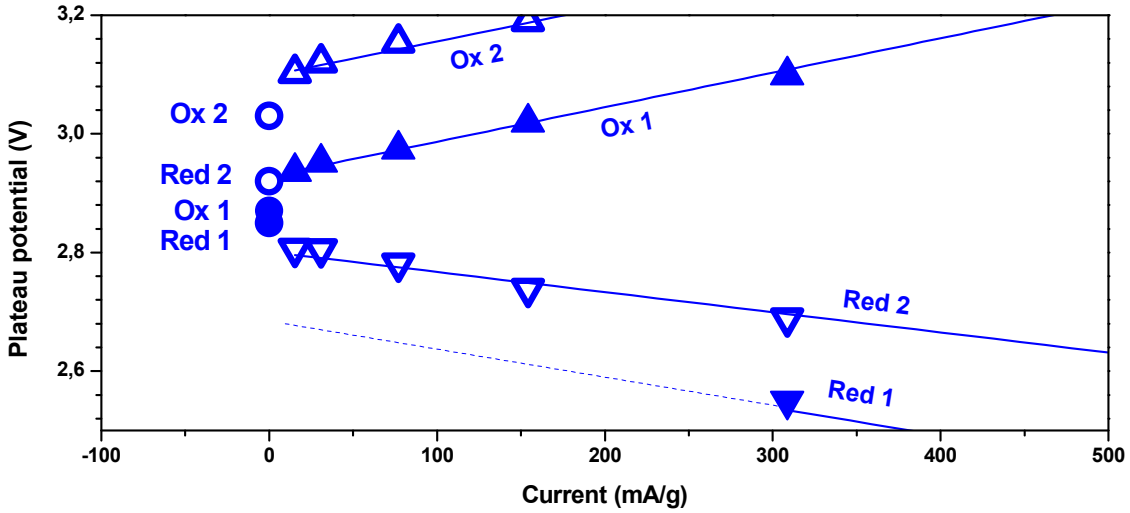

Figure 4-10 : Low current zoom of Figure 4-6 (c) in which the equilibrium potentials determined upon GITT have been added (circular symbols).

4.4.2. PITT

The parasitic reaction observed upon GITT in charge, ascribed to decomposition of the electrolyte, was facilitated by the large increase of the cell polarization at the end of charge, which prevented to achieve the completion of the charge reaction. To avoid this issue, Potentiostatic Intermittent Titration Technique (PITT) has been performed. Since PITT consists in sequential scanning of the titration curve of the cell through constant potential steps between equilibrium states it is supposed to prevents high polarizations. Indeed, in the case of PITT an increase of the polarization resistance at the end of charge might increase the relaxation time, but will not raise the cell potential, which should reduce the sensitivity of the measurement to parasitic reactions.

PITT was performed on $LiFePO_4$-C and $NaFePO_4$-C half cells. Before PITT, five charge/discharge cycles at C/10 were performed on the lithium cell, and three discharge/charge cycles at C/10 on the sodium cell after electrochemical delithiation. Then the cathodes were brought to the complete lithiation/sodiation state after a CCCV down to 2V for the lithium cell and 1.5V for the sodium cell until the current would reach C/500.

Between 100 and 105% of the theoretical capacity of the lithium cells (the one tested vs Li and the one delithiated and further tested vs Na) was achieved upon cycling and after the potential hold at 2V, confirming the quality of the electrode preparation process. For the sodium cell, 83% of the theoretical capacity was achieved upon the first Na insertion and 68% upon the following insertions at C/10. 78% of the theoretical capacity of $NaFePO_4$ was later reached at the end of the CCCV discharge at 1.5V.

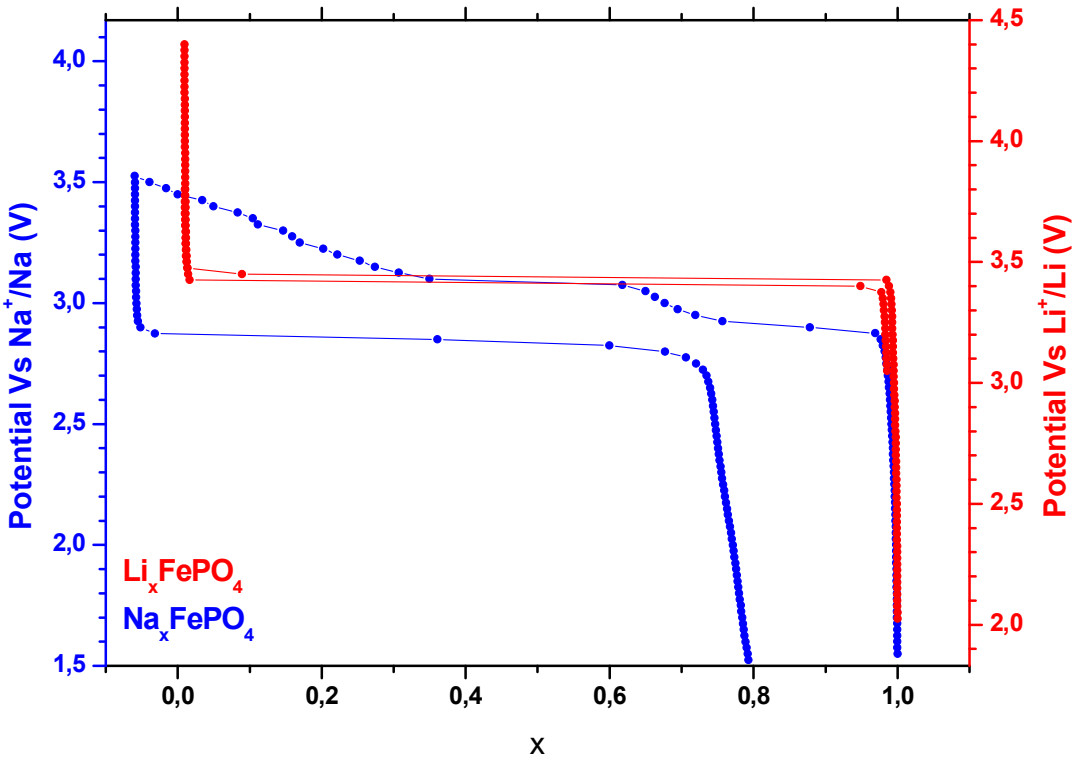

Figure 4-11: Titration curves of the $LiFePO_4$ and $NaFePO_4$ half cells upon the PITT experiment.

The equilibrium potential-composition profile of $LiFePO_4$/C plotted in Figure 4-11 shows the expected behavior for this material with a single plateau at 3.45V in charge and 3.4V in discharge, characteristic of the biphasic equilibrium state of the insertion material at intermediate compositions.[4,5] The sharp equilibrium potential jumps and drops at the beginning and end of charge and discharge, respectively, are characteristic for the narrow solid solution regime of Li_xFePO_4 transformation when the Li content approaches that of the end members, as explained in chapter 2. This marks the complete Li insertion/extraction process. 99% of the theoretical capacity of $LiFePO_4$ is reached upon both charge and discharge in between these potential drops.

The equilibrium potential-composition profile of $NaFePO_4$/C during the PITT measurement shows the behavior previously reported for this material using this technique with two plateaus of potential of reaction in charge at 2.9 V and 3.1 V and a single one in discharge at 2.85 V.[14] A single potential plateau is observed upon discharge in PITT while two plateaus were observed in discharge during the GITT experiment. However, it has to be noted that since the potential step during the PITT is 25 mV, it may not offer the precision necessary to resolve the two discharge plateaus observed in GITT that were separated by only 70 mV. Moreover, the peak of current at the beginning of the PITT voltage steps is much larger than the C/50 current of the GITT experiment, inducing a stronger perturbation of the system in the case of PITT. This stronger perturbation possibly triggers the two discharge reactions at the same time, hampering their separation.

The sharp potential drop at the beginning of charge and end of discharge indicates the completion of the Na insertion mechanism at this stage. However, at the end of charge no sharp increase of the potential profile is observed. Instead, a sluggish potential increase starts after 60% of the Na atoms

have been successfully removed, at which composition the equilibrium potential of the material was still found constant upon GITT. This suggests that a large overpotential is necessary to extract Na from the material at this stage which impedes its complete extraction, and thus that the potential profile observed at the end of charge upon the PITT does not correspond to thermodynamic equilibrium. Indeed, since the potential step is fixed in PITT mode, a large overpotential of reaction is traduced by a very small current, probably smaller than the equilibrium conditions that were defined during the experiment setup. However, in PITT, setting a too small a current limit as equilibrium condition is not advisable as parasitic reactions may append to have a non-negligible weight in the overall capacity. This behavior at the end of PITT charge confirms the observations made upon GITT suggesting hindered extraction kinetics at the end of charge and that the material is probably still biphasic at this stage.

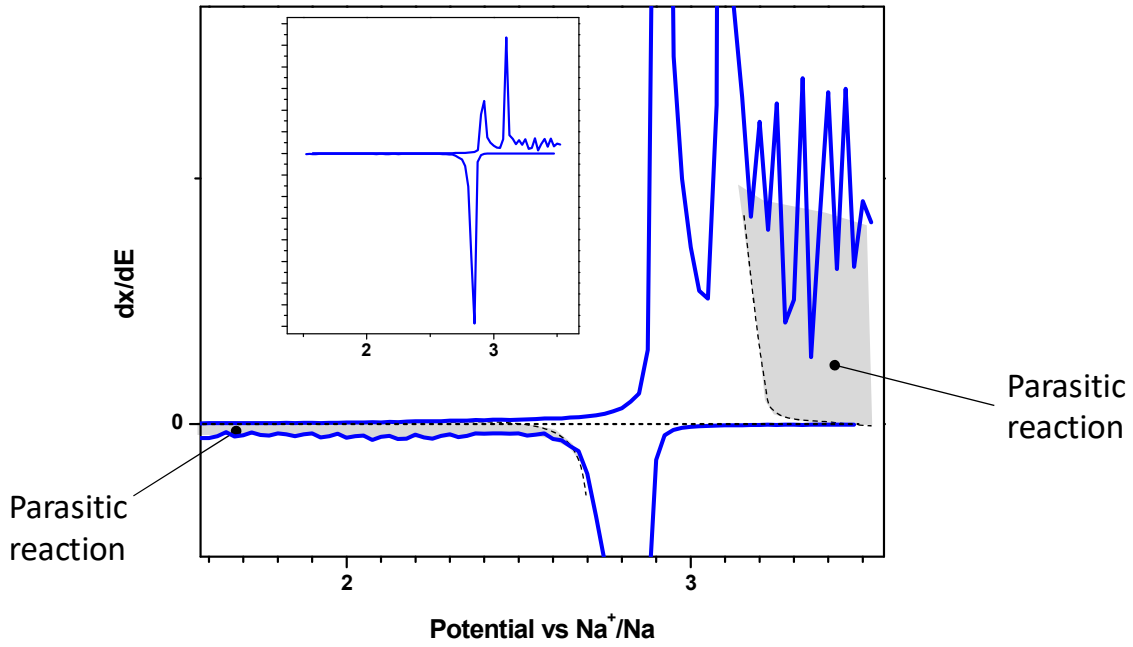

Figure 4-12 : Derivative curve dx/dE of the equilibrium voltage-composition profile of Figure 4-11 for $NaFePO_4$. The grey areas indicate the parasitic reactions, while the dashed lines represent the hypothetical profile in absence of these later.

Surprisingly, 106% of the theoretical capacity of the cell is obtained at 3.5 V at the end of the PITT charge process while only 80% is reached upon the discharge. Since the Na extraction kinetics are hindered at the end of charge and the potential of the working electrode increases at this stage, it is very probably that the parasitic reaction observed upon GITT have become preponderant upon PITT, and can be responsible for the excess capacity upon charge compared to that of discharge. This suggests that much longer relaxation times are needed to accurately obtain the equilibrium potential profile of Na_xFePO_4 with this technique, which can only be done in absence of parasitic reaction. The presence of this parasitic reaction can be better observed in Figure 4-12, which presents the derivative curve dx/dE of the equilibrium voltage-composition profile of Figure 4-11 for $NaFePO_4$. It can be observed clearly from Figure 4-12 that dx/dE is zero at the beginning of charge and beginning of discharge. However, after the second reaction potential upon charge, instead of decreasing to zero as expected for a complete reaction, dx/dE shows a rather constant value at the end of charge denoting the onset of a side redox reaction. Interestingly, dx/dE does not goes to zero neither at the

end of discharge, which denotes a possible partial reversibility of the side reaction observed upon charge.

It is interesting to note that the same 80% of the theoretical capacity of $NaFePO_4$ is obtained with both the GITT and PITT techniques upon discharge, and that this capacity corresponds to that obtained upon the first Na insertion at C/10. This suggests that 20% of the theoretical capacity is inaccessible, possibly due to irreversible microstructural or morphological changes upon the first Na intercalation, as suggested from the lower potential observed upon first intercalation at C/10. These irreversible changes occurring during the first Na insertion are most probably rooted to the large volume mismatch between the reacting phases, and may comprise deformations, dislocation as well as cracking. On the other side, the charge capacity seems to be limited at the end of charge due to kinetic limitation.

4.5. Conclusions

$LiFePO_4$-C electrodes were prepared from commercial $LiFePO_4$-C powder. These electrodes were successfully electrochemically delithiated, washed and mounted in Na half cells.

The electrochemical performances of Li_xFePO_4-C and Na_xFePO_4-C electrodes were compared through cycling, rate capability, GITT and PITT. Special care has been taken, for each technique, for using electrodes issued from the same laminate for comparing tests vs Li and Na, so as to ensure that no difference of materials as well as electrode morphology could bias the conclusions.

Nearly 100% of the theoretical capacity is reversibly achieved in $LiFePO_4$-C at C/10 with an impressive rate capability with nearly 100 mAh/g still available at 20C. On the contrary, in the case of $NaFePO_4$-C only 60% of the theoretical capacity is reversibly achieved at C/10. Moreover, a much poorer rate capability was observed for $NaFePO_4$ with a notable rate dependence even at low rates, all suggesting that kinetic limitations are responsible for the limited capacity in $NaFePO_4$ even at low rates. The $NaFePO_4$-C reaction resistance deduced from rate capacity is 4 to 10 times higher than that of $LiFePO_4$-C, second indication of kinetic limitations in the case of $NaFePO_4$.

Interestingly the first Na insertion in $FePO_4$/C at low rate (C/10) reaches 80% of its theoretical capacity with an overpotential of 150 mV compared to the following Na insertions, in which only 60% of the theoretical capacity of the electrode is achieved. This suggests that two sources of capacity limitation are present, one upon discharge and one upon charge. Likewise, only 80% of the theoretical capacity of the material has been obtained with the two titration techniques (GITT and PITT) upon discharge, which strongly suggests that some irreversible changes at cathode level occurred upon the first Na intercalation which reduced the available capacity for further cycles. The equilibrium potentials, polarization resistances and relaxation times determined upon GITT indicate incomplete Na extraction at charged state due to hindered extraction kinetics at the end of charge, which is confirmed by PITT. Two potential sources of capacity limitations have thus been observed: microstructural/morphological changes occurring upon the first Na intercalation limiting to 80% of the theoretical capacity, and kinetic limitation at the end of charge which additionally limits to 60% the capacity that can be reversibly obtained upon further cycling at low rate.

The GITT and rate capability measurements allowed to get some insight into the discharge mechanism. Comparing the equilibrium potentials from GITT with the results obtained by A. Saracibar (UPV) and J. Carrasco (CICe) allowed to confirm that the charge follows the thermodynamic equilibrium phase transformation path.[26] Moreover, while previous work proposed a single 3-phase reaction, the GITT and rate capability results of the present chapter demonstrate that this 3-phase state observed upon discharge is the consequence of the overlap of two reactions due to very close reaction potentials, which has been further confirmed by *operando* XRD measurements.[24]

[1] A. S. Andersson, B. Kalska, L. Häggström, J. O. Thomas, Solid State Ionics, 130, 41-52 (2000)
[2] http://www2.fiz-karlsruhe.de/icsd_web.html
[3] https://www.ncnr.nist.gov/resources/sldcalc.html
[4] A.K. Padhi, K. S. Nanjundaswamy, J. B. Goodenough, J. Electrochem. Soc., 144 (4) (1997)
[5] R. Malik, A. Abdellahi, G. Ceder, J. Electrochem. Soc., 160 (5), A3179 (2013)
[6] Y. Zhu, C. Wang, J. Power Sources, 196, 1442 (2011)
[7] A. Mukhopadhyay, B. W. Sheldon, Progress in material science, 63, 58-116 (2014)
[8] Y. Mutsumura, S. Wang, J. Mondori, J. Electrochem. Soc., 142 (9), 2914 (1995)
[9] E. Peled, J. electrochem. Soc., 126, 12, 2047 (1979)
[10] E. Peled, S. Menkin, J. Electrochem. Soc., 164 (7), A1703 (2017)
[11] H. Huang, S.-C. Yin, L. F. Nazar, Electrochem. Solid-State Lett., 4 (10), A170-A172 (2001)
[12] D. D. Ebbing, M. S. Wrighton, General Chemistry, Houghton Mifflin3rd edition (1990)
[13] K. Zaghib, J. Trottier, P. Hovington, F. Brochu, A. Guerfi, A. Mauger, C. M. Julien, J. Power Sources, 196, 9612 (2011)
[14] P. Moreau, D. Guyomard, J. Gaubicher, F. Bocher, Chem. Mater., 22, 4126 (2010)
[15] M. Galceran, D. Saurel, B. Acebedo, V. Roddatis, E. Martin, T. Rojo, M. Casas-Cababas, Phys. Chem. Chem. Phys., 16 (19), 8837 (2014)
[16] J. Gaubicher, F. Boucher, P. Moreau, M. Ciusinier, P. Soudan, E. Elkaim, D. Guyomard, Electrochem. Commun., 38, 104 (2014)
[17] M. Casas-Cabanas, V. V. Roddatis, D. Saurel, P. Kubiak, J. Carretero-Gonzalez, V. Palomares, P. Serras, T. Rojo, J. Mater. Chem., 22, 17421 (2012)
[18] S.-M. Oh, S.-T. Myung, J. Hassoun, B. Scrosati, Y. K. Sun, Electrochemistrycommunications, 22, 149-152 (2012)
[19] Y. Zhu, Y. Xu, Y. Liu, C. Luo, C. Wang, Nanoscale, 5, 780 (2013)
[20] Y. Fang, Q. Liu, L. Xiao, X. Ai, H. Yang, Y. Cao, Appl. Mater. Interfaces, 7 (32), 17977 (2015)
[21] C. Heubner, S. Heiden, M. Schneider, A. Michaelis, Electrochim. Acta, 233, 78 (2017)
[22] A. Ponrouch, E. Marchante, M. Courty, J.-M. Tarascon, M. Rosa Placin, Energy Environ. Sci., 5, 8572 (2012)
[23] W. Dreyer, J. Jamnik, C. Guhlke, R. Huth, J. Moskon, M. Gaberscek, Nat. Mater., 9, 448 (2010)
[24] D. Saurel, M. Galceran, M. Reynaud, H. Anne, M. Casas-Cabanas, Int. J. Energy Res. 1, 2018
[25] Kinetic study of Na insertion/extraction in olivine $FePO_4$/$NaFePO_4$ as cathode material for Na-ion batteries, Mathilde Lepoitevin, Master thesis (2013)
[26] A. Saracibar, J. Carrasco, D. Saurel, M. Galceran, B. Acebedo, H. Anne, M. Lepoitevin, T. Rjo, M. Casas-Cabanas, Phys. Chem. Chem. Phys., 18(18), 13045-51 (2016)
[27] R. Malik, F. Zhou, G. Ceder, Nat. Mater., 10, 587 (2011)
[28] Y. Zhu, C. Wang, J. Phys. Chem. C., 114, 2830 (2010)
[29] Y. Zhang, D. A. Kitchaev, J. Yang, T. Chen, S. T. Dacek, R. A. Sarmiento-Pérez, M. A. L. Marques, H. Peng, G. Ceder, J. P. Perdew, J. Sun, npj Computational Materials, 9, 1 (2018)
[30] R. Tang, X. Yu, J. Sun, H. Li, X. Huang, Electrochim. Acta, 56, 4869 (2011)

5. Diffusion coefficient

5.1. Introduction

In the previous chapter it was shown that the performances of $NaFePO_4$/C are poorer than that of $LiFePO_4$/C which seems to be caused by kinetic limitations to Na (de)intercalation at the end of charge and irreversible structural or morphological changes occurring during the first Na intercalation. This chapter aims at determining the origin of these kinetic limitations.

The electrochemical performances of a battery rely on the ability of the charges to move from one battery terminal to the other. The redox reactions rates and the diffusivity of the mobile species inside the battery materials are kinetic key factors for fast charge transport. In $LiFePO_4$/C and $NaFePO_4$/C half cells the Li/Na mass transport process occurs inside both the electrolyte and the cathode material. Lee et al. determined the diffusion coefficient of $LiPF_6$ in EC/DMC from the Levich equation applied on a rotating electrode as $1.39e^{-5}$ cm^2/s.[1] The ionic conductivity of $LiPF_6$ in various carbonate-based electrolytes was found very similar to that of $NaPF_6$.[2] In EC/DMC, in particular these ionic conductivities were determined respectively as 9 and 6.5 mS/cm.[3,4] On the other hand, as highlighted by Churikov et al. the diffusion coefficient of Li ions is several orders of magnitude higher in electrolytes (typically $D \approx 10^{-5}$ cm^2/s) than in the solid active materials of the electrodes (typically $D < 10^{-10}$ cm^2/s).[5] This indicates that if the kinetic limitations leading to the poorer electrochemical performances of $NaFePO_4$ compared to $LiFePO_4$ are diffusive type, they find their origin in the Li/Na diffusivity inside the electrode insertion material rather than in the electrolyte. Concerning the redox reaction rates, or charge transfer rate, its contribution to the overall cell impedance is typically in

between that of the diffusion in the electrolyte and the diffusion in the active material, so that this later is the most likely source of kinetic limitation in $LiFePO_4$-C and $NaFePO_4$-C half cells.[6]

Numerous studies of the diffusivity of Li in Li_xFePO_4 were published in the last 20 years,[7,8] based on computational methods,[9,10] impedance spectroscopy on single crystal as well as in pellets of polycrystalline material,[11,12] and electrochemical techniques on electrodes in half cells such as electrochemical impedance spectroscopy (EIS)[13,14,15,16,17,18,19,20], GITT[5,13,21,22,20] or PITT[5,18,22,23,24].

As explained in chapter 2, the diffusion coefficient of an inserted ion within an insertion electrode material can be determined from its dynamic response to an electrical excitation, taking into account the morphology of the electrode, the thermodynamic properties of the material, and assuming semi-infinite linear diffusion conditions(SILD), in the form:

$$D = \left(\frac{V_M}{ZFSSA}\right)^2 \left(\frac{\Delta E}{\Delta x}\right)^2 D_r \qquad t \ll L^2/D \quad (5\text{-}1)$$

In the morphological factor $\left(\frac{V_M}{ZF\ sa}\right)^2$, V_M is the molar volume of the insertion material, Z is the number of charges carried per inserted ion, F is the Faraday constant and SSA is the material-electrolyte specific surface area that is effectively available for charge transfer. The second factor, $\left(\frac{\Delta E}{\Delta x}\right)^2$, accounts for the thermodynamic properties of the material and is determined from the slope of the equilibrium potential-concentration profile of the insertion material obtained from titration techniques such as GITT or PITT. At last, the dynamic factor D_r represents the dynamic response of the cell to an excitation, which can be determined either from the time dependence of the current during a PITT titration step (see equation 5-2), from the Warburg coefficient during an EIS measurement (see equation 5-3) or from the time dependence of the potential during a GITT titration step (see equation 5-4).

$$D_r = \left(\frac{I\sqrt{t}}{m\Delta E}\right)^2 \qquad \text{for PITT}[25] \qquad (5\text{-}2)$$

$$D_r = \left(\frac{1}{m\sqrt{2}A_w}\right)^2 \qquad \text{for EIS}[26] \qquad (5\text{-}3)$$

$$D_r = \left(\frac{2I}{m\sqrt{\pi}}\frac{d\sqrt{t}}{dE}\right)^2 \qquad \text{for GITT}[27] \qquad (5\text{-}4)$$

In equations 5-2 to 5-4, m is the mass of active insertion material within the electrode. Given that in all cases the SILD conditions are supposed to be respected, the value of D_r is expected to be the same independently on the technique used.

The previously reported diffusion coefficient values of Li within Li_xFePO_4 determined from the above-mentioned techniques are summarized in table 1-3 in the introduction chapter and reported here in Figure 5-1 (a) and (b) as function of the concentration or the potential of Li_xFePO_4, respectively, depending on the methodologies followed by the authors.

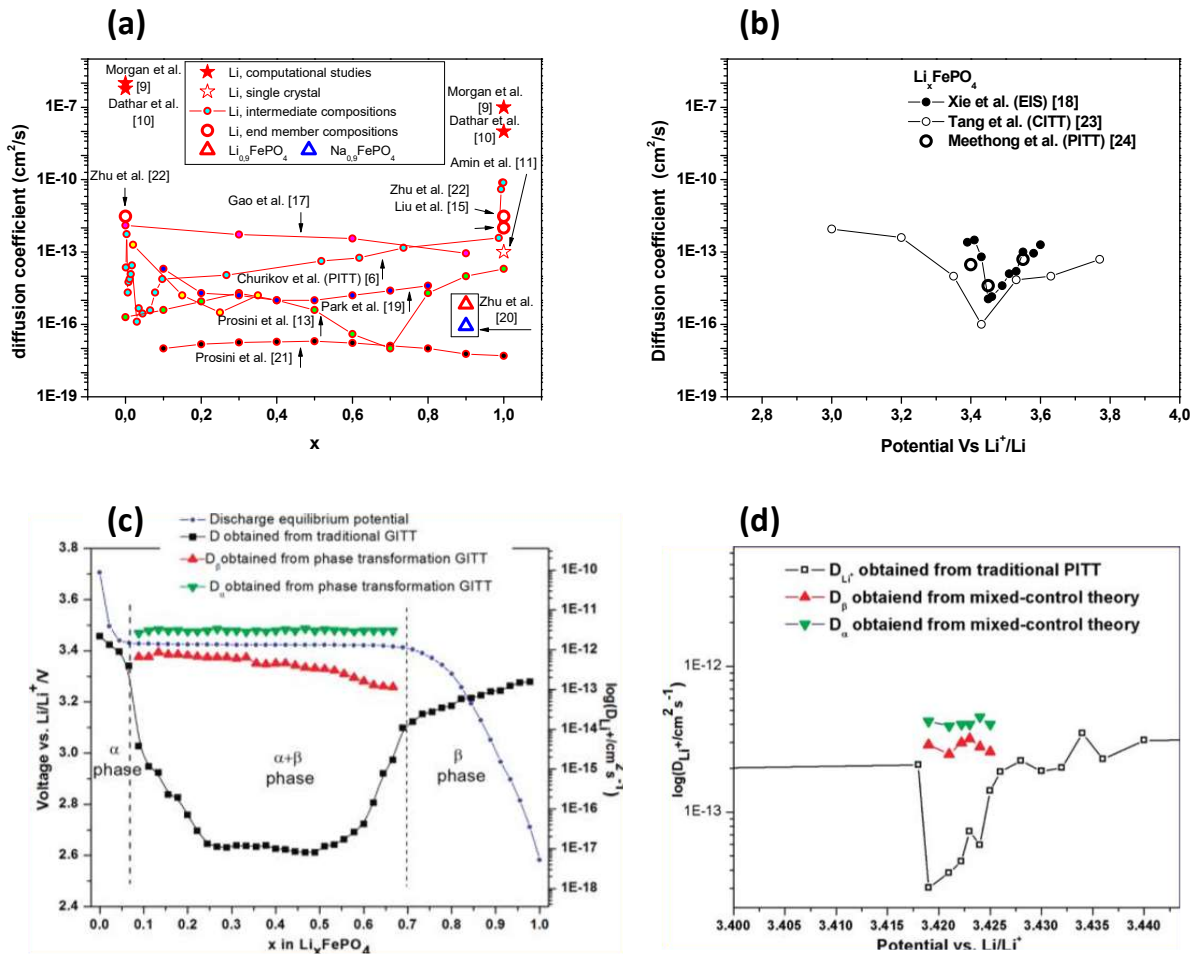

Figure 5-1: (a) and (b) Graphical comparison of reported diffusion coefficients of Li and Na within Li/Na_xFePO_4 as function of the composition of the material and its potential respectively. The value from Amin et al. (Ref. 11), displayed at room temperature, was extrapolated from their results at 200°C taking into account the activation energy they determined (700 meV). (c) and (d) Diffusion coefficients determined from phase transformation model, upon GITT and PITT respectively.[22]

The diffusion coefficient values obtained from computational methods are found between 2 and 5 orders of magnitude higher than those determined from experimental techniques which, as pointed out by Malik et al., can be ascribed to the defects in the crystalline structure and the particle size effects that might affect the diffusivity but are not taken into account in these computational studies.[7]

Moreover, a large dispersion of diffusion coefficient values found in the literature can be observed in Figure 5-1 (a), particularly from the diffusion coefficient profile determined by Churikov et al.[5] On this graph the Li diffusion coefficient within Li_xFePO_4 is found especially dispersed for compositions close to x = 0 and x = 1 and relatively constant for intermediate compositions. The large dispersion near the compositions of the end members is better observed when the diffusion coefficient value is plotted as function of the potential of the electrode as illustrated in Figure 5-1 (b), particularly from the diffusion coefficient profile determined by Tang et al.[23] On this graph it is shown that the diffusion coefficient profile presents a notch of several orders of magnitude at the reaction potential, where a small change of the composition of Li_xFePO_4 largely affects its experimentally determined diffusion coefficient value. This could explain the large dispersion of values with composition close to the end members: a slight deficiency of Li in $LiFePO_4$ or remaining Li in $FePO_4$ could induce a change

of measured diffusion coefficient of several orders of magnitude. It can also be observed from Figure 5-1 (b) that the authors who controlled the equilibrium potential of the electrode instead of its composition to determine the Li diffusion coefficient for compositions close to that of end members ($x \approx 0$ and $x \approx 1$, corresponding to electrode potentials below or above the reaction potential) found relatively close values at these compositions suggesting that a better precision can be obtained when the measurement is performed at an equilibrium electrode potential significantly below or above the reaction potential.

Several factors can explain the dispersion of the diffusion coefficient values obtained by these authors at intermediate compositions. As pointed out by Malik et al., since accurate determination of the diffusion coefficient relies on precise knowledge of the active material mass involved in the (de)lithiation mechanism, transformation of the active material particles following a "domino-cascade" model as described by Delmas et al. may bring incertitude about this effective active material mass,[28] and thus imprecision to diffusivity characterization in this biphasic concentration range.[8] Furthermore, when the electrochemical techniques (GITT, PITT, EIS) are used to determine the Li diffusion coefficient when the system is biphasic, the usual transport equations are out of their application range, leading to meaningless results. Indeed, as explained in chapter 2, the slope of the equilibrium voltage-composition profile of a biphasic system is theoretically equal to 0 because the potential does not depend anymore on concentration. This artificially decreases the diffusion coefficient value if the biphasic reaction is not taken into account in the transport equations, as did e.g. Zhu et al.[22]

Indeed, Zhu et al. developed an alternative method for the determination of the diffusion coefficient of the individual phases in the bi-phasic composition range, by writing the equations of transport considering a two-phase system separated by a mobile interface. With this model they could determine the Li diffusion coefficient in the two Li-rich and Li-poor phases separately at intermediate compositions through GITT and PITT, as well as the interface mobility.[22] Interestingly, as shown in Figure 5-1 (c) and (d), these diffusion coefficient values were found about 5 orders of magnitude higher than those determined from the classical single phase equations at the biphasic reaction potential. In addition, the diffusion coefficients within the individual phases during the biphasic transformation were found very close to those of the end members $x = 1$ and $x = 0$. This confirms that i) the diffusion coefficient drop of several orders of magnitude observed at the biphasic reaction potential using single phase theory is an artefact, and ii) the diffusion coefficient values can be accurately determined from the "traditional" single phase model as long as the measurements are performed when the material is single phase, i.e. within the solubility limits near the end members $x = 1$ and $x = 0$. The best way to ensure that these conditions are fulfilled is in ensuring that the potential at which the measurements are performed is clearly higher or lower than the biphasic reaction potential.

At the beginning of this thesis, Zhu et al. were the only authors who had compared experimentally the diffusion coefficients of Li and Na, in $(Li/Na)_{0.9}FePO_4$, through GITT and EIS.[20] They found a lithium diffusion coefficient between 8 and 20 times higher than that of sodium depending on the technique used. They also found a higher charge transfer resistance for the Na redox reaction compared to that of Li, suggesting that the diffusivity of Na within Na_xFePO_4 and its redox rate might be responsible for the poorer electrochemical performances of $NaFePO_4$ as electrode material compared to $LiFePO_4$. However, one cannot exclude that at $x = 0.9$ Li_xFePO_4 was already in a biphasic state. Moreover, Zhu

et al. performed constant concentration steps of 2.5 and 5% of the theoretical capacity for Na and Li, respectively, to determine the slope of the equilibrium potential-concentration curve of the material (second term of equation (5-1)). Since the diffusion coefficient value is strongly affected by the precision of the slope of the titration curve of the insertion material, the large titration steps these authors performed may have brought imprecision to the Li and Na diffusion coefficient values.

The objective of this chapter is to determine accurately the diffusion coefficients of Li and Na within Li/Na_xFePO_4in order to figure out the nature of the kinetic limitations responsible for the poorer electrochemical performances of $NaFePO_4$ compared to $LiFePO_4$. The diffusion coefficients of Li and Na inside Li_xFePO_4 and Na_xFePO_4 will be determined from electrochemical characterization methods and compared for the whole composition range of the insertion material.

5.2. Experimental protocol

In the present study it has not been possible to apply the method above-mentioned and developed by Zhu et al., since it requires precise knowledge of the slope of the equilibrium potential-composition profile of the insertion material in all its monophasic composition ranges which, as shown in the previous chapter, was not possible to determine in the case of Na_xFePO_4 near charged state ($x \approx 0$) neither upon GITT nor upon PITT. In the present chapter the traditional single phase-based methods were thus used, keeping in mind that the results are only reliable in the solid solution composition ranges: $x \approx 0$ and $x \approx 1$ for Li_xFePO_4, $1 \leq x \leq 2/3$ and $x \approx 0$ for Na_xFePO_4 in charge and $x \approx 0$ and $x \approx 1$ for Na_xFePO_4 in discharge. In these composition ranges, a potential controlled technique, such as PITT, seems more appropriate than a composition controlled one, such as GITT, to determine the diffusion coefficient of Li and Na within Li/Na_xFePO_4 since, as discussed in section 5.1, the potential is a more appropriate parameter to control for ensuring that the measurements are performed out of the biphasic composition range of the electrode material. From the two techniques used to scan the equilibrium potential profile of the insertion electrode with constant concentration or potential steps (PITT and GITT), PITT seems therefore the most appropriate since, in addition, it allows to concentrate the measurement points in the vicinity of the end members, bringing a better precision to the diffusion coefficient measurement. Since EIS measurements consist in small potential or current oscillations around the equilibrium state of a cell, and because they do not change its state of charge, they do not disrupt the titration process. Potential controlled EIS (PEIS) measurements were therefore performed at the end of each PITT step once the cell had reached thermodynamic equilibrium so satisfying measurement conditions were fulfilled. Following this methodology the diffusion coefficients of Li and Na within Li/Na_xFePO_4 can be determined from equations (5-1), (5-2) and (5-3).

The evolutions of the potentials of Li_xFePO_4 and Na_xFePO_4 during the PITT measurements have been discussed deeply in the previous chapter and their equilibrium potential-composition profiles are displayed in Figure 4-9. In the present chapter, which focuses on the determination of the diffusion coefficient, it is the current relaxation during each step of the same PITT measurements that will be analyzed (dynamic factor), together with the derivative of the equilibrium voltage-composition profile (thermodynamic factor). The dynamic factor will also be determined by impedance spectroscopy in order to corroborate the PITT results.

As explained in the previous chapter, Na_xFePO_4/C was obtained from the electrochemical delithiation of $LiFePO_4$/C electrodes. Thus, all the electrodes used in the present study for Li_xFePO_4 as well as Na_xFePO_4 originate from the same laminate, in order to discard the influence of extrinsic parameters like electrode architecture, carbon additive content or particle size distribution and morphology.

In this chapter the following hypothesis will be supposed valid:

i) The $LiFePO_4$ equilibrium state model presented by Padhi et al.[29] and Srinivasan et al.[30] is assumed. Following this model, the equilibrium state of Li_xFePO_4 is monophasic for compositions close to x = 0 or x = 1 where it corresponds to a Li-poor and a Li-rich phase, respectively. The equilibrium state of the material is biphasic for intermediate compositions. The same model, extended to Na_xFePO_4 is assumed. This equilibrium state is solid solution when $1 \leq x \leq 2/3$ or $x \approx 0$ in charge, and for compositions close to x = 0 and x = 1 in discharge, in accordance with the mechanism described by Moreau et al.[31] and Casas-Cabanas et al.[32] and presented in introduction.

ii) For both Li and Na the active material particles are considered spherical, and the composition homogeneous from particle to particle.

iii) The Li/Na transport follows strictly the Fick's first and second laws; the diffusion coefficient remains unchanged during the duration of a single measurement.

iv) For short time perturbations, finite size effects can be neglected and the diffusion process can be considered linear and semi-infinite at this stage.

v) The alkali insertion or extraction process occurs simultaneously in all the Li/Na_xFePO_4 particles so that in these conditions all these particles have the same chemical potential at every stage of Li/Na (de)intercalation.

5.3. Results

5.3.1. Morphology prefactor

The first factor of eq. (5-1), $\left(\frac{V_m}{FSSA}\right)^2$, depends on the molar volume of the material V_m and the specific surface area SSA of the active insertion material, which both depend on the material's Li or Na composition. The maximum molar volume difference is found between $FePO_4$ and $NaFePO_4$ and corresponds to a 17.58% difference.[33] Considering spherical particles this volume expansion will correspond to a 11.4% specific area difference, and the $\left(\frac{V_m}{FSSA}\right)^2$ value change between these two compounds will also be 11.4%, which we will consider negligible in the present chapter as, as can be observed in Figure 5-1, the values of the diffusion coefficient are expected to vary by several orders of magnitude.

The specific surface area of the active material vs Li as well as Na and at all state of charge will therefore be considered constant and approximated to that of the commercial $LiFePO_4$/C powder which was estimated as 3.24 m^2/g from SAXS. The molar volume of the particles at every

composition is also approximated to that of $LiFePO_4$ which is taken as 44.1 cm^3/mol, leading to a value of $\left(\frac{V_m}{FSSA}\right)^2$ of 1.99e^{-16} $g^2.cm^2.C^{-2}$ for both Li_xFePO_4 and Na_xFePO_4.

5.3.2. Thermodynamic factor

The second factor of eq. (5-1), $\left(\frac{\Delta E}{\Delta x}\right)^2$, is calculated from the slope of the titration curve obtained from the PITT measurements, presented in Figure 4-9. The $\left(\frac{\Delta E}{\Delta x}\right)^2$ values of Li_xFePO_4 and Na_xFePO_4 are plotted in Figure 5-2 as function of the potential.

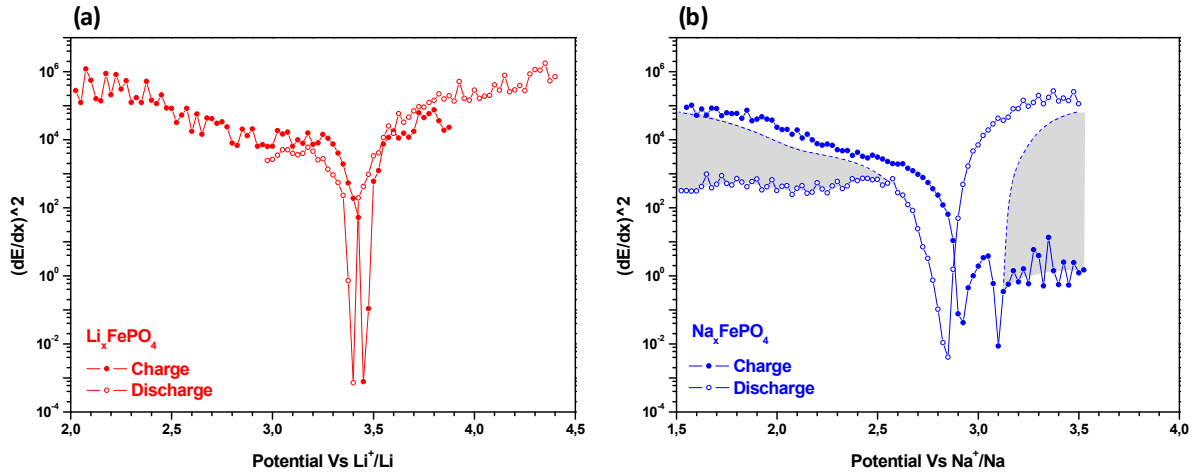

Figure 5-2: $\left(\frac{\Delta E}{\Delta x}\right)^2$ values of (a) the lithium cell and (b) the sodium cell upon charge and discharge. The dashed lines represent the hypothetical evolution of D in case of absence of side reactions, which are highlighted by the grey area.

The $\left(\frac{\Delta E}{\Delta x}\right)^2$ curves obtained upon charge and discharge of Li_xFePO_4 show a notch of 6 orders of magnitude at the potential that corresponds to the biphasic reaction (3.45V upon charge and 3.4V upon discharge), potentials at which a plateau was observed in the voltage-composition profile of Figure 4-9. Interestingly, the $\left(\frac{\Delta E}{\Delta x}\right)^2$ value is relatively steady at higher or lower potentials, and is similar at the beginning and end of charge and discharge, where the material is single phase. Also, very close values of $\left(\frac{\Delta E}{\Delta x}\right)^2$ are observed upon charge and discharge.

As can be expected from the charge profile of Na_xFePO_4 of Figure 4-9, which showed two plateaus at 2.9 and 3.1V, two notches are observed in the derivative curve of Figure 5-2 (b) at these voltages. The maximum between these two notches, which corresponds to the intermediate phase $Na_{2/3}FePO_4$, remains 5 orders of magnitude lower than that at the beginning of charge, which corresponds to $NaFePO_4$. The value of $\left(\frac{\Delta E}{\Delta x}\right)^2$ is also relatively steady at the beginning of charge of Na_xFePO_4, where the material is monophasic; but contrary to Li_xFePO_4, its value remains 5 orders of magnitude lower at the end of charge compared to the beginning of charge. As discussed in the previous chapter, this can be ascribed to an incomplete reaction (i.e. $FePO_4$ is not reached) and the influence of a parasitic reaction (probably electrolyte decomposition) that perturbed the titration for

x < 0.3. The values of $\left(\frac{\Delta E}{\Delta x}\right)^2$ in this range are thus not reliable for determination of the diffusion coefficient. Upon discharge, the potential dependence of $\left(\frac{\Delta E}{\Delta x}\right)^2$ shows a single notch of 5 orders of magnitude that corresponds to the single plateau that was observed in the voltage-composition profile of Figure 4-9. The values of $\left(\frac{\Delta E}{\Delta x}\right)^2$ for Na are also relatively steady above or below the reaction potential. However, at the beginning of discharge where the material is believed to be still biphasic, $\left(\frac{\Delta E}{\Delta x}\right)^2$ is about three orders of magnitude higher than at the end of discharge, which is almost two orders of magnitude lower than that at the beginning of charge. These differences between charged and discharged state, and between beginning of charge and end of discharge depart from the case of Li_xFePO_4 for which the same value was observed. The origin this difference is not clear, but it could be due to the fact that, due to poor kinetics of Na diffusion, the equilibrium is not reached at all state of charge, affecting the slope of the titration curve and thus of its derivative.

5.3.3. Dynamic factor

5.3.3.1. PEIS

With the EIS technique the factor describing the dynamic behavior of a cell as response to an oscillating excitation is written in the form $D_r = \left(\frac{1}{m\sqrt{2}A_w}\right)^2$. The Warburg coefficient, A_ω, is determined from the frequency dependence of the impedance where SILD conditions are fulfilled, which typically occurs in a low frequency range.

As seen in chapter 2, a myriad of phenomena can contribute to the impedance spectra of a cell, and its response will be the sum of the contribution of all these phenomena. The typical EIS Nyquist plots of a $LiFePO_4$ and a $NaFePO_4$ half-cell are represented below:

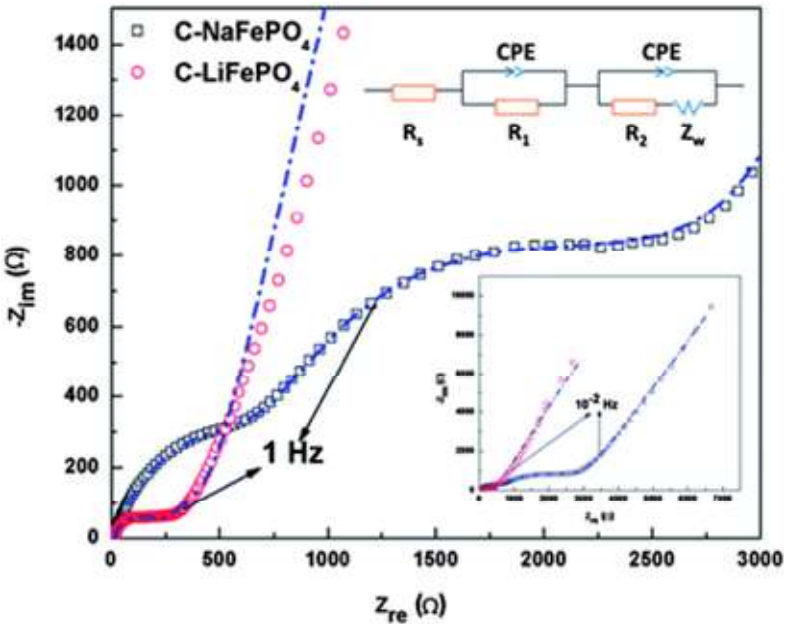

Figure 5-3: Typical Nyquist plot of an insertion electrode and equivalent circuit.[20]

In the case of $NaFePO_4$ this plot presents two semi-circles at high frequency (i.e. left hand side of the plot in Figure 5-3) characteristic respectively for the interface phenomena (charge transfer, double layer capacitance, surface layers etc…) on both electrodes, and a low frequency slope characteristic of the (de)intercalation of the Na ions within/from the insertion material in SILD conditions (i.e. right hand side of the plot in Figure 5-3). In the case of lithium only a single semi-circle is observed alongside the slope at low frequency. The second semi-circle is maybe too small to be observed, or simply overlap the first one. At very high frequencies, although not clearly seen in this plot, the Nyquist impedance spectra tend to a purely real value corresponding to the ohmic losses induced by electrical contacts and the ionic diffusion within the electrolyte. In the present chapter, it is the low frequency slope related to mass diffusion that will be studied as it allows the determination of the diffusion coefficient.

As presented in chapter 2, the impedance related to mass transport in SILD conditions can be modeled by a Warburg element and is written in the form:

$$Z_\omega = Re(Z) - j * Im(Z)$$

or

$$Z_\omega = \frac{A_w}{\sqrt{2\omega}} - j\frac{A_w}{\sqrt{2\omega}} \quad (2\text{-}55)$$

with A_w as the Warburg coefficient. As explained in chapter 2, A_w can only be determined if the limiting factor of the current of the cell is the diffusion of Li/Na within the working electrode, all other contributions being negligible. Fortunately, while both the working electrode under study and the metal counter electrode are expected to present high frequency semicircles, only the working electrode is expected to display the typical mass transport response at intermediate frequencies. Indeed, the metal counter electrode reacts through platting-stripping, which does not involve mass diffusion within the electrode material. EIS measurements performed on 3-electrodes cells allow

measuring the contribution of each electrode to the impedance of the cell separately. Such measurements were performed on three-electrode $LiFePO_4$/Li/Li and $NaFePO_4$/Na/Na cells in order to confirm this hypothesis; (Li/Na)$FePO_4$ being the working electrode and the metallic Li/Na electrodes as counter and reference electrodes. The Nyquist plots of the impedances of the net lithium and sodium half cells and of the individual electrodes are plotted in Figure 5-4 (a) and (b).

For both cells the working electrode impedance spectra show a depleted semi-circle at high frequency and a slope at low frequency characteristic of mass transport. The Li and Na counter electrode impedance spectra also show a depleted semi-circle at high frequency but the impedance value remains limited for lower frequencies and no diffusion part is observed.

The plots of the imaginary part of the impedances of the net cells and of the individual electrodes are reported in Figure 5-4 (c) and (d) as function of the excitation frequency in log scale. A linear evolution of the imaginary part of the impedance of the insertion electrode is observed at low frequency in the mass diffusion regime while the impedance of the metal counter electrodes remains negligible, between one and two orders of magnitude lower. This confirms that, in the mass diffusion regime, the net cell impedance reflects the behavior of the working electrode alone, allowing the reliable use of measurements on half-cells to determine the Warburg coefficient.

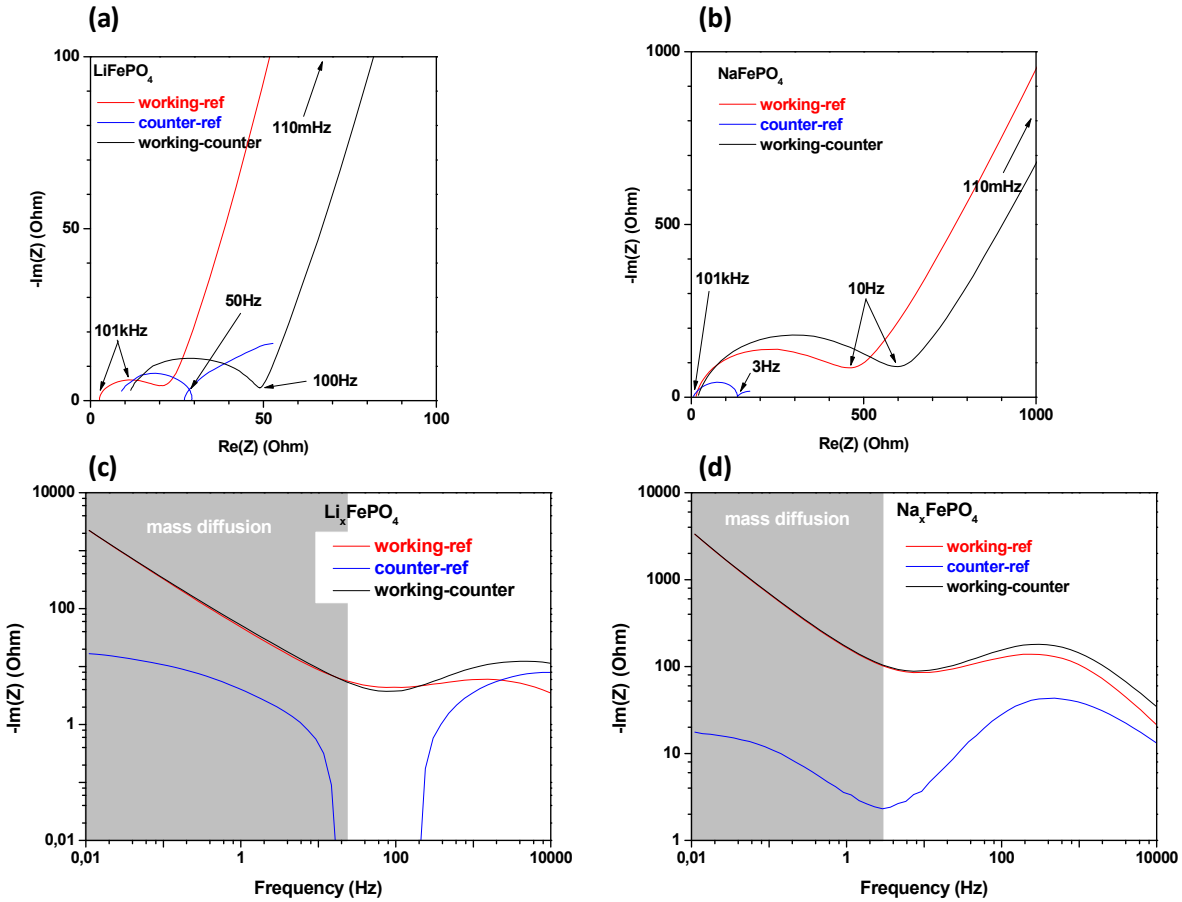

Figure 5-4: (a) and (b) Nyquist plots of the impedance spectroscopy measurements performed on the three-electrode lithium and sodium cells, red = cathode, blue = anode, black = full cell. (c) and (d) Imaginary parts of the impedances of the lithium and sodium cells. In grey, mass diffusion frequency range.

A typical Nyquist plot of the PEIS measurement performed on the half cells after a PITT step is displayed in Figure 5-5 (a). This plot shows the expected behavior with two semi-circles at high frequency corresponding to the surface and charge transfer response of the two electrodes and a slope at high frequency characteristic of mass transport within the insertion electrode. These contributions appear slightly shifted to the right because of the ohmic losses induced by the electrical contacts and of the ionic diffusivity within the electrolyte.

The sum of the ohmic losses induced by the electrical contacts and the electrolyte resistance to ionic transport can be estimated by the abscissa of the beginning of the high frequency semi-circle on the Nyquist impedance spectra. This resistance is 10 mΩ.g for the lithium cell while it is 30 mΩ.g for the sodium cell. The lower resistance for the lithium cell suggests higher conductivity of $LiPF_6$ within the electrolyte than $NaPF_6$ which is consistent with previous reports.[3,4]

According to equation 2-56, when SILD conditions are reached the contributions of mass transport to the real and imaginary parts of the impedance are expected to behave as $\frac{A_W}{\sqrt{2\omega}}$ and $-\frac{A_W}{\sqrt{2\omega}}$, respectively, leading theoretically to a constant slope at 45° in the Nyquist plot. However, in practice the real part is cumulative, while the imaginary part is expected to go to zero between the charge transfer semicircle and the mass diffusion part. In consequence, the imaginary part tends to show a better asymptotic Warburg behavior at lower frequencies than the real part. Moreover, the frequency range dominated by charge transfer and mass diffusion often overlap, and the Warburg regime does not always extend very far toward low frequency, especially when the particles are small or when their size distribution is broad. As a consequence, the asymptotic Warburg behavior is hardly seen in the real part, forbidding the clear observation of the typical 45° in the Nyquist plot. When this is the case, the more reliable option is to analyze the frequency dependence of the Imaginary part at low frequency. For these reasons, $Im(\omega)$ will be used in the present study to extract the Warburg coefficient. SILD conditions will be thus theoretically reached when the $-Im(\omega) * \sqrt{\omega}$ plot reaches a minimum. The Warburg coefficient A_w can be directly read from the height of this minimum. Similarly the $\left(\frac{1}{m\sqrt{2}A_w}\right)^2$ value can be graphically determined from the local maximum of the $\left(\frac{1}{m\sqrt{2}*Im(\omega)*\sqrt{\omega}}\right)^2$ plot as shown in Figure 5-5 (b) which is based on the data of the PEIS measurement displayed in Figure 5-5 (a). The characteristic frequency at which the SILD conditions are fulfilled can be determined from the position of this maximum which has been highlighted by a grey background in Figure 5-5 (a) and (b). Impedance spectra performed on Li_xFePO_4 and Na_xFePO_4 are displayed in Figure 5-5 (c) and (e) respectively, for particular potentials indicated on the voltage titration curve in Figure 5-5 (g) and (h). If two semi-circles are easily identified on the Nyquist plots of Na_xFePO_4 (Figure 5-5-d), they seem to overlap each other for Li_xFePO_4 (Figure 5-5-c).

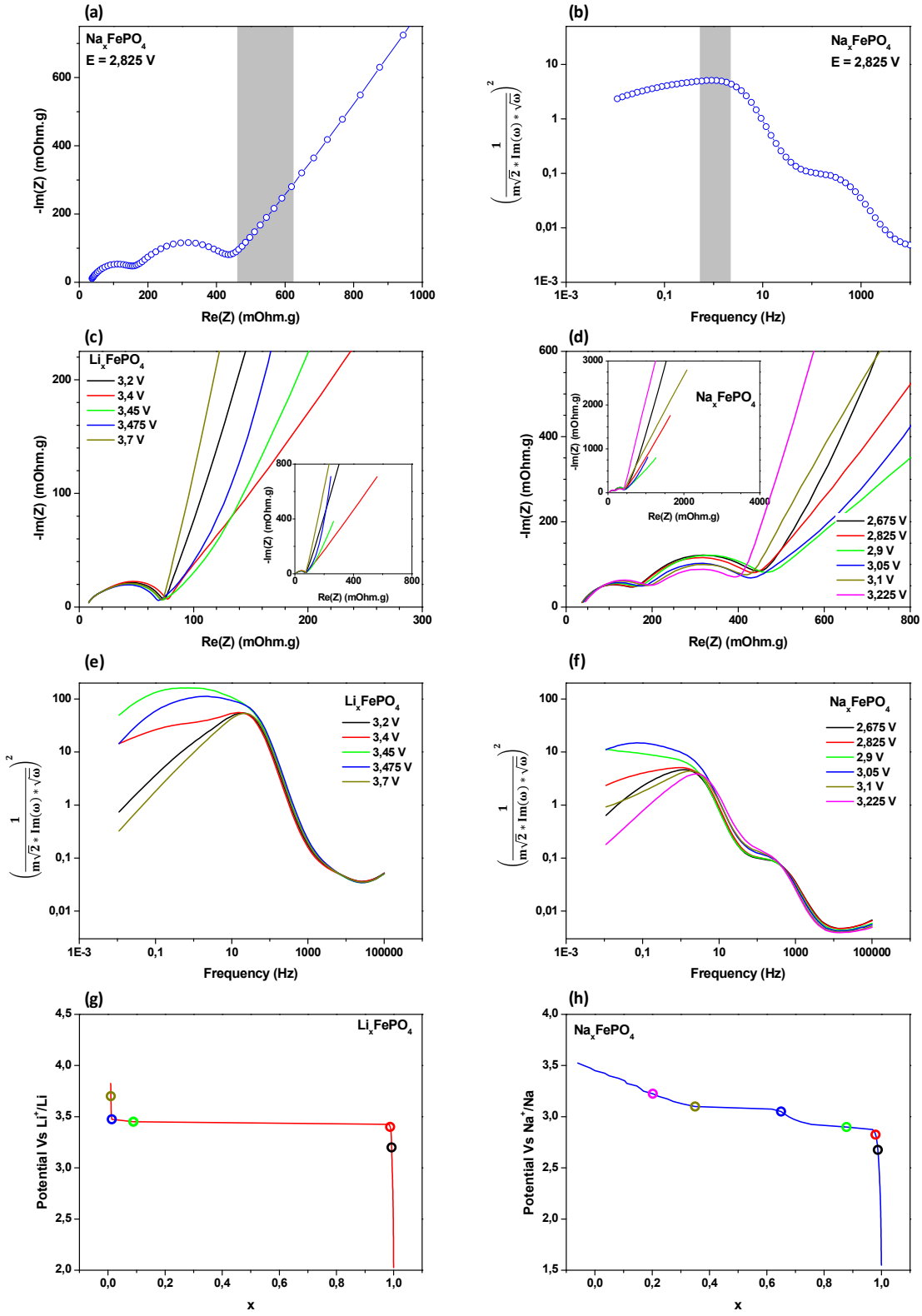

Figure 5-5:(a) Nyquist plot of the impedance spectroscopy measurement performed on the sodium cell at 2.825V. (b) $-Im(f)*\sqrt{f}$ vs f curve of the same cell at the same potential. The grayish zone represents the frequency interval for which the SILD conditions are fulfilled. (c) and (d) Nyquist plots of the impedance of the lithium and sodium cells at several potential. (e) and (f) $\left(\frac{1}{m\sqrt{2}A_w}\right)^2$ evolutions with the frequency for the same potential steps. (g) and (h) Representation of the potentials of previous plots on the titration curves of both cells.

The values of $\left(\frac{1}{m\sqrt{2}*Im(\omega)*\sqrt{\omega}}\right)^2$ deduced from the impedance spectra displayed in Figure 5-5 (c) and (d) are presented as function of ω in Figure 5-5 (d) and (f). Clear maxima can be observed on each of these plots allowing precise determination of the corresponding value of $\left(\frac{1}{m\sqrt{2}A_w}\right)^2$ which are gathered in Figure 5-6 upon charge and discharge of the lithium and sodium cells. They present relatively constant values with a slight increase of less than one order of magnitude at the reaction potentials (3.4-3.5V for Li and 2.7-3.1V for Na), when notches were observed at the same potentials in the evolution of $\left(\frac{\Delta E}{\Delta x}\right)^2$ (Figure 5-2). The values for the Li cell are slightly higher, suggesting better diffusion of Li compared to Na.

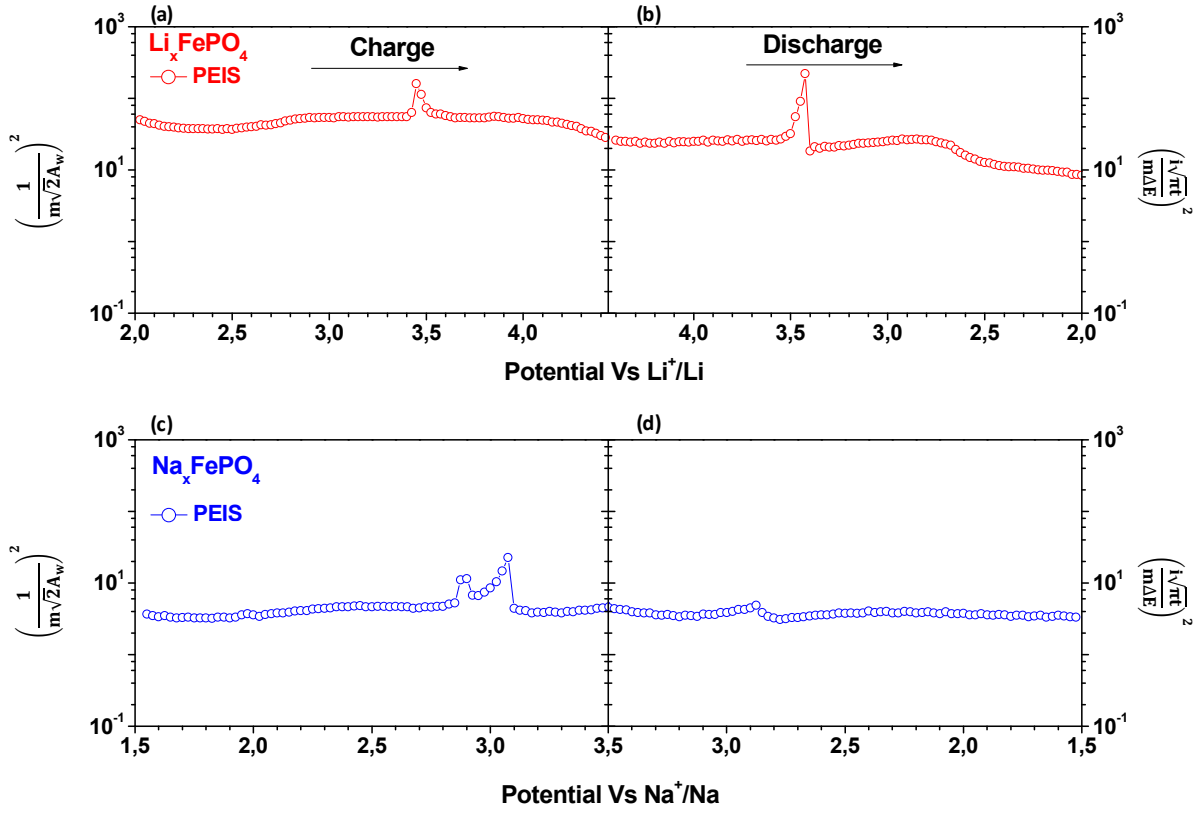

Figure 5-6: $\left(\frac{1}{m\sqrt{2}A_w}\right)^2$ values determined from PEIS for the lithium cell in (a) charge and (b) discharge and for the sodium cell upon (c) charge and (d) discharge.

The characteristic time τ_{SILD}^{PEIS} at which the semi-infinite linear diffusion conditions are fulfilled can be approximated as $\tau_{SILD}^{PEIS} = 1/f_{SILD}$ where f_{SILD} is the excitation frequency at which $\left(\frac{1}{m\sqrt{2}*Im(\omega)*\sqrt{\omega}}\right)^2$ reaches a maximum. τ_{SILD}^{PEIS} is plotted in Figure 5-7 as function of the equilibrium potential of the material. For both Li_xFePO_4 and Na_xFePO_4 this characteristic time is relatively steady for potentials lower or higher than that of the reaction potentials and found about one order of magnitude higher for Na compared to Li, suggesting faster Li diffusion. Peaks of characteristic time τ_{SILD}^{PEIS} of up to two orders of magnitude are also observed at the reaction potentials, which will be discussed later in this chapter.

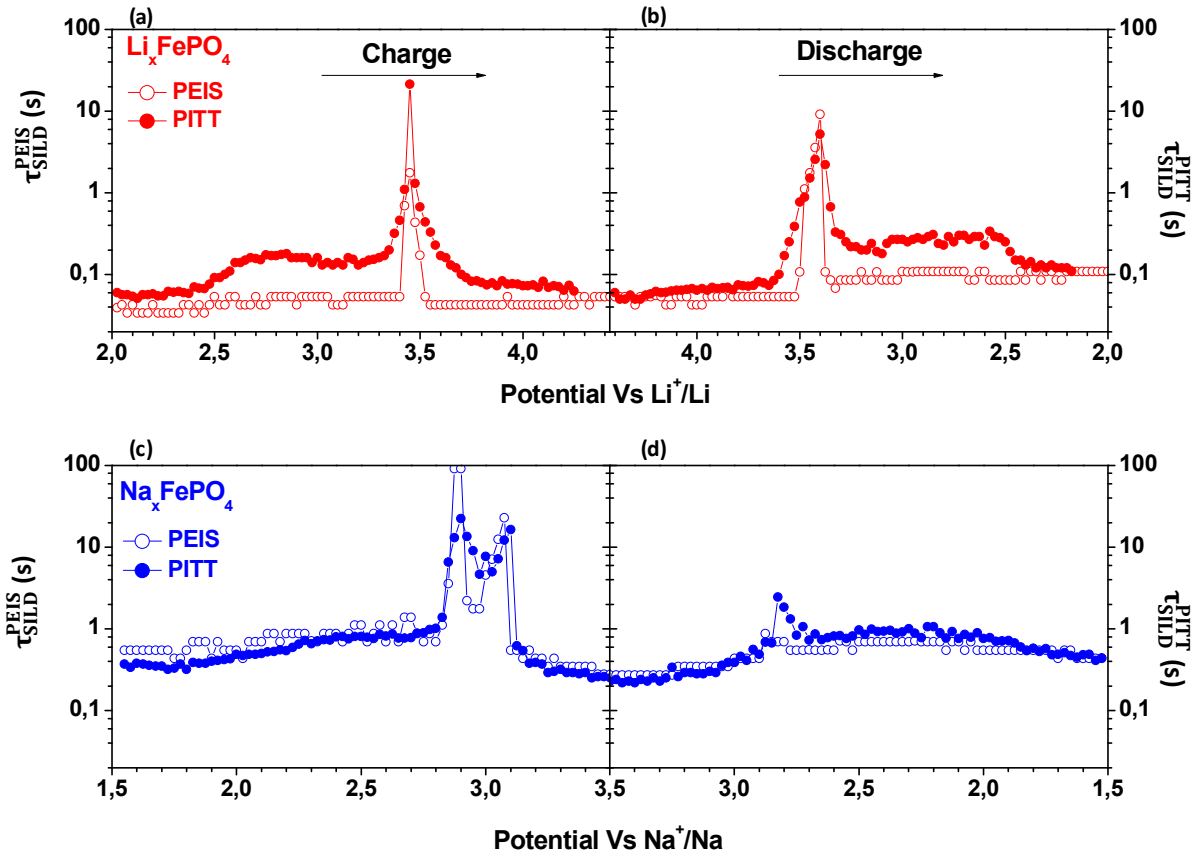

Figure 5-7: Characteristic time for SILD conditions determined from PEIS and PITT for the lithium cell in (a) charge and (b) discharge and for the sodium cell upon (c) charge and (d) discharge.

5.3.3.2. PITT

As mentioned at the beginning of this chapter, the dynamic factor can also be determined from the current relaxation during the PITT titration steps.

As the current is supposed to follow a Cottrellian behavior and relax as the square root of the time when SILD conditions are fulfilled, the product $i\sqrt{t}$ shall be constant in the time range during which these conditions are fulfilled.[25] A graphical method to determine the $\left(\frac{i\sqrt{\pi t}}{m\Delta E}\right)^2$ value and the characteristic time at which the SILD conditions are fulfilled τ_{SILD}^{PITT} has been described by Levi et al.[34] and Meethong et al.[24] This method consists in plotting $|i|\sqrt{t}$ as function of the time. The maximum of this curve indicates τ_{SILD}^{PITT}. In the present study the whole dynamic factor $\left(\frac{i\sqrt{\pi t}}{m\Delta E}\right)^2$ was plotted instead of $|i|\sqrt{t}$ as a function of time for convenience. Since the denominator of $\left(\frac{i\sqrt{\pi t}}{m\Delta E}\right)^2$ is a constant independent of time, it should not interfere in the determination of the time range for which the Cottrellian (SILD) conditions are fulfilled. An example of the graphical determination of the $\left(\frac{i\sqrt{\pi t}}{m\Delta E}\right)^2$ value following this method is shown in Figure 5-8 (b) from the current of the 2.825V potential step

of the sodium cell displayed in Figure 5-8 (a). The SILD conditions are fulfilled on the flat local maximum of the curve, enlightened by the grey zone, from which the $\left(\frac{i\sqrt{\pi t}}{m\Delta E}\right)^2$ value and the time range at which the SILD conditions are fulfilled are determined. The model Cottrellian current calculated from the constant $\left(\frac{i\sqrt{\pi t}}{m\Delta E}\right)^2$ value at the top of the peak is plotted in Figure 5-8 (a) alongside the experimental current. As seen from this plot the Cottrellian model current fits the experimental current of the cell in a narrow time range around 1s, where the SILD conditions are fulfilled, while the experimental current is lower than the model Cottrellian current out this time range. At very short response times the experimental current has a fixed initial value while the Cottrellian model current tends to an infinite value. At this stage it is in fact limited by the short time transport phenomena which are neglected in the Cottrellian diffusion model. These phenomena (sum of the electrical contact resistances in addition to the diffusion into the electrolyte, and electrode/electrolyte interfaces and charge transfer processes on both electrodes) can be modeled by a single resistance R^0_{PITT}. This resistance can be estimated by the ratio of the potential step value over the initial current value. It has to be noted that the value of the experimental current in the mass diffusion regime is not negligible compared to its value when it is controlled by these short time transport phenomena. This point will be discussed further. On the other side, for larger response times, the current decay is faster than predicted by the Cottrellian model. This behavior was observed on several insertion materials including $LiFePO_4$, $Li_{1-\delta}CoO_2$ and $Li_{1-\delta}Mn_2O_4$ and was typically ascribed to transition of mass diffusion from semi-infinite diffusion conditions, where the current decays as the inverse of the square root of the time, toward finite space diffusion (FSD) conditions where the current is expected to decay exponentially with the time.[5,35,36]

Interestingly a second maximum of $\left(\frac{i\sqrt{\pi t}}{m\Delta E}\right)^2$ is also observed for higher response times in the voltage region corresponding to the biphasic transformation regimes (near 3.45 V for $LiFePO_4$ and 3.05 V for $NafePO_4$). Although in Figure 5-8 (e) and (f) these peaks could be interpreted as a second SILD regime, they are notably broader than the maximum observed for lower times. The SILD regime corresponds to mass diffusion due to the concentration gradient induced by the voltage step where the current is expected to decrease as it is the case at the time the first maximum of $\left(\frac{i\sqrt{\pi t}}{\Delta E}\right)^2$ is observed. However, when the second maximum is observed at larger time in Figure 5-8 (e) and (f), the current as seen in Figure 5-8 (c) and (d) is clearly increasing, indicating that the process here is different from a relaxation through mass diffusion since, in all cases (SILD as well as FSD), the current is expected to decay with time. This increase of current related to the second $\left(\frac{i\sqrt{\pi t}}{\Delta E}\right)^2$ maximum was also observed upon PITT on $Li_5W_2O_7$[37], $LiNbO_3$[38], $LiMn_2O_4$[39] or $LiFePO_4$[40] at potentials corresponding to their biphasic transformation reactions and attributed to a transition in the biphasic transformation mechanism, from nucleation and growth of the new phase when the current reaches its minimum value due to the kinetic limitations related to this process, to transformation through interface movement when the current reaches a maximum when there are no more kinetic limitations related to the nucleation and growth mechanism. The current of the cell under a potential excitation in the biphasic state of the electrode is therefore controlled by diffusion under SILD conditions for short response times, and for larger response times by the rate of nucleation and growth of the new phase followed by interface movement.

As a consequence, in the case two $\left(\frac{i\sqrt{\pi t}}{\Delta E}\right)^2$ maxima were observed the one with shorter response time was selected for the calculation of the diffusion coefficient. Interestingly the second maximum, in the case of $NaFePO_4$, is only observed for the second voltage plateau upon charge. This is an indication that although the first plateau is very flat it probably does not correspond to a biphasic transformation, in accordance with previous reports concerning the mechanism in $NaFePO_4$.[33,41]

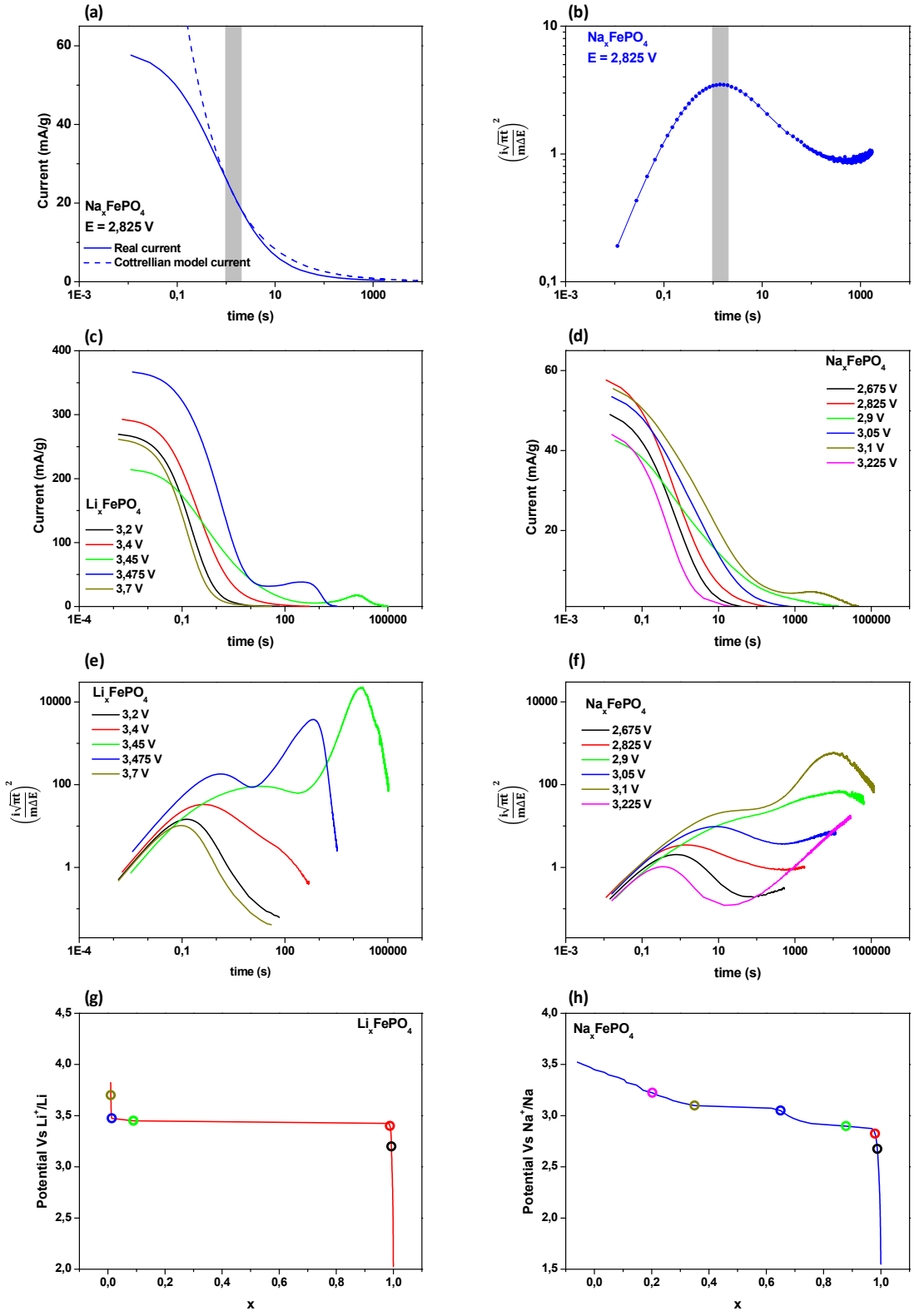

Figure 5-8: (a) Current and Cottrelian model current upon the 2.826V potential step on the sodium cell. (b) $\left(\frac{i\sqrt{\pi t}}{m\Delta E}\right)^2$ upon the 2.826V potential step on the sodium cell. The grayish zone represents the time interval for which the SILD conditions are fulfilled. (c) and (d) Evolution of the current of the lithium and sodium cells upon several potential steps. (e) and (f) $\left(\frac{i\sqrt{\pi t}}{m\Delta E}\right)^2$ evolutions for the same potential steps. (g) and (h) Representation of the potentials of previous plots on the titration curves of both cells.

The time τ_{SILD}^{PITT} at which the SILD type response is observed is reported in Figure 5-7 alongside that of PEIS, τ_{SILD}^{PEIS}. The same tendency is observed for PITT and PEIS, with shorter times for the Li cell. This indicates faster kinetics of mass diffusion for Li compared to Na. While these two values are in good accordance for the sodium cell, τ_{SILD}^{PITT} is found slightly higher than τ_{SILD}^{PEIS} for the lithium cell suggesting that one of the techniques has more difficulty to track properly the SILD mass diffusion in the case of Li.

The average R_{PITT}^{0} values of the lithium and sodium cells are found as 177 and 523 mΩ.g respectively, suggesting that the short time transport phenomena (diffusion into the electrolyte, electrode/electrolyte interfaces and charge transfer processes on both electrodes) are also faster in the case of lithium compared to sodium. However, it is worth noting that these values are negligible compared to the impedance value obtained at the lowest frequency of 11 mHz (see insets in Figure 5-5 (c) and (d)) indicating that the contribution of these phenomena to the kinetic limitations of the overall cell is negligible compared to Li/Na diffusion within $(Li/Na)_xFePO_4$, as mentioned in part 5.1.of this chapter.

The $\left(\frac{i\sqrt{\pi t}}{m\Delta E}\right)^2$ values determined upon PITT in charge and discharge of Li_xFePO_4/C and Na_xFePO_4/C from the graphical determination method described above are plotted in Figure 5-9, alongside with the $\left(\frac{1}{m\sqrt{2}A_w}\right)^2$ values deduced from PEIS. The former shows a very similar behaviour to the later, being relatively constant with a slight increase of about one order of magnitude at the reaction voltages. For both Li and Na, the dynamic term evolution is found significantly noisier and about one order of magnitude lower for EIS compared to PITT, except at the reaction potentials where they are in good accordance. Comparing these two techniques with a similar methodology as within the present study on thin graphite electrodes, Aurbach et al. also found value differences up to one order of magnitude between the two techniques.[34] At first sight the steadier variations of the PEIS term suggest that the diffusion coefficient values determined from this technique should be more precise that those determined from the PITT.

The dynamic term has been determined, from EIS, using the imaginary part of the impedance when SILD conditions are respected. As discussed before, in the mass diffusion regime the contribution of the higher frequency phenomena (charge transfer, surface layer, etc…) to the imaginary part of the impedance is expected to be negligible. In the PITT experiment, however, the current i during the relaxation is function of the sum of the polarizing processes, including of the contact resistances, surface layers and charge transfer. These fast phenomena, which can be gathered into the initial resistive term R_{PITT}^{0}, determine the initial current at the beginning of the PITT step:

$$R_{PITT}^{0} = \frac{\Delta E}{i(t=0)}$$

Contrary to the imaginary part of an EIS measurement, the contribution of these fast phenomena to the total cell resistance R_{tot} during the PITT current relaxation is still present at larger times and sums up with the contribution of the mass transport, R_{mt}, reducing the measured value of the total current i in the mass diffusion regime:

$$R_{tot} = R_{PITT}^{0} + R_{mt}$$

$$i_{tot} = \frac{\Delta E}{R_{tot}}$$

A corrected current $i_{mt} = \Delta E / R_{mt}$ in the mass transport regime can thus be determined as

$$i_{mt} = i_{tot} \frac{1}{1 - \frac{i_{tot}}{i(t=0)}} \quad (5\text{-}5)$$

A similar correction has been proposed by Montella et al.[42] and applied with success to Li diffusion in Si by Li et al.[43] New values of the dynamic factor $\left(\frac{i\sqrt{\pi t}}{m\Delta E}\right)^2$, determined by replacing the experimental current i_{tot} with i_{mt} are represented in Figure 5-9. These values are in much better accordance with the dynamic factor $\left(\frac{1}{m\sqrt{2}A_w}\right)^2$ deduced from PEIS although remaining significantly noisier.

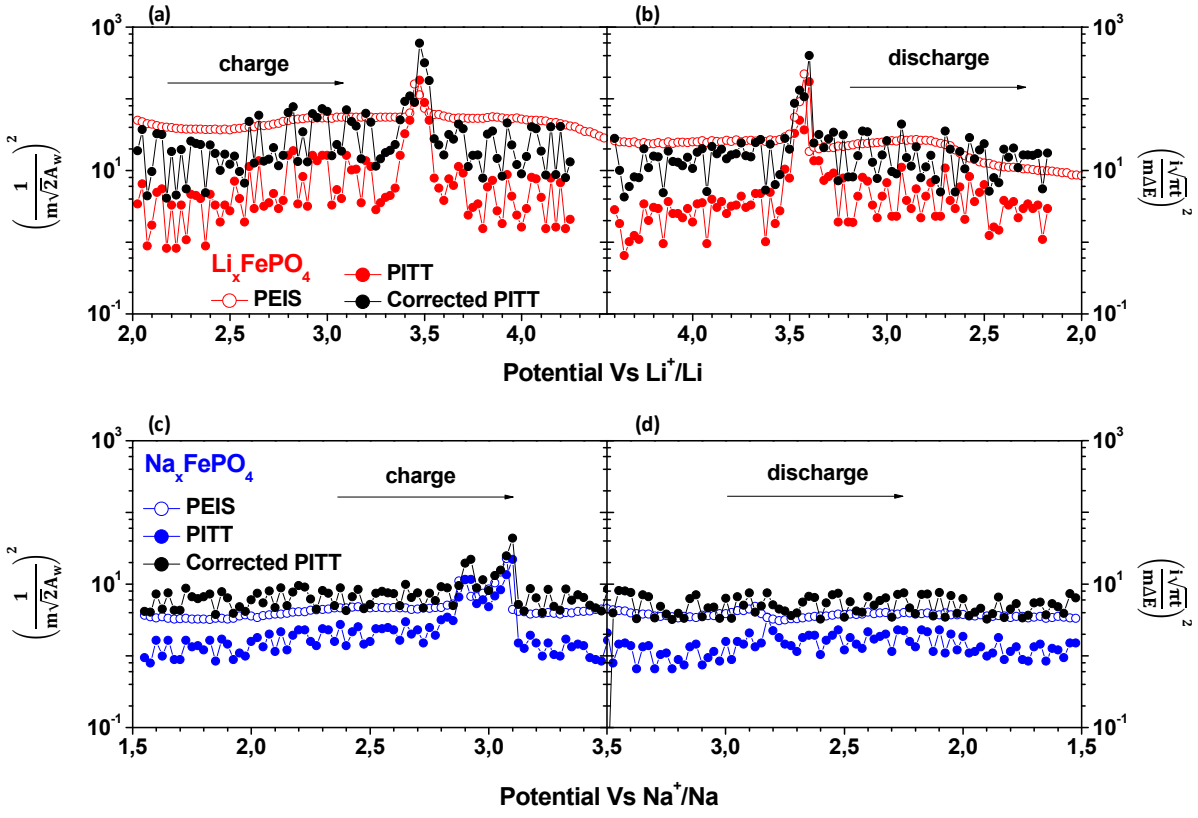

Figure 5-9: Comparison of $\left(\frac{1}{m\sqrt{2}A_w}\right)^2$ and $\left(\frac{i\sqrt{\pi t}}{m\Delta E}\right)^2$ with and without R^0_{PITT} correction for the lithium cell in (a) charge and (b) discharge and for the sodium cell in (c) charge and (d) discharge.

5.3.4. Diffusion coefficient

The diffusion coefficient values of Li and Na obtained upon charge and discharge from EIS according to eq. (5-1) and (5-3), are displayed in Figure 5-10 as function of the potentials of the working electrodes, together with the value of the dynamic term of the PITT corrected according to equation (5-5). A very good agreement can be observed between the results of the two techniques, the only difference being that the values determined from EIS show more fluctuations than these determined from PITT.

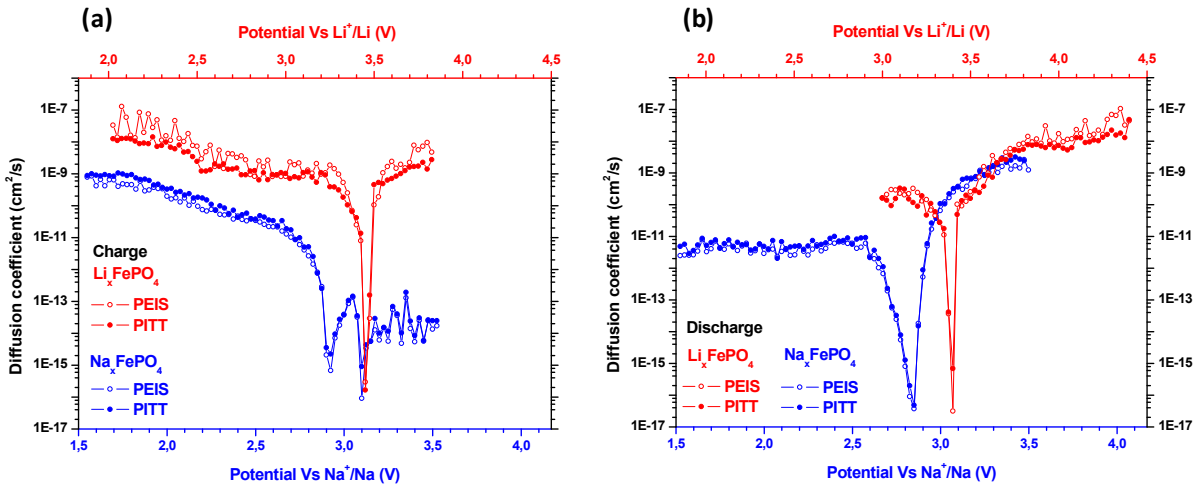

Figure 5-10: Comparison of the diffusion coefficients of Li (red) and Na (blue) inside Li/Na_xFePO_4, determined from PEIS and PITT upon (a) charge and (b) discharge, as function of the potential of the working electrode.

The comparison between the $\left(\frac{i\sqrt{\pi t}}{m\Delta E}\right)^2$ and the $\left(\frac{1}{m\sqrt{2}A_w}\right)^2$ values showed that the latter have much steadier variations which suggested at first sight that a more precise diffusion coefficient value might be obtained from the PEIS. It is interesting however to note that the $\left(\frac{\Delta E}{\Delta x}\right)^2$ variations appear to compensate that of the $\left(\frac{i\sqrt{\pi t}}{m\Delta E}\right)^2$ factor, which makes the PITT diffusion coefficient curves much smoother than those obtained from PEIS.

The opposite variations of the thermodynamic and dynamic factors could be predictable. Indeed, as seen in chapter 2, the amplitude of the current of the cell under a potential excitation is proportional to the concentration fluctuation at the surface of the active insertion material induced by the potential excitation, which is itself inversely proportional to the slope of the voltage-composition profile of the insertion material. Therefore, as seen in chapter 2, when the transport equations have been established (equations 2-31 and 2-53), the net response of the mass diffusion to an electrical excitation will be a combination of the dependency on the slope of the voltage-composition titration curve (hence the thermodynamic factor) and the dependency on the diffusion impedance (hence the dynamic factor) and, in order to depict accurately the ionic diffusivity of the insertion material at electrode scale, the dynamic factor has to be balanced with the thermodynamic factor.

Since the thermodynamic factor $\left(\frac{\Delta E}{\Delta x}\right)^2$ is estimated from the length of the titration steps, Δx, which is determined from the integration of the current during each potential step, and since the $\left(\frac{i\sqrt{\pi t}}{m\Delta E}\right)^2$ dynamic factor depends on this same current, it can be expected that the fluctuations of one of them will be reported on the other so they compensate each other. On the other side the dynamic factor $\left(\frac{1}{m\sqrt{2}A_w}\right)^2$ of the PEIS is determined from a distinct measurement performed at the end of each PITT step. It is therefore not surprising that the fluctuations of one measurement are not correlated with the fluctuations on the other, and thus do not vanish.

As expected from the evolutions of both thermodynamic and dynamic factors, the evolution of the diffusion coefficient of Li presents a notch of five orders of magnitude centered at the reaction potential (3.45 V). At lower voltages, the diffusion coefficient slowly decreases at the beginning of charge while the potential of the electrode increases from 2 to 3.3 V. At higher voltages, when the bi-phasic transformation is complete, another sloppy region is observed with values close to that observed below 3.3 V. Upon discharge the diffusion coefficient value follows a symmetrical behavior, decreasing slowly as the potential decreases before a notch of about five orders of magnitude at the potential corresponding to the bi-phasic transformation, near 3.45 V, after which a flat diffusion coefficient region is observed between 3.3 V and 3 V.

The Na diffusion coefficient within Na_xFePO_4 also slowly decreases at the beginning of charge while the potential increases. After this sloppy region two notches of about three orders of magnitude are observed at the reaction potentials 2.85 and 3.1 V, with a local maximum at 3.05V. The Na diffusion coefficient at the end of charge does not recover a value close to that of the beginning of charge as in the case of Li, but remains about four orders of magnitude lower instead. Upon discharge the Na diffusion coefficient slowly decreases before a notch of about eight orders of magnitude is observed in its evolution at the reaction potential corresponding to the 3-phase reaction (around 2.8 V), followed by a region with rather flat diffusion coefficient values below 2.6 V.

In the case of Na, the notch at 2.85V upon charge is caused by the first potential plateau identified as solid-solution by Galceran et al.[33] In the case of solid solution the dynamic term is expected to follow the evolution of the thermodynamic term leading to constant or slightly changing values of D. Here the thermodynamic term drops by several orders of magnitude, in a similar fashion as observed in the case of a biphasic reaction but the dynamic term increases only slightly by less than one order of magnitude. As pointed out in the previous chapter, Galceran et al.[33] also observed a discontinuity in the (*b*) parameter of Na_xFePO_4 at $x \approx 0.8$ upon charge which, in addition to the theoretical predictions of Saracibar et al.[44], suggests that a phase transformation mechanism more complex than solid solution occurs at this composition possibly involving an intermediate phase $Na_{5/6}FePO_4$. In this case, during the titration steps performed around 2.85V, the current is not only limited by the Na diffusion in the electrode but also by the rate of the phase transformation mechanism above mentioned, in which case the equations (5-1), (5-2) and (5-3) are possibly out of their application range. Therefore, the notch in the diffusion coefficient profile of Na upon charge near 2.85 V is probably not real and reflects the occurrence of a phase transition rather than the actual value of the diffusion coefficient.

The reliable values of the diffusion coefficients of Li and Na should therefore be determined far enough from the reaction potentials at which phase transitions occur, and where the system is

expected to behave as a pure solid solution. In the case of Li, it corresponds to potentials far below or far above 3.45V upon charge, and 3.4V upon discharge. For Na, it corresponds to potentials far below 2.8V and close to 3.05V upon charge, and far below 2.7V upon discharge. Indeed, as discussed earlier in this chapter, the biphasic transformation is incomplete upon charge for Na, either due to a side reaction or a limitation of the reaction for kinetic reasons or a combination of the two, forbidding reaching the solid solution regime at the end of charge and leading to meaningless values of D_{Na} at this stage.

Below the reaction potentials, i.e. in the (Na,Li)$FePO_4$ phase, the diffusion coefficient is found ranging from $1e^{-10}$ to $1e^{-8}$ cm^2/s for Li and from $5e^{-12}$ to $1e^{-9}$ cm^2/s for Na. The Na diffusion coefficient at 3.05V, for $x \approx 2/3$ is determined as $1.4e^{-13}$ cm^2/s, between 1.5 and 4 orders of magnitude lower than at $x \approx 1$. Above the reaction potential, i.e. in the $FePO_4$ phase, only the diffusion coefficient of Li can be determined and is found ranging from $1e^{-10}$ to $1e^{-8}$ cm^2/s. The diffusion coefficient variations below or above the reaction potentials suggest that the diffusivities of Li and Na within Li/Na_xFePO_4 are affected by the composition of the material; the diffusion coefficient increasing when the composition gets closer to that of the end members i.e. x = 0 or 1.

In order to be easily compared, the Li and Na diffusion coefficients obtained at the beginning of charge and end of discharge are plotted as function of the alkali metal concentration in log scale in Figure 5-11. Upon charge the Li and Na diffusion coefficients decrease steadily by almost two orders of magnitude while their concentration decrease before they suddenly drop when approaching the reaction potential. Before this drop upon charge, the Li diffusion coefficient is found approximately 10 times higher than that of Na. Upon discharge the Li and Na diffusion coefficients are found nearly constant at low potential and the Li diffusion coefficient is found 20 times higher than that of Na.

This Li/Na diffusion coefficient ratio suggests a lower diffusivity of Na compared to Li for concentrations close to x = 1. This ratio is 3 orders of magnitude larger than the 11.4% variations of the morphology prefactors, $\left(\frac{V_M}{FSSA}\right)^2$, between $FePO_4$ and $NaFePO_4$ estimated in section 5.3.1 of this chapter confirming that the error made by considering a constant value is negligible.

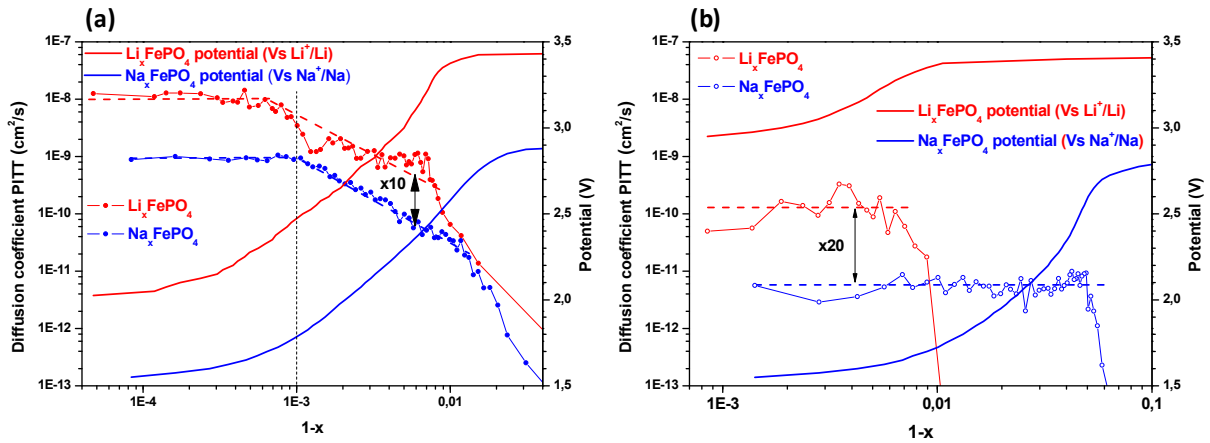

Figure 5-11: Comparison of the diffusion coefficients of Li (red) and Na (blue) inside Li/Na_xFePO_4, determined from PITT upon (a) charge and (b) discharge, as function of the Li/Na concentration. On these graphs, the red and blue lines represent the Li_xFePO_4 and Na_xFePO_4 equilibrium potentials respectively.

5.4. Comparison with literature

The diffusion coefficient values of Li in Li_xFePO_4 obtained in the present study are compared in Figure 5-12 with those published by other authors as function of the composition (Figure 5-12 a, b, d, e) or the potential of the insertion material (Figure 5-12 (c)). The diffusion coefficient values of Na in Na_xFePO_4 obtained in the present study are also compared in Figure 5-12 (d) and (e) with the results of recent studies comparing Li_xFePO_4 and Na_xFePO_4.

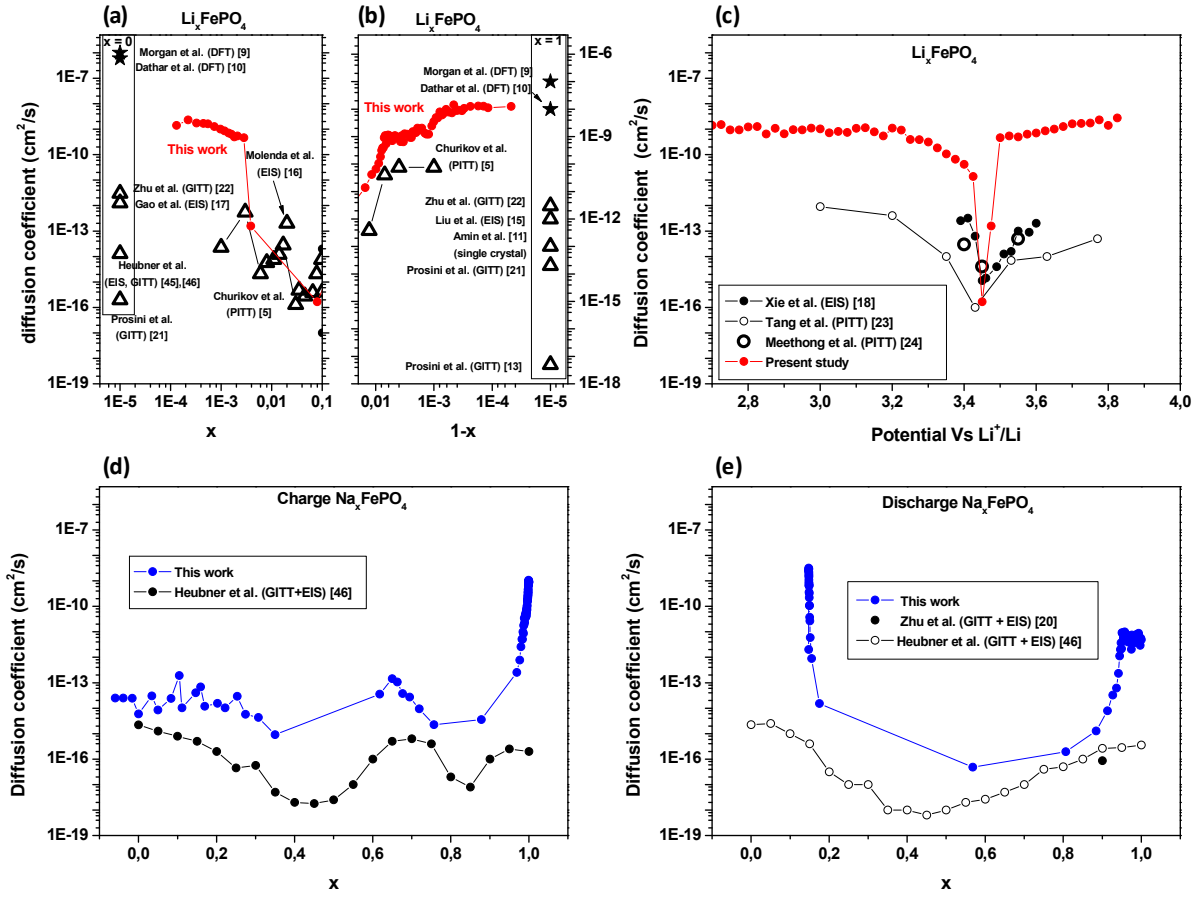

Figure 5-12: Graphical comparison of the previously reported diffusion coefficients of Li and Na and those determined in this study. The compositions at the end of charge and discharge were shifted in order to superimpose the solid-solution state compositions.

It can be clearly seen from Figure 5-12 (a, b and c) how the PITT measurement of the present study concentrates the measurement points in two very narrow composition ranges close to x = 0 and x = 1. This is due to the small constant potential step that has been used, and to the fact that the measurement has been performed in a voltage window that extends far from the reaction potentials. On the contrary, reported measurements based on constant GITT steps tend to spread better the data at the intermediate compositions, but at the cost of very few points near the end members, as seen from Figure 5-1 (a, b, d and e). As discussed earlier in this chapter, it is near the end members x = 0 and x = 1 that the D values are reliable, where the system is expected to behave as a solid solution, while at intermediate compositions the values are biased by the phase transformation reactions which induce drops of several orders of magnitude of the value of the apparent diffusion coefficient for both Li and Na at the reaction potentials. Since most reported diffusion coefficient

values have been measured at intermediate compositions while extracted using the classical single-phase SILD theory based on Fick's laws, the values reported are extremely dependent on the composition in alkali metal. This explains probably why there is a so large dispersion of reported values at apparently similar compositions.

The diffusion coefficient values experimentally determined by other authors close to x = 1 and x = 0, reported on Figure 5-12 (a), (b) and (c), are found between two and five orders of magnitude lower than that determined in the present study at the same composition or voltage. This could be explained by the fact that the composition or potential steps between the measurements performed by these authors are much larger than within the present study; and that, in the case of potential controlled techniques, the potential ranges under study are relatively narrow compared to that of the present study. As explained in the introduction part of this chapter, the monophasic composition range (solubility limit) near the end members is very narrow, and as seen from Figure 5-2 a slight deviation of composition can pull the material out of its solubility limit, i.e. trigger phase transformation, which can lead to an underestimation of the slope dE/dx of the equilibrium potential-composition profile, which will lead to an underestimation of the thermodynamic factor, and as a consequence of the diffusion coefficient, by several orders of magnitude. This may occur prior to the measurement, such as when the potential is too close to the reaction potential, as well as induced by the measurement such as in the case of too large titration steps compared to the solubility limits. This is further confirmed by the fact that our results close to x = 1 and x = 0 for $LiFePO_4$ are very close to the values predicted by Morgan et al. from computational studies.

Heubner et al. studied the diffusivities of Li and Na in Li/Na_xFePO_4 through EIS and GITT. They determined first the diffusion coefficient of Li and Na in $FePO_4$ through impedance spectroscopy measurements, where they found a Na diffusion coefficient of $2.2e^{-15}$ cm^2/s, i.e. 6 times lower than that of Li;[45] and later the diffusion coefficient of Na within the whole concentration range of Na_xFePO_4 through GITT.[46] The evolution of the diffusion coefficient of Na within Na_xFePO_4 as function of x in the present study is similar to that determined by Heubner et al. through GITT, with values within the same order of magnitude reached for the intermediate composition range. Furthermore, at x = 0.9, these values also have the same order of magnitude than those determined by Zhu et al. from EIS and GITT[20]. However, at the beginning of charge and beginning and end of discharge the diffusion coefficient profile determined in the present study increases by several orders of magnitude while approaching the end members compositions. On the contrary, the values determined by Heubner et al. are nearly constant while approaching the end members, leading to values 5 to 7 orders of magnitude lower than those of the present study. Since these authors used the GITT technique to estimate the slope of the equilibrium potential profile of Li/Na_xFePO_4 with a rather large concentration step, it is likely that they performed too large titration steps, and therefore underestimatedthe slope of the equilibrium potential-concentration profile of the material, lowering artificially their diffusion coefficient values near the end members.

5.5. Conclusions

The diffusion coefficients of Li and Na in Li_xFePO_4 and Na_xFePO_4 were determined from PITT and the combination of PITT and PEIS in the whole composition range of the insertion electrodes with a very good accordance between the two methods.

The Li diffusion coefficient in Li_xFePO_4 was found ranging from $1e^{-10}$ to $1e^{-8}$ cm^2/s near x = 0 and x = 1. The Na diffusion coefficient in Na_xFePO_4 could only be determined for compositions close to x = 1 and x = 2/3, and was found ranging from $5e^{-12}$ to $1e^{-19}$ cm^2/s in the former case and equal to $1.4e^{-13}$ cm^2/s in the latter case, indicating better diffusivity of Na in $NaFePO_4$ than in $Na_{2/3}FePO_4$.

At x = 1, the Na diffusion coefficient in Na_xFePO_4 was found between 10 and 20 times lower than that of Li in Li_xFePO_4. This suggests a significantly lower ionic conductivity in the case of Na at the discharged state. This could explain the poorer rate performance of Na_xFePO_4 compared to Li_xFePO_4.

EIS measurement also allowed to get an estimation of the net value of the impedance related to the high frequency processes (electrolyte conductivity, surface layers and charge transfer resistance) in the whole half cell (Li/Na counter electrode, electrolyte and $(Na/Li)_xFePO_4$ working electrode). This impedance value has been found four times higher for sodium than for lithium, which suggests that, in addition to the poorer mass diffusion, the charge transfer rate of Na is also slower than that of Li.

At intermediate Na and Li compositions, a rather good agreement was found between the present results and previous reports in the literature. However, close to the end members x =1 and x = 0, a strong discrepancy of the present results was found with most of the previous experimental reports, these later presenting in addition a large dispersion of the determined values.

A thorough analysis of the literature dedicated to the determination methods of the diffusion coefficient of Li in Li_xFePO_4 revealed that the large dispersion of values obtained from electrochemical characterization techniques seems to be caused by large titration steps commonly used when performing GITT or PITT to determine the slope of the equilibrium potential-concentration profile of the insertion material, together with a possibly too narrow voltage window.

All in all, the results of the present chapter confirm what was suggested from the poorer electrochemical performances of $NaFePO_4$ as cathode material compared to $LiFePO_4$: that Na suffers from intrinsic kinetic limitations. This seems to be related to poorer mass diffusion of Na compared to Li.

---

[1] S.-I. Lee, U.-H. Jung, Y.-S. Kim, M.-H. Kim, D.-J. Ahn, H.-S. Chun, Koren J. Chem. Eng., 19(4), 638 (2002)
[2] A. V. W. Cresce, S. Russell, O. A. Borodin, J. L. Allen, M. Schroeder, M. Dai, J. Peng, M. Gobet, S. G. Greenbaum, R. Rogers and K. Xu, Phys. Chem. Chem. Phys., 19, 574 (2017)
[3] M. Dahbi, F. Ghamouss, F. Tran-Van, D. Lemordant, M. Anouti, J. Power Sources, 196, 9743 (2011)
[4] A. Bhide, J. Hofmann, A. K. Dürr, J. Janek, P. Adelhem, Phys. Chem. Chemm. Phys., 16, 1987 (2014)
[5] A. V. Churikov, A. V. Ivanishchev, I. A. Ivanishcheva, V. O. Sycheva, N. R. Khasanova, E. V. Antipov, Electrochim. Acta, 55, 2939-2950 (2010)
[6] A. J. Bard, L. R. Faulkner, Electrochemical methods Fundamentals and applications, chapter 3: kinetics of electrode reactions, pp87-136, Second edition, John Wiley & sons, inc (2001)
[7] W.-J. Zhang, J. Power Sources, 196, 2962 (2011)
[8] R. Malik, A. Abdellahi, G. Ceder, J. Electrochem. Soc., 160 (5), A3179 (2013)

[9] D. Morgan, A. Van der Ven, G. Ceder, Electrochem. Soild State Lett., 7 (2), A30 (2004)
[10] G. K. P. Dathar, D. Sheppard, K. J. Stevenson, G. Henkelman, Chem. Mater., 23, 4032 (2011)
[11] R. Amin, P. Balaya, J. Maier,Electrochem. Solid State Lett., 10, A13 (2007)
[12] C. Wang, J. Hong, Electrochem.Solid State Lett., 10, 3, A65 (2007)
[13] P.P. Prosini, M. Lisi, D. Zane, M. Pasqualini, Solid State Ionics 148 45 (2002)
[14] S. Franger, F. L. Cras, C. Bourbon, H. Rouault, Elec. Solid State Lett., 5, A231 (2002)
[15] H. Liu, C. Li, H.P. Zhang, L.J. Fu, Y.P. Wu, J. Power Sources, 159, 717 (2006)
[16] J. Molenda, W. Ojczyk, K. Swierczek, W. Zajac, F. Krok, J. Dygas, R.-S. Liu, Solid State Ionics, 177, 2617 (2006)
[17] F. Gao, Z. Tang, Electrochim. Acta, 53, 5071 (2008)
[18] J. Xie, N. Imanishi, T. Zhang, A. Hrano, Y. Takeda, O. Yamamoto, Electrochimica Acta, 54 4631 (2009)
[19] C. K. Park, S. B. Park, H. C. Shin, W. I. Cho, H. Jang, Bull. Korean Chem. Soc., 32 (1), 191 (2011)
[20] Y. Zhu, C. Wang, Nanoscale, 5, 780 (2013)
[21] P. P. Prosini, M. Lisi, S. Scaccia, M. Carewska, F. Cardellini, and M. Pasquali, J. Electrochem. Soc., 149, A297 (2002)
[22] Y. Zhu, C. Wang, J. Phys. Chem. C, 114, 2830 (2010)
[23] X.-C. Tang, L.-X. Li, Q.-L. Lai, X.-W. Song, L.-H. Jiang, Electrochimica Acta, 54, 2329 (2009)
[24] N. Meethong, Y.-H. Kao, W. C. Carter, Y.-M. Chiang, Chem. Mater., 22, 1088 (2010)
[25] C. J. Wen, B. A. Boukamp, R. A. Huggins, W. Weppner, J. Electrochem. Soc., 126, 12, 2258 (1979)
[26] C. Ho, I. D. Raistrick, R. A. Huggins, J. Electrochem. Soc., 127, 343-350 (1980)
[27] W. Weppner, R. A. Huggins, J. Electrochem. Soc., 124, 10, 1569 (1977)
[28] C. Delmas, M. Maccario, L. Croguennec, F. Le Cras, F. Weil, Nat. Mater., 7, 665 (2008)
[29] A. K. Padhi, K. S. Nanjundaswamy, J. B. Goodenough, J. Electrochem. Soc., 144(4), 1188 (1997)
[30] V. Srinivasan, J. Newman, J. Electrochem. Soc., 151(10), A1517 (2004)
[31] P. Moreau, D. Guyomard, J. Gaubicher, F. Boucher, Chem. Mater., 22, 4126 (2010)
[32] M. Casas-Cabanas, V. V. Roddatis, D. Saurel, P. Kubiak, J. Carretero-Gonzalez, V. Palomares, P. Serras, T. Rojo, J. Mater. Chem., 22, 17421 (2012)
[33] M. Galceran, D. Saurel, B. Acebedo, V. Roddatis, E. Martin, T. Rojo, M. Casas-Cababas, Phys. Chem. Chem. Phys., 16 (19), 8837 (2014)
[34] M. D.Levi, D. Aurbach, J. Phys. Chem. B, 101, 4641-4647 (1997)
[35] H.-C. Shin, S.-I. Pyun, Electrochem. Acta, 44, 2235-2244 (1999)
[36] S.-I. Pyun, S.-W. Kim, J. Power Sources, 97-98, 371-376 (2001)
[37] V. Pralong, G. Venkatesh, S. Malo, V. Caignaert, R. Baies, B. Raveau, Inorg. Chem.,53 (1), 522 (2014)
[38] V. Pralong, M. AnjiReddy, V. Caignaert, S. Malo, O. I. Lebedev, U. V. Varadaraju, B. Raveau, Chem. Mater., 23, 1915 (2011)
[39] M. D. Levi, K. Gamolsky, D. Aurbach, U. Heider, F. Oesten, J. Electrochemical Soc., 147(1), 25-33 (2000)
[40] G. Oyama, Y. Yamada, R.-I. Natsui, S.-I. Nishimura, A. Yamada, J. Phys. Chem. C, 116, 7306 (2012)
[41] J. Gaubicher, F. Boucher, P. Moreau, M. Cuisinier, P. Soudan, E. Elkaim, D. Guyomard, Electrochem. Commun., 38, 104 (2014)
[42] C. Montella, J. Electroanal. Chem., 518, 61 (2002)
[43] J. Li, X. Xiao, F. Yang, M. W. Verbrugge, Y.-T. Cheng, J. Phys. Chem. C, 116, 1472 (2012)
[44] A. Saracibar, J. Carrasco, D. Saurel, M. Galceran, B. Acebedo, H. Anne, M. Lepoitevin, T. Rjo, M. Casas-Cabanas, Phys. Chem. Chem. Phys., 18(18), 13045-51 (2016)
[45] C. Heubner, S. Heiden, B. Matthey, M. Schneider, A. Michaelis, Electrochim. Acta, 216, 412-419 (2016)
[46] C. Heubner, S. Heiden, M. Schneider, A. Michaelis, Electrochim. Acta, 233, 78-84 (2017)

6. Activation energy for diffusion

6.1. Introduction

In the previous chapter the diffusion coefficients of Li and Na in Li/Na_xFePO_4 have been determined from electrochemical techniques. However, the results have been limited by several requisites (SILD conditions fulfillment, solid solution state, absence of parasitic side reactions) to a limited composition range near x = 1 and x = 2/3 for Na and near x = 0 and x = 1 for Li. Moreover, extracting information at material's level from electrochemical methods applied to a cell implies a precise knowledge and control of the morphology of the electrode, which is reflected in the morphological factor of the expressions (2.36) and (2-63) of the diffusion coefficient.

In the present study, electrodes were taken from the same laminate to compare the diffusion coefficients of Li and Na within $(Li,Na)_xFePO_4$, thus with same electrode architecture, particle morphology and size distribution. In addition, the very good performance of the $LiFePO_4$ electrodes reported in chapter 3 confirmed their optimum preparation, and thus their optimum architecture. This is of prime importance as the diffusivity of a mobile specie at electrode scale can be strongly influenced by the morphology of the particles, their electrical connection, particularly in the case of anisotropic diffusion,[1] and the porosity of the electrode. Despite the protocol used, there can still be differences between Na and Li that may affect the effective morphology. Indeed, it is known that the lithium diffusion is two-dimensional due to facilitated Li jumps between the one-dimensional diffusion channels thanks to the Li-Fe antisites, but no insight is known so far about the influence of these defects on the dimensionality of Na diffusivity, which may change the effective diffusion geometry as well,[1,2] and thus the correlation between morphology and effective diffusion at particle level. Moreover, given the large volumetric expansion in the case of insertion-extraction of Na in Na_xFePO_4 compared to Li in Li_xFePO_4, one cannot exclude the possibility for Na insertion-extraction to

induce morphological changes of the material that may affect its response at electrode level by affecting, for instance, the electrical connectivity of the material within the electrode.

In this context, the activation energy of the ionic mass diffusion is an interesting parameter to access as it represents the energy necessary for a single jump of the alkali metal between two neighboring interstitial sites within the crystalline structure of the insertion material. It gives an insight of the diffusion at molecular scale, with fewer assumptions made about the morphology of the particles and the architecture of the electrode to estimate its value compared to the diffusion coefficient determination from PITT or PEIS. It is also less dependent on the phase transformation mechanism. It can therefore corroborate and complement the diffusion coefficient results of the previous chapter.

As explained in chapter 2, the activation energy for diffusion of a mobile specie within an insertion material, E_a, is defined from the Arrhenius dependence of its diffusion coefficient with the temperature:

$$D = D_0 e^{-\frac{E_a}{k_B T}} \quad (2\text{-}73)$$

with k_B as the Boltzmann constant, T as the temperature of the system and D_0 a prefactor dependent on the entropy of the hoping mechanism, the distance between the two interstitial sites and the vibration frequency of the inserted specie. E_a and D_0 can be determined experimentally from the dependence of the diffusion coefficient with the temperature at a given constant composition.

As mentioned in the general introduction chapter, at the beginning of this thesis, several groups had determined the activation energies of electronic, ionic or polaronic diffusion within $(Li/Na)_xFePO_4$ from computational or experimental techniques at various compositions of the material. In particular, two of them had determined and compared the activation energies for Li and Na diffusion in $(Li/Na)FePO_4$ from computational methods. Ong et al. found activation energies values of 280 and 350 meV for Li and Na, respectively.[3] This suggests a better diffusivity of Li, in accordance with the diffusion coefficient results obtained by Zhu et al.[4] and those of the present study presented in the previous chapter. However, it is in contradiction with the results of Fisher and Tripathi et al. who determined a larger activation energy value of 550 meV for Li ionic diffusion compared to the 320 meV for Na.[5,2] This discrepancy might be ascribed to the fact that distinct computational methods have been used in these various studies: CGA for Ong et al., semi-empirical pseudo potential method for Fisher and Tripathi et al. Indeed, the results of computational simulations are strongly dependent on the computational method, the nature of the particle under study (ion, polaron)[3,6] and if the dependence of the Li and Na diffusivities to the presence of defects and impurities are taken into account.[1]

There is thus an urgent need for an estimation of the activation energy for diffusion of Na in Na_xFePO_4 in the whole composition range of this material upon charge as well as discharge, in order to gain more insights about the kinetic limitations to Na insertion/extraction.

6.2. Methodology

Experimental determination of the activation energy for ionic or electronic diffusion in Li_xFePO_4 has been reported by several authors on pellets made from polycrystalline powder sample pressed and then sintered at high temperature (≈ 800 - 900°C)[7,8] as well as on single crystals.[9] To date, this type of experiment is not possible to perform on $NaFePO_4$ because of the impossibility to directly synthesize the phase due to irreversible structural changes occurring above 450°C.[10] $NaFePO_4$ has to be prepared from $LiFePO_4$ by ion exchange, either chemically or electrochemically. In both cases, the presence of carbon coating was found necessary for complete removal of Li and insertion of Na. However, if a pellet is made from carbon coated material, the conductivity measurement will reveal the conductivity of the carbon coating, rather than that of the active material which conductivity is short-circuited by that of the conducting carbon.[8]

The determination of the activation energy requires, as discussed above, repetitive mass diffusion measurements at a same given composition but various temperatures. The technique used for the determination of the diffusion coefficient has thus to be carefully chosen for not affecting the composition of the insertion material. In this context, electrochemical impedance spectroscopy (EIS) which consists in small excitations around an equilibrium composition is particularly interesting since, as shown in the previous chapter, it allows precise determination of the diffusion coefficient of Li/Na in semi-infinite linear diffusion (SILD) conditions in the insertion electrode; and consecutive EIS measurements can be performed at different temperatures and a given state of charge without changing the composition of the insertion material during the measurement. On the contrary, PITT or GITT measurements induce a change of the composition during the measurement of the mass diffusion and are thus not suitable.

As explained in chapter 2, in the frequency range where the main limiting factor for movement of mobile species is the mass diffusion within the insertion material, and assuming it occurs in SILD conditions, the impedance of the electrode asymptotically tends toward the Warburg impedance:

$$Z(\omega) = \frac{A_W}{\sqrt{2\omega}} - j\frac{A_W}{\sqrt{2\omega}} \tag{2-56}$$

With A_W as the Warburg coefficient which can be written as:[11]

$$A_W = \frac{V_M}{zFS\sqrt{D}}\left(\frac{dE}{dx}\right) \tag{2-58}$$

V_M being the molar volume of the insertion material, z the number of charges carried by each charge carrier, F the Faraday constant, S as the total surface from which the mobile specie flows within the insertion material, ω the excitation frequency, D the diffusion coefficient of the mobile specie and $\left(\frac{dE}{dx}\right)$ the slope of the equilibrium potential-composition profile of the insertion material.

In the expression of the Warburg coefficient presented in eq. 2-58, only the $\left(\frac{dE}{dx}\right)$ factor and the diffusion coefficient itself shall depend on the temperature of the system. Neglecting the variations

of $\left(\frac{dE}{dx}\right)$ the Arrhenius dependence of the diffusion coefficient with the temperature can be extended to the Warburg coefficient and, combining equations (2-73) and (2-57) written in the form:

$$ln(A_W) = \frac{2E_a}{k_B T} - B \tag{6-1}$$

with B as a parameter independent from the temperature accounting for the contributions of the morphology of the electrode and the thermodynamic properties of the insertion material. The value of the activation energy can thus be determined from a linear regression of $ln(A_W)$ as a function of $\frac{1}{T}$.

Several factors limit the temperature range over which the diffusion coefficient measurements can be performed. EC/DMC based organic electrolytes have poor stability for temperatures higher than 60°C.[12,13] Also, it was shown that the low Li^+ diffusivity in EC/DMC below -20°C affects the electrochemical performances of Li-ion batteries at these temperatures.[14] We thus decided to cautionary limit the temperature range to 20-40°C (294-312 K). However, the accuracy of this method depends on the number of measurements performed in this temperature window and the precision of the temperature control. Reducing the temperature range requires reducing the size of the temperature step, which asked for improved precision of the temperature control.

The Swagelock cell components are massive compared to the electrode mass, which let envisaging a slow response to outer temperature changes, with impossibility to know with certitude the temperature of the electrode material. Moreover, the large size of Swagelok type cells imposes the use of a large temperature chamber which does not offer the desired precision of temperature control and only allow poor gas-solid thermal coupling with no direct control of the temperature in the core of the cell. In the other hand, coin cell bodies are much smaller, thinner and lighter. They can fit the sample space in the PPMS instrument, as shown in the inset of Figure 6-1, taking advantage of its precise temperature control, with a good solid-solid thermal contact coupling. Moreover, due to their light construction, coin cells react faster to temperature changes and the cell active materials (electrodes and electrolytes) are in direct contact with the thin steel receptacle. In order to ensure a precise tracking of the material's temperature, a temperature sensor was tied directly to the cathode side of the coin cell to control the temperature of the cathode with precision, allowing a temperature control with an accuracy of +/- 0.02K after only five minutes of temperature stabilization as seen from Figure 6-1.

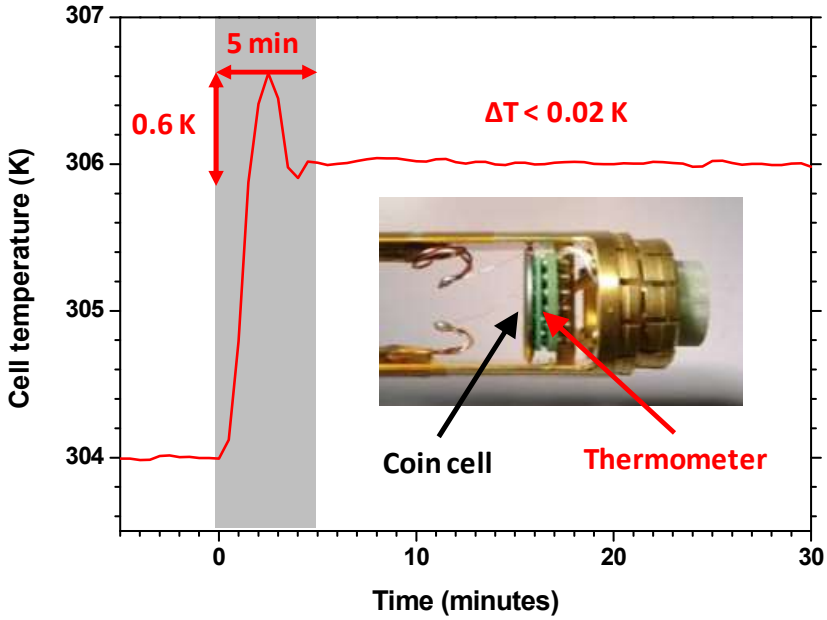

Figure 6-1 : Temperature control of a coin cell within the PPMS during a 2K step.

A series of impedance spectroscopy measurements were performed at several states of charge, while scanning the temperature of both a lithium and sodium cells from 312 to 294K with 2K steps. Experimental determination of the activation energy of a transport process within a battery containing an organic $LiPF_6$ or $LiClO_4$ type electrolyte was already performed by several authors within a large temperature range ($\Delta T \approx$ 30-65°C), with measurements performed approximately every 6-15 °C.[21,15,16,17,18,19] The temperature ranges and number of diffusion coefficient measurements performed in the temperature windows within these studies are reported in Table 6-1. The use of the PPMS, thanks to its precise temperature control, allowed quadrupling the number of measurements per °C, which had never been reported so far. With this density of diffusion coefficient measurements per °C, the experiments are ensured to be performed within the temperature stability window of the electrolytes.

reference	Temperature range (°C)	Number of measurements	ΔT^o between measurement
Jow et al.[15] (2012)	-40-25	5	13
Liao et al.[16](2012)	-40 - 20	7	9
Nobili et al.[17] (2013)	0 - 30	5	6
Heins et al.[18] (2016)	-15 - 35	6	8
Heubner et al.[21](2016)	10 - 40	4	7
Mertens et al.[19] (2016)	10 - 50	4	10
This work	**20 - 40**	**10**	**2**

Table 6-1 : Measurement conditions of activation energies for transport mechanism within electrodes containing organic $LiPF_6$/$LiClO_4$ type electrolyte.

6.3. Results

The activation energy for diffusion was determined for several alkali metal compositions of $(Li/Na)_xFePO_4$ upon charge and discharge. Galvanostatic charges or discharges of the lithium and sodium half cells were performed in order to obtain the desired composition of the working electrode. At the end of each galvanostatic charge or discharge steps the cells were left relaxing until they reached their equilibrium potential, e.g. until the potential became stable.

The voltage composition profile of the half-cells upon charge and discharge are displayed in Figure 6-2 (a) and (b). The equilibrium potentials and compositions at which the activation energy measurements were performed are indicated by plain (charge) and open (discharge) circles on these figures.

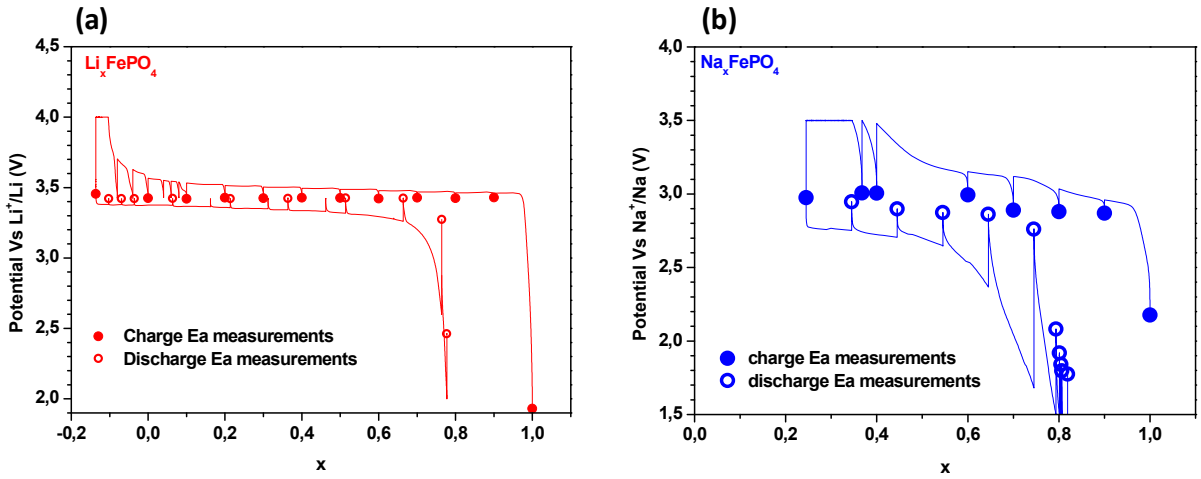

Figure 6-2: Potential-composition plots of the (a) Li_xFePO_4 and (b) Na_xFePO_4 electrodes between activation energy measurements at different compositions. Rounds and circles represent the voltages and compositions at which the activation energy measurements were performed upon charge and discharge respectively.

The theoretical capacity of the lithium cell is exceeded upon charge by approximately 13% and only 91% is obtained upon discharge. Furthermore, the rather low equilibrium voltage of the cell at the beginning of this experiment and its absence of clear increase at the end of the charge process (only a very slight increase is observed) suggest a slight self-discharge of the cell. The activation energy measurements lasted approximately five hours at each state of charge, and since the synchronization between electrochemical control and temperature control were not automatized, measurements were only performed during the day, so at least 24h separates each measurement point. As a consequence, the total charge-discharge of the cell lasted more than one month. Taking this into account, the 20% self-discharge observed over this period can be considered negligible in the time range of the activation energy measurement, although it brings incertitude to the composition of the insertion electrode at intermediate compositions. The fact that the equilibrium potential of the cathode at the end of charge and end of discharge is respectively higher and lower than the reaction potential indicates however that the delithiation and lithiation reactions, respectively, have reached completion.

The low equilibrium potential of the sodium cell (1.8-2.2 *vs* Na^+/Na, i.e. 0.7-1.1 V below the reaction potential) at the end of discharge also indicates complete sodiation of Na_xFePO_4. However only 75 %

of the theoretical capacity of the cell is reached at the end of charge, and the equilibrium potential of the cathode at this stage remains at the same value than that of the second charge potential plateau, indicating non-complete extraction of the sodium from the cathode at the end of charge, similarly to the GITT and PITT measurements presented in chapter 4. Moreover, the capacity of the cell obtained upon discharge is lower than upon charge, similar to what was previously observed upon GITT and PITT. This suggests that a parasitic reaction occurring at the end of charge artificially increases the charge capacity of the cell, which brings incertitude to the composition of the insertion electrode at the end of charge.

The Nyquist plots of the impedance spectroscopy measurements of the lithium and sodium cells performed at compositions of x = 1 and x = 0.4 at various temperatures are displayed in Figure 6-3. These graphs show the expected behavior for this type of half cells with a high frequency semi-circle characteristic for the double layer capacitances and charge transfer resistances at the surface of both the working and counter electrodes and a low frequency slope characteristic for the diffusion of the mobile specie within the insertion electrode.

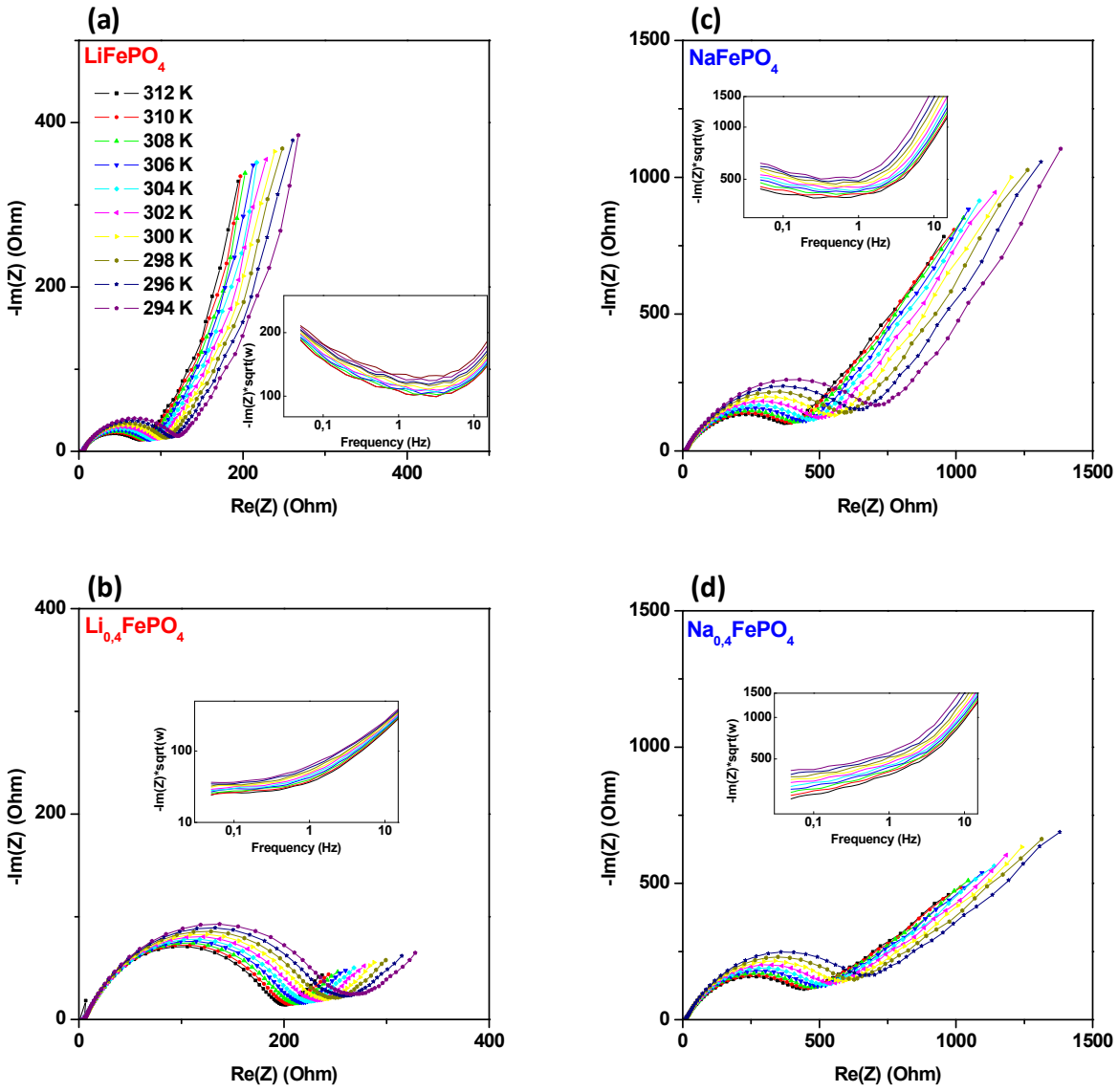

Figure 6-3 : Nyquist plot of the impedance spectroscopy spectra performed at several temperatures on (a) $LiFePO_4$, (b) $Li_{0.4}FePO_4$, (c) $NaFePO_4$, (d) $Na_{0.4}FePO_4$. As insets: plots of $-\boldsymbol{Im(Z)} * \sqrt{\boldsymbol{\omega}}$ vs $\boldsymbol{\omega}$ at these same frequencies.

The Warburg coefficients were extracted from each of these impedance spectra following the graphical method described in chapter 5. This method consists in determining the local minimum of the plot of $-Im(Z) * \sqrt{\omega}$ *vs* ω. These plots are displayed as insets in Figure 6-3 (a), (b), (c) and (d).

As explained in chapter 2 and in the previous chapter, the response of the cell under an excitation in the biphasic state of the electrode is controlled by diffusion under SILD conditions for short response times, and for larger response times by nucleation and growth of the new phase followed by interface movement. The diffusion at short response times is theoretically as well characterized by a Warburg behavior of the impedance of the cell. It was shown in chapter 5 that in these conditions the Warburg behavior is shifted to very low frequencies, sometimes out of the frequency range of the EIS measurement. When no local minimum could be observed on the $-Im(Z) * \sqrt{\omega}$ plot, as on the example displayed in Figure 6-3 (d), the values of $-Im(Z) * \sqrt{\omega}$ where read at the lowest measured frequency.

The average potential of the lithium and sodium cells at x = 1, measured during the EIS measurements during the temperature scanning is plotted in Figure 6-4. As seen from this plot there are no visible variations of the voltage of the cell with the temperature, which confirms that the potential and thus its derivative $\left(\frac{dE}{dx}\right)$, on which the thermodynamic factor of the diffusion coefficient depends (equation 5-1), does not have appreciable dependence on the temperature. This confirms the pertinence of using equation (6-1) to determine the value of the activation energy from the EIS measurements.

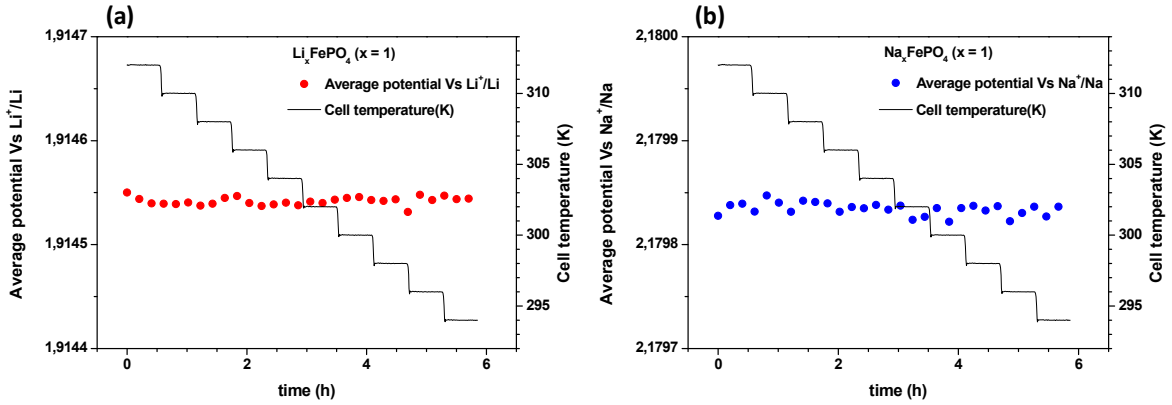

Figure 6-4 : Temperature dependence of the potential of the working electrodes at composition of x = 1.

As explained in the previous chapter, the diffusion coefficient of the charge carriers within the insertion material is determined from the impedance spectroscopy measurement through a dynamic factor that depends on the Warburg coefficient in the form:

$$\left(\frac{1}{m\sqrt{2}A_w}\right)^2 \tag{2-68}$$

with m as the mass of insertion material. These values determined at 300 K upon charge and discharge of the lithium and sodium cells as function of the composition of the insertion electrode and their voltage are displayed in Figure 6-5 (a) and (b) respectively. They are higher for intermediate composition than for compositions close to x = 0 or 1, and the values corresponding to the sodium diffusion in Na_xFePO_4 are about one order of magnitude lower than those corresponding to lithium diffusion within Li_xFePO_4, confirming the observations made in chapter 5 from PITT and EIS measurements.

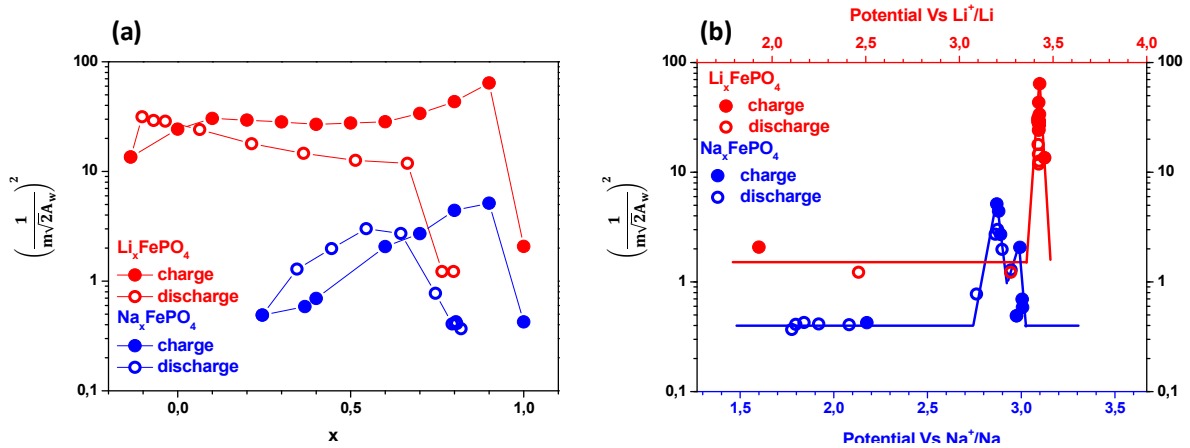

Figure 6-5 : $\left(\frac{1}{m\sqrt{2}A_w}\right)^2$ values upon charge (filled circles) and discharge (open circles) of the lithium and the sodium cells at 300 K as function of (a) the composition of the cathodes and (b) their voltage.

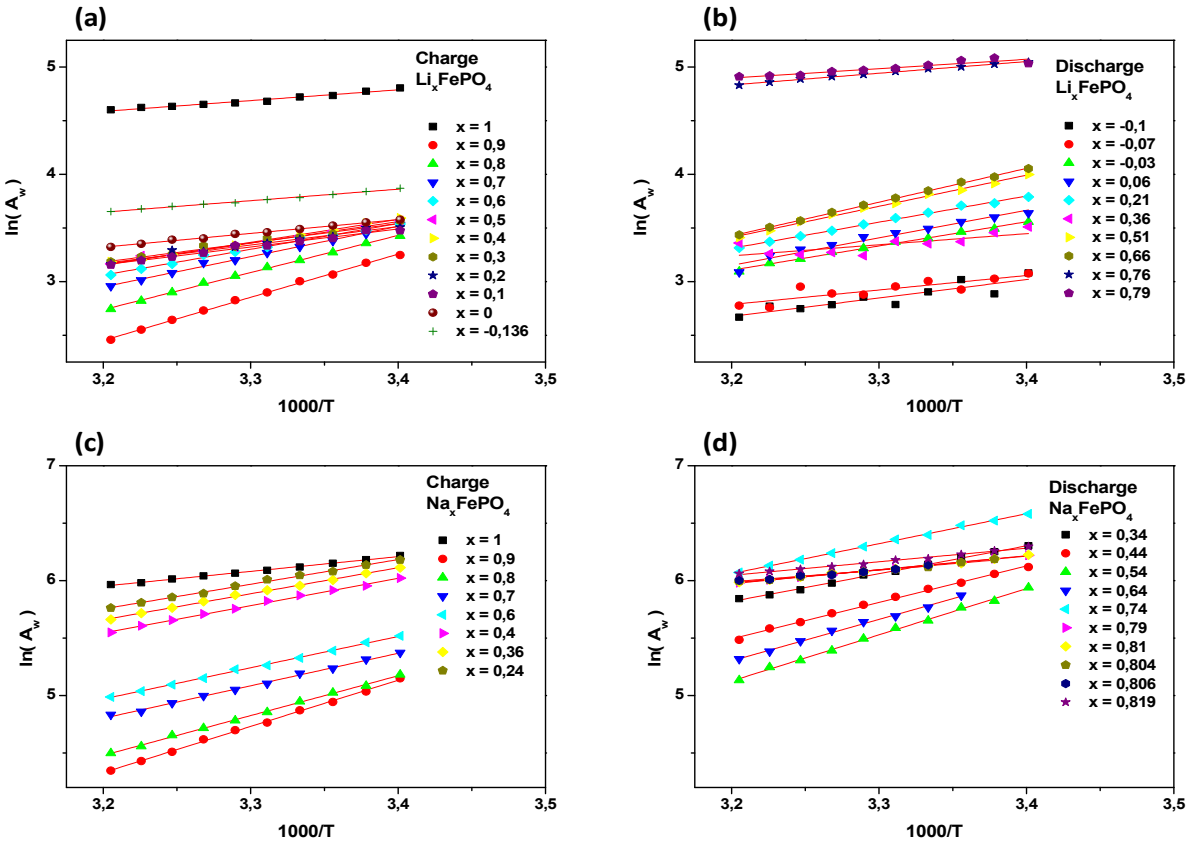

Figure 6-6: Arrhenius plots of $ln(A_w)$ as function of $\frac{1000}{T}$ of Li/Na_xFePO_4 as for each composition upon charge and discharge.

The Arrhenius plots of $ln(A_W)$ as function of $\frac{1000}{T}$ for each composition of the lithium and sodium cells upon charge and discharge are displayed in Figure 6-6. The values of activation energies obtained from these plots are displayed in Figure 6-7 (c) and (d) as function of the Li/Na content and

in Figure 6-7 (e) as function of the equilibrium potential of the electrodes immediately before the EIS measurement. As discussed in the previous chapter, representing the diffusion data as function of the potential of the insertion material instead of its composition allows a better separation of the end members ($x \approx 0$ or 1) from intermediate compositions. On Figure 6-7 (c) and (d), the composition of the electrodes upon discharge has been shifted to the right to compensate the self-discharge of the cell in the case of Li and the parasitic reaction in the case of Na, and in order for the end of discharge to correspond to a composition of $x = 1$.

The activation energy values previously reported by other authors are gathered in Table 6-2 and reported in Figure 6-7 (c) and (d). The activation energies for Li jumping from one tunnel to another through the Fe_{Li} antisite defects are also displayed. Compared to the references gathered in Table 1-5 of the introduction chapter, here are also reported the results of two reports that were published since the beginning of this thesis, about the determination and comparison of the activation energies for diffusion of Li and Na in $(Li/Na)_xFePO_4$ from computational and experimental techniques. From a computational technique and at a composition of $x = 0.25$, Dixit et al. found a Li activation energy ranging from 401 to 452 meV and a Na activation energy ranging from 426 to 470 meV.[20] From EIS applied on three electrode cells, at compositions near $x = 0$, Heubner et al. found activation energies of 410 and 460 meV for Li and Na, respectively,[21] in accordance with the predictions of Dixit et al. However, the composition $x = 0.25$ does not exist as a single phase, but rather as a mixture of $Na_{2/3}FePO_4$ and $FePO_4$, so that it is not clear how far the predictions of Dixit et al. calculated on a hypothetical single phase at $x = 0.25$ can be extrapolated to other compositions.

Activation energies for Li/Na diffusion (eV)								
Computational studies								
authors	**Mobile specie**	**defects**	**direction**	**method**	**x in Li_xFePO_4**		**x in Na_xFePO_4**	
					0	**1**	**0**	**1**
Morgan et al. (2004)[22]	ion	no	(010)	GGA	0.2	0.27	na	na
Ouyang et al. (2004)[23]	ion	no	(010)	GGA	na	0.51	na	na
Fisher et al. (2008)[5]	ion	no	(010)	PM	na	0.55	na	na
Liu et al. (2010)[24]	ion	no	(010)	GGA+U	0.27	0.5	na	na
Malik et al.(2010)[1]	ion	yes	(101)	GGA+U	na	0.49	na	na
Ong et al. (2011)[3]	ion	no	(010)	GGA	0.17	0.28	0.27	0.37
Dathar et al.(2011)[6]	Ion	no yes	(010) (101)	DFT+U	0.19 0.35	0.29 0.71	na na	na na
Hoang et al. (2011)[25]	ion Ion -polaron	no no	(010) (010)	GGA+U	na na	0.32 0.48	na na	na na
Tripathi et al. (2013)[2]	ion	no	(010)	PM	na	na	na	0.32
Xu et al. (2014)[26]	ion	no	(010)	GGA+U	na	0.32	na	na
Dixit et al. (2015)[20]	ion	no	(010)	GGA+U	0.40*	na	0.43*	na
Experimental studies								
authors	**sample**	**technique**	**Fe_{Li} (%)**	**direction**	**x in Li_xFePO_4**		**x in Na_xFePO_4**	
					0	**1**	**0**	**1**
Amin et al. (2008)[9]	Single crystal	IS vs Tº	3%	(100) (010) (001)	na na na	0.96 0.70 0.75	na na na	na na na
Heubner et al. (2016)[21]	electrode	EIS vs Tº	na	na	0.41	na	0.46	na
Present study	electrode	EIS vs Tº	na	na	0.178	0.185	na	0.20

* x = 0.25

Table 6-2 : Activation energies for diffusion of Li and Na migration within Li/Na_xFePO_4. Ion = Li^+/Na^+, polaron = e^-/hole + local distortion, ion-polaron = bound ion-polaron as quasiparticle. DFT = density functional theory. GGA = generalized gradient approximation (type of DFT). GGA+U = GGA with electronic correlation parameter. PM: semi-empirical interatomic potential method.

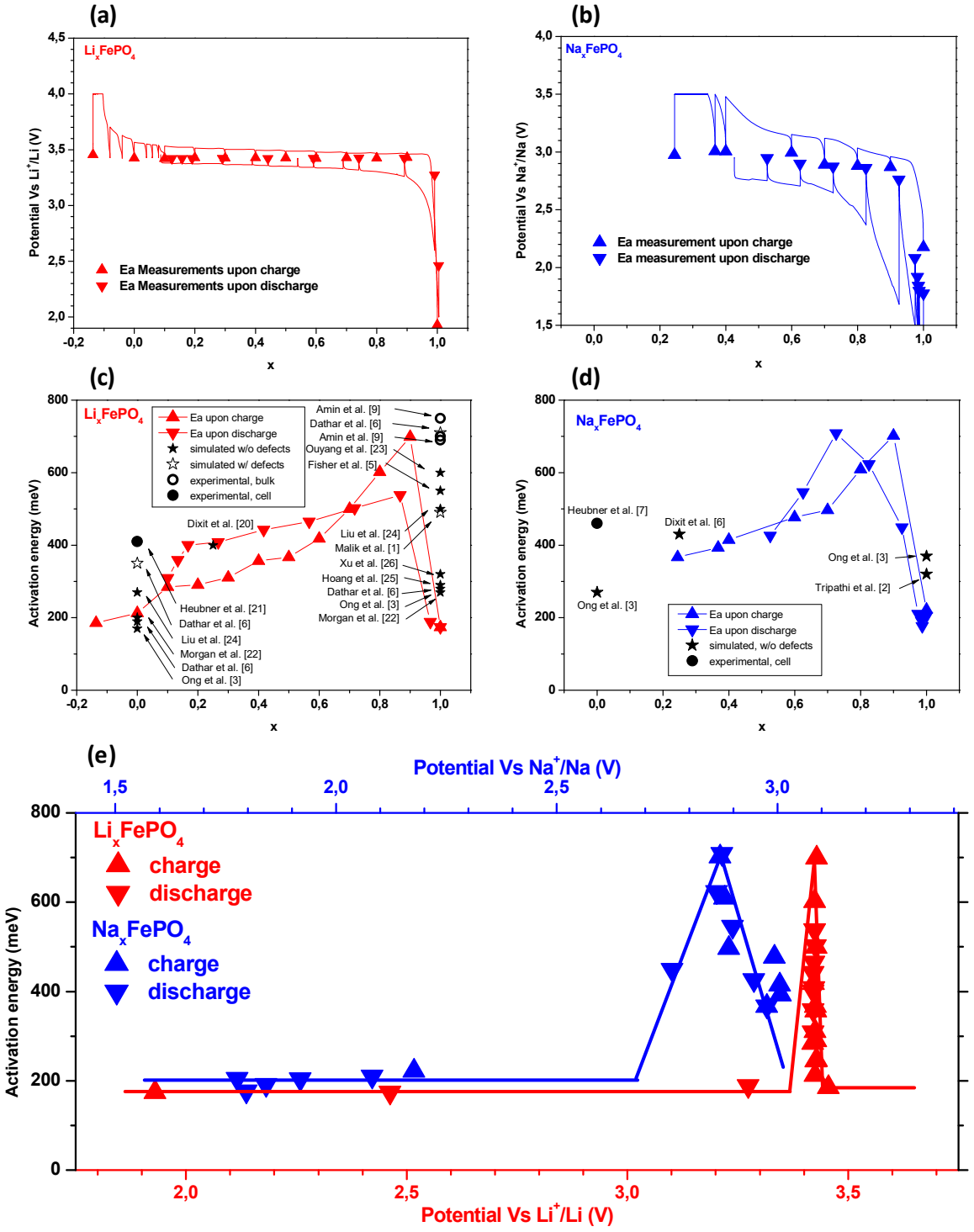

Figure 6-7 : (a) and (b) Potential vs composition plots of the Li_xFePO_4 and Na_xFePO_4 electrodes between activation energy measurements at different electrode compositions. Rounds and circles represent the voltages and compositions at which the activation energy measurements were performed upon charge and discharge respectively. (c) and (d) Values of activation energy for diffusion as function of the overall composition of the electrode, and comparison with activation energies published by other authors. (e) Activation energies for diffusion of Li (red) and Na (blue) inside Li/Na_xFePO_4 as function of the equilibrium potential of the electrodes during measurement. The continuous lines are guides for the eye.

6.4. Discussion

6.4.1. Li_xFePO_4

As seen in Figure 6-7 (c) and (e), an activation energy value of 173 meV is found in the present study for Li at x = 1 upon charge. As soon as some Li is extracted this activation energy increases to 698 meV near x = 0.9 before gradually decreasing upon further Li extraction down to 185 meV at the end of charge. Upon further lithium insertion, the activation energy increases rapidly to 400 meV in the first 10% of the discharge, after which it gradually increases to reach a maximum value of 540 meV near x = 0.9, followed by a fast drop down to 180 meV at the end of discharge. As observed in Figure 6-7 (e), when observed as a function of the equilibrium cell potential, the maximum of activation energy observed near x = 0.9 in Figure 6-7 (c) corresponds to a peak centered at the reaction potential (3.45 V) while the activation energy values remain low in the potential ranges corresponding to the solid-solution state (x close to 1 and 0). Indeed, the activation energy at the beginning of charge and end of discharge (173 and 180 meV, respectively), thus for vacancy diffusion in $LiFePO_4$, is found very close to the value determined at the end of charge (185 meV), thus for Li diffusion in $FePO_4$. This is in accordance with the results of Chapter 5, in which the diffusion coefficients where found very close for $LiFePO_4$ and $FePO_4$.

The activation energy value for diffusion of Li in $FePO_4$ found in the present study (185 meV) is in very good agreement with the values of 0.2, 0.17 and 0.19 eV obtained respectively by Morgan et al., Ong et al. and Dathar et al. from computational calculations.[22,3,6] The experimental value determined by Heubner et al. for Li in $FePO_4$ is however twice as high, at 410 meV.[21] This value is close to what was measured in the present study upon discharge after insertion of about 10% Li, which suggests that Heubner et al. may not have reached a completely delithiated state prior to the measurement of Ea. The activation energy value obtained in the present study at the beginning of charge (175 meV) and end of discharge (185 meV), e.g. for $x_{Li} \approx 1$, is however slightly smaller than those determined theoretically by Morgan et al., Ong et al., Dathar et al., Hoang et al. and Xu et al. who found values in the range 0.27-0.32 eV at x = 1,[22,3,6,25,26] and notably smaller than those determined by Ouyang et al., Fisher et al., and Liu et al., which found values in the range 0.51-0.55 eV at the same composition.[23,5,24] These authors all used DFT derived techniques, except Fisher et al. which used a semi empirical techniques based on interatomic potentials. This later lead to the larger value, which could be ascribed to the fact that this method is known to be less precise than DFT based techniques. For the DFT based techniques, some authors used the "U" factor, which accounts for electronic correlations. According to Ceder et al., this factor when used for determining activation energies, may lead to overestimated Ea values.[3] However, considering or not this factor "U" in the simulation does not seem to influence the Ea value, as Ouyang et al. found a larger value using GGA than Hoang et al. using GGA+U,[23,25] while the smallest values have been found by the group of Ceder using GGA+U.[22,3] The differences are thus probably rooted to other parameters such as the size of the unit cell, the concentration of vacancies that are considered etc… It has to be noted that the above mentioned authors consider their result in relative good agreement, which suggests that the difference is probably within the commonly accepted precision of prediction for these techniques.

It is important to note that while, in all the reports we found mention of, the activation energy is calculated or measured at only one or a few compositions, our measurements in the whole composition range of Li_xFePO_4 reveal a strong dependence of the activation energy to the Li concentration near x = 1 and x = 0. As in the case of the diffusion coefficient values discussed in chapter 5, this could explain the relatively broad distribution of the reported experimental results as a slight error in the composition can induce a strong change in the measured value of activation energy. This is the first time, to our knowledge, that the activation energy dependence on potential and composition is reported.

Interestingly, the activation energy values determined in the present study near x = 0.9 (698 meV) and near x = 0.2 (309 meV) are in good accordance with the ones determined by Dathar et al. for the jumps between the diffusion channels assisted by the presence of Fe_{Li} antisite defects,[6] which they found equal to 710 meV in the Li rich phase and 350 meV in the Li poor phase. This suggests that at the above-mentioned compositions the diffusion is controlled by inter-channel defect-assisted diffusion path, while the lower values found at x = 1 and x = 0 would correspond to unrestricted diffusion in the (010) direction, that is, not affected by the presence of antisite defects.

As discussed in the introduction chapter, in defect-free $LiFePO_4$ the diffusion is expected to be unidimensional in the *b* direction.[27] Experimentally, however, $LiFePO_4$ materials tend to systematically present antisite defects, with Fe occupying Li sites, which block the diffusion channels in the *b* direction and open paths between these channels in the ac plane, see inset of Figure 6-8.[1,6]

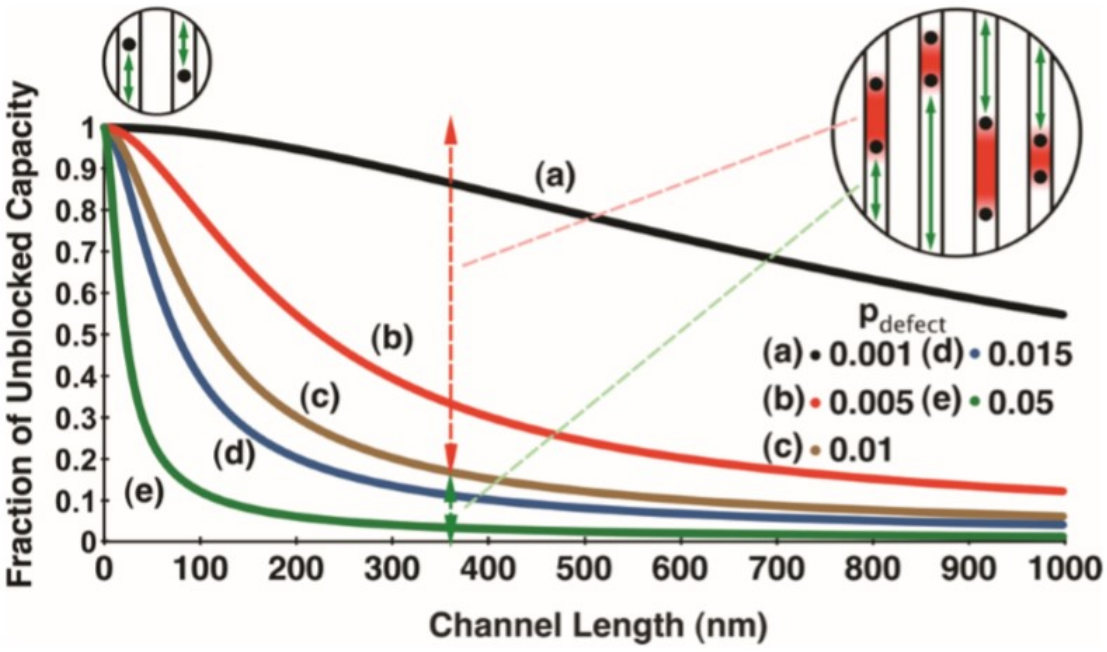

Figure 6-8 : Unblocked capacity as function of the channel length in $LiFePO_4$ for various defect concentrations. From Malik et al.[1]

As seen in the main panel of Figure 6-8 Malik has shown that, considering the typical amount of Fe_{Li} antisite defects (up to 5-10% with the usual synthesis routes),[1,2] the available "unblocked" capacity is considerably reduced even for submicron particles. This unblocked capacity can be reached from the outer part of the particles with an unrestricted Li diffusion. The blocked part can still be accessible thanks to the channel-to-channel jumps allowed by the defects, but the diffusion is not as easy as in

the case of defect free channels in the *b* direction as the activation energy for these channel-to-channel jumps is significantly larger.[1,6] The low value of Ea observed in the present study for Li_xFePO_4 at x = 1 and x = 0 suggests that at these compositions the EIS measurements probed the unrestricted diffusion in the *b* direction. The higher activation energies measured at the intermediate compositions suggest that in this case the diffusion was sensitive to the presence of the anti-site defects, which suggests that the EIS measurements occurred in the blocked portion of the capacity, that is, deeper into the bulk of the particles.

The characteristic diffusion length can be estimated from the characteristic diffusion time through the simple relation:[28]

$$L = \sqrt{\tau D} \tag{6-2}$$

with τ the average time at which SILD mass diffusion is observed (τ = 0.05 s at x = 1 and x = 0 as deduced from both EIS and PITT in the previous chapter) and D the diffusion coefficient ($D \approx 1e^{-9}$ cm^2/s as deduced from both EIS and PITT in the previous chapter at x = 1 and x = 0), one finds a depth of diffusion of 70 nm which is indeed small compared to the average radius of the particles (D50 = 500um). This is consistent with the value of Ea measured at this composition, which suggest the probed diffusion occurred in the unblocked portion of the particles.

It can be clearly seen in Figures 5-7 (a) and (b) that the diffusion time increases by about two orders of magnitude at the reaction potential, that is, at intermediate compositions when the system is biphasic. It is known from the work of Zhu et al. that at these compositions the diffusion coefficient of the separated phases can be considered equal to that of the end members x = 1 and x = 0,[29] so that the increase of diffusion time shown in Figures 5-7 (a) and (b) can be directly interpreted as the consequence of an increase of the diffusion depth L. This increase of diffusion depth can be understood considering the technique used, EIS, the mechanism occurring at intermediate compositions (biphasic transformation) and the voltage-composition profile of Li_xFePO_4. EIS consists in small (10mV) potential oscillations around the equilibrium voltage of the cell. As seen in Figure 6-9, when close to x = 1 and x = 0, the slope of the voltage-composition profile of Li_xFePO_4 is very large, leading to very small concentration perturbation. On the contrary, at the intermediate compositions, when the bi-phasic reaction takes place, the voltage-composition profile is flat, leading to a very low value of its slope. As can be seen in Figure 6-9, this is observed here for $0.1 < x < 0.9$. In this case, even the small 10mV amplitude of the EIS excitation can lead to large amplitudes of variation of the concentration x, and thus a migration of the phase boundary. As a consequence, instead of being restricted to the outer shell of the particles according to Fick's law in a solid solution system, the diffusion will occur in the core of the particles, inducing a strong dependence of the diffusion on the presence of defects.

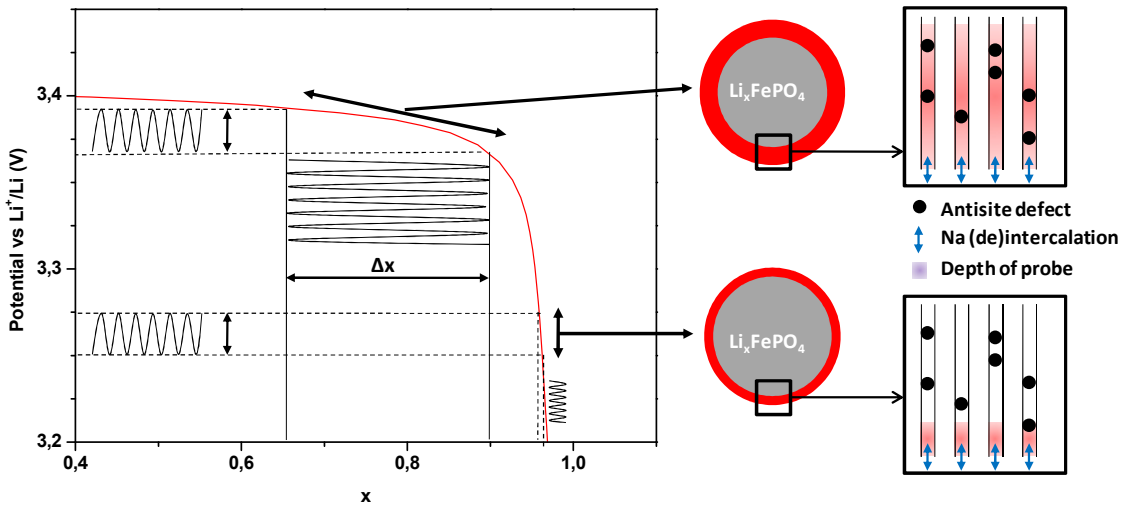

Figure 6-9 : Depth probe upon EIS measurements as function of the composition of Li_xFePO_4.

This explains why for compositions immediately below x = 1 and immediately above x = 0, the activation energy values correspond to diffusion in defect free $LiFePO_4$, and that at intermediate compositions they correspond to anti-site defects-controlled diffusion. For intermediate compositions, when Li_xFePO_4 is in a biphasic state, the EIS response of the electrode corresponds actually to the combination of the mass diffusion within both phases, and the activation energy values measured from 309 meV for x ≈ 0.1 to 698 meV for x ≈ 0.9 corresponds to an intermediate between these two values, weighted by the amount of each phase in the electrode.[30]

6.4.2. Na_xFePO_4

Surprisingly, the activation energy for Na diffusion in Na_xFePO_4 shows a very similar dependence to the alkali content as that of Li in Li_xFePO_4, with very close values.

An activation energy of 222 meV is found at discharged state of the cell i.e. for complete sodium insertion (x ≈ 1). As soon as some sodium is extracted this activation energy jumps to 701 meV (at x ≈ 0.9) before gradually decreasing to 367 meV at the end of charge, obtained for a composition of x = 0.25. Upon discharge this value gradually increases up to 708 meV near x ≈ 0.7, before dropping again to about 200 meV at the end of discharge. At this stage, after five repeated measurements, the activation energy values are found ranging from 176 to 210 meV which, taking account the measurement performed at the beginning of charge, gives a mean value of 201 meV for x = 1, enlightened by the blue horizontal line on Figure 6-7 (e). This is a very surprising and unexpected result, as the diffusion coefficient values deduced from PITT and EIS in the previous chapter, in agreement with previous works,[4,21] were about one order of magnitude smaller for Na compared to Li.

Indeed, applying equation 2-72 with the activation energy value determined above, with the hoping distance a, which corresponds to the size of the unit cell along the *b* axis at the given composition (6.01 and 6.207 Å for $LiFePO_4$ and $NaFePO_4$, respectively)[31,32,33], and considering that the variation of entropy in solid solution Li_xFePO_4 and Na_xFePO_4 during the hopping mechanism is the same, one finds

a ratio D_{Li}/D_{Na} of 2.6 at x = 1. This is about one order of magnitude lower than the 10-20 ratio that was determined in chapter 5 using equations 2-36 (PITT) or 2-63 (PITT+PEIS).

Moreover, while the activation energy values obtained for Li_xFePO_4 are in very good agreement with what was predicted by the computational study from Ceder's group at $x \approx 1$ and $x \approx 0$,[22,3] they also predicted Ea_{Na} to be about 100 meV larger than Ea_{Li}. On the other side, while the value of Ea_{Na} found here is also smaller than the prediction by Islam's group,[3] these later predicted Ea_{Na} to be actually about 230 meV smaller than Ea_{Li}.[5] Although the method used by Islam's group is considered less precise than the DFT method used by Ceder's group,[34] the discrepancy between their predictions of the Na/Li diffusion differences suggests that further computational study is required to fully understand the particularities of Na diffusion in Na_xFePO_4.

The 460 meV experimental value determined by Heubner et al.[21] for Na diffusion in $FePO_4$ is relatively close to that obtained in the present study at x = 0.4. Considering that x = 0 is hardly achieved electrochemically vs Na as discussed in the previous chapters, this suggests that Heubner et al. may not have reached the completely desodiated state, and that they performed the activation energy measurement at a biphasic state of Na_xFePO_4, similarly to their measurement on Li_xFePO_4.

The similar evolution of Ea with x_{Na} compared to Li_xFePO_4 suggests that a similar evolution of the depth of probe, and a similar mechanism of defect assisted diffusion occur at larger depth vs Na and vs Li. This can be explained by the fact that, as for Li_xFePO_4, the slope of the voltage-composition profile is large near x = 1 and very low at intermediate compositions. The values of activation energy of Na can therefore be interpreted similarly to those of Li, probing unrestricted diffusion near x = 1 and defect-controlled diffusion at intermediate compositions. In the case of Na, as discussed above, the composition x = 0 is not reached, which is probably the reason why the value of Ea at the end of charge is higher than that measured at the beginning of charge (x = 1).

As discussed in introduction, the diffusion of Na is believed to be one-dimensional, along the (*b*) direction, similarly to that of Li.[2] Furthermore, as pointed out by Tripathi et al. and similarly to $LiFePO_4$, punctual Na-Fe antisite defects may be responsible for the blocking of the (*b*) diffusion channels,[2] although their influence on Na diffusivity is not known yet. The formation energy of Na-Fe antisite defects in $NaFePO_4$ was determined by Tripathi et al. and found lower than that of the Li-Fe antisite effects in $LiFePO_4$. This lower formation energy suggests they are also present in olivine $NaFePO_4$, and is consistent with the better stability of the maricite $NaFePO_4$ phase over its olivine counterpart, in which the Na and Fe sites are switched compared to the olivine[2].

Remarkably the values of activation energy for diffusion measured at intermediate compositions when the diffusion is dominated by inter-channel Li/Na jumps assisted by anti-site defects have been found nearly the same for Na and Li (about 400meV near x = 0.2 and 700 meV near x = 0.9). These results indicate that Na_xFePO_4 is actually nearly as good an ionic conductor as Li_xFePO_4, independently of the Na content. This is a very surprising result given the clear indication of kinetic limitation in the electrochemical performance of $NaFePO_4$, which was also reflected in the value of diffusion coefficient determined in the previous chapter from PITT and PEIS.

A possible explanation is that the morphological factor, that was supposed equal for Li_xFePO_4 and Na_xFePO_4, may have changed from Li to Na, that could be due to morphological change of the material such as cracks or carbon coating's degradation.

As suggested in chapter 4, the behavior of $NaFePO_4$ upon the first Na (de)intercalation cycles (irreversible capacity and over-polarization) suggests that morphological changes of the material indeed occur upon the first Na insertion, which could be responsible for the modification of the morphological factor $\left(\frac{V_M}{ZFSSA}\right)^2$ of the diffusion coefficient, and for the poorer electrochemical performances of $NaFePO_4$ compared to $LiFePO_4$.

6.5. Conclusions

The activation energies for diffusion of Li and Na inside Li/Na_xFePO_4 were determined from impedance spectroscopy measurements performed on half cells at different states of charge and varying the temperature. The use of the PPMS offered a very fine temperature control, allowing a higher density of measurement points in a narrow temperature range compared to other reports, which ensures a better precision of the activation energies. To our knowledge this is the first time that the dependence of the activation energy on the alkali metal concentration is determined in $(Na,Li)FePO_4$ in the whole composition range.

The Li activation energy for diffusion in $LiFePO_4$ and $FePO_4$ was found relatively close to theoretical predictions for the diffusion of Li^+ along the (*b*) axis. For intermediate compositions, larger values of Ea_{Li} were found, relatively close to the theoretical predictions for antisite defects-assisted Li^+ diffusion. This suggests an increase of the diffusion depth at intermediate compositions as a consequence of the bi-phasic transformation mechanism.

Interestingly, the profile of the activation energy for Na diffusion in Na_xFePO_4 as function of the Na content was found similar to that of Li in Li_xFePO_4, with a low activation energy value for x = 1 and higher values for intermediate compositions. This suggests that, similarly to the case of Li, the diffusion depth was changing with the Na content during the activation energy measurements, and the activation energy measured at x = 1 corresponds to unrestricted diffusion of Na along the (*b*) axis while the activation energy values measured at intermediate compositions corresponded to Na-Fe antisite defects-controlled diffusion. The charged state Na_xFePO_4 (x = 0) was not reached, similarly to the PITT measurements of the previous chapter.

Surprisingly, the activation energy values for Na were found very similar to that of Li, with 201 and 185 meV at x = 1, respectively, a maximum of 701 and 698 meV at x = 0.9, respectively, and approximately 350 meV at x = 0.2 for both alkali metals. This suggests that the unrestricted diffusion (x = 1) as well as defects-controlled diffusion ($0.4 < x < 0.9$) for Na is very similar to that of Li. At x = 1 the slight difference of activation energy suggests that the diffusion coefficient of Na should be about 2.6 times lower than that of Li. It was however experimentally found between 10 and 20 times lower than that of Li at the same composition x = 1 in the previous chapter based on coupled PITT and PEIS measurements. Since Ea was deduced from Arrhenius plots in the present chapter, its value does not depend on extrinsic parameters such as materials and electrode morphology, contrary to the diffusion coefficient determined from EIS or PITT. The apparent discrepancy of the results of the present chapter with that of chapter 5 suggests that the assumption that the morphology does not change with the alkali content was not true: morphological changes most probably occur when Li is

substituted with Na. The occurrence of morphological change was already suspected in chapter 4 based on the larger polarization observed during the first Na insertion.

[1] R. Malik, D. Burch, M. Bazant, G. Ceder, Nano Letters, 10, 4123 (2010)
[2] R. Tripathi, S. M. Wood, M. S. Islam, L. F. Nazar, Energy Environ. Sci, 6, 2257 (2013)
[3] S. P. Ong, V. L. Chevrier, G.Hautier, A. Jain, C. Moore, S. Kim, X. Ma, G. Ceder,Energy Environ. Sci., 4, 3680 (2011)
[4] Y. Zhu, Y. Liu, C. Lou, C. Wang, Nanoscale, 5, 780 (2013)
[5] C. A. J. Fisher, V. M. H. Prieto, M. S. Islam, Chem. Mater., 20 (18) (2008)
[6] G. K. P. Dathar, D. Sheppard, K. J. Stevenson, G. Henkelman, Chem. Mater., 23, 4032 (2011)
[7] S.Y. Chung, J. T. Bloking, Y.-M. Chiang, Nat. Mater., 1, 123 (2002)
[8] C. Delacourt, L. Laffont, R. Bouhet, C. Wurm, J.-B. Leriche, M. Morcrette, J.-M. Tarascon, C. Masquelier, J. Electrochem. Soc., 152 (5), A913 (2005)
[9] R. Amin, J. Maier, P. Blaya, D. P. Chen, C. T. Lin, Solid State ionics, 179, 1683 (2008)
[10] P. Moreau, D. Guyomard, J. Gaubicher, F. Boucher, Chem. Mater., 22, 4126 (2010)
[11] C. Ho, I. D. Raistrick, R.A. Huggins, J. Electrochem. Soc., 127 (2), 343 (1980)
[12] C.L. Campion, W. Li, B. L. Lucht, J. Electrochem. Soc., 152 (12), A2327-A2334 (2005)
[13] A. Ponrouch, E. Marchante, M. Courty, J.-M. Tarascon, M. R. Palacin, Energy Environ. Sci., 5, 8572 (2012)
[14] Y. Ji, Y. Zhang, C.-Y. Wang, J. Electrochem. Soc., 160 (4), A636-A649 (2013)
[15] T. R. Jow, M. B. Marx, J. L. Allen, J. Electrochem. Soc., 159 (5), A604 (2012)
[16] L. Liao, P. Zuo, Y. Ma, X. Chen, Y. An, Y. Gao, G. Yin, Electrochimica Acta, 60, 269 (2012)
[17] F. Nobili, R. Tossici, R. Marassi, F. Croce, B. Scrosati, J. Phys. Chem. B, 106, 3909-3915 (2002)
[18] T. P. Heins, N. Harms, L.-S. Schramm, U. Schröder, Energy Technol., 4, 1-6 (2016)
[19] A. Mertens, I. C. Vinke, H. Tempel, H. Kungl, L. G. J. de Haart, R.-A. Eichel, J. Granwehr, J. Electrochem. Soc, 163 (7), H521-H527 (2016)
[20] M. Dixit, H. Engel, R. eitan, D. Aurbach, M. D. Levi, M. Kosa, D. T. Major, J. Phys. Chem. C, 119 (28), 15801 (2015)
[21] C. Heubner, S. Heiden, B. Matthey, M. Schneider, A. Michaelis, electrochemica acta, 216, 412 (2016)
[22] D. Morgan, A. Van der Ven, G. Ceder, Electrochem. Solid State Lett., 7 (2), A30-A32 (2004)
[23] C. Ouyang, S. Shi, Z. Wang, X. Huang, L. Chen, Physical Review B 69, 104303 (2004)
[24] Z. Liu, X. Huang, Solid State Ionics, 181, 907 (2010)
[25] K. Hoang, M. Johannes, Chem. Mater., 23(11), 3003 (2011)
[26] G. Xu, K. Zhong, J.-M. Zhang, Z. Huang, Journal of Applied Physics, 116, 063703 (2014)
[27] M. S. Islam, D. J. Driscoll, C. A. J. Fisher, P. R. Slater, Chem. Mater., 17(20), 5085 (2005)
[28] C. J. Wen, B. A. Boukamp, R. A. Huggins, W. Weppner, J. Electrochem. Soc., 126, 12, 2258 (1979)
[29] Y. Zhu, C. Wang, J. Phys. Chem. C, 114, 2830 (2010)
[30] C. Zener, J. Appl. Phys., 22, 4, 372 (1951)
[31] A.K. Padhi, K. S. Nanjundaswamy, J. B. Goodenough, J. Electrochem. Soc., 144(4), 1188 (1997)
[32] W.-J. Zhang, J. Power Sources, 196, 2962 (2011)
[33] M. Galceran, D. Saurel, B. Acebedo, V. V. Roddatis, E. Martin, T. Rojo, M. Casas-Cabanas, Phys. Chem. Chem. Phys., 16, 8837 (2014)
[34] M. S. Islam, C. A. Fisher, Chem. Soc. Rev., 43(1), 185 (2014)

7. Influence of morphological changes

7.1. Introduction

In the present study, Na_xFePO_4/C electrodes were obtained through electrochemical delithiation and sodiation of $LiFePO_4$/C electrodes in order to ensure that the morphology and particle size distribution would be the same when comparing the electrochemical performances of $LiFePO_4$ and $NaFePO_4$ upon Li/Na (de)intercalation. While 100% of the theoretical capacity of the electrodes could be reached upon Li (de)intercalation, only 80% of their theoretical capacity could be reached upon the first Na insertion in $FePO_4$, which was associated with a high overpotential compared to the following Na insertions, and upon GITT and PITT. As explained in chapter 4, these observations suggest that some morphological changes occur upon the first Na insertion and are responsible for the reduction of the reversible capacity of the material to 80% of its theoretical value, by lowering the effective specific surface area of the material or the effective mass of active material.

The diffusivities of Li and Na in Li/Na_xFePO_4 were studied in chapter 5 and 6 in order to find the origin of the kinetic limitations responsible for the poorer electrochemical performances of $NaFePO_4$ compared to those of $LiFePO_4$. Two parameters were experimentally determined: their effective diffusion coefficient and its activation energy. The Na diffusion coefficient in $NaFePO_4$ was found between 10 and 20 times lower than that of Li in $LiFePO_4$, suggesting that the lower Na diffusivity in Li/Na_xFePO_4 was responsible for its poorer electrochemical performances. These results however presented an apparent discrepancy with the activation energy values as, compared to the Li diffusion coefficient in $LiFePO_4$, the Na diffusion coefficient in $NaFePO_4$ was found between 4 and 10 times lower than predicted by their activation energies. As explained in chapter 6, this discrepancy suggests that the morphological changes occurring during the first Na insertion are responsible for the poorer diffusivity of Na in the electrode material.

Evidence of morphological changes of $LiFePO_4$ after cycling has been previously reported by Wang et al. and Chen et al. through SEM and TEM observation of cycled $LiFePO_4$ particles, respectively.[1,2] These authors observed cracks in the (*bc*) plan of these particles, as shown in Figure 7-1 (a), (b) and (c), which formation was attributed to strain accommodation caused by the volume mismatch between the lithiated and delithiated phases. The orientation of these cracks was ascribed to the largest cell mismatch along the (*a*) axis (see Table 7-1).[3] Indeed, having the interface between the two phases in the (*bc*) plane keeps the largest mismatch direction perpendicular to the interface, which minimizes the interfacial energy and facilitates further strain accommodation.[1,2]

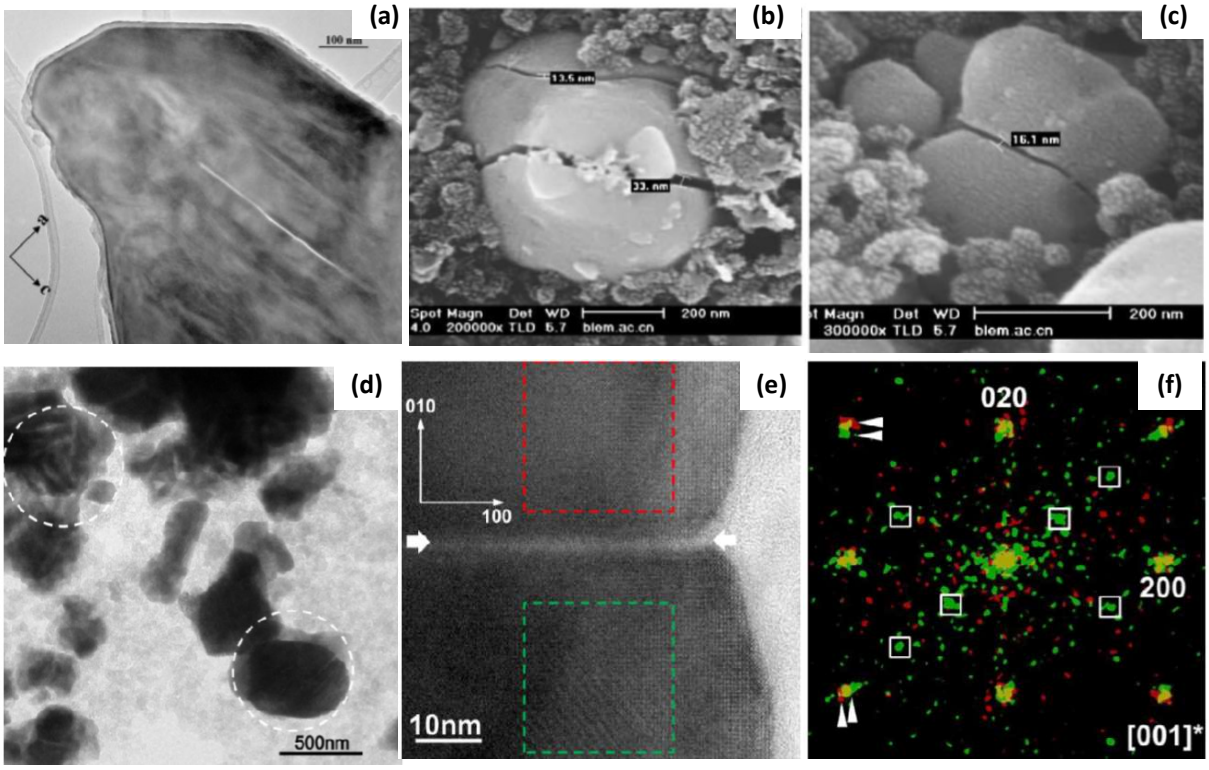

Figure 7-1 : (a) TEM image of thin $Li_{0.5}FePO_4$ crystal with crack in the (*bc*) plane.[2] (b) and (c) SEM images of cycled $LiFePO_4$ electrodes.[1] (d) TEM images of Na_xFePO_4 particles by Galceran et al., areas with cracks are highlighted.[4] (e) High magnification TEM image of the zone in the vicinity of a crack.[4] (f) Diffraction pattern of the zones in the vicinity of the crack displayed in (e).[4]

Interestingly, TEM observation of previously cycled Na_xFePO_4 particles reported by Galceran et al. showed cracks in their (*ac*) plane, as displayed in Figure 7-1 (d) and (e), which were also ascribed to accommodation to the volume mismatch.[4] The diffraction pattern of zones taken on each side of a crack (see Figure 7-1 (f)) allowed the identification of a $Na_{2/3}FePO_4$ and a $FePO_4$ phase. Galceran et al. thus concluded that in the case of $NaFePO_4$ the interface between these two phases should be comprised in the (*ac*) plane as it keeps the largest mismatch direction out of the interface and lowers the strain between the phases; the cell parameter expansion being higher following the (*b*) axis for Na while it is in the (*a*) direction for Li, as seen from Table 7-1. The cell parameter mismatch along the (*ac*) and the (*bc*) planes of these two phases being very close, Galceran et al. suggested that the interface between them might as well be found in the (*bc*) plane depending on the history of the sample.[4]

	Cell parameter mismatch (%)		
axis	$LiFePO_4$ Vs $FePO_4$	$Na_{2/3}FePO_4$ Vs $FePO_4$	$NaFePO_4$ Vs $FePO_4$
(a)	5.11	4.67	5.86
(b)	3.69	4.98	7.37
(c)	1.94	3.27	3.45
total	6.87	13.48	17.58

Table 7-1 : Cell parameter mismatches between the Li/Na_xFePO_4 phases[4]

In the case of $LiFePO_4$, since the diffusion of Li in the olivine structure is one-dimensional along the (*b*) axis,[5] i.e. parallel to the cracks, these later should not directly affect Li diffusion within the particles. They might however isolate fractions of particles from each other and impede the movement of the interface within the whole particle. In this case the separated fractions of $LiFePO_4$ should transform individually following the biphasic transformation mechanism, as illustrated in Figure 7-2 (a) and (b), which should not affect the available capacity. Moreover, Malik et al. showed that the $LiFePO_4$/$FePO_4$ transformation mechanism can follow a non-equilibrium path being solid-solution. The transformation mechanism is faster following this mechanism and the two distinct phases appear after relaxation of the material.[6] If $LiFePO_4$ follows this transformation mechanism, the cracks in the (*bc*) plane shall have a marginal influence on the rate capability of the material.

In the case of $NaFePO_4$, the cracks found in the (*ac*) plane by Galcerán et al. are actually perpendicular to the diffusion channels in the (*b*) direction. They would therefore cut the Na diffusion channels, contrary to the case of $LiFePO_4$. As discussed in the previous chapter, a non-negligible amount of antisite Fe-(Na,Li) antisite defects are expected to be present in these materials. These defects affect the diffusion in the (*b*) direction, but also allow jump from channel to channel and thus, the defect assisted diffusion is two dimensional. Taking this into account, having cracks in the (ac) plane of $NaFePO_4$ particles would force the mobile Na to jump from one channel to another, inducing a more tortuous two-dimensional or three-dimensional diffusion path through the antisite defects to reach the totality of the active insertion material as illustrated in Figure 7-2 (d). It was shown in the previous chapter that the activation energy necessary for this path is much higher than for one-dimensional unrestricted diffusion along the (*b*) axis, which would induce a significantly lower effective diffusion coefficient for Na.

In addition to the cracks, Wang et al. suggested that the volume expansion of $LiFePO_4$ upon Li (de)intercalation might be responsible for carbon coating degradation, leading to poorer electrical contacts within the electrode.[1] Since the volume expansion of Na_xFePO_4 upon Na (de)intercalation is much higher than that of $LiFePO_4$, it could lead to larger carbon coating degradation which would degrade even more the electrochemical performances of the electrode.

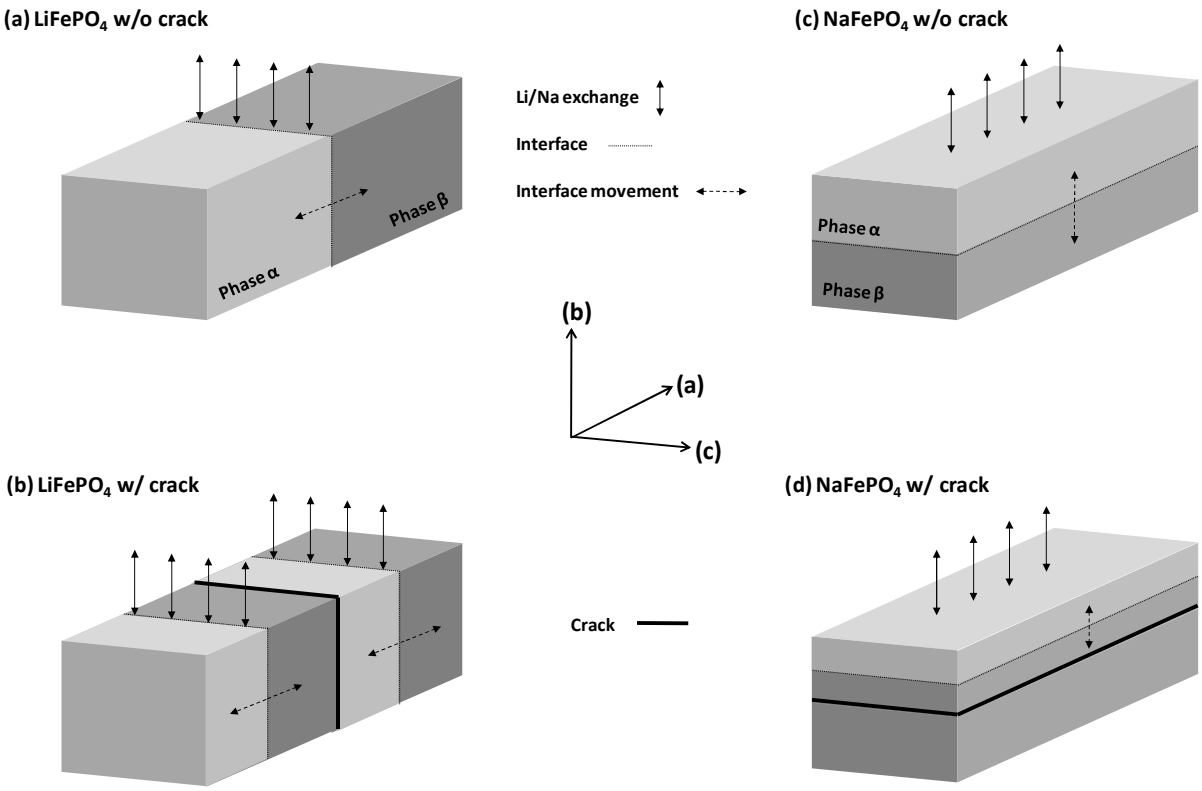

Figure 7-2 : Schematic view of the Li intercalation process (a) without cracks (b) with cracks. (c) and (d) Same views of the Na intercalation process.

If confirmed, the presence of cracks in the (*ac*) plane of cycled Na_xFePO_4 particles might thus explain its poorer electrochemical performances compared to $LiFePO_4$. The objective of this chapter is therefore to corroborate the presence of these cracks, and to confirm their influence on the electrochemical performances of $NaFePO_4$.

7.2.Confirmation of the presence of cracks

TEM images of Na_xFePO_4/C particles extracted from an electrode that had previously undergone 50 Na insertion-extraction cycles at C/10 were taken in order to confirm the presence of cracks in their (*ac*) plan. Clear cracks are indeed observed on some of these particles, as shown in Figure 7-3 (a), (b), (c) and (d), where they are enlightened by the white arrows. Several parallel cracks are found in the particles shown in Figure 7-3 (b), (c), and (d) which was not reported by Galceran et al.[4] No cracks could be found upon the observation of cycled $LiFePO_4$ particles.

Although not clearly seen at this scale, the TEM images in Figure 7-3 contain a geometrical pattern created by the planes of the crystalline structure of the material. This pattern contains information about the unit cell parameters, thus their orientation within the particle. Identification of the direction of the [100], [010] and [001] Miller vectors will indicate in which plane the cracks are contained.

The Fourier transform of a zone taken in the vicinity of the cracks of the particles in Figure 7-3 (c) is displayed in Figure 7-3 (f). It shows a distribution of points in different directions with regular

spacing. Since this Fourier transform is equivalent to the diffraction pattern of the material, each point represents a symmetry of the crystalline structure, and the spacing between each point is related to the spacing between the crystalline plans. These points are linked to the miller vectors, from their relative angle and distance to the center of the diffraction pattern.

The scattering vector h_{hkl} is determined from the distance between the diffraction points and the center of the diffraction pattern, in the form $d_{hkl} = \frac{1}{h_{hkl}}$. Two of these vectors, indicated on Figure 7-3(c), are identified, which correspond to d_{hkl} distances of 4.853 and 6.145 nm, respectively, with relative angle of 87.87°. These distances are close to that of the [010] and [001] Miller vectors of Na_xFePO_4 (see Table 7-2), and their relative angle is also close to the 90° expected between them, confirming the indexation. The [001] axis is thus found perpendicular to the plane of the image of Figure 7-3 (c). The slight difference between the present and previously reported distance of Table 7-2 can be explained by a slight inclination of the plan of the image with respect to the (*bc*) plane. The (*b*) and (*c*) directions identified from the diffraction pattern are reported on the TEM image of the particle, which reveal that the cracks are found in the (ac) plane, perpendicular to the (*b*) diffusion channels, confirming the observations of Galceran et al.[4]

Since multiple parallel cracks are found in the (*ac*) plan of several particles, they might isolate some fractions of particles within which Na (de)intercalation would be much more difficult, which would therefore reduce the effective available capacity. This could explain the limitation of the reversible capacity of $NaFePO_4$ to 80% of its theoretical value.

Na_xFePO_4	[100]	[010]	[001]
x = 1	10.410	6.220	4.950
x = 2/3	10.290	6.080	4.950
x = 0	10.190	6.030	4.950

Table 7-2 : Interplanar distances in the Na_xFePO_4 phases, in Å.

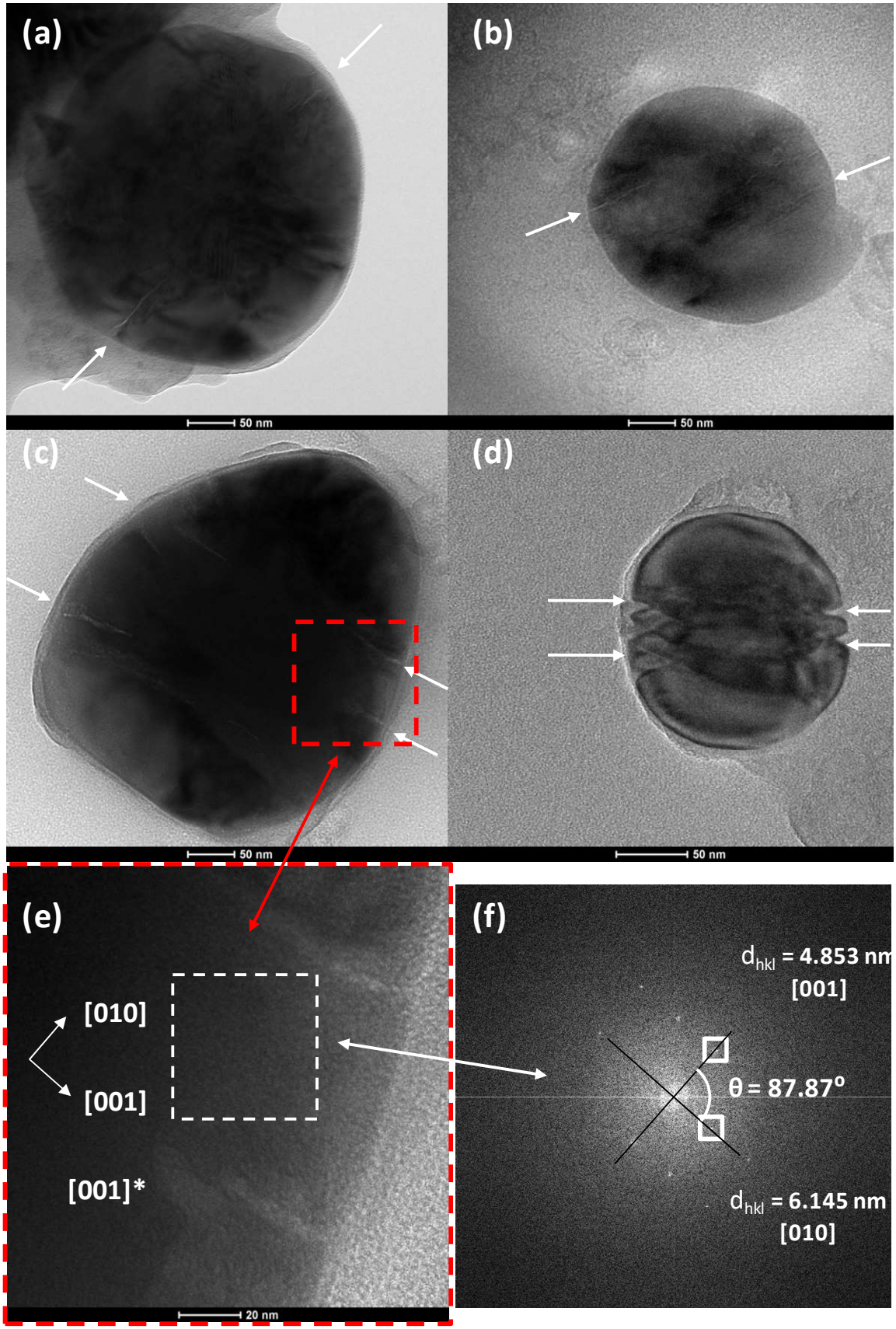

Figure 7-3 : (a), (b), (c), (d) and (e): Low magnification TEM images of Na_xFePO_4/C particles after 50 Na insertion/extraction cycles. (f) Fourier transform of a zone taken in the vicinity of the cracks of the particle in (c) and (e).

7.3. Electrochemical verification of the influence of the cracks on the electrochemical performances of $NaFePO_4$

7.3.1. Cycling

In order to confirm that the cracks formed in the (*ac*) plane of the $NaFePO_4$ particles are responsible for its poorer electrochemical performances compared to $LiFePO_4$, several Li insertion/extraction cycles were performed on a $FePO_4$/C electrode that had previously undergone several Na insertion/extraction cycles. Indeed, once formed upon Na insertion, the cracks remain present in the material and are thus expected to affect the Li (de)intercalation kinetics as well when cycled vs Li after cycling vs Na. This experiment is expected to provide a better understanding on how the cracks may affect the electrochemical performance of the material.

Three Na insertion extraction cycles at C/10 were performed on an electrochemically delithiated $FePO_4$/C electrode, after which the sodium was electrochemically removed following a desodiation procedure similar to the delithiation one. This procedure consists in charging the sodium half cell up to 4V at C/10 then applying a constant 4V voltage for 24 hours. The cell was then disassembled and the electrode washed and assembled again in a fresh lithium half cell before 30 Li insertion-extraction cycles at C/10.

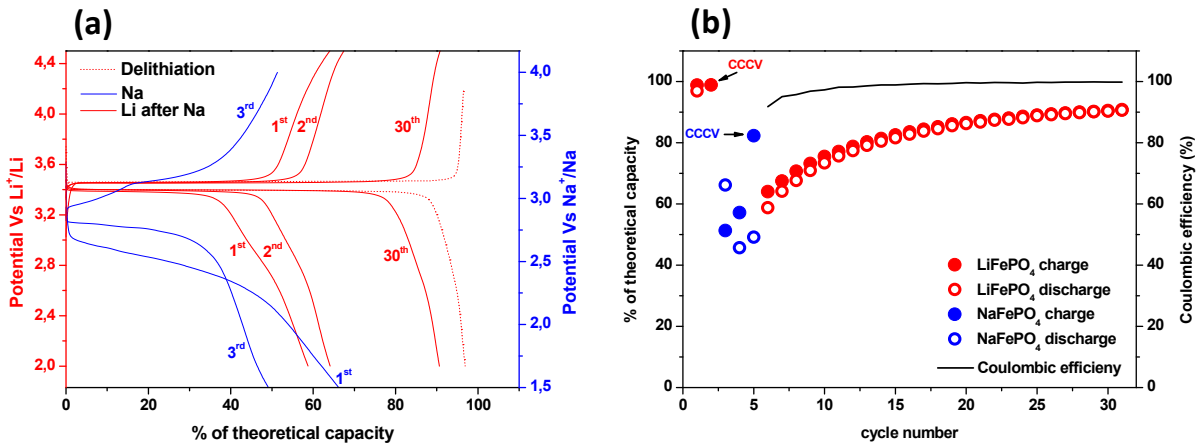

Figure 7-4 : (a) Voltage-composition profile, (b) Capacity and coulombic efficiency of a $LiFePO_4$/C electrode upon desodiation, Na insertion/extraction and subsequent Li insertion/extraction.

A selection of voltage-capacity profiles of the electrode upon cycling vs Na and Li are displayed in Figure 7-4 (a). The electrode shows the expected behavior upon the initial electrochemical delithiation procedure with a single potential plateau upon charge and discharge. 97% of its theoretical capacity is reached at this stage. A high polarization is observed upon the first Na insertion where 66% of the theoretical capacity of the cell is reached. The following Na insertions and extractions follow the previously reported behavior with a single discharge plateau at 2.85 V and two charge plateaus at 2.9 and 3.1 V respectively. Approximately 50% of the theoretical capacity of the cell is reversibly reached upon cycling vs Na. Upon the desodiation (i.e. CCCV charge to 4V), the constant potential hold was stopped after 35h, when 80% of the theoretical capacity of the cell was reached. After desodiation of the electrode, further cycling vs Li shows the expected behavior with a

large and flat potential plateau observed at 3.4V upon discharge and 3.45V upon charge. However, the potential-capacity profile vs Li presents a smaller slope at the end of charge compared to the initial cycles, which gradually disappears with further cycling vs Li. This could be related to remaining Na content that had not been totally extracted during the previous CCCV charge vs Na.

The capacity reached upon each Li and Na insertions and extractions is displayed in Figure 7-4 (b) as function of the cycle number. One can observe from this figure that the consequence of the Li-Na-Li sequence on the capacity is totally asymmetric. Indeed, while the capacity drops from nearly 100% vs Li to about 50-60% vs Na, when further cycled vs Li the capacity is initially the same as vs Na, about 60%, and only gradually increases upon further cycling to reach 90% at cycle 30. This confirms that a change in the material occurred while cycling vs Na which affects as well further Li insertion/extraction. Remarkably, the polarization between charge and discharge vs Li remains unchanged before and after cycling vs Na, only the available capacity is affected. This suggests that whole domains of phase become unreactive, possibly due to blocked mass diffusion for these domains, but that the domains that still react do so with apparently unaffected kinetics of insertion-extraction. This is totally consistent with the mechanism proposed in the introduction of the present chapter in which the cracks are expected to totally isolate phase domains when cycled vs Na.

However, the continuous increase of the capacity upon Li (de)intercalation indicates that the limitation of the capacity of the material upon Na (de)intercalation is not totally irreversible, as would be expected considering cracks isolating phase domains. Furthermore, the coulombic efficiency of the first Li insertion/extraction cycle is close to 90% and gradually closes in to 100% as the capacity of the cell stabilizes, indicating that more capacity is obtained upon charge (extraction) than discharge (insertion) upon the first cycles, which could suggest that some Na have been trapped within the material and is gradually extracted upon charge. The sloping of the voltage-capacity profile of the post-Na electrode at the end of charge could correspond to this Na extraction. Since the capacity of the cell still increases, although very slightly, after 30 Li insertion/extraction cycles, it can be expected that some Na is still extracted from the electrode after these 30 cycles.

These results indicate that the presence of cracks is not the sole responsible for the poorer electrochemical performances of $NaFePO_4$ compared to $LiFePO_4$. Moreover, the stabilization of the reversible capacity of the electrode to 90% of its theoretical value after 30 Li (de)intercalation cycles suggests that the cracks would isolate about 10% of the accessible active material's mass.

7.3.2. Charge transfer resistance

In order to confirm that some residual sodium is still extracted after replacing Na by Li, EIS measurements were performed at the end of each charge and discharge of the cell, after relaxation until an equilibrium condition of 2mV/h was reached. The Nyquist impedance spectra obtained after discharge of the cell are displayed in Figure 7-5 (a).

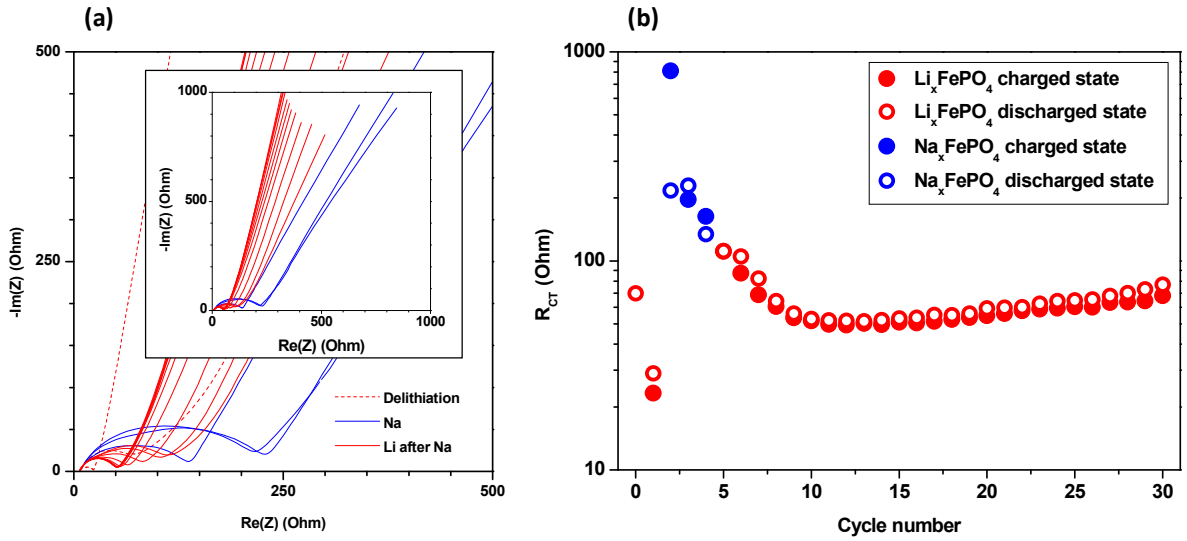

Figure 7-5: (a) Nyquist plots of the impedance of the cell at discharged state after every Li/Na (de)intercalation cycle. (b) Charge transfer resistance of the net cell deduced from the impedance spectra at charged and discharged state.

It was shown in chapter 5, from electrochemical impedance spectroscopy measurements performed on three electrodes Li/$NaFePO_4$ cells, that the contributions of the Li and Na counter electrodes and that of the $LiFePO_4$ working electrode to the total charge transfer resistance of the cell are comparable and negligible with regard to that of the $NaFePO_4$ working electrode. The total charge transfer resistance of the half cells used in the present study is therefore mainly due to the working electrode, is dependent on the alkali metal involved in the extraction/insertion mechanism, and thus is a useful parameter to confirm that some Na is still extracted from the post-Na Li_xFePO_4 electrode. As explained in chapter 5, this total charge transfer resistance is estimated from the width of the semi-circle at high frequency on the Nyquist plots of the impedance of the cells and its values are reported in Figure 7-5 (b).

As can be seen in Figure 7-5 (b), the net cell charge transfer resistance (R_{CT}) is found much lower upon Li (de)intercalation before incorporation of Na within the cell than upon Na (de)intercalation, as could be expected from the impedance spectroscopy measurements performed in chapter 5, and in accordance with reports by Zhu et al.[7] and Heubner et al.[8] Surprisingly R_{CT} remains the same when, near cycle 4, Na^+ is replaced by Li^+, suggesting that Na^+ is still mainly involved in the charge transfer reaction. During the 6 subsequent cycles vs Li, R_{CT} progressively decreases before stabilizing, which suggests that most the remaining Na has been extracted. The R_{CT} value obtained after 6 Li insertion/extraction cycles is found about two times higher than that before Na (de)intercalation, suggesting that the large volume expansion upon Na (de)intercalation might have indeed degraded the carbon coating. The fact that it does not seem to affect the polarization upon Li(de)intercalation at C/10 can be simply explained by R_{CT} having a negligible weight in the overall cell impedance.

The charge transfer resistance value being inversely proportional to the electrochemically active surface area,[9] the fact that R_{CT} vs Li after stabilization is about twice its value for the initial cycles suggests that the effective electroactive surface area S is reduced by a factor 2 after cycling vs Na, possibly due to degradation of the electrical contact between the carbon coating and the active material after Na (de)intercalation, which could explain the apparent discrepancy between the Li/Na diffusion coefficient determined in chapter 5 and the activation energy results obtained in chapter 6. Indeed, as explained in chapters 2 and 5, the diffusion coefficients of Li and Na calculated from PITT

and PEIS result as the product of several factors, one of them taking into account the morphology of the electrode in the form $\left(\frac{V_M}{ZFSSA}\right)^2$. The SSA value used to determine the Li and Na diffusion coefficients corresponded to that of the pristine electrode, while it should have been taken approximately two times lower in the case of Na to take into account the carbon coating's degradation. The Na diffusion coefficient in $NaFePO_4$ was thus underestimated by a factor of approximately 4, and would therefore be between 2.5 and 5 times lower than that of Li in $LiFePO_4$, which is in much better accordance with the activation results, which predicted a ratio of 2.5 between them.

7.4.Discussion

The progressive recovering of R_{CT} and the reversible capacity upon cycling vs Li after cycling vs Na suggest that there are two cumulative origins to the limited reversible capacity of Na_xFePO_4 as consequences of the volume expansion of the material upon the first Na (de)intercalation:

i) Morphological changes of active material's particles, in the form of cracks in the (*ac*) plan induced by Na insertion/extraction which, as mentioned above, isolate some phase domains leading to a limitation of the capacity after further cycling vs Li.

ii) Degradation of the carbon coating at the surface of the active material particles, which decreases the effective surface area for charge transfer and leads to poorer electrical connections at electrode scale.

The formation of cracks was acknowledged by TEM observation of the particles, and carbon coating degradation can be deduced from the evolution of the charge transfer resistance of the cell upon the Li-Na-Li cycling sequence. These two can explain the lower apparent diffusion coefficient as deduced from the PEIS and PITT measurements in chapter 5, sorting out the discrepancy between the diffusion coefficient and activation energy results. It also explains part of the limitation of the capacity vs Na. The formation of cracks is also in accordance with the larger overpotential observed in chapter 4 upon the first Na insertion. However, the formation of cracks and the degradation of the carbon coating cannot explain the poorer kinetics of Na extraction at the end of charge of Na_xFePO_4 which, as it was shown in chapter 4, impedes reaching the fully desodiated state $FePO_4$.

Although the poorer Na extraction kinetics at the end of charge could suggest a poorer diffusivity of Na in $FePO_4$ compared to that in $NaFePO_4$, it has to be noted that the Na diffusivity could not be experimentally characterized in $FePO_4$ due to parasitic reactions or to impossibility to reach this stage, and that this goes in direct contradiction with the theoretical results of Ong et al. which determined a lower activation energy for diffusion of Na in $FePO_4$ compared to that in $NaFePO_4$.[10] Moreover, the first insertion occurs from $FePO_4$, with an overpotential of about 150 mV, which can be ascribed to the formation of the cracks and is too low to explain the limitation of capacity at the end of charge. The main source of the capacity limitation of $NaFePO_4$ upon cycling could be intrinsic to the interactions between Na and the host structure but seems apparently not related to the ionic conductivity of the material and remains unidentified so far. It could be related to the interaction between the phase separation geometry, the defect assisted diffusion and the orientation of the

cracks inducing an extrinsic limitation to the Na diffusion in some phase domains, to a drop of the electronic conductivity of the material with low Na content, or to the dynamic formation of antisite defects. Further study is needed or its identification.

7.5.Conclusion

The experimental results presented in the chapters 4, 5 and 6 of the present study suggested that some morphological changes of Na_xFePO_4/C were responsible for the poorer apparent Na diffusivity compared to that of Li in Li_xFePO_4/C. The TEM observation of cycled Na_xFePO_4 particles presented in this chapter confirmed the presence of cracks in their (*ac*) plan, which can be multiple in the same particle leading to the electrical isolation of part of the particle.

However, the comparison of the polarization of an electrode upon cycling vs Li, before and after cycling vs Na, i.e. with and without cracks in the (*ac*) plan of the olivine material, demonstrated that these cracks are not the unique source of kinetic or capacity limitations when cycled vs Na. The evolution of the charge transfer resistance suggested that the carbon coating is also affected, limiting the effective surface area for charge transfer. In addition, the fact that an important part of the capacity lost vs Na is recovered vs Li suggests that there is another source of limitation for Na insertion-extraction, that is not related to morphological changes such as cracks or carbon coating degradation, and which forbids approaching the fully charged state $FePO_4$. Based on the capacity evolution when cycled alternatively vs Li, Na and then Li, we estimated to about 10% of the theoretical capacity the irreversible loss attributed to the formation of cracks in the (*ac*) plan, and 20 to 30% the loss that is related to the limitation of Na extraction approaching charged state and reversible when further cycled vs Li. This limitation of the Na extraction approaching charged state remains unknown, but is probably related to the topology of the phase separation, the interphase mobility or energy, or the dynamic formation of Fe_{Na} antisite defects.

[1] D. Wang, X. Wu, Z. Wang, L. Chen, J. Power Sources, 140, 125 (2005)
[2] G. Chen, X. Song, T. J. Richardson, Electrochem. Solid State Lett., 9(6), A295 (2006)
[3] A. Van der Ven, K. Garikipati, S. Kim, and M. Wagemaker, J. Electrochem. Soc., 156, A949 (2009).
[4] M. Galceran, D. Saurel, B. Acebedo, V. Roddatis, E. Martin, T. Rojo, M. Casas-Cabanas, Phys. Chem. Chem. Phys., 16, 8837 (2014)
[5] S. Nishimura, G. Kobayashi, K. Ohoyama, R. Kanno, M. Yashima, A. Yamada, Nat. Mater., 7(9), 707 (2008)
[6] R. Malik, F. Zhou, G. Ceder, Nat. Mater., 10, 587 (2011)
[7] Y. Zhu, C. Wang, Nanoscale, 5, 780 (2013)
[8] C. Heubner, S. Heiden, B. Matthey, M. Schneider, A. Michaelis, Electrochim. Acta, 216, 412-419 (2016)
[9] Z. Ogumi, Electrochemistry, 78(5), 319 (2010)
[10] S. P. Ong, V. L. Chevrier, G.Hautier, A. Jain, C. Moore, S. Kim, X. Ma, G. Ceder,Energy Environ. Sci., 4, 3680 (2011)

General conclusions

This study aimed at understanding the fundamental differences between the (de)intercalation of lithium and sodium in $(Li,Na)FePO_4$ in order to identify the origin of the limitation of the performances of $NaFePO_4$, as well as to get more insight into the fundamental differences between Na and Li intercalation dynamics that could be extrapolated to other compounds. For that purpose, advanced electrochemical techniques were applied to $LiFePO_4$/C and $NaFePO_4$/C electrodes, these later being prepared by electrochemical ion exchange from $LiFePO_4$/C electrodes in order to ensure similar values of the extrinsic parameters such as materials morphology and electrode's architecture.

Basic electrochemical performance tests (low rate cycling and rate capability) confirmed the quality of the electrode preparation process, as $LiFePO_4$/C electrode showed state of the art performance, and the presence of kinetic limitations for $NaFePO_4$/C that affect its rate capability as well as its low rate capacity. Indeed, the reaction resistances to Na insertion/extraction, determined from rate capability, were found higher than those corresponding to Li insertion/extraction, confirming that some kinetic limitations are responsible for the poorer performances of this material upon Na (de)intercalation.

Titration techniques (PITT and GITT) allowed to verify the known equilibrium voltage-composition profile upon charge, formed by two plateaus separated by an intermediate phase near x = 2/3. In collaboration with Amaia Zaracibar at UPV and the computational study group at CIC Energigune, we have shown that this corresponds to the thermodynamic equilibrium path. Upon discharge, which was reported to occur by a single reaction voltage with coexistence of three phases, our GITT measurements allowed the identification of two distinct potential plateaus upon Na insertion corresponding to two very close equilibrium potentials of reaction. In collaboration with the Advanced Electroactive Materials group of CIC Energigune, we have shown that it is caused by two successive biphasic transformations mechanisms. While these two mechanisms overlap at low rate, generating the 3 phases state already reported at intermediate compositions, their reaction potentials tend to separate at higher rate due to distinct reaction resistance, inducing a shrinking of composition range at which they overlap.

The comparison of the Li and Na mass diffusivies in $(Li,Na)_xFePO_4$ was then studied as potential origin of the kinetic limitations to Na (de)intercalation, from PEIS coupled with PITT. At x = 1, the effective diffusion coefficient of Na in Na_xFePO_4 was found between 10 and 20 times lower than that of Li in Li_xFePO_4. If this could be at origin of the poorer rate capability vs Na, D_{Na} was not found low enough to explain the limited capacity at low rate. Although D_{Na} could not be calculated at the end of charge due to unfinished reaction, its Warburg coefficient evolution suggests that D_{Na} is probably close at x = 0 and x = 1.

In order to confirm the poorer Na diffusivity determined from PITT and PEIS and get deeper insight into their diffusion mechanism, the activation energies for Li and Na diffusion were determined in the whole composition range of $(Li,Na)_xFePO_4$ from temperature dependent PEIS measurements. These measurements were performed in a very narrow temperature range of 20°C in order to avoid electrolyte degradation. The Li activation energies for diffusion in Li_xFePO_4 at x = 0 and 1 were found

relatively close to theoretical predictions for the diffusion of Li^+ along the one-dimensional diffusion channels in absence of defects. For intermediate compositions, larger activation energy values were found, relatively close to the theoretical predictions for antisite defects-assisted Li^+ diffusion. This allowed concluding that at x = 0 and x = 1, where the system is expected to behave as a solid solution, the activation energy had been measured for shallow diffusion in the outer skin of the particles, to a depth in the order of the average defect-defect distance. On the contrary, at intermediate compositions a larger diffusion depth is induced by the transition to a biphasic reaction, inducing a defect-assisted diffusion. The evolution of the activation energy for diffusion of Na vs x_{Na} presented a very similar profile to that of Li, which allowed concluding that the Na diffusivity occurs similarly to that of Li, unrestricted at x = 1 and assisted by antisite defects at intermediate compositions, and allowed the determination of the activation energies for diffusion of Na for defect-free diffusion along the one-dimensional diffusion channels and for defect-controlled diffusion across the antisite defects in $NaFePO_4$.

Surprisingly, the minimum (unrestricted) and maximum (defect assisted) activation energies for diffusion of Li and Na in Li/Na_xFePO_4 were found very close, corresponding at $x \approx 1$ to a ratio of diffusion coefficients one order of magnitude lower than that of the effective diffusion coefficients determined from PITT and PEIS. This suggests that extrinsic factors affect the effective Na diffusivity at electrode level such as morphological changes. Evidences of morphological changes were found in $NaFePO_4$/C, in the form of cracks in the (*ac*) plane observed from side to side of the particles, along with hints of degraded carbon coating at the surface of the particles. These morphological changes were indeed found responsible for the reduction of the effective Na diffusion coefficient, which explained the discrepancy between the activation energy and diffusion coefficient results and confirmed that $NaFePO_4$ is nearly as good an ionic conductor as $LiFePO_4$. They also account for part of the limitation of capacity of $NaFePO_4$ at low rate, probably by isolating whole phase domains.

The alternative cycling of an electrode following the sequence Li-Na-Li have shown that part of the capacity limitation vs Na is reversible vs Li. This suggests that there is either another unidentified intrinsic source of kinetic limitations to Na insertion/extraction, or differences between how the morphological changes affect the effective Li and Na diffusion, especially near x = 0. These could be related to difference in electronic conductivity, dynamic formation of antisite-defects or distinct phase separation geometry. Further study would be needed for their identification, in particular computational work on the basis of the findings of the present thesis.

The present results based on the study of $(Na,Li)_xFePO_4$ demonstrate that, despite of the larger ionic radius of Na compared to Li, its intrinsic ionic diffusivity may be as good as that of Li. However, this larger ionic radius may induce larger volumetric changes that can lead to morphological changes which affect the effective diffusion and limits both rate capability and low rate capacity. This suggests that beyond intercalation chemistry, the route for improvement of Na compounds should not overlook the importance of morphological changes that can be induced by the intercalation of the larger Na ions compared to Li.

Henri-Virgile ANNE
39700 Castro-Urdiales
Spain
Henri.hva.anne@gmail.com
0034 645 860 061

Electrochemist engineer
Ph.D. candidate

Academic formation

2014-2018 **Doctoral researcher**, CIC Energigune, Understanding the kinetic limitations of $NaFePO_4$ as cathode active material for Na-ion batteries.

2008-2012 **Grenoble Institute of Technology – Phelma**, Engineer's degree (equivalent to master), Electrochemistry and processes for energy and environment.

2010-2011 **Ecole supérieure de Commerce de Grenoble**, Management master.

Scientific activities

Publications

M. Hilder, P. C. Howlett, D. Saurel, H. Anne, M. Casas-Cabanas, M. Armand, T. Rojo, D. R. MacFarlane, M. Forsyth, *Stable cycling of $NaFePO_4$ cathodes in high salt concentration ionic liquid electrolytes*, J. Power Sources, 406, 70, 2018

D. Saurel, M. Galceran, M. Reynaud, H. Anne, M. Casas-Cabanas, *Rate dependance of the phase transformation in olivine $NaFePO_4$*, Int. J. Energy Res., 1, 2018

A.Saracibar, J. Carrasco, D. Saurel, M. Galceran, B. Acebedo, H. Anne, M. Lepoitevin, T. Rojo, M. Casas-Cabanas, *Investigation of sodium insertion-extraction in olivine Na_xFePO_4 ($0 \leq x \leq 1$) using first principle calculations*, Phys. Chem. Chem. Phys., 18(18) 13045, 2016

Oral presentation

H. Anne, D. Saurel, F. Nobili, *A comparative study of the ionic diffusion kinetics in Li_xFePO_4 and Na_xFePO_4 for Li and Na ion batteries*, E-MRS-Fall 2016, Varsovia

Posters

D. Saurel, H. Anne, F. Nobili, Deciphering the kineti limitarions of $NaFePO_4$: a comparative experimental study of Na^+ and Li^+ diffusion in $(Li,Na)_xFePO_4$, ICNaB 2018

H. Anne, D. Saurel, *New insights into the kinetics of Na insertion/extraction into the $FePO_4$/$NaFePO_4$ system*, Lithium battery discussions, Arcachon, june 2015

D. Saurel, H. Anne, M. Galceran, B. Acebedo, M. Lepoitevin, T. Rojo, M. Galceran, *New insights into the kinetics of Na insertion and extraction into the $FePO_4$/$NaFePO_4$ system*, ECS Meetings, 2015

D. Saurel, H. Anne, M. Galceran Mestres, B. Acebedo, M. Lepoitevin, T. Rojo, M. Casas-Cabanas, *New insights into the kinetics of Na insertion and extraction into the $FePO_4$/$NaFePO_4$ system*, 228th ECS meeting, Phoenix, 2015 (poster)

D. Saurel, H. Anne, M. Galceran Mestres, B. Acebedo, M. Lepoitevin, T. Rojo, M. Casas-Cabanas, *New insights into the kinetics of Na insertion and extraction into the $FePO_4$/$NaFePO_4$ system*, International Battery Association, Nantes, 2016 (poster)

Professional experience

2014-2018 **CIC Energigune**, Vitoria-Gasteiz (Spain), PhD in preparation about (de)intercalation kinetics on cathode insertion materials for sodium-ion batteries. Synthesis and physical characterization of electrode materials, formulation of electrodes and electrolytes, electrochemical characterization of electrodes. Collaboration with the universities of Camerino and Deakin. Three months stay at Camerino university in 2016 for the study of advanced electrochemical characterization techniques.

2013 **McDonald's**, Paris, crew, one year.

2012 **Renault/CEA Grenoble**, Paris/Chambéry, intern research engineer, six months, studies on fast electrical characterization of battery packs in collaboration with the CEA Grenoble; development of a project management tool.

2012 **Arkema**, Grenoble, six months, analysis post-mortem of electrodes and electrolytes for production of sodium chlorate.

2011 **Tata Steel Myriad**, Maubeuge, purchasing service assistant, three months.

2010 **Oberthur technologies**, Rennes, intern engineer, three months, evaluation of surface treatments as alternatives to electrolytic hard chromium coating of nickel plates.

2009 **ST Microelectronics**, Grenoble, nightworking maintenance technician in cleanroom, three months.

Language skills

French, English, Spanish